

Towards a Search for Heavy Neutral Leptons Decaying into Neutral Pions in the Short-Baseline Near Detector



Nguyen Vu Chi Lan

Supervisors: Prof. Vitaly Kudryavtsev
Prof. Neil Spooner

Department of Physics & Astronomy
University of Sheffield

This dissertation is submitted for the degree of
Doctor of Philosophy

October 2024

Abstract

The capability of the Short-Baseline Near Detector (SBND) to search for Heavy Neutral Leptons (HNLs) is assessed in this thesis. HNLs are proposed to be the right-handed heavy partner to the left-handed Standard Model (SM) neutrino, motivated by mechanisms of neutrino mass generation. HNLs can be produced from kaon decays in the Booster Neutrino Beam (BNB) and subsequently decay inside SBND, producing observable signals. This thesis focuses on HNLs decaying into a neutral pion that results in di-photon showers, of which this channel spans over the mass range of 140–260 MeV. SBND is a 112 ton liquid argon time projection chamber, which offers an exceptional energy, spatial and timing resolution, enabling the identification of the boosted topology and late arrival features of HNLs compared to SM neutrinos. In preparation for the search, the characterisation of the readout electronics' timing resolution is outlined and the calibration of charge signals addressing is also discussed. Selections of HNLs are presented, demonstrating a background rejection efficiency $\mathcal{O}(10^{-4})$ while maintaining $\sim 30\%$ of signals. An assessment of the detector performance under the assumption of an improved timing reconstruction is also given. A treatment of statistical and systematics uncertainties is outlined, followed by a procedure to set upper limits on the coupling $|U_{\mu 4}|^2$ of Majorana HNLs at the 90% confidence level. Three result scenarios are presented, demonstrating the current and potential capability of SBND.

Declaration

This thesis represents the original work of the author except for where specific references are made to the work of others. The presented work has not been submitted in whole or in part for consideration for any other degree or qualification in this, or any other university. Due to the collaborative nature of particle experiments, the thesis relies upon the work of collaborators from the Short-Baseline Near Detector (SBND) and other experiments.

The overviews of Heavy Neutral Leptons (HNLs) and physics of liquid argon time projection chambers, given in Chapters 2 and 3 respectively, contain work to which the author did not contribute. References assign credit for the work and figures presented.

The overview of SBND given in Chapter 4 relies on work performed by the entire SBND collaboration [1, 2]. Figures not made by the author are labelled with references to the source. In the scope of detector installation, the author carried out the cabling of the Photon Detection System (PDS) boxes and their installation to the detector alongside B. Carlson and B. Bogart. The author also installed the PDS readout electronics, under the guidance of M. Stancari and W. Badgett.

Also in Chapter 4, the flux prediction employs the Booster Neutrino Beam simulation developed in MiniBooNE [3]. The author validated the fluxes at SBND after an update to the kaon weights from SciBooNE [4]. The flux simulation was performed by Z. Pavlovic and the flux validation tool was developed by M. Del Tutto.

In Chapter 5, the generation of HNLs was done with the MeVPrtl generator, that was developed by G. Putnam and collaborators from SBND and ICARUS. The author implemented the timing simulation and validated the physics of HNL models employed by the generator with R. Alvarez-Garrote and L. Pelegrina-Gutierrez. The integration of the generator into SBND was performed together with R. Alvarez-Garrote. The author also identified a bug in the GENIE generator, that was fixed to enable the timing simulation of neutrino interactions.

Reconstruction and analysis tools presented in Chapter 6 were contributed by SBND collaborators with credits provided in the references. The Wirecell [5] and Pandora [6] packages were developed before the author's involvement. The author updated the track-shower separation algorithm within Pandora, building on earlier work by E. Tyley and D. Brailsford. The light reconstruction was pioneered by F. Nicolas-Arnaldos, R. Alvarez-Garrote, D. Garcia-Gamez and J. I. Crespo-Anadon and the cosmic ray tagger reconstruction was developed by H. Lay.

Assessments of the data acquisition timing performance in Chapter 7 rely on the setup of the White Rabbit timing system and the CRT Sharps before the author's involvement. The author installed and calibrated the SPEC-TDC module, and cabled timing signals under the guidance of M. Stancari, G. A. Lukhanin and W. Badgett. The author performed the timing characterisation of FEB modules with the inputs from M. Stancari and H. Lay. The author also validated the synchronisation of CAEN digitisers that lead to a new hardware implementation, with advices from M. Stancari.

In Chapter 8, the presented work in the scope of charge calibration was performed under the guidance of M. Mooney and many discussions with G. Putnam and J. Mueller. A summary of results from the ICARUS collaboration is included, with references assigned credit in the work and figures presented.

The selection of HNLs in Chapter 9 contains many elements shared among SBND collaborators. The author generated MC samples used in the selection together with H. Lay and R. Alvarez-Garrote. The author built the selection software using the framework from H. Lay. The selection employed the cosmic rejection tool CRUMBS developed by H. Lay, the flash matching tool OpT0 developed by L. Tung and the particle identification tool Razzled developed by H. Lay with groundwork from E. Tyley. The author also had many useful discussions with R. Alvarez-Garrote, L. Pelegrina-Gutierrez and J. I. Crespo-Anadon that guided the analysis.

The uncertainty reweighting in Chapter 10 was performed using the framework shared across the SBND and ICARUS collaboration, developed before the author's involvement. The author would like to thank H. Lay, J. Mueller, and J. Kim for their help in understanding uncertainty treatments. The procedure to set upper limits was performed using the pyhf package [7], with references assign credit for the employed statistical methods [8–10].

Nguyen Vu Chi Lan
October 2024

Acknowledgements

First and foremost, I would like to thank my mom and dad for supporting me emotionally and financially through my PhD. I appreciate their trust in me to follow my passion in a foreign country away from home. Without them, I would not be where I am today.

I would like to thank my supervisors Neil for accepting me into the physics program at Sheffield and Vitaly for taking the lead in the supervisor role. I am grateful for the autonomy and freedom to explore my physics interests. I understand that my PhD journey was a wild card with unfamiliar research topics and multiple last minute trips to Fermilab. Yet, they remained as accommodating and guiding as ever to keep me on the right track.

October 2020, at the peak of Covid, was certainly an odd time to move to a new city. Somehow, the Sheffield group made it feel like home. Anthony and Ala, thank you for teaching me about actual hardware. Ed, thank you for teaching me every possible thing that a first year PhD student should know. Rhiannon and Anna, despite your later arrival, your support and positivity only add to my experience at Sheffield.

Ali, you were my very first friend in Sheffield and another fellow sharing the same PhD boat as me. As promised, I truly appreciate our Wednesday KFC after lab teaching, late night fried chicken orders and many more chicken-related memories that keep me afloat through difficult times.

Working at SBND has only been an amazing experience that reassures my decision to pursue physics. I owe thanks to so many people across various working groups for their support towards the completion of this thesis, and many more thanks to everyone in SBND for giving into my ideas during my term as SBND young representative. Most importantly, I would like to give a special thanks to Michelle for her guidance not only at Fermilab but also on my journey at SBND.

the-real-sbnd, your friendships cannot go unmentioned. Especially, Henry, this thesis would not exist without your help on every front. Jiaoyang, thank you for joining the production team with me. Rodrigo, thank you for cross checking every step of my analysis.

Fran, thank you for answering all my dumb PDS-related questions. Lynn, thank you for all the plants and cat photos. Bear, thank you for gaining me access to Zuko and Roo. Mun, thank you for my very first Chicago tour. Thanks you guys for all the jokes and rants as we were doing our best to navigate our PhDs.

Finally, Lane, words cannot describe your unconditional support through this entire journey. Thank you for everything!

Table of contents

List of figures	xv
List of tables	xxi
Nomenclature	xxiii
1 Introduction	1
2 Heavy Neutral Leptons	3
2.1 Motivation of Heavy Neutral Leptons	4
2.2 Production of Heavy Neutral Leptons	7
2.3 Decay Channels of Heavy Neutral Leptons	9
2.4 Previous Searches For Heavy Neutral Leptons	12
2.4.1 Peak Searches	13
2.4.2 Decay Searches	14
2.5 Concluding Remarks	17
3 Physics of Liquid Argon Time Projection Chambers	19
3.1 Overview of Liquid Argon Time Projection Chambers	20
3.2 Particle Interactions in Liquid Argon	22
3.2.1 Production of Ionisation Electrons	22
3.2.2 Production of Scintillation Photons	24
3.2.3 Recombination	26

3.3	Particle Propagation in Liquid Argon	28
3.3.1	Ionisation Electron Drift	28
3.3.2	Scintillation Photon Propagation	30
3.4	Detection of Electrons and Photons	32
3.4.1	Wire Planes	32
3.4.2	Photomultiplier Tubes and X-ARAPUCAs	33
3.5	Concluding Remarks	35
4	The Short-Baseline Near Detector and Booster Neutrino Beam	37
4.1	The Short-Baseline Near Detector Physics Program	38
4.2	The Short-Baseline Near Detector	40
4.2.1	Time Projection Chamber	41
4.2.2	Photon Detection System	42
4.2.3	Cosmic Ray Tagger	44
4.2.4	Readout Electronics	45
4.2.5	Hardware Trigger	46
4.2.6	Data Acquisition	47
4.2.7	Event Building	48
4.3	The Booster Neutrino Beam	50
4.4	Concluding Remarks	53
5	Simulation Framework of SBND	55
5.1	Overview of the Simulation Framework	55
5.2	HNL Generator: MeVPrtl	56
5.3	Standard Model Generators	61
5.3.1	Neutrino Generator: GENIE	61
5.3.2	Cosmic Generator: CORSIKA	63
5.4	Particle Propagation and Detector Response Simulation	64
5.4.1	Particle Propagation Simulation	64

Table of contents

5.4.2	Wire Response Simulation	65
5.4.3	Photon Detection System Response Simulation	65
5.4.4	Cosmic Ray Tagger Response Simulation	66
5.5	Concluding Remarks	67
6	Reconstruction Framework of SBND	69
6.1	Overview of the Reconstruction Framework	70
6.2	Time Projection Chamber Reconstruction	70
6.2.1	Signal Processing and Hit Finding	71
6.2.2	Pandora Pattern Recognition	72
6.2.3	Track-Shower Separation Boosted Decision Tree	73
6.3	Photon Detection System and Cosmic Ray Tagger Reconstruction	77
6.3.1	Photon Detection System Reconstruction	77
6.3.2	Cosmic Ray Tagger Reconstruction	79
6.4	High Level Analysis Tools	80
6.4.1	Subsystem Matching	81
6.4.2	Cosmic Rejection	82
6.4.3	Particle Identification	82
6.5	Concluding Remarks	83
7	Timing Performance of the Data Acquisition System	85
7.1	Timing Reference System of the Data Acquisition	85
7.1.1	Time and Frequency Transfer to Subsystems	86
7.1.2	Precise Timestamping	87
7.2	Timing Performance of Front End Board Modules	89
7.2.1	Evaluation of Internal Clock Resolution	89
7.2.2	Alternative Timing Reconstruction	92
7.3	Timing Performance of CAENV1730 Digitisers	94
7.3.1	Internal Clock and Timestamp Structure	94

7.3.2	Evaluation of Clock Synchronisation	96
7.3.3	Clock Jittering Correction	99
7.4	Concluding Remarks	103
8	Calibration of Time Projection Chambers	105
8.1	Electron Lifetime Measurement	105
8.1.1	Electron Lifetime Extraction Procedure	106
8.1.2	Bias Study of Diffusion and Space Charge Effects	109
8.2	Delta Ray Fluctuations on Recombination	111
8.2.1	Simulation of Delta Rays and Recombination	112
8.2.2	Impacts of Delta Rays on Recombination Magnitude	114
8.2.3	Impacts of Delta Rays on Recombination Smearing	117
8.2.4	Recombination Studies from the ICARUS Experiment	119
8.3	Concluding Remarks	121
9	Selection of Heavy Neutral Leptons	123
9.1	Selection Introduction	124
9.1.1	Signal and Background Definitions	124
9.1.2	Description of Monte Carlo Samples	126
9.1.3	Selection Efficiency Definition	127
9.1.4	The Arrival Time Distribution	128
9.2	Cosmic Background Removal	129
9.2.1	Pandora Cosmic Removal	129
9.2.2	Beam Spill Cut	129
9.2.3	CRUMBS Cut	130
9.3	Neutrino Background Removal	131
9.3.1	Fiducial Volume Cut	131
9.3.2	Number of Hits Cut	132
9.3.3	Neutrino Track Removal	133

Table of contents

9.4 Heavy Neutral Lepton Shower Selection	135
9.4.1 Electron Shower Removal	137
9.4.2 Track Score Cut	138
9.4.3 Calorimetry Cut	139
9.4.4 Theta Angle Cut	140
9.4.5 Neutral Pion Invariant Mass Cut	142
9.5 Selection Results	142
9.6 Study of Timing Resolution Improvement	146
9.7 Concluding Remarks	149
10 Limits Predictions for Heavy Neutral Leptons at SBND	151
10.1 Uncertainty Assessment	152
10.1.1 The Reweighting Method	152
10.1.2 Uncertainty Propagation	154
10.1.3 Uncertainties of Heavy Neutral Leptons	154
10.1.4 Uncertainties of Neutrino and Cosmic Backgrounds	157
10.2 Limits Setting Procedure	160
10.2.1 Hypothesis Definition	160
10.2.2 Likelihood-based Test Statistic	161
10.2.3 The CL_s Method	163
10.2.4 Computing Test Statistic Distributions	164
10.2.5 Setting the Upper Limits	164
10.3 Results	166
10.3.1 Comparison Across Different Arrival Time Distributions	168
10.3.2 Comparison With Other Experiments	170
10.4 Concluding Remarks	173
11 Conclusions	175
References	179

Appendix A	Hardware Triggering at SBND	187
Appendix B	Data Streaming at SBND	189
Appendix C	Timing Distribution at SBND	191
Appendix D	Lenient Arrival Time Distributions	193
Appendix E	Stringent Arrival Time Distributions	195
Appendix F	Smeared True Arrival Time Distributions	197

List of figures

2.1	Neutrino and Heavy Neutral Lepton Production Feynman Diagrams	7
2.2	Kinematic Factor of Heavy Neutral Leptons	9
2.3	Branching Ratio of Heavy Neutral Leptons	11
2.4	Heavy Neutral Lepton and Neutral Pion Decay Feynman Diagrams	12
2.5	Experimental Limits on the Coupling $ U_{\mu 4} ^2$ of Heavy Neutral Leptons	16
3.1	Liquid Argon Time Projection Chamber Diagram	21
3.2	Muon Energy Loss in a Copper Medium	23
3.3	Mean Free Path of Photons in Liquid Argon	24
3.4	Event Display of a Neutrino Interaction	25
3.5	Energy Deposition in Liquid Argon Diagram	25
3.6	Recombination Factor in Liquid Argon	26
3.7	Charge and Light Yield as a Function of Electric Field	28
3.8	Impacts of Space Charge Effects on Tracks	30
3.9	Group Velocity and Rayleigh Scattering Length of Photons in Liquid Argon .	31
3.10	Induced Currents on an Induction and a Collection Wire Plane	33
3.11	X-ARAPUCA Diagram	34
4.1	Short-Baseline Neutrino Program	38
4.2	Short-Baseline Near Detector 3D Model	40
4.3	Anode Plane Assemblies Schematic	41
4.4	Time Projection Chamber Photographs	42

4.5	Photon Detection System 3D Model	43
4.6	Cosmic Ray Tagger Diagrams	44
4.7	Data Acquisition Flow Chart	48
4.8	Chronological Structure of a Physics Event Diagram	49
4.9	Booster Neutrino Beam Measured by SBND CRTs in 2017-2018	50
4.10	Particle Production in the Booster Neutrino Beam	51
4.11	Simulated Fluxes of Secondary Mesons	52
4.12	Simulated Neutrino Fluxes at the Front Face of SBND	53
5.1	Simulation Framework of SBND	56
5.2	MeVPrtl Generator Workflow	57
5.3	Simulated Energy Spectra of HNLs Decaying Inside SBND	58
5.4	Simulated Kinematics Distributions of Neutral Pions from HNLs	59
5.5	Time of Flight of Particles from the BNB to SBND Diagram	60
5.6	Arrival Time of SM Neutrinos and HNLs at the Front Face of SBND	60
5.7	Modulus of the Arrival Time Distibutions of SM Neutrinos and HNLs	61
5.8	Volume Boundary of the GENIE Generator	63
6.1	Reconstruction Framework of SBND	70
6.2	Event Displays of a Neutrino Interaction Before and After Signal Processing	71
6.3	Hit Finding Diagram	72
6.4	Cone-like Variable Diagrams	75
6.5	New Variable Distributions of the Track-Shower Separation BDT	76
6.6	Score Distributions of the Updated Track-Shower Separation BDT	77
6.7	Waveform Deconvolution and Hit Finding on PMT Waveforms	78
6.8	Reconstructed Light Yield and Reconstructed Timing Resolutions and Biases at SBND	80
7.1	White Rabbit Timing System Distribution	86
7.2	SPEC-TDC Module and Its Input Signals	88

List of figures

7.3	CRT Sharps Setup	90
7.4	Variation of T0 Timestamps of T0 Clock Reset Events Against Event Number	91
7.5	Variation of T0 Timestamps of T1 Clock Reset Events Against Event Number	91
7.6	Variation of T0 Timestamps of T1 Clock Reset Events Against T0 Timestamp	92
7.7	Reconstructed Beam Spill Using CRT Sharps	93
7.8	Reconstructed Beam Bucket Using CRT Sharps	94
7.9	Timing Structure of a Waveform Digitised by CAEN	95
7.10	Clock Synchronisation Schemes	96
7.11	Variation of CAEN Timestamps Using the Daisy Chain Clock Scheme	98
7.12	Variation of CAEN Timestamps Using the Fan Out Clock Scheme	98
7.13	Digisted Waveforms of Trigger Signals	100
7.14	Clock Jittering Correction Performed on Trigger Waveforms	101
7.15	Results of Clock Jittering Correction	102
8.1	Cathode Stitching Diagram	107
8.2	dQ/dx Profile Fitted With a Laundau-Gaussian	108
8.3	Most Probable Value dQ/dx Against Drift Time	109
8.4	Electron Lifetime Measurement Biases	110
8.5	Event Display of a Cosmic Muon and Delta Rays	112
8.6	Charge to Energy Loss Conversion of a 1 GeV Proton	115
8.7	Impacts of Delta Ray Fluctuations on Protons	115
8.8	Charge to Energy Loss Conversion of a 1 GeV Muon	116
8.9	Impacts of Delta Ray Fluctuations on Muons	117
8.10	Energy-Residual Range of Protons at Different Delta Ray Thresholds	119
8.11	Energy-Residual Range of Muons at Different Delta Ray Thresholds	120
8.12	Recombination Factor Against Delta Ray Threshold	121
9.1	Event Display of Di-Photon Showers From Heavy Neutral Leptons	125
9.2	Event Display of a Neutral Current Interaction Containing a Neutral Pion . .	125

9.3 Event Display of a Charged Current Interaction Containing a Muon and a Proton	126
9.4 Beam Spill Cut	130
9.5 CRUMBS Cut	131
9.6 Fiducial Volume Cut	132
9.7 Number of Hits Cut	133
9.8 Muon Cuts	134
9.9 Proton and Pion Cuts	136
9.10 Electron Cut	137
9.11 Track Score Cut	138
9.12 Calorimetry Cut	140
9.13 Theta Angle Cut	141
9.14 Neutral Pion Invariant Mass Cut	142
9.15 Arrival Time Distributions After Selection	145
9.16 Summary of Selection Efficiency.	145
9.17 Smearing Contributors to the Arrival Time	146
9.18 Arrival Time of SM Neutrinos from True and Reconstructed Variables	147
9.19 Arrival Time of SM Neutrinos with an Improved Timing Resolution	148
9.20 Arrival Time of SM Neutrinos and HNLs with an Improved Timing Resolution	149
10.1 Uncertainties of Heavy Neutral Leptons	156
10.2 Total Uncertainty and Fractional Uncertainties of Heavy Neutral Leptons . .	156
10.3 Uncertainties of SM Neutrinos and Cosmic Backgrounds	159
10.4 Total Uncertainty and Fractional Uncertainties of SM Neutrinos and Cosmic Backgrounds	159
10.5 Distribution of Test Statistics Acquired from Asymptotic Approximation . .	164
10.6 Arrival Time Distributions input to the Limits Setting	167
10.7 Expected Limits on the Coupling $ U_{\mu 4} ^2$ for Majorana HNLs	168

List of figures

10.8 Comparison Between Limits Setting using the Entire Distribution and Only Edge Bins	169
10.9 Comparison Between Limits Setting using the Lenient, Stringent and Smeared True Distribution	170
10.10 Comparison Between SBND Expected Limits and Existing Limits	172
A.1 Hardware Triggering Distribution	188
B.1 Grafana Online Monitoring Web Page	190
B.2 Minargon Online Monitoring Web Page	190
C.1 Clock Signal Distribution	191
C.2 PPS Signal Distribution	192
D.1 Lenient Arrival Time Distributions in the Mass Range 140 - 160 MeV	193
D.2 Lenient Arrival Time Distributions in the Mass Range 180 - 260 MeV	194
E.1 Stringent Arrival Time Distributions in the Mass Range 140 - 160 MeV	195
E.2 Stringent Arrival Time Distributions in the Mass Range 180 - 260 MeV	196
F.1 Smeared True Arrival Time Distributions in the Mass Range 140 - 160 MeV	197
F.2 Smeared True Arrival Time Distributions in the Mass Range 180 - 260 MeV	198

List of tables

9.1 Summary of the Lenient and Stringent Selection	144
10.1 Summary of Uncertainty Constraints	166
10.2 Summary of Expected Limits on the Coupling $ U_{\mu 4} ^2$ of Majorana HNLs . . .	171

Nomenclature

AC Alternating Circuit

APA Anode Plane Assemblies

ArgoNeuT Argon Neutrino Teststand

AV Active Volume

BDT Boosted Decision Tree

BNB Booster Neutrino Beam

BSM Beyond the Standard Model

C.L. Confidence Level

CC Charged Current

CE Cold Electronics

CERN European Organisation for Nuclear Research

CPA Cathode Plane Assembly

CPT Charge Parity Time symmetries

CRT Cosmic Ray Tagger

CRUMBS Cosmic Rejection Using a Multi-system Boosted decision tree Score

CV Central Value

DAQ Data Acquisition

DCA Distance of Closest Approach

DUNE Deep Underground Neutrino Experiment

ETRIG Event TRIGger

FD Fine Delay

FEB Front End Board

FMC Field programmable gate arrays Mezzanine Card

FTRIG Flash TRIGger

FV Fiducial Volume

HNL Heavy Neutral Lepton

ICARUS Imaging Cosmic And Rare Underground Signals

KDAR Kaon Decay At Rest

KE Kinetic Energy

KEK High Energy Accelerator Research Organization (Kō Enerugī Kasokuki Kenkyū Kikō)

LArTPC Liquid Argon Time Projection Chamber

LSND Liquid Scintillator Neutrino Detector

MC Monte Carlo

MCS Multiple Coulomb Scattering

MicroBooNE Micro Booster Neutrino Experiment

MiniBooNe Mini Booster Neutrino Experiment

MIP Minimum Ionising Particle

ModBox Modified Box

MTC/A Master Trigger Card Analog

NC Neutral Current

Nomenclature

NTB Nevis Trigger Board

NTP Network Time Protocol

NuMI Neutrinos at the Main Injector beam

NuTeV Neutrino at the Tevatron

PDF Probability Density Function

PDS Photon Detection System

PE PhotoElectron

PID Particle IDentification

PIENU Pion → Electron + Neutrino

PMNS Pontecorvo-Maki-Nakagawa-Sakata

PMT PhotonMultiplier Tube

POT Protons On Target

PPS Pulse Per Second

PTB Penn Trigger Board

QCD Quantum Chromodynamics

QE Quantum Efficiency

RWM Resistor Wall Monitor

SBN Short-Baseline Neutrino

SBND Short-Baseline Near Detector

SCE Space Charge Effect

SER Single Electron Response

SIN Swiss Institute for Nuclear Research

SiPM Silicon PhotoMultiplier

SM Standard Model

SPEC Simple PCIe FMC Carrier

SVEC Simple VME FMC Carrier

T2K Tokai to Kamioka

TAI Coordinated Universal Time

TDC Time to Digital Converter

TPB TertraPhenyl Butadiene

TPC Time Projection Chamber

UTC International Atomic Time

VUV Vacuum Ultraviolet

WIB Warm Interface Board

WR White Rabbit

Chapter 1

Introduction

This thesis provides the first assessment of the Short-Baseline Near Detector (SBND) capability to search for Heavy Neutral Leptons (HNLs). Chapter 2 begins with the motivation of HNLs that allows for the generation of Standard Model (SM) neutrino mass. An overview of a minimal HNL model is given, covering the production and decay of HNLs. The focus is on kinematically allowed channels that can be produced from the Booster Neutrino Beam (BNB) and subsequently decay inside SBND.

A description of the Liquid Argon Time Projection Chamber (LArTPC) is provided in Chapter 3, which is the main detection technology of SBND. The operating principles are presented, identifying key physical processes of the two main observable signals, ionisation electrons and scintillation photons, that underpin the performance of LArTPCs.

An overview of the SBND and the BNB is covered in Chapter 4. The chapter begins with the physics program of SBND, followed by the detector design, describing each subsystem that comprises the detector. The BNB is discussed next, detailing the beam design and presenting the secondary meson fluxes and neutrino fluxes arriving at SBND.

The simulation framework at SBND is outlined in Chapter 5, to produce Monte Carlo (MC) samples representing data. A description of different generators to simulate SM neutrinos, cosmic muons and HNLs is first provided. The HNL generator is covered in detail to illustrate the physics behind the late arrival of HNLs compared to SM neutrinos, which the work presented in later chapters relies upon. Finally, the simulation of the particle propagation and the detector response is summarised.

Moreover, the reconstruction framework is provided in Chapter 6, covering the reconstruction for each detection subsystem: (1) TPC, (2) Photon Detection System (PDS) and (3) Cosmic Ray Tagger (CRT). Specifically in the TPC reconstruction workflow, an update

to an algorithm separating track-like and shower-like reconstructed objects is detailed. An overview of some high-level analysis tools, combining complementary signals from all subsystems, is given next.

Chapter 7 outlines the timing performance of the Data Acquisition (DAQ) at SBND. The chapter begins with a description of the White Rabbit timing system to maintain timing synchronisation across different DAQ subsystems. The timing precision of the readout electronics of the CRT and PDS are then assessed, which are the two detection subsystems with timing resolution $\mathcal{O}(2\text{ ns})$.

Charge calibration is discussed in Chapter 8 with two specific studies. The first study is on the measurement of electron lifetime, performed on MC samples of anode-to-cathode crossing cosmic muon tracks that fully traverse the detector volume. The second study is to assess the impacts of delta ray fluctuations on recombination, also performed on MC samples with varying delta ray thresholds.

Selection procedures to identify HNL signals and reject backgrounds from SM neutrinos and cosmic muons are presented in Chapter 9. Signal and background definitions are provided, followed by a description of MC samples used to perform the selection. Cuts for rejecting tracks from cosmic muons and SM neutrinos are detailed, followed by cuts optimised to identify HNL showers. Results of the selection are summarised next, followed by a study under the assumption of an improved timing reconstruction.

The capabilities of SBND to search for HNLs are assessed in Chapter 10. The sensitivity is chosen to be the upper limits on the coupling $|U_{\mu 4}|^2$ of Majorana HNLs at the 90% confidence level assuming no detected signals, such that the results can be directly compared against existing limits. Treatments of uncertainties of HNLs, SM neutrinos and cosmic muons are discussed. The limits setting procedure is detailed next. Expected limits are presented for three scenarios that can be achieved at SBND. A discussion of the results is then given with some suggestions for future iterations of this work.

Chapter 2

Heavy Neutral Leptons

The Standard Model (SM) of particle physics is a successful theory describing the fundamental particles and the forces that govern them. Neutrinos are the neutral particles of the lepton family, only interacting via weak and gravitational forces. Observations of neutrino flavour oscillations arise from the mixing between the flavour and mass neutrino eigenstates, implying that neutrinos have mass. However, the mass generation of neutrinos remains a phenomenon that cannot be explained by the SM.

The mass generation of neutrinos motivates a new neutrino state. If the new state is right-handed, the Dirac mass term can be constructed via the Higgs mechanism. On the other hand, if the new state is its own particle and antiparticle, the Majorana mass term can be built instead. Under the assumption that the new state is heavier than neutrinos, it enables the seesaw mechanism that can explain the lightness of neutrinos. The heaviness of this new state gains it the name *Heavy Neutral Lepton* (HNL). HNLs are proposed to interact with SM gauge bosons, allowing them to be produced and decay via SM gauge interactions. This leads to the focus of this work on the search for HNLs in the mass range $\mathcal{O}(100 \text{ MeV})$ that are produced from the Booster Neutrino Beam (BNB) and then decay into SM observables inside the Short-Baseline Near Detector (SBND).

This chapter provides an overview on the theory of HNLs and a summary of search results for their existence. In Section 2.1, the motivation of HNLs as a minimal extension to the SM is presented. Section 2.2 provides the explanation for the production mechanism of HNLs from meson decays. Following this, Section 2.3 covers the details of HNLs decaying into SM observables. Section 2.4 then summarises the existing upper limits on the coupling and mass phase space of HNLs through two different experimental methods: peak searches and decay searches. Finally, Section 2.5 provides some concluding remarks.

2.1 Motivation of Heavy Neutral Leptons

The phenomenon of three-flavour neutrino oscillation is well-established. Neutrinos are produced and detected as their flavour eigenstates ν_μ , ν_e , ν_τ , where the flavour eigenstate is a linear combination of mass eigenstates ν_1 , ν_2 , ν_3 . Neutrino oscillations are a consequence of the mixing between the flavour and mass eigenstates [11]. The mass eigenstate dictates the propagation of neutrinos in space and time. Over a propagation distance, each mass eigenstate evolves at a different rate due to their momenta differences, resulting in a different composition of mass eigenstates, and consequently, a different flavour eigenstate.

The three-flavour oscillations can be alternatively approximated to two-flavour oscillations, involving only two flavour eigenstates and two mass eigenstates. In this simplified model, the probability of detecting the neutrino flavour ν_α as another neutrino flavour ν_β with energy E after travelling a distance L is as follows [11]:

$$P(\nu_\alpha \rightarrow \nu_\beta) = \sin^2(2\theta)\sin^2\left(\frac{\Delta m^2 L}{4E}\right), \quad (2.1)$$

where θ is the mixing angle describing how different the flavour eigenstate is to the mass eigenstate and Δm^2 is the mass squared difference of the two mass eigenstates. For neutrino oscillations to occur, Δm^2 must be non-zero, directly implying that neutrinos must have mass. In the context of the three-flavour oscillations, this requires the existence of non-zero mass for at least two out of the three neutrino eigenstates. Whilst the SM of particle physics has proved extremely successful, unfortunately, it currently provides no mechanism for the mass generation of neutrinos. The absence of a right-handed chiral partner to the left-handed chiral neutrino means that no Dirac mass term can be built via the Yukawa coupling of the Higgs to the opposite chirality fields.

This motivates the introduction of a right-handed neutrino such that the neutrino mass can be constructed using the same recipe as all other SM particles. The Dirac mass term in the neutrino Lagrangian after spontaneous symmetry breaking is as follows [11]:

$$\mathcal{L}_D = -m_D (\bar{\nu}_L \nu_R + \bar{\nu}_R \nu_L), \quad (2.2)$$

where $m_D = Y \nu / \sqrt{2}$ is the Dirac mass, Y is the Yukawa coupling, ν is the Higgs vacuum expectation value, and the subscript R and L denotes the right and left chiral state of the ν neutrino and $\bar{\nu}$ anti-neutrino field.

2.1 Motivation of Heavy Neutral Leptons

While the Dirac mass term requires the existence of both left and right-handed chiral states, the Majorana mass term proposed by Ettore Majorana in 1937 requires only one chiral state [12]. Under the condition that a particle is its own antiparticle, the charge conjugation operator C can be applied to ν_R such that $\nu_R^C = C\bar{\nu}_R^T$, where the resulting ν_R^C has the correct properties to be used in place of ν_L in Eq. 2.2 [13]. The construction of the Majorana state violates the charge conservation and is forbidden for any other SM particles except for neutrinos due to their neutral charges. In this case, the Majorana mass term in the neutrino Lagrangian is as follows [13]:

$$\mathcal{L}_M = -\frac{1}{2}M\left(\bar{\nu}_R^C\nu_R + \bar{\nu}_R\nu_R^C\right), \quad (2.3)$$

where M is the Majorana mass. The factor of a half is introduced to account for double counting since the term $\bar{\nu}_R$ and ν_R^C are not independent.

A right-handed neutral state provides a hypothetical neutrino mass mechanism not only via the Dirac or the Majorana mass term but also by combining both mass terms. A generalised Lagrangian in this case is as follows [11]:

$$\mathcal{L}_{DM} = -\frac{1}{2}\left[m_D\bar{\nu}_L\nu_R + m_D\bar{\nu}_R^C\nu_L^C + M\bar{\nu}_R^C\nu_R\right] + h.c. \quad (2.4)$$

The Lagrangian presented here allows for the seesaw mechanism to construct the physical masses of SM neutrinos assuming the Majorana mass term is much larger than the Dirac mass term, $M \gg m_D$ [11, 14]. Under the assumption of only two neutrino states for simplicity, the seesaw mechanism would give the mass of a left-handed neutrino state $m_\nu \approx \frac{m_D^2}{M}$ and a right-handed neutrino state $m_N \approx M$, such that the heaviness of m_N suppresses the physical mass of the left-handed neutrino m_ν . For the existing upper limits on $m_\nu \ll 1$ eV, this simple model would predict $M \sim 10^{15}$ eV. Thus, a right-handed heavy neutrino state is a very attractive addition to the SM as an answer to the neutrino mass mechanism, explaining the extreme lightness of SM neutrinos.

The neutral nature of right-handed neutrinos requires all SM charges to be zero, implying that they do not interact directly via the strong, electromagnetic, or weak forces. These weaker-than-weak right-handed particles are often referred to as *sterile neutrinos*. The only direct coupling to the new sterile state is the neutrino-Higgs interaction. This leads to mixing-mediated interactions with SM gauge bosons, allowing them to be produced and decay via SM gauge interactions with a rate suppressed by the coupling [15]. The mass range of sterile neutrinos can span over many orders of magnitudes, and the number of flavour or mass states is unconstrained.

In the mass range $\mathcal{O}(1 \text{ eV})$, they are known as *light* sterile neutrinos and are proposed to participate in oscillation with SM neutrinos. Over a short baseline distance, the addition of a single light sterile neutrino to neutrino oscillations might enhance or reduce the number of observed neutrino interactions for a given channel. Particularly, this model can explain the outstanding anomaly observed by the LSND [16] and MiniBooNE experiments [17], where an excess of ν_e and $\bar{\nu}_e$ interactions was measured at low energy [18].

In the mass range $>\mathcal{O}(10 \text{ eV})$, sterile neutrinos are now considered *heavy* since they are significantly more massive compared to SM neutrinos. This gains them the name *Heavy Neutral Leptons* (HNLs). HNLs do not participate in oscillation with SM neutrinos due to coherence loss [15]. As a consequence of being heavier than SM neutrinos, the wave packet of HNLs moves much slower compared to that of neutrinos and immediately undergoes propagation decoherence. Instead, HNLs are proposed to travel over some distance before decaying into SM observables.

Different theoretical models of HNLs have been developed, and a comprehensive review can be found in Ref. [19]. One particular model is the extension of the Minimal Standard Model, νMSM , which introduces three flavours of HNLs [20, 21]. It aims to solve some key problems of the SM while staying consistent with existing neutrino oscillation results, provided that the masses and couplings of HNLs are within a specific domain. The first and lightest HNL can serve as a candidate for dark matter, whereas the two heavier HNLs enable the seesaw mechanism to generate neutrino masses. Having two heavier HNLs also explains leptogenesis. As they are produced in the early Universe, the CP violation of their oscillations leads to lepton asymmetry, and consequently, matter-antimatter asymmetry.

In the search for HNLs presented here, the existence of HNLs is explored in a minimal way by assuming an addition of a single HNL to the SM. From a generic phenomenological approach, an HNL can be added to the SM by extending the Pontecorvo-Maki-Nakagawa-Sakata (PMNS) matrix. The PMNS matrix, describing the coupling of the SM neutrino flavour eigenstate ν_α ($\alpha = e, \mu, \tau$), and the mass eigenstate ν_i ($i = 1, 2, 3$), is as follows:

$$U_{PMNS} = \begin{pmatrix} U_{e1} & U_{e2} & U_{e3} \\ U_{\mu 1} & U_{\mu 2} & U_{\mu 3} \\ U_{\tau 1} & U_{\tau 2} & U_{\tau 3} \end{pmatrix}. \quad (2.5)$$

The flavour eigenstate ν_α undergoes weak interaction, whilst the mass eigenstate ν_i describes the neutrino propagation in space and time. For the addition of a single right-handed neutrino with mass m_N , the PMNS matrix can be extended to describe the mass

2.2 Production of Heavy Neutral Leptons

mixing between SM neutrinos and the new flavour eigenstate N as follows:

$$U_{PMNS}^{Extended} = \begin{pmatrix} U_{e1} & U_{e2} & U_{e3} & U_{e4} \\ U_{\mu 1} & U_{\mu 2} & U_{\mu 3} & U_{\mu 4} \\ U_{\tau 1} & U_{\tau 2} & U_{\tau 3} & U_{\tau 4} \\ U_{N1} & U_{N2} & U_{N3} & U_{N4} \end{pmatrix}, \quad (2.6)$$

where the index 4 is reserved for the new mass eigenstate. The flavour eigenstate ν_α of SM neutrinos can be written as the linear combination of the mass eigenstate ν_i and the HNL flavour eigenstate N as follows:

$$\nu_\alpha = \sum_i U_{\alpha i} \nu_i + U_{\alpha 4} N, \quad (2.7)$$

where the coupling $U_{\alpha i}$ ($\alpha = e, \mu, \tau$ and $i = 1, 2, 3$) are elements of the SM PMNS matrix, and the coupling $U_{\alpha 4}$ are the extension. For simplicity, this work only considers an HNL coupling to only one flavour at a time, such that at most only one of the three couplings U_{e4} , $U_{\mu 4}$ and $U_{\tau 4}$ is non-zero.

2.2 Production of Heavy Neutral Leptons

In any SM neutrino production processes, HNLs can be produced in place of neutrinos with a rate suppressed by the coupling $|U_{\alpha 4}|^2$, if kinematically allowed. Fig. 2.1a illustrates the two-body decay of a charged kaon K^+ producing a muon neutrino ν_μ and Fig. 2.1b illustrates the substitution of the ν_μ with an HNL N having $L = +1$ mediated by the coupling $|U_{\alpha 4}|^2$. This implies that HNLs can be probed from the BNB, which is an abundant source of mesons and is further detailed in Section 4.3. Since the BNB is primarily made up of positively charged mesons, the following section mainly focuses on the mesons K^+ and π^+ .



Fig. 2.1 Feynman diagrams of (a) $K^+ \rightarrow \mu^+ \nu_\mu$ and (b) $K^+ \rightarrow \mu^+ N$.

In general, the branching ratio $Br(m^+ \rightarrow l_\alpha^+ N)$ of a two-body decay of a charged meson m^+ into a lepton l_α^+ ($\alpha = e, \mu, \tau$) and an HNL N can be expressed in terms of the analogous branching ratio into an SM neutrino as follows [22]:

$$Br(m^+ \rightarrow l_\alpha^+ N) = Br(m^+ \rightarrow l_\alpha^+ \nu_\alpha) \left(\frac{|U_{\alpha 4}|^2}{1 - |U_{\alpha 4}|^2} \right) \rho_N \left(\frac{m_{l_\alpha}^2}{m_{m^+}^2}, \frac{m_N^2}{m_{m^+}^2} \right), \quad (2.8)$$

where $Br(m^+ \rightarrow l_\alpha^+ \nu_\alpha)$ is the branching ratio of the charged lepton m^+ decaying into a lepton l_α^+ and an SM neutrino ν_α , m_{m^+} is the mass of the charged meson, m_{l_α} is the mass of the daughter lepton and m_N is the mass of the daughter HNL. The kinematic factor ρ_N accounts for the available phase space of the daughter HNL in the decay. The complete expansion of the factor is as follows [22]:

$$\rho_N(x, y) = \frac{(x + y - (x - y)^2) \sqrt{1 + x^2 + y^2 - 2(x + y + xy)}}{x(1 - x)^2}, \quad (2.9)$$

where $x = m_{l_\alpha}^2 / m_{m^+}^2$ and $y = m_N^2 / m_{m^+}^2$.

The kinematic factor ρ_N in Eq. 2.9 is plotted in Fig. 2.2, for $l_\alpha = \mu^+, e^+$ and $m^+ = \pi^+, K^+$ in the range $0 \leq m_N \leq 500$. Four HNL production channels that are probable at the BNB are shown: (1) $K^+ \rightarrow Ne^+$ in the dashed red line, (2) $K^+ \rightarrow N\mu^+$ in the solid pink line, (3) $\pi^+ \rightarrow Ne^+$ in the dashed dark blue line and (4) $\pi^+ \rightarrow N\mu^+$ in the solid light blue line. Production channels associated with the τ -flavour coupling are not shown since they are kinematically forbidden for the BNB energies. The kinematic factor for each illustrated channel is constrained by the available mass after the two-body decay of the parent meson. The upper limit of the HNL mass is therefore $m_N = m_{m^+} - m_{l_\alpha}$ ($\alpha = e, \mu$), as shown by the vertical grey lines. Here it can be seen that the HNL production from π^+ decays limits the HNL mass to < 140 MeV while the HNL production from K^+ decays allows for the HNL mass up to 495 MeV. Thus, the search for HNLs presented here focuses on the HNL production channel from K^+ to probe mass as high as 495 MeV.

Furthermore, the magnitude of the kinematic factor of the HNL production shown in Fig. 2.2 is larger than 1, indicating an enhancement to the production rate relative to the SM neutrino. This is because of the helicity suppression observed in mesons decaying into an SM neutrino having an opposite effect for mesons decaying into an HNL [22]. Instead, it is helicity *enhancement* as HNLs prefer to emerge from the decay as right-handed. For the HNL production channel that this work focuses on, a significant enhancement is evident for the production rate of $K^+ \rightarrow Ne^+$ as it increases by a factor of 10^5 . On the other hand,

2.3 Decay Channels of Heavy Neutral Leptons

the kinematic factor of $K^+ \rightarrow N\mu^+$ only peaks at 4, implying a negligible enhancement in the production rate.

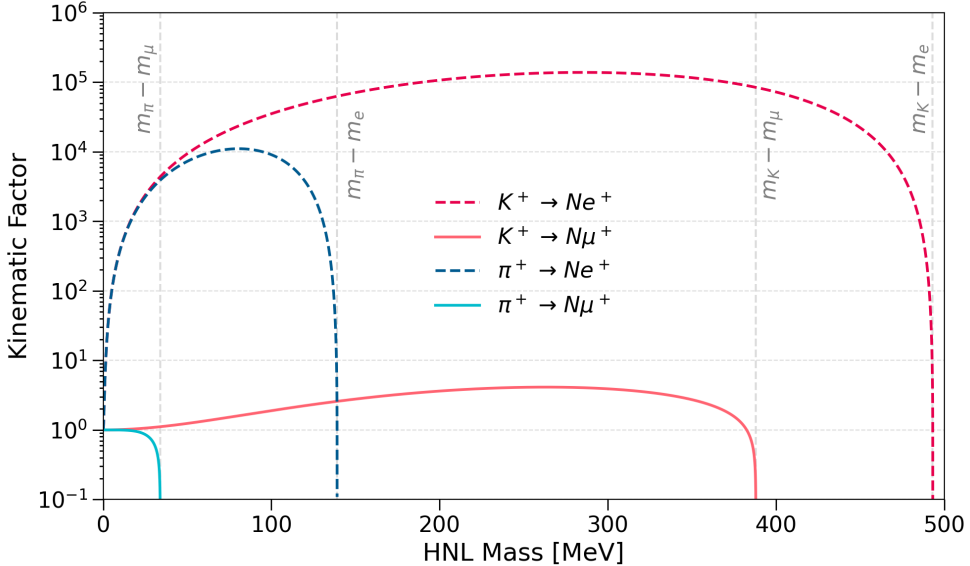


Fig. 2.2 Kinematic factor of the HNL production from meson decays that are probable from the BNB.

2.3 Decay Channels of Heavy Neutral Leptons

HNLs are hypothesised to decay into SM observables, with various decay channels depending on the flavour of the coupling $|U_{\alpha 4}|^2$. Decay widths of HNLs are proportional to the coupling $|U_{\alpha 4}|^2$ and their masses m_N [15, 23, 24]. Subsequently, lifetimes of HNLs can be computed from their decay widths, such that smaller $|U_{\alpha 4}|^2$ and m_N result in longer lifetimes. For HNLs being produced from the BNB and surviving long enough to reach SBND, the probable lifetime of HNLs is $c\tau \sim 10^2$ m.

In the mass range < 495 MeV, the kinematically-allowed decay channels of an HNL are as follows [15]:

$$\begin{aligned} N \rightarrow e^- \pi^+, \quad & N \rightarrow \mu^- \pi^+, \quad N \rightarrow \nu \pi^0, \quad N \rightarrow \nu \gamma, \\ N \rightarrow \nu e^- e^+, \quad & N \rightarrow \nu \mu^- \mu^+, \quad N \rightarrow \nu \mu^- e^+, \quad N \rightarrow \nu \nu \nu. \end{aligned} \tag{2.10}$$

These decay channels conserve the lepton number under the assumption that HNLs are Dirac particles with $L = +1$. If HNLs are Majorana particles, such that the lepton

number conservation is violated, then the charge conjugates for these decays that would be forbidden in the Dirac case are allowed.

Fig. 2.3 depicts the branching ratios of the decay channels shown in Eq. 2.10, as a function of the HNL mass. Solid lines are branching ratios via the μ -flavour coupling and dashed lines are branching ratios via the e -flavour coupling. The branching ratios were plotted referencing decay widths from Ref. [15, 23, 24]. Decay widths of HNLs have been derived independently across various literature sources and an overview of the discrepancies is summarised in Ref. [24]. The sources used here have been found to be in good agreement with each other.

For $m_N < 135$ MeV, the dominant branching ratio occurs in the channel $N \rightarrow vvv$ as shown by the light green lines. However, this channel is almost unobservable since the detection of SM neutrinos relies on the already-small cross section of neutrino scattering with the detector material. The other two channels in this mass range are $N \rightarrow ve^-e^+$ and $N \rightarrow v\gamma$, as shown by the light pink and grey lines. The channel $N \rightarrow v\gamma$ is highly suppressed compared to the channel $N \rightarrow ve^-e^+$, and thus, the final state of an e^-e^+ pair provides the best sensitivity within this mass range.

For $m_N > \sim 140$ MeV, an HNL has sufficient mass to decay into either a neutral pion ($m_{\pi^0} = 135$ MeV) or a charged pion ($m_{\pi^\pm} = 140$ MeV). For the e -flavour coupling, the channel $N \rightarrow e^-\pi^+$ dominates over the channel $N \rightarrow v\pi^0$ across the mass range from 135 to 495 MeV, as shown by the dashed dark blue and dashed pink line respectively. In the case of the μ -flavour coupling, the leading channel within the mass range of $135 < m_N < 245$ MeV is $N \rightarrow v\pi^0$ as shown by the solid pink line. Beyond $m_N > 245$ MeV, equivalent to the mass of a muon and a charged pion combined, the dominant decay channel begins to shift to the channel $N \rightarrow \mu^-\pi^+$ as shown by the solid light blue line. Finally, both channels $N \rightarrow v\mu^-e^+$ and $N \rightarrow v\mu^-\mu^+$ are not competitive compared to other channels at the same mass value.

Based on the assessment above it was decided in this work to focus on the decay channel $N \rightarrow v\pi^0$. This is the leading channel of the μ -flavour coupling and the second-leading channel of the e -flavour coupling within the mass range of $135 < m_N < 245$ MeV. However, since sensitivity in the same mass range of the e -flavour coupling has been extensively explored by many experiments as summarised by Ref. [19], the focus is on the decay channel $N \rightarrow v\pi^0$ via the μ -flavour coupling.

2.3 Decay Channels of Heavy Neutral Leptons

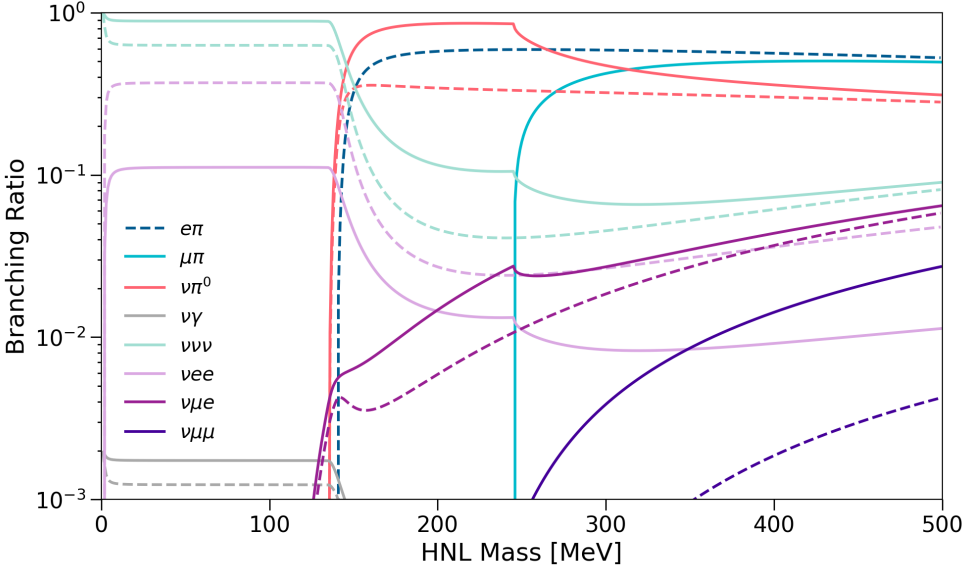


Fig. 2.3 Branching ratios of probable decay channels of an HNL produced from the BNB, with the $U_{\mu 4}$ ($U_{e 4}$) coupling plotted as solid (dashed) lines.

The decay width for the $N \rightarrow v\pi^0$ channel as taken from Ref. [24] is as follows:

$$\Gamma(N \rightarrow v\pi^0) = \frac{G_F^2 m_N^3}{32\pi} f_\pi^2 |U_{\mu 4}|^2 \left(1 - \left(\frac{m_{\pi^0}}{m_N}\right)^2\right)^2, \quad (2.11)$$

where G_F is the Fermi constant, f_π is the pion decay constant and m_{π^0} is the mass of a neutral pion. It is noted that the equivalent equations from Ref. [15, 23] contain an additional factor of 2 in the denominator. Eq. 2.11 was chosen from Ref. [24] since the source is more recently dated.

Fig. 2.4a shows the diagram of the HNL decaying into the final state $v\pi^0$. The SM neutrino is expected to leave no detectable signatures due to the very small scattering cross section. Meanwhile, the neutral pion is a particle made up of the superposition of the quark pair $u\bar{u}$ and $d\bar{d}$. The annihilation of the quark and antiquark makes it a very short-lived particle with a mean lifetime of $8.52 \pm 0.18 \times 10^{-17}$ s [25]. The neutral pion has been measured to decay into two photons $98.823 \pm 0.034\%$ of the time. Fig. 2.4b shows the Feynman diagram for this decay.

The photon pair results in a clear signature inside SBND, which is a Liquid Argon Time Projection Chamber (LArTPC): two electromagnetic showers without any associated hadronic activities at the decay vertex. This signal topology faces very challenging background separation from some SM neutrino channels also containing a π^0 in the final state.

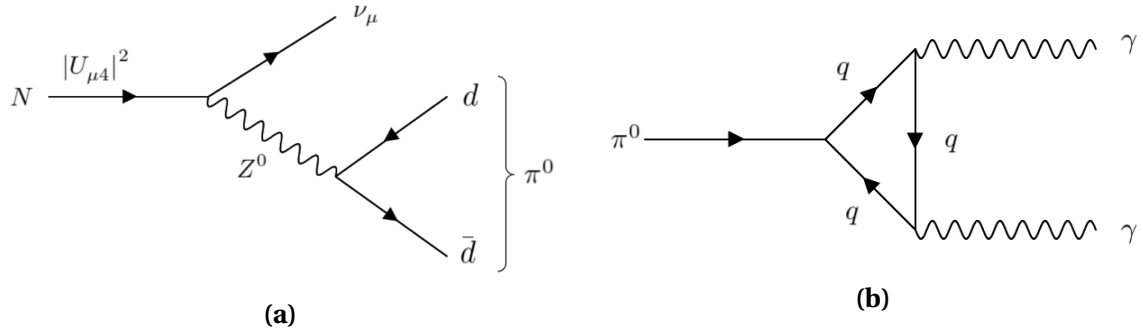


Fig. 2.4 Feynman diagrams of (a) $N \rightarrow \nu\pi^0$ and (b) $\pi^0 \rightarrow \gamma\gamma$.

As described in more detail in Chapters 9, differences in the kinematics from the HNL signal to the SM neutrino background enable an effective separation.

As previously discussed in Section 2.2, HNLs can be either Dirac or Majorana particles in nature. The difference between Dirac and Majorana HNLs is not only the lepton number conservation but also the polarisation of the decay products. For the neutral current final state $\nu\pi^0$, Majorana HNLs decay isotropically, whereas in the case of Dirac HNLs, the angular distribution of the daughter particles is no longer isotropic [26]. The helicity of the daughter neutrino determines the direction of the daughter neutral pion. The angular distributions of the two charge conjugate final states, $\nu\pi^0$ and $\bar{\nu}\pi^0$, add up to an isotropic distribution. As the neutrino is undetectable, the observed angular distribution of the neutral pion is expected to be insufficient to determine the Dirac or Majorana nature of HNLs. For simplicity in this search for HNLs via the channel $\nu\pi^0$, it is therefore assumed that HNLs are Majorana particles.

2.4 Previous Searches For Heavy Neutral Leptons

Searches for HNLs have been conducted by various experiments over the decades across a wide range of masses. Oscillation experiments and precise β -decay experiments have probed HNLs in the mass range between eV and keV, neutrino beam dump experiments have targeted the MeV-scale HNLs and collider experiments have primarily explored HNLs with masses in the GeV-scale and above. To date, no evidence of HNL existence has been found, and thus, experiments have set upper limits on the coupling $|U_{\alpha 4}|^2$ ($\alpha = e, \mu, \tau$). Commonly, the contour on the experiment sensitivity is expressed in terms of the coupling $|U_{\alpha 4}|^2$ as a function of the HNL mass.

2.4 Previous Searches For Heavy Neutral Leptons

Here, existing experimental limits on HNLs around $\mathcal{O}(100 \text{ MeV})$ are presented, focusing specifically on the mass range of $0 < m_N < 265 \text{ MeV}$ relevant to the final states $\nu\pi^0$. In this mass range, two key experimental methods are used, so-called peak searches and decay searches. Peak searches probe only the production rate of HNLs, whereas decay searches probe both production and decay rates. Fig. 2.5 summarises the presented upper limits at 90% Confidence Level (C.L.) from both experimental methods, with details on individual limits to be discussed in Section 2.4.1 and 2.4.2.

2.4.1 Peak Searches

Peak search experiments measure the energy spectrum resulting from the meson decay that would produce an HNL. Typically, the two-body leptonic decay of a meson is modelled as $m \rightarrow l + \text{Missing}$, where m is the parent meson, a pion or a kaon, and l is the daughter particle, a pion or a lepton [27]. The *missing* decay products are attributed to either HNLs or SM neutrinos. HNLs are expected to exit the detector before decaying, whereas SM neutrinos escape the detector before interacting, serving as the primary background. Since the momenta of m and l can be measured, the missing invariant mass can therefore be derived as $m_{\text{missing}}^2 = (P_m - P_l)^2$, where P_m and P_l are the 4-momenta of the parent and daughter particle. Given the near-zero mass of SM neutrinos, the mass of the daughter HNL can be treated as $m_N = m_{\text{missing}}$. Consequently, an excess over the background at m_{missing} potentially indicates the existence of HNLs.

To infer the upper limits on the coupling, the flavour α ($\alpha = \mu, e$) of the daughter lepton determines the flavour of the coupling $|U_{\alpha 4}|^2$, and the amplitude of the decay spectrum at m_{miss} determines the upper limits. Limits placed by the peak searches are insensitive to the Dirac or Majorana nature of HNLs as this does not impact the kinematics of the meson decay. For the coupling $|U_{\mu 4}|^2$, the most competitive limits have been established by the following experiments on the pion and kaon decay spectrum, and are plotted in Fig. 2.5 as dashed lines.

Pion Decay Spectrum Peak Searches

- **SIN** (Swiss Institute for Nuclear Research) performed a peak search using stopping positive pions decay via the channel $\pi^+ \rightarrow \mu^+ + \text{Missing}$, with a scintillator in 1981 and a germanium detector in 1987. The pion enabled probing HNLs within the low mass range $\mathcal{O}(10 \text{ MeV})$. Upper limits of $|U_{\mu 4}|^2$ were placed at the level of 10^{-4} in the mass range 1-20 MeV [28–30].

- The **PIENU** collaboration at TRIUMF also searched for HNLs using stopping pions. The most recent result in 2019 set the most stringent upper limits on $|U_{\mu 4}|^2$ at the level of 10^{-5} in the mass range of 15-34 MeV, extending beyond the results reported by SIN [31].

Kaon Decay Spectrum Peak Searches

- The **KEK** collaboration conducted an experiment known as E89 to search for HNLs using the muon range spectrum resulting from stopping kaon decays during 1981-1982. Following this, experiment E104 in 1983 was carried out with an improved momentum resolution and background suppression. The kaons were produced using a 0.5 GeV proton beam, and 3×10^6 muons from kaon decays were analysed using a magnetic spectrograph. The E89 experiment result set limits on $|U_{\mu 4}|^2$ between 10^{-4} - 10^{-6} within the mass range of 70-300 MeV. The combined results from the E89 and E104 experiments extended the limits towards the lower mass range between 45-300 MeV, although these findings were unpublished at the time of writing and therefore plotted as the dotted line in Fig. 2.5 [32-34].
- The **E949** collaboration at Brookhaven National Laboratory performed a kaon decay experiment using 21.5 GeV protons in 2002. The analysis of 2×10^{12} stopping kaon decays resulted in upper limits on $|U_{\mu 4}|^2$ at the level of 10^{-7} - 10^{-9} within the mass range of 175-300 MeV [35].
- The **NA62** collaboration, a kaon decay experiment at the CERN super proton synchrotron, analysed 10^8 stopping kaons from 400 GeV protons extracted from the synchrotron in 2015. The result from this data set set upper limits on $|U_{\mu 4}|^2$ at the level of 10^{-7} - 10^{-6} for the HNL mass between 250-373 MeV. Updated results using a larger dataset collected in 2016-2018 significantly improved the limits by an order of magnitude to 10^{-8} - 10^{-7} , and extended the mass range to 200-384 MeV [36, 37].

2.4.2 Decay Searches

Decay searches look for decay products from HNLs. HNLs are hypothesised to be produced outside the detector and then decay in flight into SM observables inside the detector. Different combinations of HNL production and decay channels yield different observed event rates of the decay products. The flavour of the HNL production and decay channel

2.4 Previous Searches For Heavy Neutral Leptons

both determine the flavour of the coupling $|U_{\alpha 4}|^2$ and the observed event rate determines the upper limits on the coupling.

Historically, decay searches have been performed in beam dump experiments, which were designed explicitly to suppress SM background thereby enabling the search for rare decay processes. Recently, modern neutrino oscillation experiments have emerged as competitive beam dump experiments alongside their neutrino physics programme. This is due to the resolution enhancement in their detection technologies that enable excellent SM background rejection, of which SBND is a prime example to be further detailed in this work. For the coupling $|U_{\mu 4}|^2$ within the mass range of 0-265 MeV, the most competitive limits have been set by the following experiments using neutrino beams, and are plotted in Fig. 2.5 as solid lines.

- The CERN **PS191** experiment in 1984 utilised an exposure of 19.2 GeV protons on a beryllium target, generating 10^{19} Protons On Target (POT). The detector was positioned at 128 m from the target at an off-axis angle of 2.3° to the beam. The detector volume was filled with helium, which was a sparse medium to reduce background rates arising from SM neutrino interactions. The large volume of 216 m^3 provided a high rate of HNL signals. Upper limits on $|U_{\mu 4}|^2$ within the mass range of 120-350 MeV were placed at the level of 10^{-5} - 10^{-9} [38, 39]. A re-evaluation in 2022 found the limits to be lower than the original published results [40].
- The **NuTeV** collaboration at Fermilab conducted HNL searches in 1996 using a high energy neutrino beam produced by protons accelerated from the Tevatron ring. The dataset comprised an exposure of 3×10^{18} POT with an energy of 800 GeV. HNLs were produced from the D mesons resulting from proton collisions with the target. This enabled an exploration of the HNL mass up to 2000 MeV, surpassing any other beam-dump experiments described here. The experiment established limits on $|U_{\mu 4}|^2$ at the level of 10^{-6} - 10^{-7} within the mass range of 225-2000 MeV [41].
- The **T2K** collaboration searched for HNLs using their near detector ND280 located off-axis to the beam target at an angle of 2.04° . Only events occurring in the three gaseous TPC volumes were selected to minimise background from SM neutrinos. A kinematic selection was performed on a dataset of 2×10^{21} POT and no signals were observed. The result constrained the coupling $|U_{\mu 4}|^2$ at the level of 10^{-8} - 10^{-9} in the mass range of 250-380 MeV. The limits plotted in Fig. 2.5 are of a single-channel $K^\pm \rightarrow N\mu^\pm$ and $N \rightarrow \mu^\pm\pi^\pm$ combined. More stringent limits on $|U_{\mu 4}|^2$ were also presented assuming the couplings $|U_{e 4}|^2$ and $|U_{\tau 4}|^2$ are non-zero. This allows for

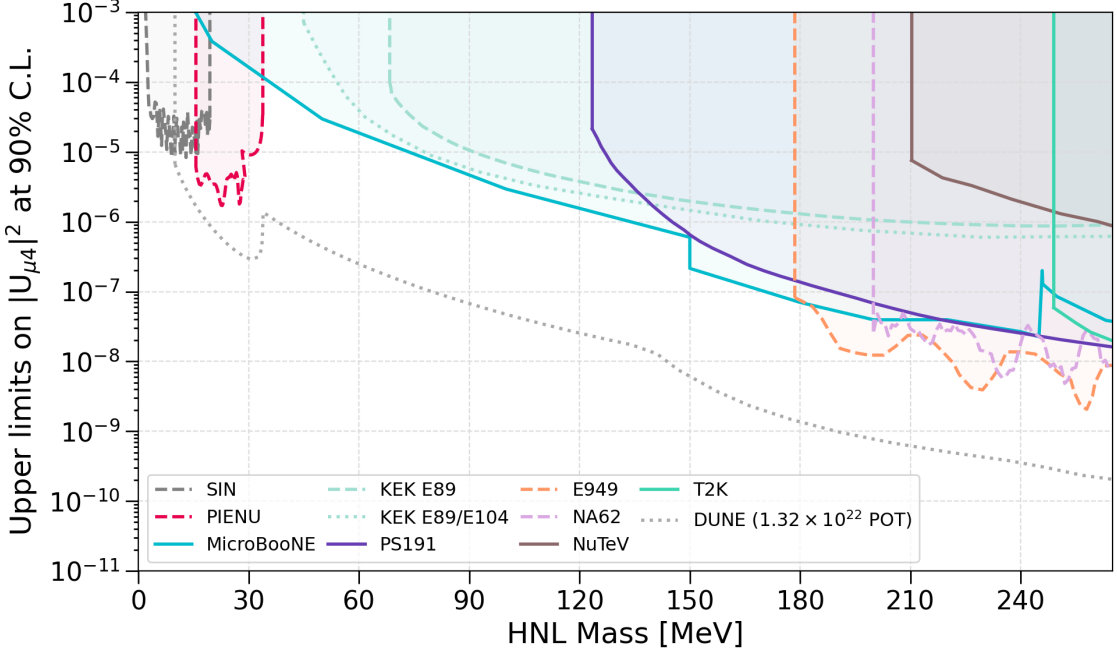


Fig. 2.5 Upper limits on the coupling $|U_{\mu 4}|^2$ at the 90% confidence level for Majorana HNLs in the mass range of $0 < m_N < 265$ MeV, including results from SIN [30], PIENU [31], MicroBooNE [43–45], KEK E89 [33], KEK E89/E104 [34], PS191 [40], E949 [35], NA62 [37], NuTeV [41], T2K [42] and expected results from DUNE [26].

marginalised limits on $|U_{\mu 4}|^2$ derived from other coupling results, which are not directly comparable here [42].

- The **MicroBooNE** collaboration conducted a series of searches for HNLs using their LArTPC, with the first result in 2020 and subsequent results in 2022 and 2023. The initial analysis was performed using an exposure of 2×10^{20} POT obtained from the on-axis BNB. A special delayed trigger was implemented to identify HNLs arriving at the detector later than SM neutrinos. Limits on $|U_{\mu 4}|^2$ were set at 10^{-7} for HNL masses spanning between 260–385 MeV. The latter two searches focused on HNLs resulting from kaon decays in the NuMI beam absorber, which arrived at the detector at an angle to SM neutrinos from the BNB. The dataset included two runs with exposures of 2×10^{20} and 5.01×10^{20} POT. The combined results incorporated multiple HNL decay channels, probing a wide mass spectrum between 10–385 MeV. Notably, these recent results set the most stringent limits to date on $|U_{\mu 4}|^2$ at the level of 10^{-4} – 10^{-7} within the mass range of 34–175 MeV, extending the findings from 2020 [43–45].

2.5 Concluding Remarks

- The **DUNE** collaboration plans an extensive search for HNLs using the near detector (ND), projected to take place in 2030s [22, 26, 46]. The DUNE ND will be located 574 m from the target and have two TPC modules: (1) a LArTPC and (2) a magnetised gaseous argon TPC. Assuming an exposure of 1.32×10^{22} POT of energy 80 GeV over 12 years of physics data taking, Ref. [26] deduced the expected upper limits on $|U_{\mu 4}|^2$ across a wide mass range of 10-2000 MeV. Due to the abundant statistics, the limits achieved by DUNE ND will surpass any existing limits in the mass range of 0-265 MeV presented here. Since these are expected limits, they are plotted as the dotted line in Fig. 2.5.

2.5 Concluding Remarks

HNLs are beyond the SM particles that can provide a natural explanation not just for the mass generation of SM neutrinos but also for their extreme lightness. SBND, located only 110 m from the BNB, is capable of detecting HNLs resulting from meson decays in the beam, which then decay in flight inside the detector. Fig. 2.5 provides a summary of existing limits on the coupling $|U_{\mu 4}|^2$ of Majorana HNLs in the mass range of 0-265 MeV, showing that this phase space has been well-explored by various experiments. For SBND to be competitive in this region, a high background rejection rate without comprising signal efficiency must be achieved. This can be obtained by exploiting the unique kinematics of HNL decay products for background rejection, including their late arrival compared to SM neutrinos as well as their boosted topologies due to HNLs being massive. Toward this goal, novel detection technologies and reconstruction techniques of SBND have demonstrated an excellent timing, spatial and calorimetry resolution. Chapters 3 and 4 provide an overall description of the LArTPC technology, followed by details of the technology at SBND.

Chapter 3

Physics of Liquid Argon Time Projection Chambers

The Liquid Argon Time Projection Chamber (LArTPC) stands as a high precision detector in neutrino physics. In contrast to liquid scintillator neutrino experiments, LArTPCs collect both light and charges thereby providing a superior granularity for imaging neutrino interactions. The detector concept was first proposed in 1977 by Rubbia [47], bringing together the time projection chamber technology developed by Nygren [48, 49] and the liquid argon ionisation chamber developed by Willis and Radeka [50]. LArTPCs provide an excellent spatial, calorimetry and timing resolution while enabling a high neutrino interaction rate. Thus, this novel technology remains the primary choice for many neutrino experiments at Fermilab.

The following chapter delves into the operating principles of LArTPCs, which are the detection technology employed by the Short-Baseline Near Detector (SBND) to be discussed in Chapter 4. Section 3.1 provides an overview of the design of a LArTPC and the choice of liquid argon. In Section 3.2, a comprehensive discussion is presented on particle interactions with the liquid argon and the production of ionisation electrons and scintillation photons, which are the detectable signals of LArTPCs. Following that, Section 3.3 outlines the propagation of the electrons and photons through the liquid argon medium. The detection mechanisms of the ionisation electrons and scintillation photons using wire planes and novel optical detection technologies are given in Section 3.4. Finally, Section 3.5 concludes the chapter with some remarks.

3.1 Overview of Liquid Argon Time Projection Chambers

LArTPC is the technology of choice for the Fermilab's neutrino programs due to its ability to facilitate a high rate of neutrino interactions while maintaining an exceptional spatial, energy, and timing resolution. Moreover, the abundance and low cost of argon are ideal for scaling detectors to a large target mass, reaching up to tens of kilotons in volume. Notably, the Short-Baseline Neutrino (SBN) program [1] comprises three LArTPC experiments each of size in the hundreds of tons, located along the Booster Neutrino Beam (BNB): SBND [2], MicroBooNE [51], and ICARUS [52]. This novel technology will also be utilised at the upcoming long baseline Deep Underground Neutrino Experiment (DUNE), of which two of the four far modules are LArTPCs, each with a volume of 17 kilotons [53].

Fig. 3.1 shows a diagram illustrating a general LArTPC. The TPC comprises a volume of liquid argon with a uniform electric field provided by a surrounding field cage, which is not shown in the diagram. To the right of the TPC is a cathode plane assembly grounded at a high negative voltage and to the left is the anode plane assembly. Thus, the resulting electric field direction is from left to right. The anode plane assembly is made up of three wire planes oriented at different angles, of which the diagram here shows three planes at the angle of 0° and $\pm 60^\circ$ to the vertical. Behind the wire planes is the Photon Detection System (PDS), of which the example consists of 9 PhotoMultiplier Tubes (PMTs).

The centre of the LArTPC in Fig. 3.1 depicts an example interaction of an incoming neutrino scattering off an argon nucleus, shown as the dashed line since the neutral track of the neutrino is unobservable by the detector. Charged particles resulting from the neutrino interaction ionise and excite argon atoms as they traverse through the detector medium. Ionisation electrons and scintillation photons are produced in the process as shown by the solid lines. Ionisation electrons drift towards the anode in the opposite direction of the electric field. Upon arrival at the anode, ionisation electrons induce signals on the two inner wire planes and are collected on the outermost wire plane. The combination of signals from the three planes results in a high granularity 3D image of the charged particle path. Moreover, since the liquid argon and wire planes are transparent to scintillation photons, the photons drift past the wire planes and are detected by the PDS. Scintillation photons provide additional information about the deposited energy and precise timing information of the neutrino interaction.

3.1 Overview of Liquid Argon Time Projection Chambers

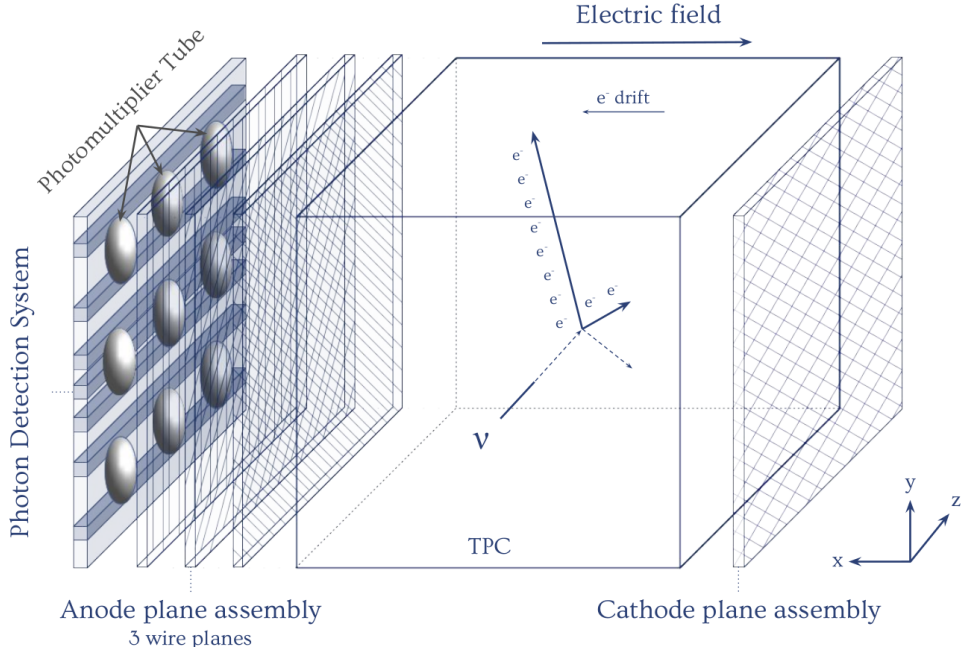


Fig. 3.1 Diagram illustrating the operating principles of a LArTPC [54].

Liquid argon makes an excellent medium for TPCs. Given that liquid argon has a reasonably high density of $1.39 \text{ g}\cdot\text{cm}^{-3}$ and an atomic mass of 40, it enables a high rate of neutrino interactions since the probability of neutrino interactions increases with the number of nucleons in the detector volume. Since argon is a noble element, most of the energy deposited by particles traversing through the medium is used for ionising and exciting atoms, producing ionisation electrons and scintillation photons in the processes. This maximises the efficiency of energy transfer into detectable signals. In addition to argon being an abundant and cheap material for scaling the detector target mass, recent technology advancements in purification have resulted in a stable and pure liquid argon condition for LArTPC operations. This ensures that electrons and photons can traverse the drift distance towards detection without being captured by contaminants [55].

Having ionisation electrons as detectable signals enables a wide range of energy thresholds for physics applications [56]. For energy ranging from $> 100 \text{ MeV}$ to GeV , LArTPC makes an excellent fine-grained detector for studying neutrino interactions. In the tens of MeV , LArTPC is able to detect electrons resulting from absorption interactions of supernova ν_e on argon nuclei. In the sub-MeV threshold, LArTPC can identify keV-signatures from solar neutrinos or radiogenic ^{39}Ar beta decay with further advancements in energy reconstruction. Consequently, LArTPCs stand out as an advantageous technology for neutrino experiments.

3.2 Particle Interactions in Liquid Argon

Particle interactions in liquid argon and the production of ionisation electrons and scintillation photons as detectable signals are discussed next. Section 3.2.1 provides a description of the energy loss of charged particles traversing liquid argon and producing ionisation electrons. Following that, Section 3.2.2 details the production mechanism of scintillation photons via argon excitation and recombination. Finally, the physics of recombination that determines the yield of ionisation electrons and scintillation photons is given in Section 3.2.3

3.2.1 Production of Ionisation Electrons

Charged particles traversing a medium, such as liquid argon, undergo energy loss via ionisation, producing electrons. The typical energy loss profile is illustrated in Fig. 3.2, specifically for a muon traversing in a copper medium. However, the underlying principle still applies to liquid argon. The plot depicts the stopping power, which is the energy loss per unit length divided by the density of the target medium, against the momentum of the traversing particle. Heavy particles such as muons, pions, and protons, experience energy loss in liquid argon described by the Bethe-Bloch formalism [57]. For lighter and highly relativistic particles, such as > 100 MeV electrons in liquid argon, the primary mechanism for energy loss is through radiative effects.

Muons, pions and protons interact with argon atoms as they propagate through liquid argon primarily via ionisation, freeing electrons along their trajectories. These straight-line trajectories are referred to as *tracks*. The trajectories can also be deflected by many small angle scatterings, a phenomenon known as multiple Coulomb scatterings due to charged particles Coulomb scattering from nuclei [57]. In the low momentum region, the energy deposited per unit length via ionisation dE/dx remains generally constant, referred to as the Minimum Ionising Particle (MIP). The distribution of dE/dx of a MIP particle is often described by a Landau-Gaussian convolution [57]. When the particle comes to a stop, the deposited energy increases, forming the Bragg peak. The energy loss profile described here is dependent on the mass of the traversing particle, making it a valuable tool for particle identification [58]. This method is the most effective for protons separation from muons and pions as protons are significantly heavier.

Electrons with energy above the critical energy, which is the point losses due to ionisation are equal to losses from radiation, deposit energy via radiative effects. The critical

3.2 Particle Interactions in Liquid Argon

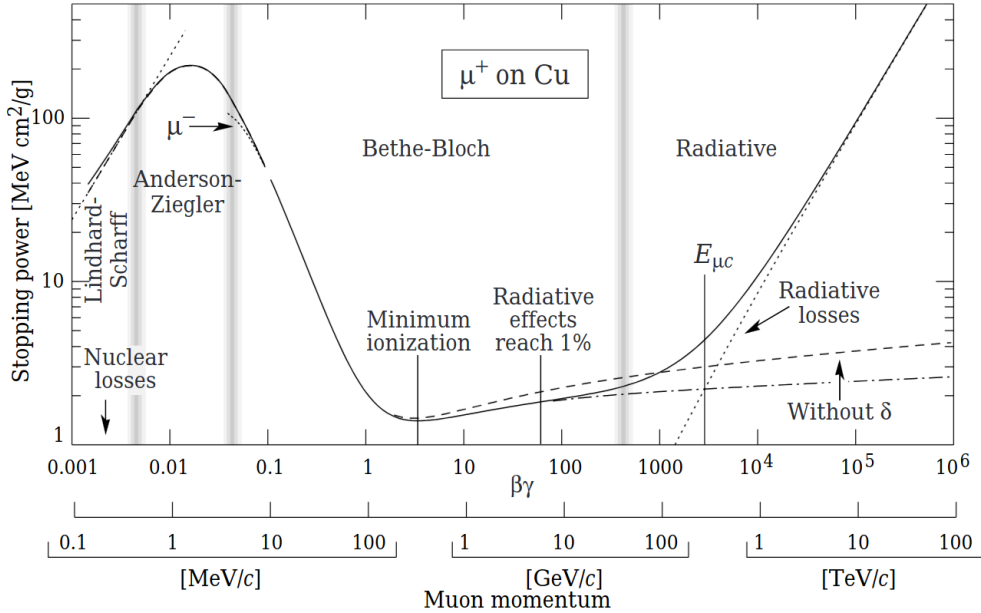


Fig. 3.2 Energy loss in matter for a muon traversing a copper medium [57].

energy for electrons in liquid argon is 39 MeV [59]. This process typically results in cones of electromagnetic activities, commonly referred to as *showers*. In the energy range relevant in a LArTPC, typically between 100-1000 MeV, showers deposit energy over a distance of ~ 1 m and the shower length is logarithmic in energy. For electrons resulting from a muon decay with a lower energy of ~ 50 MeV, they neither resemble an ionisation track nor an electromagnetic shower. Instead, they result in a short linear segment of ionisation followed by a few clumps of deposited charge in the energy range of 1-10 MeV. This unique energy deposition of electrons is referred to as a *Michel electron* and is often used by LArTPC experiments for energy calibration and muon identification [60].

Photons deposit energy via Compton scattering and e^+e^- pair production, also producing electromagnetic showers similar to electrons. Fig. 3.3 shows the mean free path of photons in liquid argon as a function of the photon energy for the two modes, Compton scattering by the solid blue line and pair production by the solid red line. At the low energy range < 50 MeV, the main interaction mode is via Compton scattering while at the high energy range > 50 MeV, pair production becomes the dominant effect. The mean free path for a photon for pair production is defined as $9/7$ of the radiation length of an electron and it is plotted as the solid cyan line at 18.1 cm [57]. Consequently, in the photon energy range of 100-1000 MeV relevant for LArTPCs, photons typically travel 20-30 cm without causing ionisation. This creates a gap between the interaction vertex and the start of the

shower, known as the *conversion gap*. Both the energy loss profiles and the conversion gaps can be utilised to distinguish between electrons and photons.

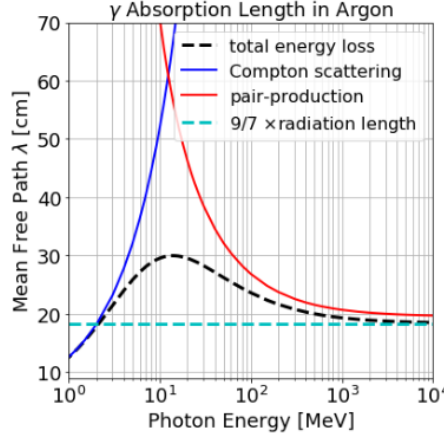


Fig. 3.3 Mean free path of photons traversing in liquid argon as a function of their energies [59].

Fig. 3.4 shows an event display of a simulated charged current ν_μ interaction containing a muon, a proton and a neutral pion in the final state. The colour scale corresponds to the magnitude of the energy deposition, where the colour green is lower in energy and the colour red is higher in energy. The muon results in a long minimum ionising track whilst the proton results in a short energetic stub, demonstrating the distinct difference between the energy loss profile of a muon and a proton. As the muon comes to a stop, the colour scale changes from green to red, indicating the increase in energy forming the Bragg peak. At the end of the muon track, it decays into a Michel electron that can be seen as a short linear segment low in energy. On the other hand, the neutral pion decays into two photons, which both undergo pair production producing electromagnetic showers. The photon showers are detached from the interaction vertex where both muon and proton tracks begin. This is the conversion gap feature unique to a photon shower.

3.2.2 Production of Scintillation Photons

Charged particles traversing liquid argon also produce scintillation photons, through two different processes that result in an argon excimer Ar_2^* as shown in Fig. 3.5. The first process is known as recombination, denoted by the arrows labelled *ionize* and *recombine*. Ionisation in liquid argon produces a free electron and an argon ion Ar^+ . The electron can either escape and drift towards the anode for detection, or recombine with an argon compound ion Ar_2^+ , forming an argon excimer Ar_2^* . The second process is known as a

3.2 Particle Interactions in Liquid Argon

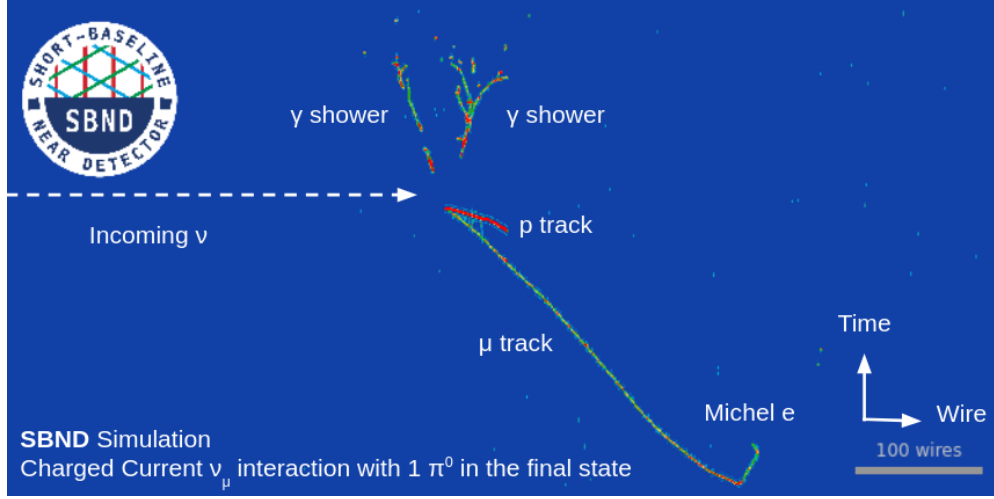


Fig. 3.4 Event display showing a simulated charged current ν_μ interaction containing a muon, a proton and a neutral pion in the final state.

self-trapped exciton, denoted by the arrow labelled *excite*. This begins when the charged particle does not have sufficient energy for ionisation, instead it excites the argon atom upon collision. The excited argon atom Ar^* self-traps with another argon atom Ar , forming an argon excimer Ar_2^* . Resulting argon excimers are short-lived and undergo radiative decay into two ground-state argon atoms. This produces scintillation photons with a wavelength of 128 nm in the Vacuum Ultraviolet (VUV) range [61].

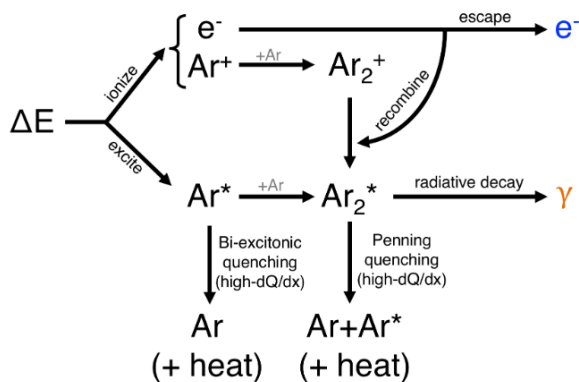


Fig. 3.5 Production of ionisation electrons and scintillation photons from energy deposition processes in liquid argon [61].

The timing constant of the radiative decay depends on the excitation state of the argon excimer. This can be either a singlet state, where the excited electron has the same spin as in the ground state; or the triplet state, where the excited electron has the same spin as another unpaired electron. The singlet state has a shorter mean lifetime with a decay

constant $\tau_1 \approx 6 - 7$ ns, while the triplet state has a longer mean lifetime with a decay constant $\tau_3 \approx 1.5 - 1.6$ μ s [62]. These are referred to as the prompt and late components respectively. The time-dependent probability of light emission in pure liquid argon is modelled as:

$$l(t) = \frac{A_1}{\tau_1} \exp\left(-\frac{t}{\tau_1}\right) + \frac{A_3}{\tau_3} \exp\left(-\frac{t}{\tau_3}\right), \quad (3.1)$$

where A_1 and A_3 are the decay amplitudes of the singlet and triplet state.

Since scintillation photons have energy less than the critical energy in liquid argon, they propagate without producing electromagnetic activities. Moreover, liquid argon serves as an excellent medium for producing scintillation photons, where the light yield is as high as $\sim 40,000$ photons per MeV of deposited energy in the absence of an electric field [63]. In an electric field at 500 V/cm as configured in SBND, the light yield decreases to $\sim 20,000$ photons per MeV of deposited energy due to ionisation electrons drifting away before recombination can occur [64]. Furthermore, high ionisation density can lead to quenching effects [61]. Contaminants in liquid argon, such as oxygen and nitrogen, can absorb energy from argon excitons and excimers, without emitting any photons.

3.2.3 Recombination

The electron-ion recombination, as depicted by the arrow labelled *recombine* in Fig. 3.5, is a key physics process affecting the yield of ionisation electrons and scintillation photons. Recombination occurs almost immediately within 1-2 ns following the ionisation process

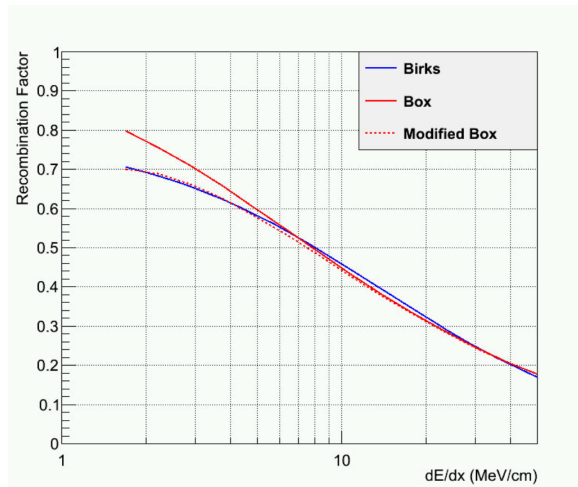


Fig. 3.6 Recombination factor in liquid argon as a function of the deposited energy density for an electric field of 500 V/cm [65].

3.2 Particle Interactions in Liquid Argon

[65]. The recombination factor R is defined as the survival probability of electrons that do not recombine. Fig. 3.6 shows a comparison of various R models with a non-linear dependence on the energy density dE/dx for liquid argon at an electric field of 500 V/cm. The Birks model, shown by the solid blue line, has been disfavoured due to spurious values at high charge density. The Box model, shown by the solid red line, is based on the columnar theory around the charge deposition and can resolve the issue suffered by the Birks model. It has been modified for a better agreement with the Birks model at low charge density to account for the presence of an electric field and local ionisation density. The modified Box model, as shown by the dotted red line, also contains experimentally derived parameters measured by the ArgoNeuT experiment [65].

The dependence of recombination on the electric field leads to an anti-correlation between the charge and light yield Q and L respectively, such that [61]:

$$Q = N_i R, \quad (3.2)$$

$$L = N_{ex} + N_i(1 - R), \quad (3.3)$$

where N_i is the number of electron-ion pairs and N_{ex} is the number of argon excitons. The charge yield Q results from the number of electrons N_i surviving recombination. The light yield L depends on the number of excitons N_{ex} and the number of electrons that recombine $N_i(1 - R)$ to produce scintillation photons, assuming 100% light efficiency.

Fig. 3.7 illustrates the anti-correlation as a function of the electric field strength for various noble elements, of which argon is shown as dashed lines. A stronger electric field results in a higher number of ionisation electrons being separated from argon ions and drifting towards the anode for detection before recombination can occur, thus increasing the charge yield. Conversely, scintillation photons are produced from the recombination process. In the presence of an electric field, recombination decreases, leading to a reduction in light yield. Furthermore, recombination can be influenced at a local scale due to ionisation density resulting from interacting particles. SBND is expected to operate with an electric field of 500 V/cm, a region where yields of ionisation electrons and scintillation electrons are approximately equal as can be seen in Fig. 3.7. The impact of recombination on the observed physics is further discussed in Section 8.2.

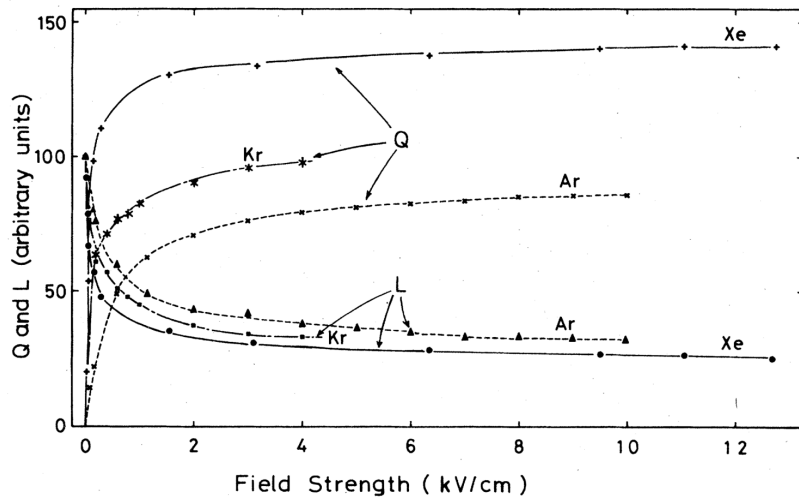


Fig. 3.7 Anti-correlation of charge yield Q and light yield L as a function of the electric field strength [66].

3.3 Particle Propagation in Liquid Argon

The following section provides a description of the transportation of ionisation electrons and scintillation photons through the liquid argon medium. Section 3.3.1 covers the details of different physics processes that electrons experience as they drift towards the anode, including diffusion, attenuation and the space charge effect. A discussion on the propagation of scintillation photons is presented in Section 3.3.2, detailing the process of Rayleigh scattering, absorption and wavelength shifting.

3.3.1 Ionisation Electron Drift

Ionisation electrons that do not recombine drift towards the anode under the effect of an electric field. In a LArTPC with an electric field of 500 V/cm and a temperature of 88.4 K, the drift velocity of electrons is approximately $0.156 \text{ cm}/\mu\text{s}$ [67]. As the electrons drift, they undergo diffusion, causing perturbations in their trajectories due to various effects. For example, it can be due to inelastic collisions with argon atoms. Diffusion causes the shape of an electron cluster produced in a point-like energy deposition to grow in volume while drifting. The effects increase with the drift distance, smearing both spatial and temporal resolutions.

Diffusion is parameterised in both the longitudinal and the transverse direction, which are parallel and perpendicular to the drift direction respectively. Longitudinal diffusion

3.3 Particle Propagation in Liquid Argon

affects the temporal resolution, as individual electrons arrive at the wire either earlier or later relative to the electron cluster moving at the average drift velocity. The temporal smearing due to the longitudinal diffusion can be approximated as [68]:

$$\sigma_L \approx \sqrt{\frac{2D_L}{v_d^2} t}, \quad (3.4)$$

where D_L (cm²/s) is the longitudinal diffusion, v_d (cm/s) is the drift velocity and t (s) is the drift time. On the other hand, transverse diffusion broadens the cross section of the electron cluster arriving at the original wire, causing electrons to migrate to neighbouring wires. The spatial smearing due to the transverse diffusion can be approximated as [69]:

$$\sigma_T \approx \sqrt{2 \cdot D_T \cdot t}, \quad (3.5)$$

where D_T (cm²/s) is the transverse diffusion and t (s) is the drift time. Collectively, both longitudinal and transverse diffusion smear the electron clusters seen by each wire, thereby impacting the measured energy loss profile of a particle [69]. At the conditions expected for the SBND detector, the diffusion coefficients have been measured to be $D_L = 4.0$ cm²/s by MicroBooNE [68] and $D_T = 8.8$ cm²/s by ProtoDUNE [70].

In addition to diffusion, drifting electrons undergo attenuation. In this process, electrons are captured by electronegative impurities present in the liquid argon, most commonly oxygen and water [70]. This results in a reduction of electrons arriving at the wires, proportional to the drift distance. The number of charges collected on a wire Q_{Wire} is typically modelled as an exponential suppression:

$$Q_{\text{Wire}}(t) = Q_{\text{Dep}} \cdot \exp\left(\frac{-t}{\tau}\right), \quad (3.6)$$

where Q_{Dep} is the original number of deposited charges, t (ms) is the drift time and τ (ms) is the electron lifetime characterising the level of charge attenuation.

A high electron lifetime, resulting from a low level of contamination, is a critical operational factor for achieving high efficiency in energy reconstruction. Recently reported from ProtoDUNE, which utilised the same membrane cryostat technology as SBND, the experiment measured a lifetime of ~ 10 ms, equivalent to an oxygen purity of 3.4 ppt [70]. This lifetime is significantly larger than the drift time of SBND, which is projected to be 1.3 ms, making the effect of attenuation almost negligible. A procedure to measure electron lifetime at SBND is presented in Section 8.1.

A final important issue in electron transportation is the Space Charge Effect (SCE). Argon ions, produced as part of the ionisation process, drift towards the cathode at a slower velocity than electrons. Typically, they have a drift velocity more than five orders of magnitude lower than that of electrons [71]. Since SBND is a surface detector without an overburden, high exposure to cosmic rays leads to a high rate of ionisation. The resulting accumulation of slow-moving argon ions distorts the uniformity of the electric field, affecting both its intensity and direction.

Fig. 3.8 illustrates the deformation of tracks drifting in the distorted electric field due to SCE. Track trajectories are impacted two-fold: (1) bending away towards the detector edges as shown by the middle plot and (2) bowing towards the cathode as shown by the right plot [72]. Track deformations smear both spatial and temporal resolutions. For instance, temporal smearing can introduce uncertainties $\mathcal{O}(1 \text{ cm})$ in reconstructing the x -position of a track. Moreover, distortions of the electric field also affect recombination previously discussed in Section 3.2.3, since the recombination factor depends on the electric field strength. Local fluctuations of recombination can subsequently impact the local charge yield resulting from an energy deposition. Careful calibration at SBND will be required to better understand the magnitude of SCE.

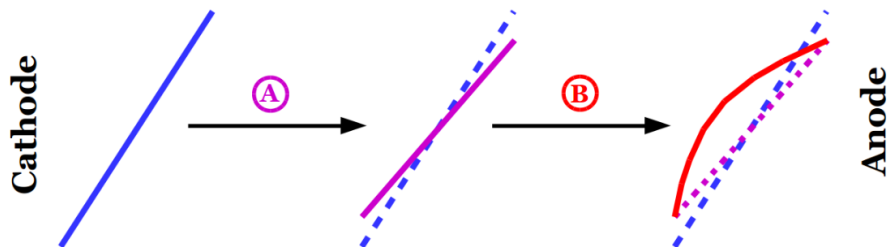


Fig. 3.8 Impacts of SCE on tracks: bending away towards the detector edges (middle) and bowing towards the cathode (right) [72].

3.3.2 Scintillation Photon Propagation

Scintillation photons can propagate over long distances in liquid argon since the medium is transparent to its own light. As scintillation photons travel, they undergo Rayleigh scattering as the first-order effect, involving the photons elastically scattering off atoms, altering their trajectories. Reflections and refractions at the detector boundaries are the second-order effects. While these effects do not change the number of photons, they modify the propagation path and lengthen the travel time [73].

3.3 Particle Propagation in Liquid Argon

The impact of these effects on the probability of photons reaching the PDS for detection depends on the photon production location and the path taken to arrive at the PDS. This consequently leads to a non-trivial distribution of photon arrival time at the PDS, and the travel time can range from a few to several tens of nanoseconds. Particularly, it is the most impactful on the prompt component of scintillation photons. The Rayleigh scattering length λ_{RS} for VUV photons in liquid argon has been reported to be around 50 cm [74] up to 110 cm [75], which is comparable to the size of SBND.

In addition to Rayleigh scattering, scintillation photons also undergo absorption, which arises due to contaminants in liquid argon. Contaminants like nitrogen [76] and methane [77] have a high absorption cross section for VUV photons. Other contaminants, like oxygen and water, have also been observed in commercial argon and can also reduce the number of photons [78]. The absorption of scintillation photons is modelled as an exponential suppression similar to Eq. 3.6 modelling the ionisation electron attenuation. The number of photons surviving absorption N_γ is as follows:

$$N_\gamma(d) = N_0 \cdot \exp\left(\frac{-d}{\lambda_A}\right), \quad (3.7)$$

where N_0 is the original number of scintillation photons, d is the propagation distance and λ_A the absorption length. The absorption rate also depends on the Rayleigh scattering length. Photons with a shorter λ_{RS} undergo longer and more indirect propagation paths, increasing their probability of absorption before being reaching the PDS [79].

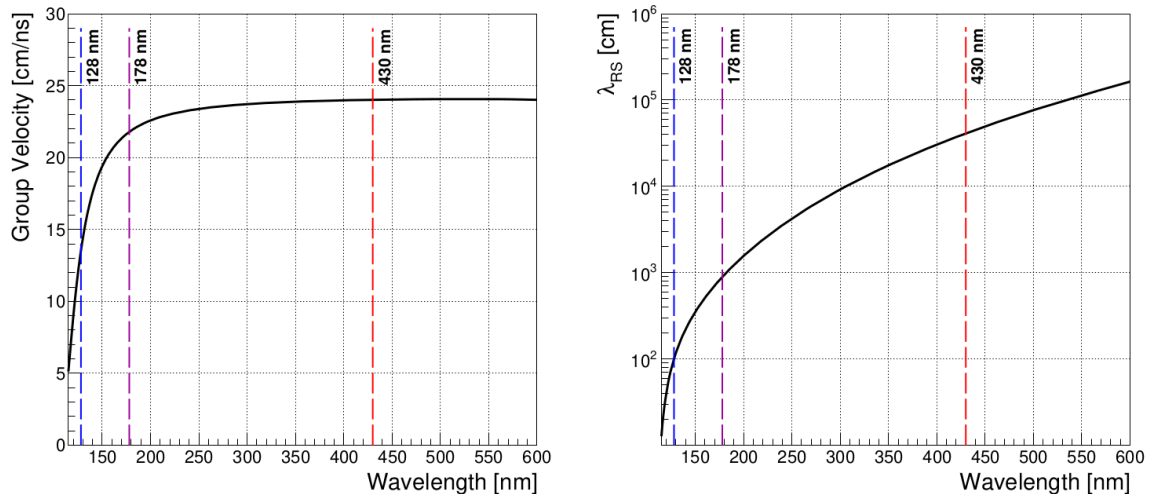


Fig. 3.9 Group velocity (left) and the Rayleigh scattering length (right) as a function of the photon wavelength in liquid argon [79].

Finally, an enhancement method for light collection efficiency in LArTPC is wavelength shifting scintillation photons. Specifically at SBND, TetraPhenyl Butadiene (TPB) is employed to shift the wavelength of VUV photon from 128 nm to 430 nm, which falls within the visible light range. This is to better match the detection spectrum of optical detectors installed at SBND [73], of which a description of the SBND PDS is detailed in Section 4.2.2. The time delay of TPB emission of visible photons has been reported to contain several time constants, of which the most dominant constants are 10 ns (60%) and 49 ns (30%) and the rests are $\mathcal{O}(300\text{-}3000\text{ ns})$ [80]. The direction of emitted photons from TPB is isotropic.

Fig. 3.9 shows the group velocity on the left and the Rayleigh scattering length on the right as a function of the photon wavelength in liquid argon. The vertical dashed blue and red lines at 128 and 430 nm respectively are the wavelengths of scintillation photons in liquid argon and of photons re-emitted by TPB wavelength shifting. Here, it can be seen that the group velocity of VUV photons is slower than that of visible photons. Moreover, the Rayleigh scattering length of VUV photons is two orders of magnitude smaller compared to visible photons. This results in VUV photons being more susceptible to Rayleigh scattering and having a higher probability of absorption [79]. Differences between the propagation of VUV and visible photons provides extra handles for timing reconstruction using the light information, which is further discussed in Section 6.3.1.

3.4 Detection of Electrons and Photons

Upon arrival at the anode for detection, ionisation electrons and scintillation photons are detected by different technologies. Ionisation electron signals are recorded by the wire planes as detailed in Section 3.4.1. Following that, Section 3.4.2 provides a description of two different optical detectors for detecting scintillation photons.

3.4.1 Wire Planes

Upon arrival at the anode, ionisation electrons produce signals on the wire planes, which are made up of three planes separated by a few mm as previously depicted in Fig. 3.1. A bias voltage is applied to each plane to create a drift field across the three planes. This ensures wire transparency so that all ionisation electrons can reach the third plane without being collected by the two innermost planes. As electrons drift towards and pass the two innermost planes, they induce bipolar signals, of which the planes are referred to as

3.4 Detection of Electrons and Photons

induction planes. Finally, electrons are collected on the outermost plane producing a unipolar signal, of which the plane is referred to as the collection plane. Fig. 3.10 shows an example of induced currents on a wire as a function of time. Here, it can be seen a bipolar signal on an induction plane in red and a unipolar signal on a collection plane in blue.

The three planes are typically oriented at an angle of 60° with respect to each other, of which the diagram in Fig. 3.1 shows three planes at the angle of 0° and $\pm 60^\circ$ to the vertical. While 3D spatial reconstruction of a signal requires a minimum of at least two wire planes, many modern LArTPC experiments use all three planes to improve the spatial resolution [2, 51–53, 58, 70].

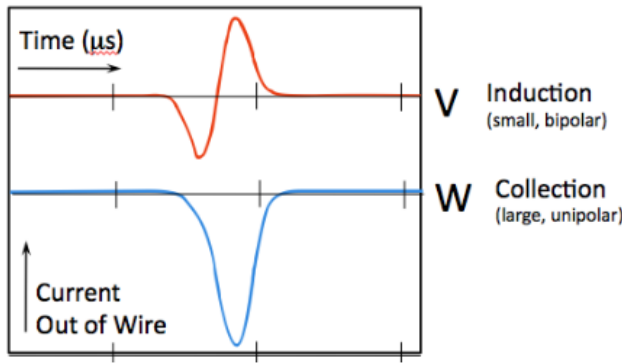


Fig. 3.10 Current signals on the induction and collection wire plane induced by a point-like charge deposition [58].

The signals induced or collected on the wire planes are shaped, amplified, and digitised before acquisition. Signal processing is then applied to the measured charge per wire, including noise removal, field and electronic response deconvolution and baseline removal. The amount of charge collected is correlated with the energy deposited in the detector. This step is crucial as the energy reconstruction requires charge depositions on at least two or more wires to deduce the wire pitch, thus requiring careful consideration of the angle of the charge deposition to the wire. Finally, the 3D spatial reconstruction is performed, which allows for high level analysis like particle identification. The reconstruction of charge signals at SBND is further discussed in Section 6.2.

3.4.2 Photomultiplier Tubes and X-ARAPUCAs

Scintillation photons are detected by the PDS located behind the wire planes, as depicted in Fig. 3.1. For SBND, the primary PDS detection technology is Photomultiplier Tubes

(PMTs), which have a Quantum Efficiency (QE) of up to 30% [81]. However, PMTs are typically large and require sufficient volume inside the detector for installation. Current and future LArTPC experiments are adopting Silicon PhotoMultipliers (SiPMs) due to their advantageous smaller size, lower power consumption, excellent signal-to-noise ratio, and a high QE of up to 40% [79, 82]. The X-ARAPUCA device is a novel light collection technology utilising SiPMs, currently developed by Unicamp and being tested at SBND. Details of X-ARAPUCA can be found in Ref. [83] and [73], while a short description is provided below.

X-ARAPUCA is a light guide designed to trap light through a combination of dichroic filters and wavelength shifters. The dichroic filter is transparent to a narrow range of wavelengths and reflective otherwise, allowing only photons of specific wavelengths to pass through the filter and preventing their escape. Fig. 3.11 illustrates a device with dichroic filters for detecting VUV photons with a cut-off at 400 nm. The para-terphenyl layer first shifts 128 nm photons to 350 nm, allowing them to pass through the dichroic filter. Once the photons are trapped, there are two main mechanisms for detection. As shown in the left panel, the wavelength shifter plate converts 350 nm photons to 430 nm, trapping them by total internal reflection until reaching the SiPM. As shown in the right panel, 350 nm photons are captured inside the reflective cavity until absorbed or detected.

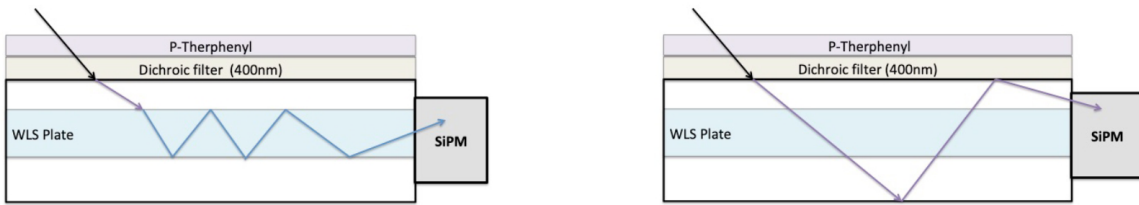


Fig. 3.11 Diagram illustrating the operating principles of a X-ARAPUCA [83].

Both PMTs and X-ARAPUCAs are coated with wavelength shifting materials. The re-emitted light direction is isotropic, causing coated optical detectors to suffer a 50% reduction in efficiency due to photons being emitted away from the detection surface. PMTs are coated specifically with TPB, which also impacts the detection time as the emission of visible photons is not instantaneous. Multiple time components of re-emitted photons from TPB have been observed, with the majority of photons re-emitted within nanoseconds and a subset re-emitted as long as a few microseconds [84].

Photon signals measured by PMTs are digitised and readout with a very high sampling frequency of 500 MHz [2], where the timing resolution attributed to the electronics is $\mathcal{O}(0.6 \text{ ns})$. Since PMT signals provide the most precise timing information available in

3.5 Concluding Remarks

the detector, they are crucially important across different areas of SBND. PMT signals are utilised for triggering to determine in real-time if a neutrino interaction occurs, to be discussed in Section 4.2.5. The signals also enable the timing resolution of the light reconstruction using PMT signals to reach $\mathcal{O}(2\text{ ns})$, to be covered in Chapter 6.3.1. The timing performance of the data acquisition to enable a stable and high frequency sampling of PMT signals is assessed in Chapter 7. All of these pave the way for the search for HNLs which is the focus in this thesis, exploiting the timing difference between HNL signals and SM neutrino backgrounds with more details covered in Chapters 9 and 10.

3.5 Concluding Remarks

Since originally proposed in 1977, the LArTPC concept has proven its potential in precision neutrino experiments. The understanding of particle interactions and their propagation within the detector, along with the detector's response to these particles, has significantly improved over time. Technological advancements in detection and readout now enable the scaling of LArTPCs from volumes of only several tons to even tens of kilotons, making them suitable for high multiplicity environments. This allows for the next generation of LArTPCs like the DUNE experiment to advance the field of neutrino physics. As described in the following Chapter 4, the SBND experiment and physics programme at Fermilab is a key part of this future.

Chapter 4

The Short-Baseline Near Detector and Booster Neutrino Beam

The Short-Baseline Near Detector (SBND) is the near detector of the Short-Baseline Neutrino (SBN) program at Fermilab. The program is motivated by anomalous results observed across various detectors involving accelerator, nuclear reactor, and solar neutrino experiments. For instance, the low energy excess in the ν_e and $\bar{\nu}_e$ interaction measurement observed by both LSND and MiniBooNE experiments is an outstanding anomaly for the past decade [16, 17]. In addition to being part of the SBN program, SBND also has its own extensive physics program focusing on high precision ν -Ar cross section measurements and physics beyond the Standard Model. This will not only benefit future long baseline neutrino experiments such as the DUNE but also significantly advance the field of neutrino physics as a whole.

This chapter contains an overview of the SBND detector and the Booster Neutrino Beam (BNB), which are the detector and beam source used in the search for Heavy Neutral Leptons (HNLs) in this thesis. The chapter begins with a discussion on the physics program of the SBND experiment in Section 4.1. Section 4.2 provides a detailed description of the detection technology of SBND, covering the time projection chamber, photon detection system, and cosmic ray tagger system. This section also elaborates on the hardware triggering system and the data acquisition system employed at SBND. Finally, an overview of the BNB is presented in Section 4.3, detailing the particle production process of the beam and the flux prediction at SBND. Finally, Sec 4.4 provides some concluding remarks.

4.1 The Short-Baseline Near Detector Physics Program

SBND is part of the Short-Baseline Neutrino (SBN) program located at Fermilab [1], consisting of three Liquid Argon Time Projection Chambers (LArTPCs): SBND, MicroBooNE, and ICARUS, positioned at distances of 110 m, 470 m, and 600 m on-axis to the target of the BNB as shown in Fig. 4.1. The near-far detector setup is located on the same baseline and beam source as the MiniBooNE detector. This was designed to search for the potential existence of sterile neutrinos in the mass $\mathcal{O}(1 \text{ eV})$, driven by a series of anomalies observed not only by MiniBooNE but also by previous short baseline experiments.

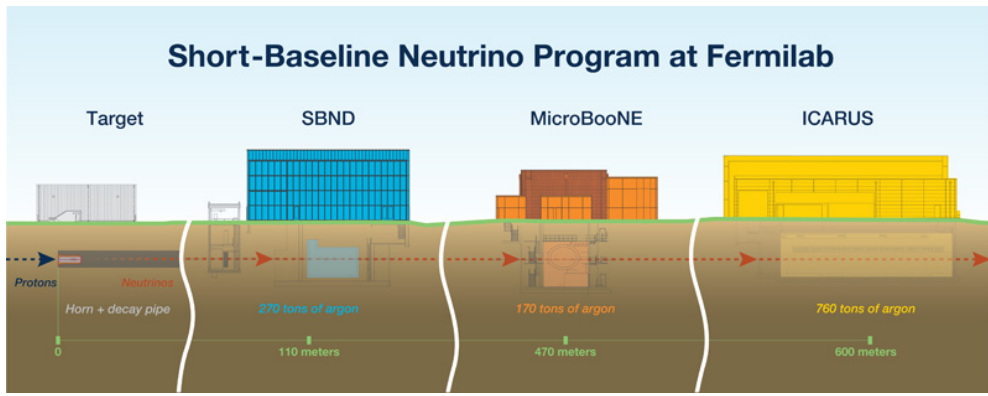


Fig. 4.1 Graphic showing the three LArTPC detectors made up the Short-Baseline Neutrino program: SBND, MicroBooNE and ICARUS [1].

Amongst these earlier experiments was LSND which utilised a stopping pion source to probe $\bar{\nu}_e$ via inverse β -decay and reported an excess of signal to the background at low energies with a 3.8σ level [16]. MiniBooNE was a neutrino accelerator experiment designed to measure the entire phase space covered by the LSND result [17]. It observed an excess of ν_e ($\bar{\nu}_e$) in ν_μ ($\bar{\nu}_\mu$) beam mode showing a discrepancy from the SM with a significance level of 4.5σ (2.8σ), reaching 6.0σ when combined with the LSND data. Additionally, a re-evaluation of results from nuclear reactor experiments indicated a deficit of $\bar{\nu}_e$ fluxes to the theoretical expectation at a 3σ level [85, 86]. Moreover, gallium solar neutrino experiments observed an overall deficit in ν_e fluxes at a 3σ level during calibration using radioactive neutrino sources [87, 88]. These anomalous results collectively suggest the mass mixing of SM neutrinos with an addition eV-scale sterile neutrino at a short baseline to energy ratio of $L/E \approx 1 \text{ m/MeV}$. This can enhance or reduce the number of observed neutrino interactions for a given channel [1]. The goal of the SBN program is to pioneer the search for eV-scale sterile neutrino oscillations, covering the parameter phase space previously allowed by past experiments but at a significance level of $\geq 5\sigma$.

4.1 The Short-Baseline Near Detector Physics Program

Additionally, precise measurements of ν -Ar interactions play a crucial role in the physics program of SBND, serving as a critical element in understanding neutrino oscillations [89]. Being the nearest to the beam target, SBND is presented with a unique opportunity to observe the largest unoscillated neutrino fluxes among the three detectors. Over the 3-year operational span, SBND aims to record a staggering 10 million neutrino events, originating from an exposure of 1×10^{21} Protons On Target (POT) [1]. This will establish SBND as the world leader in statistics for ν -Ar cross section measurements. More than 6 million Charged Current (CC) ν_μ events will be collected, reducing the statistical uncertainty to well below the percent level. Moreover, SBND is expected to record 45,000 CC ν_e events, providing the most extensive statistics for both inclusive and exclusive measurements of this channel. These measurements will be extremely beneficial for advancing the objectives of the SBN physics program, as well as contributing to the physics goals of the long baseline DUNE experiment, which employs argon as its detector medium.

Finally, a key aspect of the physics program at SBND is the exploration of new scenarios leading to Beyond Standard Model (BSM) physics. Proximity to a high intensity beam and the resulting large statistics enable searches for very weakly coupled interactions coming from the BNB [1]. A key example is HNLs, the primary focus of this thesis. These can be produced from meson decays in the BNB and decay in flight into SM observables for detection (See Chapter 2). Another compelling BSM candidate is light dark matter, which can be produced from neutral meson decay or proton bremsstrahlung [90]. The particles may scatter and decay, resulting in electron-positron pairs inside SBND. Moreover, the dynamic mass mechanism of SM neutrinos opens avenues for new physics in the dark sector. The dark neutrino model proposes that right-handed neutrinos can scatter with nuclei to produce dark gauge bosons, subsequently decaying into di-lepton pairs [91]. In the case where the leptons are electrons, this could potentially explain the low energy excess anomalies observed by LSND and MiniBooNE [92]. These represent just a few examples of the diverse BSM scenarios that can be explored at SBND. Other unmentioned possibilities such as new interactions, extra dimensions, and violations of Lorentz and CPT symmetries, among others, contribute to the rich physics program of SBND [1].

At the time of writing, SBND is currently in its commissioning phase, in preparation for physics data taking when the BNB beam returns in November 2024. The physics run is planned to begin shortly after the beam return and will last for three years. During the period, the delivery of the BNB is projected to be 1×10^{21} POT, which provides an immense statistics to carry out the physics program of SBND.

4.2 The Short-Baseline Near Detector

The SBND detector is a LArTPC with an active volume of 112 tons and dimensions of 400 cm (x-drift) \times 400 cm (y-height) \times 500 cm (z-length) [93]. As depicted in Fig. 4.2, the detector consists of two separate TPCs, each with a drift length of 200 cm, sharing a common Cathode Plane Assembly (CPA) positioned at the centre. On the east and west side of the detector are the Anode Plane Assemblies (APAs) made up of three wire planes, and located behind the wires is the Photon Detection System (PDS). The TPCs are surrounded by a field cage that provides a uniform electric field. The entire detector is placed inside a membrane cryostat, surrounded by 7 walls of Cosmic Ray Tagger (CRT) modules to provide a 4π solid angle coverage for cosmic ray rejection. The following sections provide an overview of each of the main subsystems of SBND.

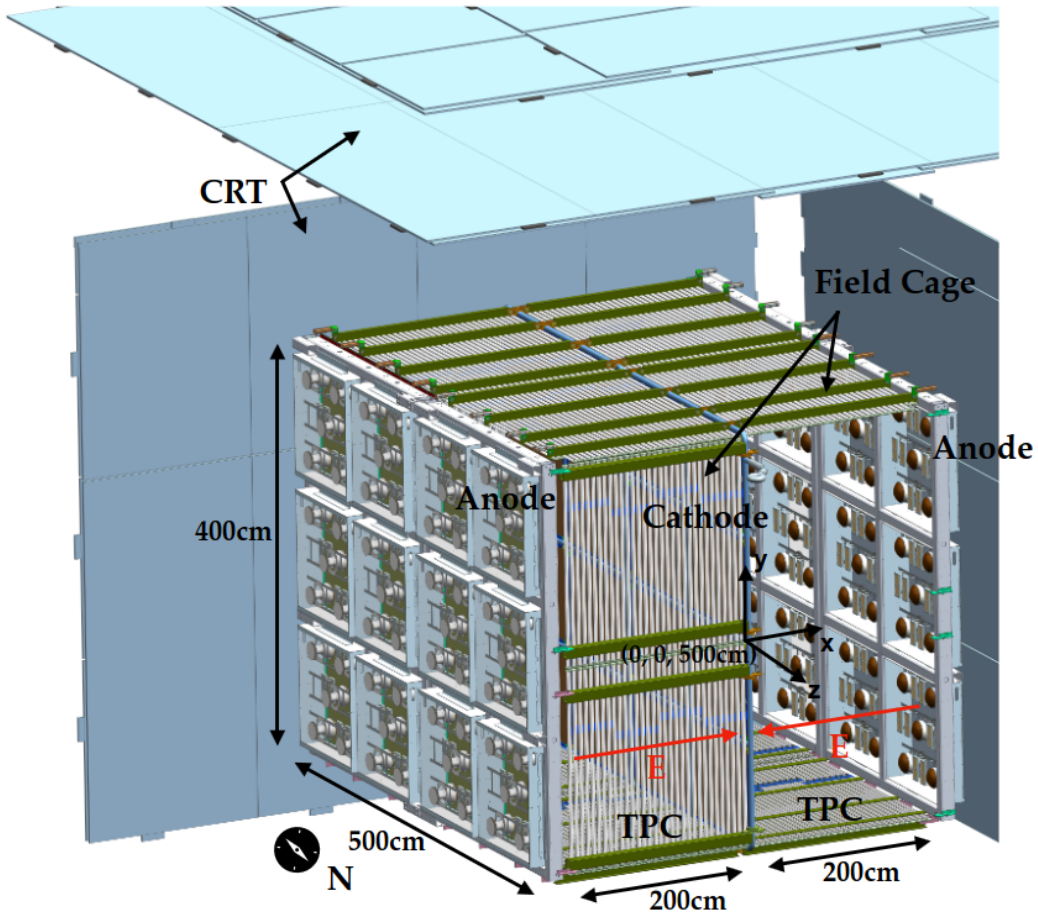


Fig. 4.2 3D model of the SBND detector, showing the LArTPC surrounded by 4 out of the 7 CRT walls [73].

4.2.1 Time Projection Chamber

Fig. 4.3 shows a complete APAs, of which each plane of APAs is located on the east and west sides of SBND. The plane is made up of two coupled APAs, where an APA measures $4\text{ m} \times 2.5\text{ m}$ and comprises a steel frame supporting three wire planes: two induction planes, denoted as U and V, oriented at angles of $\pm 60^\circ$ to the vertical collection plane denoted as Y. These wire planes U, V and Y are coloured as green, blue, and red, respectively. Each wire plane is constructed with $150\text{ }\mu\text{m}$ diameter copper-beryllium wires, with a wire pitch and plane spacing of 3 mm. The wires are tensioned to 7 N to prevent slackening when cooled down to a temperature at 88.4 K [94]. To maintain charge transparency for the induction planes and collection efficiency for the collection plane, a biased voltage of -200 V, 0 V, and 500 V is applied to planes U, V, and Y, respectively. In total, each TPC consists of 5,632 wires: 1,664 wires in the collection plane and 1,986 wires in each induction plane.

Two APAs are coupled together utilising jumper cables to bridge the 15 mm gap between the induction planes to form a single electronic channel. Attached to the top, left and right side of APAs are the cold electronics readout boards. They pre-amplify and digitise wire signals while submerged in liquid argon at a low temperature to minimise noise. Fig. 4.4a shows a photograph of a fully assembled APAs at SBND, where the PDS located behind the wires can also be seen.

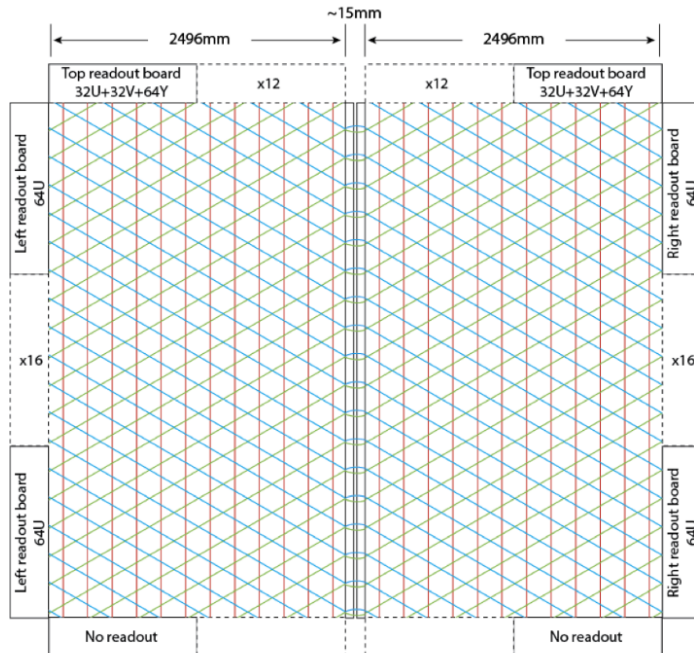
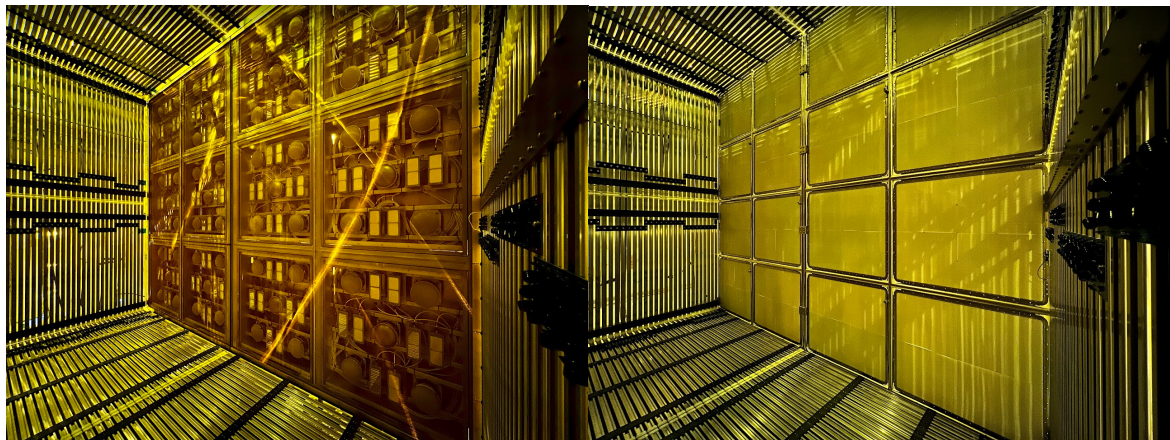


Fig. 4.3 Schematic showing two coupled APAs to form a complete APAs [93].

Fig. 4.4b shows a photograph of the fully assembled CPA. The plane consists of two steel frames, each containing 8 windows, adding to a total of 16 windows. Each window, measuring $60\text{ cm} \times 50\text{ cm}$, houses a fibreglass plate laminated on both sides with non-conductive reflective foils of $> 99\%$ specular reflection in the visible range and coated with TetraPhenyl Butadiene (TPB). Furthermore, the plate is covered by a wire mesh, providing a high voltage at -100 kV supplied by a feedthrough donut from outside the cryostat.

The field cage consists of a sequence of electrodes arranged perpendicular to the drift direction. It can be seen in both Fig. 4.4a and 4.4b as the series of metal bars surrounding the TPC. These electrodes incrementally step up the voltage from -100 kV applied at the CPA to the ground voltage in steps of 3 kV. This gradual voltage increase is implemented to maintain a uniform electric field of 500 V/cm across the drift volume.



(a) View of the APA

(b) View of the CPA

Fig. 4.4 Photographs showing the fully assembled TPC of the SBND detector.

4.2.2 Photon Detection System

The PDS design of SBND is the most sophisticated system ever installed in a LArTPC, by incorporating both active and passive optical components [73]. The active optical detector integrates two different technologies: (1) 120 Photomultiplier Tubes (PMTs) and (2) 192 X-ARAPUCA devices. The PMTs are cryogenic 8"-diameter Hamamatsu R5912-MOD models [95], which are the primary light detection system. Meanwhile, the X-ARAPUCAs serve as a research and development platform for future experiments, incorporating multiple variations in their components for performance comparison. A summary of the X-ARAPUCA specifications can be found in Ref. [73]. The TPB-coated reflective foils installed at the CPA are the passive component to improve the uniformity of light yield.

4.2 The Short-Baseline Near Detector

Fig. 4.5 shows a 3D model for each component of the SBND PDS. For the purpose of installation, the optical detectors are arranged into modular PDS boxes, of which a single PDS box is shown on the left of Fig. 4.5. Each box houses 5 PMTs, 4 coated and 1 uncoated PMT, along with 8 X-ARAPUCA devices, 4 coated and 4 uncoated. These PDS boxes are installed in a configuration of 4×3 behind each APAs as illustrated on the right of Fig. 4.5. This results in a total of 12 boxes per TPC volume. The TPB-coated reflective foils at the central cathode can also be seen on the right of Fig. 4.5.

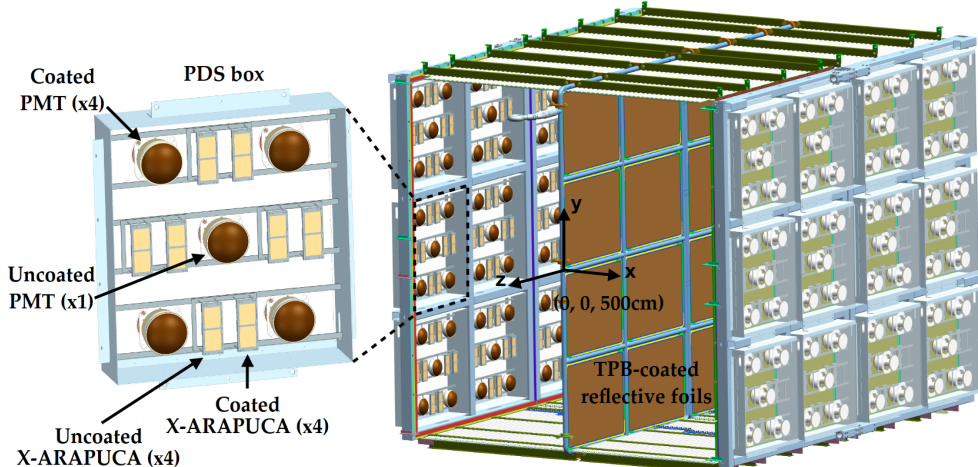


Fig. 4.5 3D model of a PDS box (left) and the PDS box arrangement on the east and west side of the TPC (right) [73].

Out of the two optical detectors, PMT signals are the primary light signals and are used to provide trigger conditions. The 120 PMTs are partitioned into two optically-isolated TPC volumes, each with 60 PMTs. Within each TPC, 48 PMTs are TPB-coated, and thus are sensitive to both direct VUV and reflected visible light, while the remaining 12 non-coated PMTs detect only reflected light. This ratio of coated to uncoated PMTs (4:1) is chosen to optimize light collection efficiency while maintaining the capability to distinguish between the two light components [73].

Having TPB is utilised at two locations: (1) evaporated onto reflective foils at the cathode, and (2) coated on the optical windows of the PMTs, leads to a difference in the spatial and arrival time distributions for direct VUV and reflected visible photons. Direct VUV photons arriving at coated PMTs are immediately wavelength shifted into the detectable range of PMTs. Reflected visible photons, resulting from VUV photons being wavelength shifted and reflected at the cathode, have to travel a longer distance before being detected by (un)coated PMTs. The TPB emission time increases the arrival time of reflected photons from fast components by 50% and from slow components by

10%. Additionally, the spatial distribution of reflected visible photons is more diffused and spread across a larger number of optical detectors compared to direct VUV photons [79]. Such difference can be exploited to perform the timing reconstruction using only PMT signals, which is further discussed in Section 6.3.1.

4.2.3 Cosmic Ray Tagger

Since SBND is a surface detector, it utilises a Cosmic Ray Tagger (CRT) system to effectively reject background from cosmic muons. Fig. 4.6 shows the operating principles of CRT strips and their orientation [54]. As shown in the middle diagram, each CRT strip consists of a plastic scintillator strip with a width of 10.8 cm, connected to a pair of SiPMs via wavelength shifting optical fibres. The right diagram shows a coincident hit from perpendicular strips that allows for a 2D reconstruction of the hit location with a spatial resolution $\mathcal{O}(2 \text{ cm})$, and the number of photons collected for each strip improves the precision of the location tagging.

The left diagram of Fig. 4.6 shows an example of 8 CRT strips arranged in parallel to form a CRT module and the modules are perpendicular to each other. Multiple CRT modules are arranged orthogonally to form a CRT wall, typically in the size of 7.5 m in height and 9 m in width. The cryostat of SBND is entirely encased by 7 CRT walls, with 1 on each side and 2 positioned on top of the detector. Fig. 4.2 shows 4 out of the 7 CRT walls, particularly the south, west and top walls are visible. Additionally, the top 2 walls function as a cosmic telescope, facilitating the tagging of vertical downward going cosmic muons. This configuration enables a comprehensive strategy for cosmic background rejection utilising both geometrical and high precision timing information.

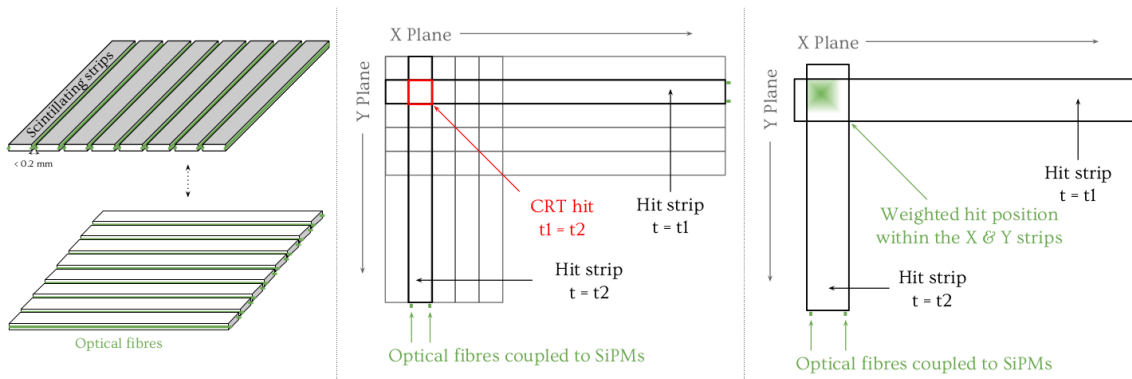


Fig. 4.6 Diagrams showing the operating principles of CRT strips (middle, right) and their perpendicular orientation (left) [54].

4.2.4 Readout Electronics

The readout electronics of each detection subsystem are detailed next. Firstly, TPC readouts comprise four components: (1) Cold Electronics (CE), (2) Warm Interface Boards (WIBs), (3) TPC crates and (4) Nevis Trigger Board (NTB). As shown in Fig. 4.3, the wires are connected to CE readout boards on the APAs. Located inside the cryostat, CE are submerged in liquid argon to reduce thermal noise as well as cable lengths [96]. They amplify and digitise signals at a sampling frequency of 2 MHz. Data from CE is sent outside of the cryostat to the WIBs via copper cold cables. The WIBs are connected to other TPC readouts through optical fibre links. This isolation architecture completely separates wire grounding from the building, thereby enabling a superior signal-to-noise ratio.

Following the WIBs, data is transmitted to 11 TPC crates for reading out, buffering, and processing the wire signals. Data from TPC crates are directed by the NTB into two parallel independent streams of data. The main stream to record neutrino beam events relies on an external trigger, which reads out data with lossless compression. An additional continuous stream requires no external triggers and outputs data with lossy compression.

Regarding the readout electronics of the PDS, CAEN digitisers are employed. 120 PMTs are readout by 8 CAEN V1730SB digitisers [97], capable of recording waveforms for 16 channels independently with a sampling frequency of 500 MHz. 192 X-ARAPUCAs are digitised by another model called V1740 [98], that can readout 64 channels at a lower sampling frequency of 62.5 MHz. Both models feature deep buffers to store longer waveforms and handle higher data rates. Additionally, the V1730SB model offers better waveform baseline stability against temperature fluctuations. Multiple V1730SB digitisers to read out PMTs are synchronised so that they collectively behave as a single digitiser, which is critical to maintain the electronics timing resolution $\mathcal{O}(0.6 \text{ ns})$. The characterisation of synchronisation across multiple V1730SB digitisers is detailed in Section 7.3.

Finally, 7 CRT walls are readout by 144 Front End Board (FEB) modules [99]. Each module is a multifunctional board capable of reading out 32 channels, with one channel per SiPM. The module provides a bias voltage, adjustable for individual SiPMs, as well as signal amplification and shaping. Once the signal is shaped, the module applies signal discrimination and self-triggering, such as coincidence for each pair of SiPMs in a CRT strip or coincidence across multiple modules for orthogonal CRT strips. Once the signal passes the self-trigger, it is digitised and timestamped with respect to an input reference clock. The clock frequency is 1 GHz and thus, the electronics timing resolution is $\mathcal{O}(0.3 \text{ ns})$. The data is stored in a buffer and sent via an Ethernet connection. The characterisation of the timing resolution of FEB modules is detailed in Section 7.2

4.2.5 Hardware Trigger

Triggering plays a vital role in the SBND detector to select only interesting physics events, given the detector is exposed to a high rate of backgrounds from cosmic muons. The main hardware trigger component in SBND is the Penn Trigger Board (PTB). It applies a programmable trigger logic based on external inputs and issues a trigger to the Data Acquisition (DAQ) subsystem if the conditions are met. Details of the hardware trigger at SBND is given in Appendix A, while a short summary is provided here.

In order to form a trigger, the PTB requires signals from the three subsystems: (1) beam subsystem, (2) PMTs, and (3) CRTs. The beam subsystem informs the PTB on the status on the BNB beam, and whether the beam has arrived at the detector hall. Signals from PMTs provides information regarding the intensity and locality of the energy deposited inside the detector, and whether it is consistent with a neutrino event. Signals from CRTs provides information of the energy deposited outside of the detector in the CRT walls, and whether it is consistent with a cosmic muon. The readout electronics of PMTs and CRTs are equipped with sub-nanosecond timing resolutions and their output signals can quickly inform the PTB to form a trigger. Additionally, incorporating CRT signals marks SBND as the first instance of a LArTPC to employ CRTs as part of its triggering scheme [100].

Different combinations of signal inputs described here can form different *flavours* of triggers. The primary *beam* trigger requires PMT signals to coincide with the beam spill window. Conversely, the *off-beam* trigger uses an anti-coincidence to the beam signal logic to select cosmic muons occurring outside of the beam spill window for background estimation purposes. The *calibration* trigger utilises coincidence across different CRT walls to select specific track topologies formed by cosmic muons. For example, anode-to-cathode-crossing cosmic tracks can be selected by requiring the east and west CRT walls to be coincident. These sets of tracks are useful for electron lifetime measurements, which is covered in Section 8.1.

The importance about the hardware triggering at SBND is that a single triggered physics event constitutes of two *types* of triggers: (1) a single Event TRIGger (ETRIG) issued to the TPC readouts and (2) multiple Flash TRIGgers (FTRIGs) issued to the PDS readouts. The ETRIG is used by the DAQ to acquire a long snapshot of the TPC waveform $\mathcal{O}(1 \text{ ms})$ while multiple FTRIGs are used to capture many short snapshots of optical detector waveforms $\mathcal{O}(10 \mu\text{s})$. The data is then assembled to build a physics event, of which the DAQ is explained in Section 4.2.6 and 4.2.7 next.

4.2.6 Data Acquisition

Upon receiving a hardware trigger, the DAQ begins to transport data from subsystem readouts to event builder machines. The SBND DAQ can assemble data from each subsystem into a physics event during real time data flow, known as the event building process. It must also be able to handle a high event rate due to the close proximity of SBND to the beam target. Additionally, the DAQ can apply software metrics to filter events for various data streams and data monitoring purposes.

Fig. 4.7 shows the data flow of the DAQ at SBND. It begins with raw signals from detection subsystems, shown as the coloured dotted arrows. The signals are acquired by readout electronics, shown as colour boxes in the first column labelled *Readout Electronics* (See Section 4.2.4). The boxes are colour-coded as red, blue and orange for the TPC, PDS and CRT readout respectively. Within this first column, two additional readout electronics are also included. The PTB, shown by the green box, is for the hardware triggering subsystem (See Section 4.2.5). The White Rabbit SPEC-TDC, shown by the purple box, is part of the White Rabbit timing subsystem and is discussed in Chapter 7.

Each readout electronics has a corresponding *boardreader*, shown by the second column labelled *Servers Hosting Boardreaders*. Boardreaders are software tools serving as a communication bridge between readout electronics and computer servers. The electronics send raw signals to the computer servers via boardreaders, shown as the grey dotted arrows. The boardreaders send configurations to the electronics, shown as the grey dashed-dotted arrows.

The event building process occurs in the third column labelled *Event Builder Machines*. The raw signals are packaged into a data format known as *fragments* by boardreaders. The fragments are sent to event builders, as shown by the coloured solid arrows. The event builders assemble fragments from different readout electronics into physics events. The event building process is discussed in Section 4.2.7 next.

Finally, the fourth column labelled *Data Stream* illustrates the last stage of the data flow. Software metrics are applied by event builders to separate physics events into different streams of data, as shown by the grey dashed arrows. This assists with data management since different flavours of triggered events can be organised into different locations. An additional data stream for online monitoring is shown by the bottom right grey box. Details of the data streaming process is provided in Appendix B.

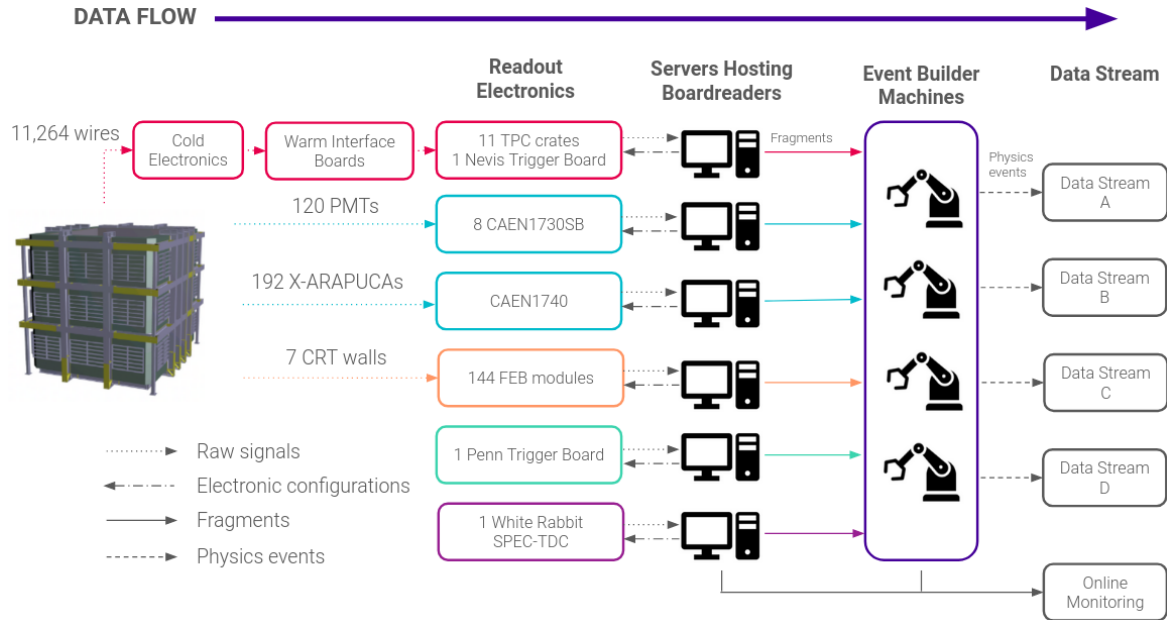


Fig. 4.7 Flow chart showing the data flow of data acquisition.

4.2.7 Event Building

One key process in the DAQ is event building. This is achieved by using the artdaq Toolkit, developed by the Real-Time Systems Engineering Department of Fermilab's Scientific Computing Division [101]. Within this framework, each readouts has a corresponding software module called *boardreader*. They facilitate communication between the readouts and the event builder machines, by sending configurations directly to the hardware in one direction and retrieving data from the hardware in the opposite direction. Data acquired from the readouts is packaged by boardreaders into a digitised format called a *fragment*. In the scope of this work interested in the timing performance of the DAQ to be given in Chapter 7, the critical information of a fragment is its timestamp corresponding to when the readout electronics receive a trigger.

Event builders assemble fragments from different boardreaders into a physics event based on their timestamps. Fig. 4.8 illustrates the chronological structure of a physics event at SBND, containing only TPC, PMT and CRT fragments for simplicity. The time axis is shown as the purple arrow, where at the centre $t = 0$ ms corresponds to when the beam spill begins. The TPC fragment, as shown in red, is coincident with the beam spill to capture the neutrino event in the TPC. The readout length of a TPC fragment is 1.7 ms, covering the entire TPC drift length of 1.3 ms and including a padding of 0.2 ms before and after the drift. Aligning the TPC fragment with the beam spill is achieved through the

4.2 The Short-Baseline Near Detector

ETRIG trigger issued to the TPC readouts so that the readout window coincides with when the beam spill begins.

PMT and CRT fragments are shown in blue and orange in Fig. 4.8. The fragment readout lengths from the PMTs and CRTs are much shorter compared to TPC fragments, $\mathcal{O}(10 \mu\text{s})$ and $\mathcal{O}(10 \text{ ns})$ respectively. For a single physics event, in contrast to only a single ETRIG issued to the TPC readouts, multiple FTRIGs are issued to the PMT readouts during the beam spill to produce multiple fragments of PMTs. Similarly, CRT readouts are self-triggered independently and produce multiple fragments. PMT and CRT fragments that have timestamps within 1.5 ms before and after the beginning of the beam spill are packaged together with the TPC fragment to form a physics event.

Here in Fig. 4.8, a time asymmetry can be seen in the chronological structure of a physics event at SBND. This is due to the different characteristics of photon signals, detected by the CRTs and PMTs, and electron signals, detected by the TPC wires. Specifically, a photon produced in a CRT scintillator strip takes approximately 5 ns to travel from the far end of the strip until reaching a SiPM [99]. Similarly, a photon produced in the TPC takes a maximum of 15 ns to propagate from a scintillation location to a PMT [73]. In contrast, an ionisation electron produced takes 1.3 ms to fully drift from the cathode to the anode [94]. This shows that photon signals propagate approximately six orders of magnitude faster than electron signals and consequently, need to be digitised and read out earlier.

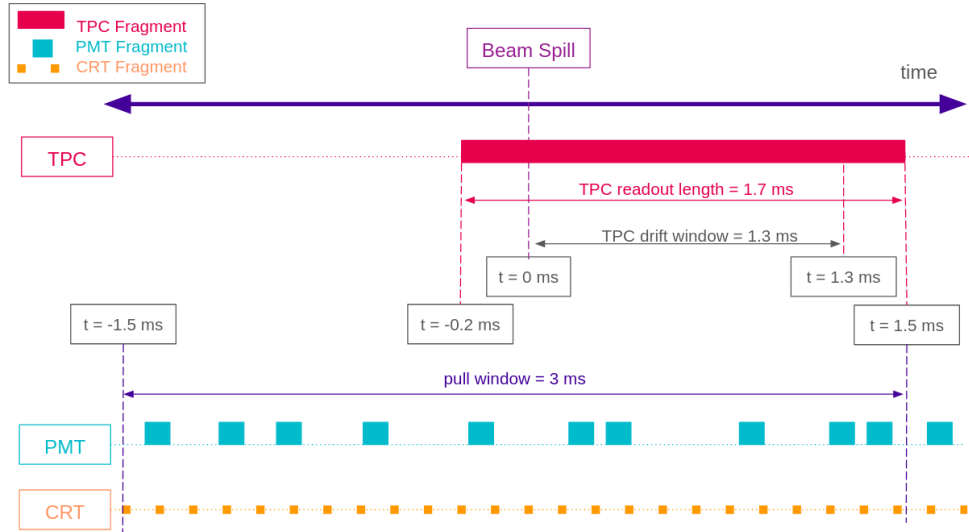


Fig. 4.8 Diagram depicting the chronological structure of a physics event.

4.3 The Booster Neutrino Beam

SBND directly measures neutrino fluxes coming from the BNB. Technical details of the BNB can be found in Ref. [102]. The BNB operates by extracting protons with a kinetic energy of 8 GeV from the Booster synchrotron in spills made up of 7 to 11 pulses in a row at a frequency of 15 Hz, averaging to a rate of ~ 5 Hz. Each spill delivers 5×10^{12} protons within a window lasting $1.6 \mu\text{s}$. The structure of a beam spill structure consists of 81 neutrino buckets, with a Gaussian width of 1.308 ns and a spacing of 19 ns [103]. Fig. 4.9 depicts the beam bucket structure as measured by the CRTs of SBND, which was set up as a beam telescope to collect data from the BNB in 2017–2018 [100]. Neutrino buckets can be seen distinctively in the distribution, indicating that the BNB structure can be resolved with a sufficient timing resolution. The timing resolution of the CRT readouts is $\mathcal{O}(2 \text{ ns})$, to be demonstrated later in Section 7.2.

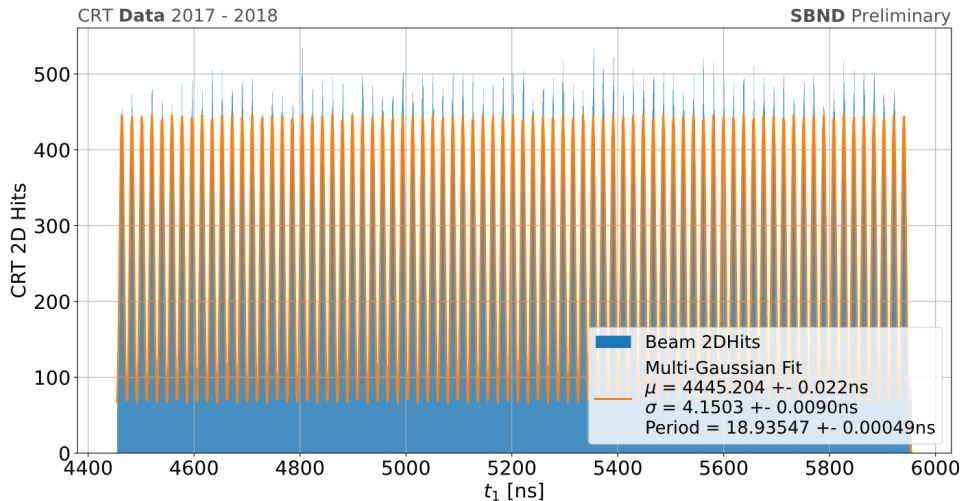


Fig. 4.9 The buckets of the BNB measured by the SBND CRTs during 2017–2018 [100].

The particle production in the BNB is illustrated in Fig. 4.10. Protons are injected into the Booster synchrotron and accelerated from 400 MeV to 8 GeV kinetic energy, as shown by the red arrows. Their intensity is measured by two toroids, while their positioning and timing are monitored by beam position monitors and Resistive Wall Monitors (RWMS). RWMS measure the current produced by protons travelling pass the beam pipe wall, and is able to capture the bunch structure of the BNB [104]. Upon exiting the Booster, the proton beam traverses focusing and defocusing quadrupole and dipole magnets before being focused onto the target of the BNB.

4.3 The Booster Neutrino Beam

The protons collide on the target to produce secondary mesons, as shown by the blue arrows. The target consists of a beryllium cylinder measuring 71.1 cm in length and 0.51 cm in radius. The choice of beryllium was motivated by its replaceable ability in the event of radioactivity issues, as well as its ability to facilitate sufficient energy loss via an air cooling system. The target is placed inside a pulsed horn system, which acts as a 170 kA electromagnet to focus the secondary mesons. The polarity of the horn can be adjusted to focus positive (negative) mesons for operating in neutrino (antineutrino) mode. Downstream of the horn assembly, a concrete collimator absorbs particles that do not contribute to the neutrino flux, thereby reducing radiation elsewhere in the beamline.

The focused mesons then propagate through an air-filled cylindrical decay region spanning 45 m, depicted as the orange box. The region is terminated by a steel and concrete absorber located 50 m from the upstream face of the target, depicted as the purple box. Secondary mesons decay into tertiary neutrinos within the decay region, while long-lived muons are absorbed by the absorber. Subsequently, tertiary neutrinos traverse through a dirt region before reaching the SBND detector, as shown by the pink arrows. The production of HNLs from kaon decays alongside neutrinos is also shown as the purple arrow.

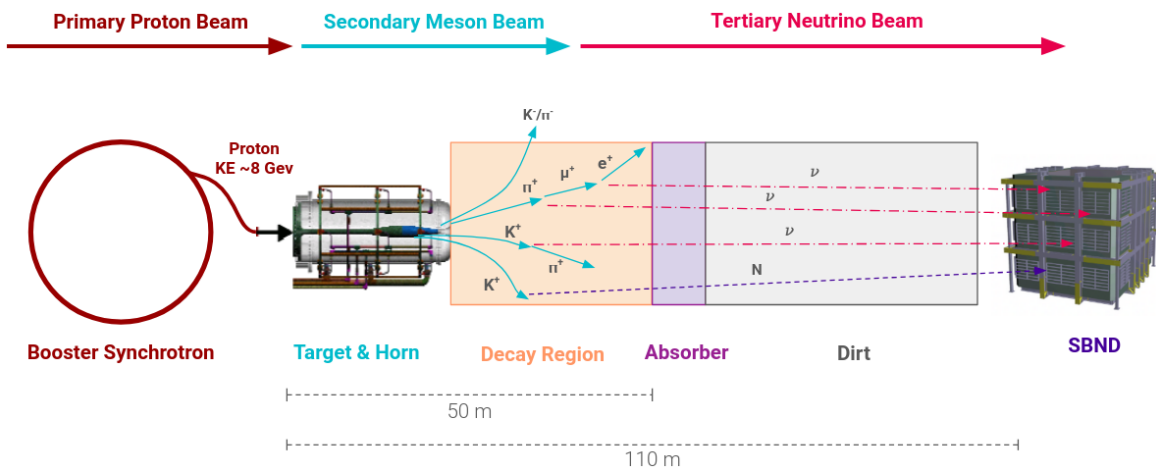


Fig. 4.10 Diagram showing the particle production in the BNB.

The beam is simulated using Geant4 [105] with different tunings for the composition of the secondary mesons and hadrons produced from $p + Be$ interactions [102]. The π^\pm production is tuned to the HARP and E910 data sets using Sanford-Wang parametrisation. The K^+ production is extrapolated to the global K^+ data using Feynman scaling-based parametrisation, and further constrained by SciBooNE's direct measurements of K^+ production from the BNB [4]. The K_L^0 production is fit to data from the E910 and KEK

experiments using Sanford-Wang parametrisation. The productions of K^- , p and n are modelled using the MARS hadronic interactions. Interaction cross sections of $p/n + \text{Be}$ and $\pi^\pm + \text{Be}$ are also incorporated in flux predictions [106]. Uncertainties associated with the flux modelling are discussed in Section 10.1.3.

Fig. 4.11 depicts the primary contributors to the secondary meson fluxes at the BNB, namely pions and kaons. A small fraction of muons resulting from pion decays also contribute to the fluxes. These fluxes are shown for the BNB operating in neutrino mode, mainly composed of positively charged mesons. As discussed in Section 2.2, the flux of HNL comes from K^+ decays, which has energy peaking at $0.5 \sim 1 \text{ GeV}$. Ref [102] has highlighted significant uncertainties in the K^+ production cross sections within this energy range. However, results from the SciBooNE experiment have demonstrated the validity of extrapolating higher energy K^+ data to the 1 GeV region using Feynman scaling [4].

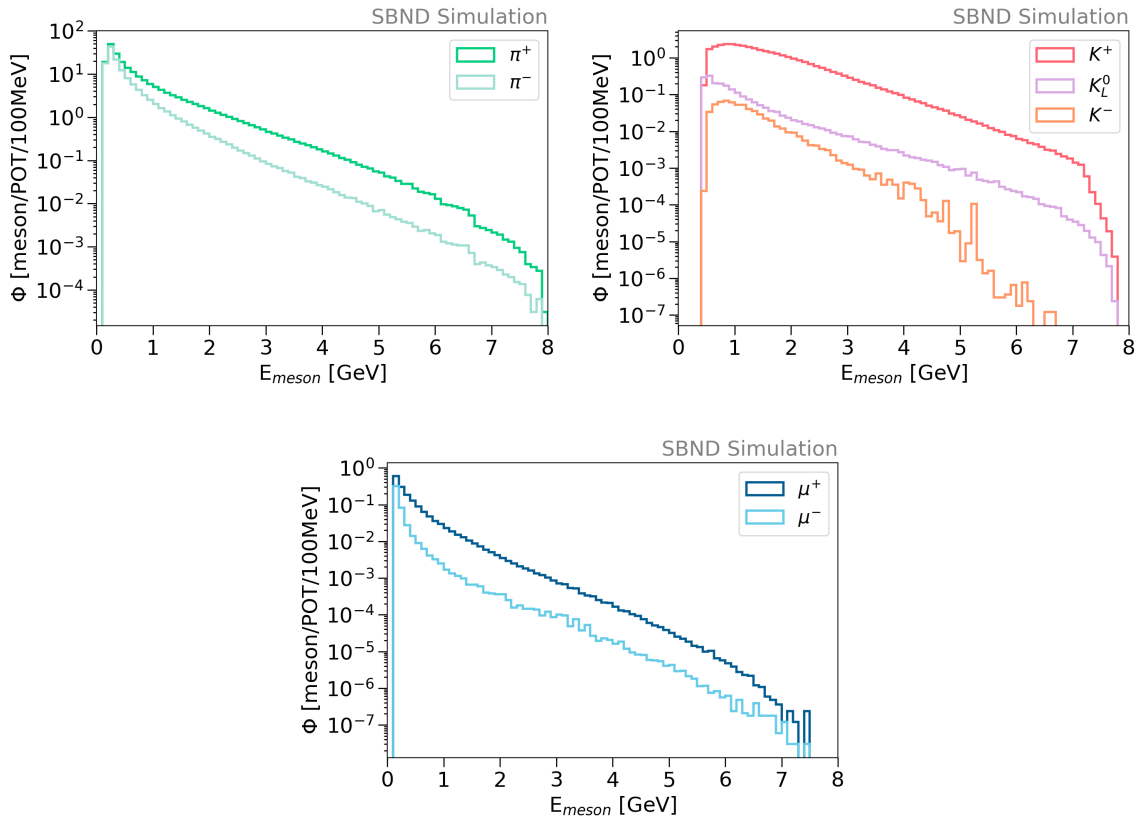


Fig. 4.11 Simulated fluxes for the secondary mesons produced in the BNB.

The simulation of the neutrino flux at the front face of SBND is depicted in Fig. 4.12, shown for different flavours of neutrinos. The flux is predominantly composed of ν_μ

4.4 Concluding Remarks

($\sim 90\%$), followed by $\bar{\nu}_\mu$ ($\sim 9\%$), while the combination of ν_e and $\bar{\nu}_e$ contributes less than 1% . Pion production is the dominant mechanism for both ν_μ and $\bar{\nu}_\mu$, followed by kaon and muon production. In the case of ν_e , muons produced from pion decay are the primary source at low energies, while kaon production becomes the dominant mode at higher energies. Finally, $\bar{\nu}_e$ mainly originates from K_L^0 production.

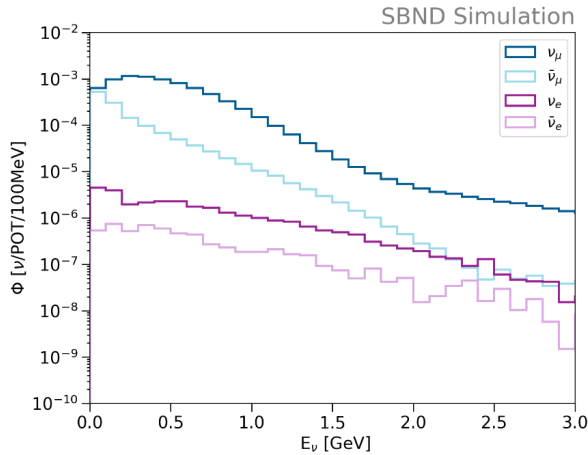


Fig. 4.12 Simulated neutrino fluxes at the front face of SBND.

4.4 Concluding Remarks

SBND, together with other experiments in the SBN program, aims to conclusively address the low energy excess observed by LSND, MiniBooNE, and other nuclear reactor and solar neutrino experiments. SBND will play a crucial role in constraining systematic uncertainties by measuring large statistics of the unoscillated neutrino flux from the BNB. Additionally, SBND has a rich physics program covering high precision ν -Ar cross section measurements and searches for BSM physics. Of particular relevance to this thesis, SBND aims to establish competitive limits on the coupling of HNLs within the probable mass range from the BNB.

The hardware of SBND comprises three detection subsystems: the TPC, the PDS, and the CRT system, alongside the hardware triggering subsystem. Each of these subsystems has dedicated readout electronics, which are managed by a complex DAQ subsystem. SBND measures the flux coming from the BNB, which has a distinctive bucket structure that can be resolved with a sufficient timing resolution. This feature can be exploited in the search for HNLs at SBND since being massive results in HNLs arriving late relative to the bucket structure of SM neutrinos. Chapter 5 provides a description of the simulation

framework at SBND to enable the exploration of the detector physics capabilities in the BSM regime using Monte Carlo.

Chapter 5

Simulation Framework of SBND

Many modern particle physics experiments heavily rely on simulations to assess the physics capabilities of the detector, to develop physics analysis tools as well as to relate experimental data to an underlying theoretical model they attempt to probe. The most common simulation technique is Monte Carlo (MC), by random sampling from Probability Density Functions (PDFs). PDFs can be modelled from theories or derived from experimental data or a combination of both. The search for Heavy Neutral Leptons (HNLs) at the Short-Baseline Near Detector (SBND) presented in this thesis employs simulated MC samples mimicking data. This enables an exploration of the detector physics capabilities in the regime of physics beyond the Standard Model (BSM).

The following chapter provides a description of the simulation framework of SBND to output simulated products representing real data. The chapter begins with an overview of the framework in Section 5.1. Following that, Section 5.2 includes details of the generator employed to generate HNLs, of which its development was contributed by the author. The summary of the generators of SM neutrinos and cosmic muons is given in Section 5.3. Section 5.4 covers the simulation of energy deposition as particles propagate through the detector and the detector response to the deposited energy. Finally, the chapter is concluded in Section 5.5 with some remarks.

5.1 Overview of the Simulation Framework

The software framework for simulation, reconstruction and analysis of SBND is provided by the LArSoft framework [107]. The framework was originally built for Liquid Argon Time Projection Chamber (LArTPC) neutrino experiments, allowing for detector-specific

customisation. This enables easy sharing of software tools across many collaborations including ArgoNeuT, MicroBooNE, ICARUS, SBND and DUNE. For example, the generator used to simulate HNLs, presented in Section 5.2 next, has been developed and shared across the SBND and ICARUS collaborations.

The simulation workflow of SBND under LArSoft is depicted in Fig. 5.1. The process begins with a generator to produce primary particles that enter the TPC, as shown by the purple box. The primary particles can be final states of neutrino interactions, cosmic muons or BSM particles depending on the generator type. The propagation of the primary particle inside and outside the TPC, and the resulting energy deposition is simulated using the Geant4 toolkit [105], as shown by the green boxes. For interactions inside the detector, the charge and light yield are calculated from the energy deposition. Ionisation electrons are propagated through the detector to the wire planes using the Wirecell toolkit [5], as shown by the red boxes. Scintillation photons are propagated to the photodetectors using a combination of a semi-analytical model and an optical library [73], as shown by the blue boxes. For interactions outside of the detector, only the energy depositions within Cosmic Ray Tagger (CRT) strips are converted into light yield, as shown by the orange box. The detector response is then simulated for each detector subsystem. By the end of this stage, the outputs from each detection subsystem ideally represent real data.

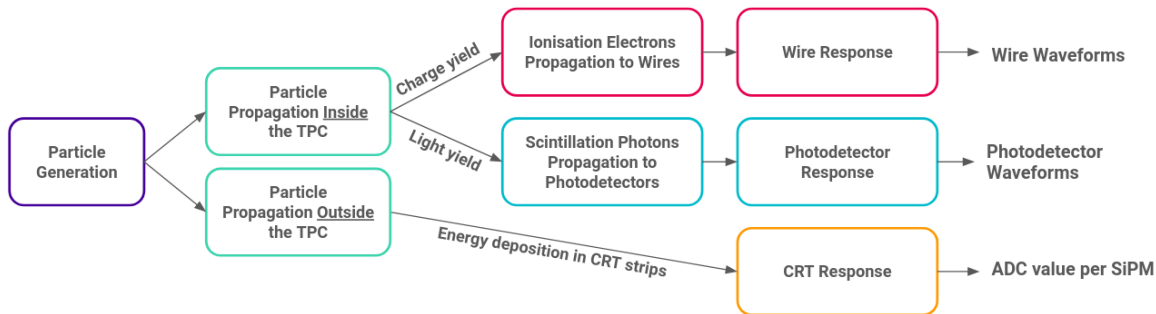


Fig. 5.1 Overview of the simulation framework of the SBND detector.

5.2 HNL Generator: MeVPrtl

BSM particles are generated using a generator called MeVPrtl, which was developed as a joint effort by collaborators from both ICARUS and SBND experiments. There are several BSM models implemented in the MeVPrtl generator, including HNLs, Higgs portal scalars [108] and heavy quantum chromodynamics axions [109]. It is a modular generator, allowing for easy adaptations for different beam sources and detectors, as well as a direct

5.2 HNL Generator: MeVPrtl

interface with LArSoft. The workflow of the MeVPrtl is broken down into four stages, as illustrated in Fig. 5.2. The generator begins with taking an input of meson fluxes produced from a beam source. It then simulates the meson decaying to a BSM particle. The BSM particle is propagated to the detector and decays back into SM observables.

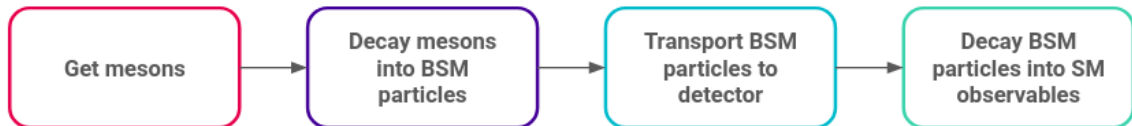


Fig. 5.2 Overview of the workflow of the MeVPrtl generator.

For generating HNLs coming from the Booster Neutrino Beam (BNB), the generator begins with sampling the K^+ fluxes of the BNB (See Fig. 4.11, Section 4.3). Instead of decaying into SM neutrinos, the kaons decay into HNLs, with the branching ratio defined by Eq. 2.8 (See Section 2.2). The daughter HNL and lepton are simulated using the two-body decay at rest in the centre of mass frame of the parent kaon and then boosted to the parent's lab frame by Lorentz boost. Due to HNLs having relatively high mass, the boost results in HNLs having less transverse momentum than the SM neutrinos, travelling preferably to the parent kaon direction. The boost can also flip the directions of HNLs that are emitted backwards, mostly originating from low energy kaons [110].

HNLs are then propagated to the detector by the ray tracing method, which picks a direction forcing HNLs to intersect SBND, defined as the TPC volume. The acceptance angle of HNLs to hit the detector is very beam-collimated at $<\sim 5^\circ$ with respect to the beam direction. This implies that only very forward-going HNLs are most likely to intersect the detector.

The simulated total energy spectra of HNLs arriving at the SBND detector are depicted in Fig. 5.3 for the mass range between 140 and 260 MeV. The spectra plotted here, and all subsequent kinematics plots in this section, are labelled *true*, indicating they are at the truth level and not yet passed through detector simulation and reconstruction. The spectra are normalised to the same coupling $|U_{\mu 4}|^2 = 1 \times 10^{-7}$ and an exposure of 1×10^{21} Protons On Target (POT) projected for 3 years of data taking. At the same coupling, the expected HNL rate decreases with lower mass since the branching ratio of $N \rightarrow \nu \pi^0$ decreases with lower mass (See Fig. 2.3, Section 2.3). Additionally, given that the K^+ total energy spectrum peaks at 0.5 GeV and decreases at higher energy (See Fig. 4.11, Section 4.3), the HNL spectra also concentrate at < 0.5 GeV, and substantially decrease at higher energy. A peak near zero can also be seen in all energy spectra across the mass range, corresponding to HNLs resulting from Kaon Decay At Rest (KDAR). Finally, the Kinetic

Energy (KE) of HNLs is expected to decrease with higher mass. This is due to HNLs coming from a kaon decay and therefore, the lighter the HNL mass, the more KE is available.

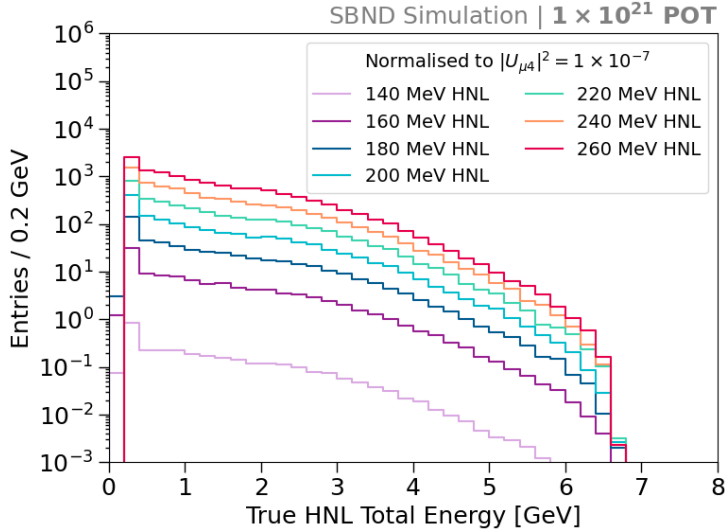


Fig. 5.3 Simulated energy spectra of HNLs decaying inside SBND.

HNLs are then simulated to decay back into the SM observables inside the TPC volume. For the $\nu\pi^0$ final state, the width of the decay is defined by Eq. 2.11 (See Section 2.3). The kinematics of the decay products are simulated for HNLs isotropically decaying in the rest frame and then boosted to the lab frame by Lorentz boost.

Fig 5.4 shows the simulated true momenta and angle to the beam distributions of the π^0 . The plots are area-normalised for direct comparison across the HNL mass of 140-260 MeV. The peak in the momenta distribution at low GeV and the peak in the angular distribution at high angle are from the π^0 resulting from low energetic HNLs from KDAR. Moreover, the momenta distribution of the π^0 decreases with increasing HNL masses. This is due to the decreased boosting of HNLs at higher masses having less KE. As a result, the angle to the beam direction of the π^0 also widens with heavier HNLs. However, at the heaviest HNL mass of 260 MeV considered in this work, the π^0 is still very beam-collimated since its angular distribution concentrates in the region $< 20^\circ$. Therefore, di-photon showers from the HNL-originated π^0 are expected to be more forward-going than those originating from SM neutrinos.

The timing delay of HNLs compared to SM neutrinos due to HNLs being more massive can be exploited in the search for HNLs at SBND. The components that make up the time of flight for an HNL or a SM neutrino produced from the BNB and propagating to the SBND detector are illustrated in Fig. 5.5. The first component is the spill time of the

5.2 HNL Generator: MeVPrtl

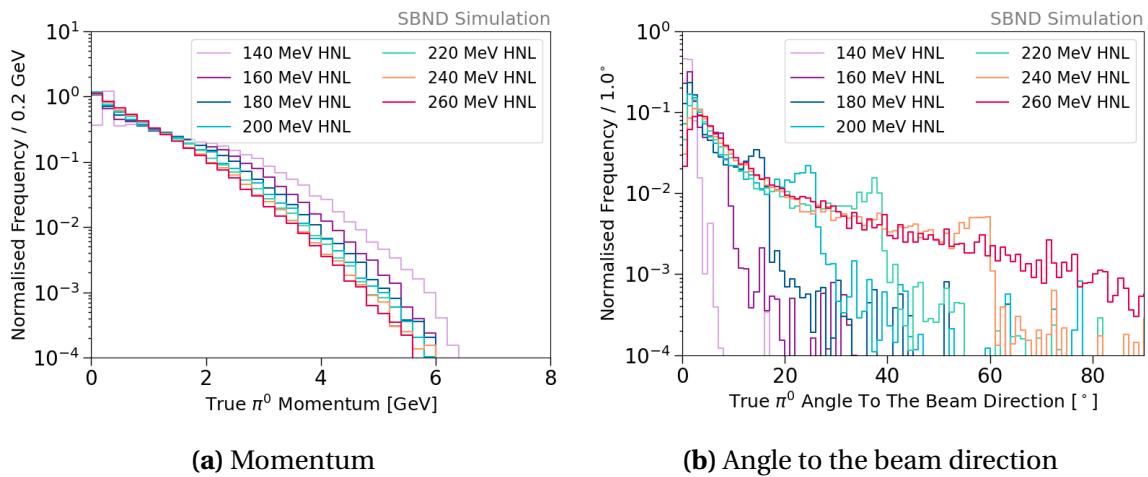


Fig. 5.4 Simulated kinematics distributions of π^0 from HNLs decaying inside SBND.

protons from the Booster synchrotron, t_{spill} , as shown by the red arrow. The structure of t_{spill} is the beam bucket structure made up of 81 Gaussian buckets with a width of 1.308 ns and a spacing of 19 ns (See Section 4.3).

The second component is the time of the secondary mesons, t_{meson} , as shown by the blue arrow. This is the period from when the mesons are produced until they decay into HNLs or SM neutrinos. This time accounts for the duration that the mesons travel down the decay pipe, and might interact, re-scatter or decay into other mesons. In the case of HNLs, t_{meson} is primarily the time of flight of the K^+ before decaying into an HNL. On the other hand, SM neutrinos come from a variety of parent mesons t_{meson} . In both cases, t_{meson} introduces some smearing to the nanosecond-bucket structure of t_{spill} .

The last component is the time of flight of the SM neutrino or the HNL from the production to the interaction location inside the SBND detector. In the case of SM neutrinos, since they are nearly massless, their velocity can be approximated as the speed of light. The time of flight of SM neutrinos is:

$$t_v = \frac{d_v}{c}, \quad (5.1)$$

where d_ν is the distance of a neutrino from the production to the interaction location inside the detector. Meanwhile, HNLs are massive and travel at a velocity $v_N < c$. The time of flight of HNLs is:

$$t_N = \frac{d_N}{\nu_N}, \quad (5.2)$$

where d_N is the distance of a HNL from the production to the decay location inside the detector. Additionally, since the KE of HNL decreases with its mass, the heavier it is, the slower its velocity.

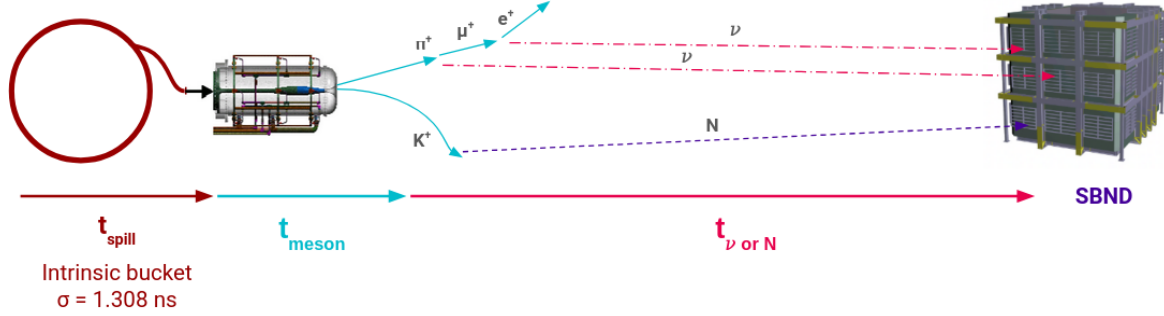


Fig. 5.5 The time of flight of a particle from the production to the detection location in the SBND detector.

The advantage of the MeVPrtl generator is the consistency of simulating the time of flight of HNLs compared to the GENIE generator [111] for simulating SM neutrinos. Fig. 5.6 shows the simulated true arrival time of SM neutrinos, in the dashed grey line, and 260 MeV HNLs, in the solid red line, at the front face of the SBND detector, recovering the beam bucket structure of the BNB. The plot is area-normalised to enable a direct comparison between the two particles. Since SM neutrinos travel nearly at the speed of light, less smearing is introduced and the arrival time distribution shows sharp Gaussian peaks. On the other hand, HNLs travel at a slower velocity, resulting in excesses on either sides of the Gaussian peaks.

For clarity, shown in Fig. 5.7 is the result of 81 Gaussian peaks overlaid into a single peak by applying a modulus of 19 ns. The arrival time distribution of HNLs is distinctively

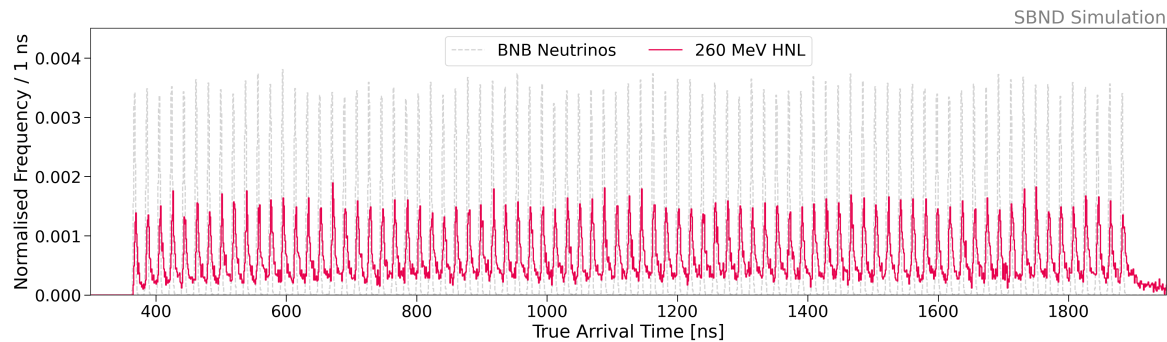


Fig. 5.6 True arrival time distribution at the front face of the SBND detector for SM neutrinos and HNLs.

5.3 Standard Model Generators

different from that of SM neutrinos, where excesses on either side of the Gaussian peak of SM neutrinos can be seen. It is important to note that excesses before the neutrino peak is due to the HNL tail of one bucket leaking into the next one. Between the mass of 140 to 260 MeV, the HNL excesses however do not increase significantly with mass.

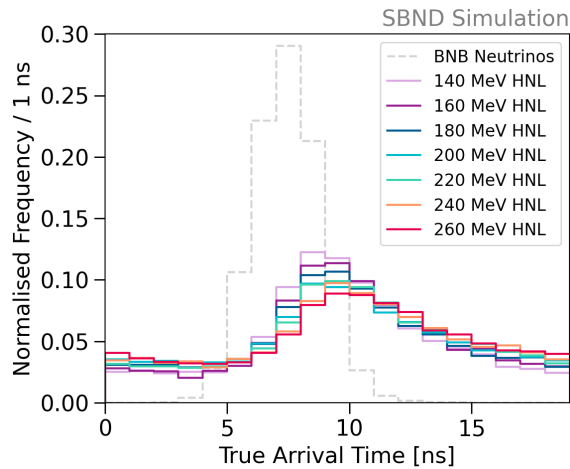


Fig. 5.7 True arrival time distribution for SM neutrinos and HNLs after applying a modulus of 19 ns .

5.3 Standard Model Generators

For generating backgrounds from SM neutrinos and cosmic muons, the two generators are GENIE [111] and CORSIKA [112] respectively. Each generator is discussed in Section 5.3.1 and Section 5.3.2.

5.3.1 Neutrino Generator: GENIE

SM neutrino interactions are generated by the GENIE generator [111], which provides a selection of theoretical and empirical models for different physical processes. These models can be combined into a *tune*, which is a set of optimised parameters used in the simulation for a better agreement between model and data. The GENIE tunes are made using an extensive dataset of electron, neutrino and hadron scattering experiments. SBND is using a tune that was developed to serve as a baseline model for the Short-Baseline Neutrino program and DUNE oscillation analysis, named AR20i_00_000. The tune was

developed using the base configuration G18_10a_02_11b, of which the details can be found in Ref. [113]. Ongoing developments of the tune is documented in Ref. [114].

GENIE first selects a nuclear model that describes the momenta and potential energy of the nucleon to model nuclear effects. Then, neutrino fluxes and integrated cross section models are used to compute the probability that a neutrino interaction occurs. Differential cross section models are used next to determine the type of neutrino interaction and the kinematic range. Neutrino interaction types include quasi-elastic, resonant, coherent, deep inelastic and ν -e elastic scatterings. In addition, a neutrino interacting with an argon nucleus can produce hadrons within the nucleus. The hadrons propagate through the nucleus, interacting via different modes such as charge exchange, elastic scattering, absorption and pion production. Consequently, hadron-nucleus interactions modify the final state particles and their kinematics. Thus, hadron transport interaction models are crucially important for predicting the final observables of neutrino interactions.

Relevant to the search for HNLs with a neutral pion in the final state, the main SM neutrino interaction backgrounds are the neutral current resonant and coherent pion production. From the tune AR20i_00_000, the model used for these two interaction modes is called Berger-Seghal [113, 115]. For resonant pion production, the model computes the cross section of baryon resonances, where the baryons are simulated to decay into pions isotropically. For coherent pion production, the model computes the pion-nucleus cross section, requiring a small momentum transfer to the target nucleus. GENIE does not apply the formation time to pions from these two modes, since the former results from baryon decays and the latter does not interact with the nucleus. The resulting pions are then simulated to propagate outside the nucleus, with a propagation time $\mathcal{O}(1\text{-}10 \text{ ys})$. This demonstrates the emission time of pions from SM neutrino interaction is almost instantaneously, significantly smaller than the late arrival of HNLs to the detector.

GENIE also provides uncertainties for a chosen model that can input to a reweighting scheme for uncertainty assessment. Due to the scarcity of neutrino interaction data, particularly for ν -Ar interactions, uncertainties of cross section modelling tend to be very large. Uncertainties of SM neutrino cross section is discussed in Section 10.1.4.

At SBND, GENIE simulates neutrino interactions occurring both inside and outside of the detector volume, with a boundary defined in Fig. 5.8. All interactions occurring inside the detector volume are kept, as shown by the dark blue box. Outside of the detector, a buffer volume is defined as 5 m surrounding the detector volume, as shown by the light blue box. An additional Rockbox volume is defined by extending the buffer volume backwards in the beam direction (z -axis) up to 15 m in front of the buffer volume, as

shown by the orange box. Neutrino interactions within this volume are kept because their products can potentially deposit energy inside the detector. These interactions are referred to as *dirt neutrinos* and constitute a significant background to the HNL search. The background rejection of dirt neutrinos is covered in Chapter 9.

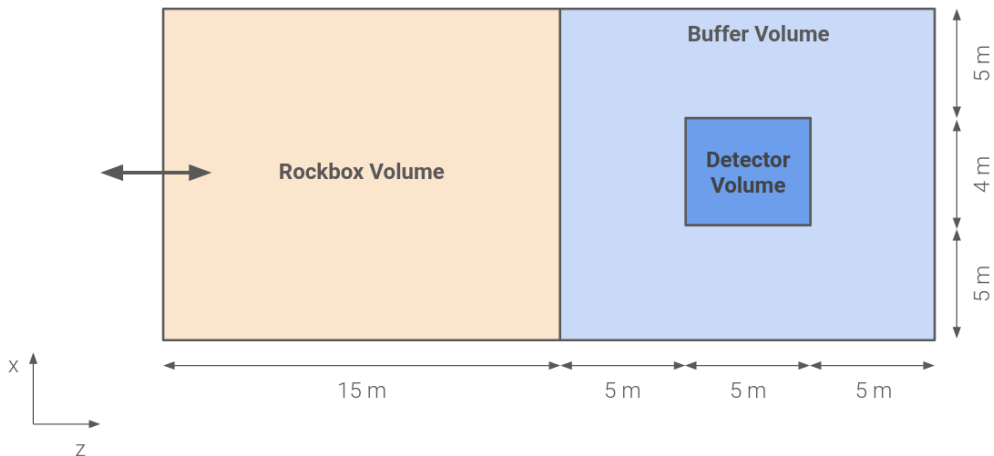


Fig. 5.8 Volume boundary defined by the GENIE generator to simulate neutrino interactions occurring inside and outside of the detector volume.

5.3.2 Cosmic Generator: CORSIKA

Cosmic interactions are simulated using the CORSIKA generator [112]. The generation begins with producing high energy primary particles incident in the Earth's atmosphere. The simulation adopts the same approach as the MicroBooNE experiment where primary particles are modelled as cosmic protons, motivated by a better data agreement as seen by MicroBooNE [116]. The primaries are then propagated through the atmosphere, interacting with the air to produce secondary hadrons that decay into long-lived particles reaching the Earth's surface. Within the SBND simulation geometry, this surface is specified to be just above the roof of the detector building. The surviving particles are then propagated to the SBND detector.

From a triggering perspective, there are two types of cosmic muons as follows:

- **In-time** cosmic muons cross the detector at the same time as SM neutrinos being present inside the detector, such that the muons are *inside* the beam spill window. The cosmic muons produce enough light to induce a beam trigger.
- **Out-of-time** cosmic muons occur regardless of the trigger conditions. The muons cross the detector *outside* the beam spill window but within the readout window.

However, at the time of writing, triggering simulation is currently a work in progress at SBND and is not simulated in the workflow. Only the timing requirement is simulated to keep only cosmic muons occurring within the readout window. The simulation currently does not accurately reflect the cosmic rate once factoring triggering conditions and therefore, a comparison to data is necessary.

Being a surface-level detector, it is vitally important to understand the cosmic background at SBND due to the high cosmic exposure. Once SBND is operational, a particularly useful measurement is the rate of cosmic muons that cause a beam trigger, however, in the absence of the beam. This is equivalent to measuring the rate of cosmic muons that produce sufficient energy inside the detector to mimic SM neutrino interactions. This measurement allows for validation against the CORSIKA generator. Moreover, it also provides an expected cosmic rate given a triggering condition, which can be added to the simulation framework to better constrain the cosmic background.

5.4 Particle Propagation and Detector Response Simulation

Simulated particles are propagated through the detector and deposit energy, producing ionisation electrons and scintillation photons. Detector responses to the ionisation electrons and scintillation photons are subsequently simulated, mimicking data. Section 5.4.1 first covers the simulation of particle propagation and energy deposition. Following that, Section 5.4.2, 5.4.3 and 5.4.4 provides a description of the simulation of the Time Projection Chamber (TPC), Photon Detection System (PDS) and CRT response.

5.4.1 Particle Propagation Simulation

Once a particle is simulated inside the detector, it is propagated through the detector using the Geant4 toolkit [105]. Geant4 propagates the particle by each step dx , where the step length is randomised and capped at 0.3 mm (one order of magnitude less than the wire pitch). At each step, physics processes are simulated, such as energy deposition, interaction, decay and so on. The step propagation also accounts for the electric field distortion caused by the space charge effect due to high exposure to cosmic muons.

The main physics process for energy deposition in the detector is ionisation by charged particles. Similarly to the theory detailed in Section 3.2, the Geant4 toolkit simulates the ionisation process following the Bethe-Bloch formalism tuned to data [117]. The number of ionisation electrons and scintillation photons from the deposited energy is computed

5.4 Particle Propagation and Detector Response Simulation

using the modified Box recombination model with ArgoNeuT parameters [65], and the charge-light anti-correlation from Eq. 3.2 and 3.3. Details of the ionisation simulation are further discussed in Section 8.2. The result from the Geant4 toolkit is a complete set of charge and light yields along the primary particle trajectories through the detector and the daughter particles produced from the primary.

5.4.2 Wire Response Simulation

Ionisation electrons are simulated to drift towards the wire planes using the WireCell toolkit [5]. The simulation transports the electrons and introduces smearing due to detector effects for transporting electrons through liquid argon under an electric field. This includes charge attenuation due to impurities, longitudinal and transverse diffusion and finally, space charge effect (See Section 3.3.1).

Once drifting electrons arrive at the wire planes, a convolution of the field response and the electronic response is performed. The field response describes the current induced on wires due to ionisation electrons drifting past the induction planes. The electronic response describes the amplification and shaping of each wire's induced current by pre-amplifiers. The response functions are in two dimensions, time versus wire, to account for the long range charge induction effect on wire signal shapes. A digitisation step is applied to produce an ADC-level, time-domain waveform for each wire channel. The waveform is parameterised by the ADC resolution, voltage range and baseline specification of the wire readouts. Finally, inherent electronic noise is added to the waveform to better match to observed data. MC waveforms at this stage should represent real data waveforms.

5.4.3 Photon Detection System Response Simulation

Scintillation photons are simulated to propagate to optical detectors, accounting for transport effects such as Rayleigh scattering and boundary effects (See Section 3.3.2). Technical details of the light simulation can be found in Ref. [73]. Instead of fully performing ray tracing of photons that can be computing intensive, the simulation uses a combination of a semi-analytical model and an optical library model to effectively estimate light detection probability. The choice of which model to use depends on the location of the photon production. The semi-analytical model, as described in Ref. [118], is used for those produced inside the TPC volume. The optical library model, readily available in LArSoft, is used for those that originate outside of this volume.

The semi-analytical model calculates on-the-flight the geometrical aperture for each optical detector to a scintillation location, given that the emission of scintillation photons is isotropic. Corrections for photon transport effects are applied to the number of photons detected by an optical detector. However, the semi-analytical method is limited by the geometrical information and does not include scintillation outside the TPC volume, for example, cosmic muons crossing behind an optical detector can produce non-negligible photons. Since PMTs are the primary subsystem for triggering, it is vital to consider this second-order contribution of photons for triggering studies. The optical library stores information of the fraction of incident photons for each optical detector for a given scintillation location, which can be looked up for any detector-location pairs during simulation.

For each type of optical detector, PMTs and X-ARAPUCAs, a respective photon detection efficiency is applied to the number of detected photons. Signal amplification and digitisation are simulated, converting photons into an output signal known as a single electron response. Then, signal shaping such as overshoot and undershoot due to the AC circuit of the optical detectors are applied. Finally, random fluctuation in the signal integral and non-linearity response at high light intensities are applied to better mimic data. The output is MC optical waveforms for each detector type, mimicking data.

5.4.4 Cosmic Ray Tagger Response Simulation

The energy deposition outside of the cryostat from the Geant4 simulation stage is considered if it is within CRT strips. It is converted into photons within a strip and propagated down optical fibres towards the SiPMs for detection. The collection efficiency per SiPM is accounted for by dividing the light yield between the fibres on either side of the strip, based on the lateral position of the energy deposition within the strip. Propagation effects and signal attenuation are also simulated. Finally, the electronic response is simulated for the CRT readout, by assessing if a pair of SiPMs within a strip goes above a threshold within a coincidence window. To better mimic the readout electronics of CRTs that process 32 SiPMs at a time, MC outputs of CRTs are in a group of 32 ADC values, where each value corresponds to a SiPM.

5.5 Concluding Remarks

The simulation framework of SBND is an end-to-end process, starting from the particle production, to its energy deposition and subsequently, the detector response to the energy deposition. MC outputs of the simulation mimic data, enabling studies to understand and improve the detector performance as well as to compare against theoretical models. For example, Chapter 6 next provides a description of the reconstruction framework at SBND, of which many algorithms have been developed using MC samples. Furthermore, calibration studies presented in Chapter 8 were carried out using MC samples of protons and muons to better understand the particle-dependent energy deposition. Finally, the search for HNLs presented in the two final Chapters 9 and 10 was also performed using MC samples to explore the physics capability of SBND.

Chapter 6

Reconstruction Framework of SBND

The process of extracting physics quantities from raw data recorded from an experiment is known as reconstruction. At the Short-Baseline Near Detector (SBND), the physics characteristics of a particle can be reconstructed using multiple detection subsystems. For instance, a contained particle inside the Time Projection Chamber (TPC) might deposit energy resulting in only waveforms recorded by the TPC wire planes and the Photon Detection System (PDS). On the other hand, an exiting particle might deposit additional energy in the Cosmic Ray Tagger (CRT) walls surrounding the TPC. For a given particle, the TPC reconstruction extracts various quantities describing its topology, deposited energy and kinematics using charge information. The PDS reconstruction provides additional high precision timing and deposited energy using light information. The CRT reconstruction indicates if the particle is fully contained inside the detector. As a result, reconstruction variables from all three detection subsystems are complementary to each other.

This chapter provides a summary of the reconstruction framework at SBND. Firstly, Section 6.1 gives an overview of the reconstruction workflow for each detection subsystem. The following Section 6.2 details of the TPC reconstruction workflow, including a track-shower separation algorithm updated by the author. The reconstruction of the PDS and CRT subsystem are summarised in Section 6.3. Descriptions of some high level analysis tools using the reconstruction variables collectively from each detection subsystem are included in Section 6.4. Finally, the chapter is concluded in Section 6.5 with some remarks.

6.1 Overview of the Reconstruction Framework

An overview of the reconstruction framework is illustrated in Fig. 6.1. The TPC reconstruction workflow is shown by the red boxes. This process begins with raw wire waveforms going through the signal processing performed by the Wirecell tool kit [5]. This is followed by a hit finding algorithm to identify hits on the waveform. Output hits are then used by the Pandora package [6] to produce a 3D-reconstructed interaction, referred to as a *slice*. The PDS reconstruction workflow also follows a similar process to the TPC, as shown by the blue boxes. A waveform deconvolution is first performed on raw PDS waveforms to filter noise. Then, a hit finding algorithm identifies optical hits on the waveform and reconstruction is performed on the hits. The equivalent output to the TPC-reconstructed interaction from the PDS reconstruction is referred to as a *flash*. Finally, the reconstruction for the CRTs is much simpler compared to the other two subsystems, consisting of only a hit finding and a reconstruction algorithm, as shown by the orange boxes. The reconstruction variables from each detection subsystem are produced independently and can be matched together if they originate from the same interaction. The variables can also be combined and input into different high level analysis tools to extract more complex properties of the underlying interaction.

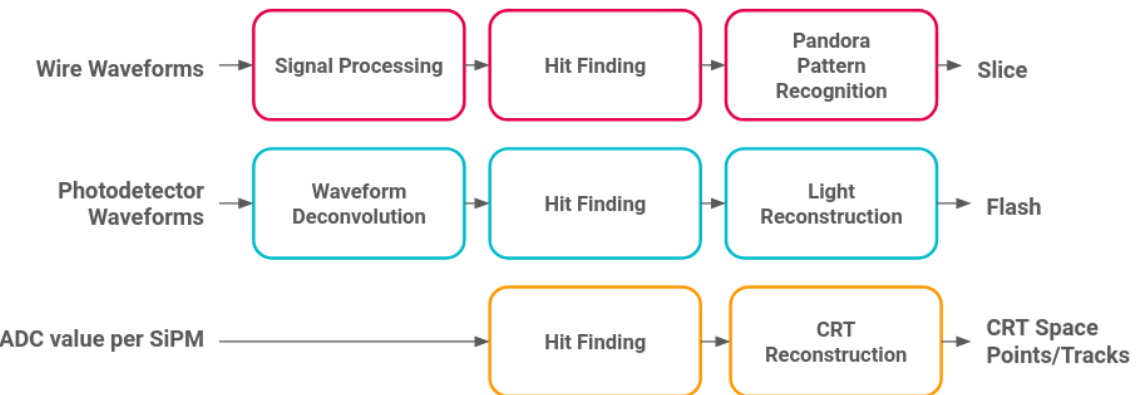


Fig. 6.1 Overview of the reconstruction workflow of the SBND detector.

6.2 Time Projection Chamber Reconstruction

This section covers the TPC reconstruction workflow, starting with Section 6.2.1 on the signal processing and hit finding. Section 6.2.2 details the 3D reconstruction using Pandora and Section 6.2.3 delves into the track-shower separation algorithm of Pandora.

6.2 Time Projection Chamber Reconstruction

6.2.1 Signal Processing and Hit Finding

Signal processing is the first crucial step of TPC reconstruction, which is to deconvolve raw waveforms, accounting for detector effects such as noise, electronics response and field response. At SBND, signal processing is implemented using the WireCell tool kit [5], which has been employed and developed by Liquid Argon Time Projection Chamber (LArTPC) experiments like MicroBooNE [5] and ProtoDUNE [119].

The first step is noise filtering to remove excess and coherent noise from raw waveforms. A 2D deconvolution of the field and electronics response is applied to recover the original charge deposited on the wire, where response functions consider the time response of a single wire as well as of neighbouring wires. This step is particularly important for the induction planes to convert bipolar into unipolar signals, so that the integral of the waveform can be used for charge estimation. High frequency filters are applied next to attenuate noise that is artificially amplified. Finally, low frequency filters are utilised for peak finding and local baseline removal.

Fig. 6.2 shows event displays of a simulated neutrino event as seen by wires on the induction plane. The left panel depicts a neutrino interaction using the true charge deposition on wires, simulated without any detector effects applied. The middle panel illustrates the interaction using raw waveforms before signal processing. The right panel shows the interaction using deconvolved waveforms after signal processing. Two tracks and two showers can be clearly seen in the right panel, demonstrating the excellent performance of

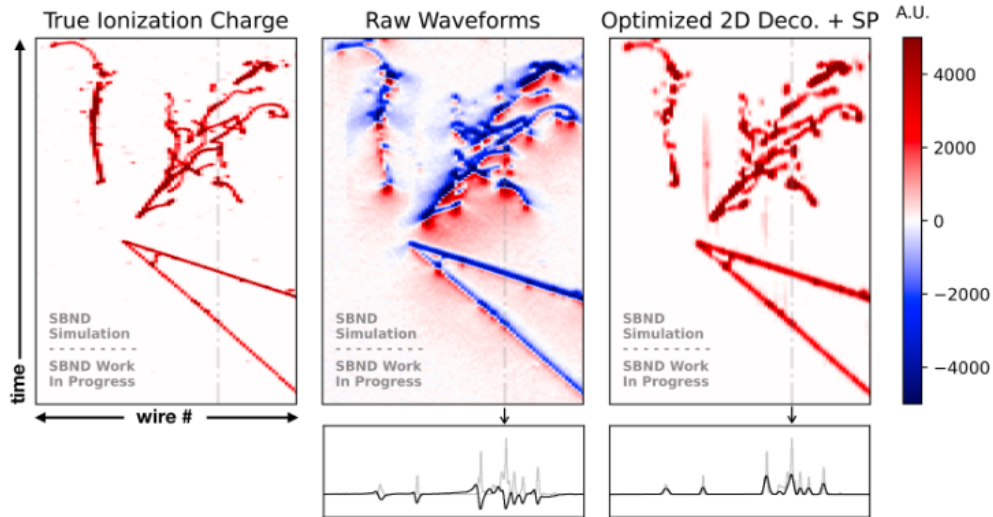


Fig. 6.2 Event displays of a simulated neutrino interaction using true charges (left), raw waveforms (middle) and deconvolved waveforms (right) [120].

the signal processing chain to de-tangle detector effects from raw waveforms and recover the original deposited charge. Signal processing in SBND is currently a work in progress, as labelled so in Fig. 6.2. At the time of writing, optimisation signal processing specifically for the SBND electronics has begun.

Hit finding is to search for Gaussian-shaped pulses above a threshold, by fitting a series of Gaussians to the deconvolved waveform [121]. The number of pulses is determined by the number of maxima found when differentiating the waveform, where each pulse represents a hit. Fig. 6.3 demonstrates the hit finding process for a deconvolved waveform, showing four identified hits and each fitted with a Gaussian. Information of the fit is extracted and used by downstream reconstruction. The peak time represents the time at which the charge arrives at the wire, used for determining the drift position and matching hit coincidence across wire planes. The height and the width of the Gaussian are used to calculate the integral of the pulse, representing the deposited charge on the wire, subsequently used in downstream analysis for energy deposition computation.

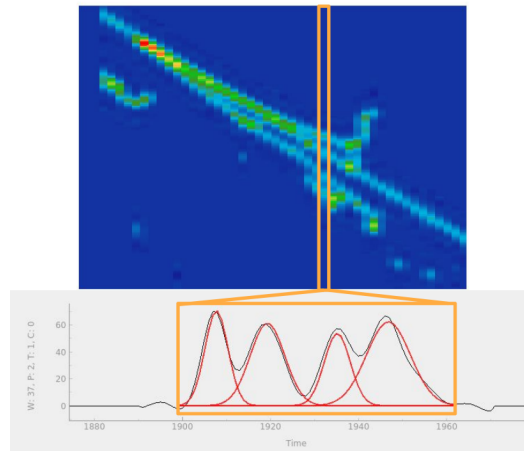


Fig. 6.3 Diagram illustrating the hit finding algorithm on a single wire [122].

6.2.2 Pandora Pattern Recognition

Output hits are used for 3D reconstruction, performed by the Pandora pattern recognition package [6]. It was first developed for the International Linear Collider and later extended to LArTPC experiments. The package is made up of over 100 individual algorithms, each performing a specific task along the reconstruction chain. Output from Pandora represents an interaction, referred to as a *slice*, containing a hierarchy of particles starting with a neutrino parent at the interaction vertex.

6.2 Time Projection Chamber Reconstruction

The reconstruction begins with a workflow to reconstruct cosmic-like objects that leave long tracks inside the detector. Hits on each wire plane independently are grouped together to form 2D clusters. Clusters across planes are matched to perform 3D reconstruction under the assumption that all clusters are track-like. A cosmic rejection is performed to identify if a 3D cluster is cosmic-like or neutrino-like, although it is deliberately cautious at this stage so that only very unambiguous cosmic-like clusters in nature are removed.

The remaining neutrino-like clusters are input into a second workflow dedicated towards neutrino reconstruction. It begins with a slicing algorithm that group clusters into *slices*, where each slice encapsulates hits coming from a single origin, representing an interaction. 2D clustering is re-performed on each wire plane independently, with a new assumption that clusters can be both track-like and shower-like. A vertexing algorithm identifies the interaction vertex of the slice and its associated clusters. A series of pattern matching algorithms grows the interaction starting from the vertex and performs 3D reconstruction by matching 2D clusters across different planes. Output 3D reconstructed objects in a slice associated with a vertex represent *particles*.

At this stage, a *track score* is assigned to a particle if it has a track-like or a shower-like topology, which is determined by a Boosted Decision Tree (BDT). Development of the track-shower separation BDT is covered in Section 6.2.3 next. Both track and shower reconstruction algorithms are performed on the particle. Finally, a hierarchy algorithm classifies the hierarchy of particles in a slice, starting with the neutrino parent vertex, and other particles are children, grandchildren, etc. of the parent.

The last stage is energy deposition computation of the reconstructed particles. Both track and shower energy computations first convert ADC units to charges by multiplying by a charge calibration constant. The track energy is computed from charge using the modified Box recombination formalism, factoring in the electric field distortion (See Eq. 8.4, Section 8.2.1). The shower energy is computed from charge by multiplying by a shower calibration constant, factoring in an averaged recombination factor regardless of the electric field. Once SBND is operational, the charge calibration constant is expected to be measured using anode-to-cathode crossing cosmic muons while the shower calibration constant can be acquired from the neutral pion invariant mass as a standard candle [59].

6.2.3 Track-Shower Separation Boosted Decision Tree

Reconstructed particles from Pandora are assigned a track score determined by a BDT, configured as a binary classification tool. The track score spans between 0 and 1 such

that if a particle has a very high track score close to 1, it is track-like. Otherwise, if its track score is very close to 0, it is shower-like.

The track-shower BDT became more important in the reconstruction as well as the analysis due to a new paradigm introduced by Pandora, where both track and shower reconstruction are performed on a particle regardless of its track score. All reconstructed particles now have two sets of reconstruction variables for track-like and shower-like. Users have the freedom to decide which variables to use depending on their signal topology, and thus not pre-determined by Pandora. The track score can inform which appropriate reconstruction variables should be used for the analysis.

The original track-shower separation BDT included variables describing the topology of a particle such as its length, distance and direction with respect to the parent vertex, as well as calorimetry variables describing the charge distribution of the particle. More details of the input variables and the training of the BDT can be found in Ref. [122]. It was updated to extend to a brand new set of variables describing how cone-like the charge distribution of a particle is as well as a new variable describing the particle hierarchy.

The cone variables were first developed in Ref. [123] for particle identification and were imported into Pandora for reconstruction purposes. There are three variables: (1) halo-total ratio, (2) concentration and (3) conicalness as depicted in Fig. 6.4. The diagrams depict the hit distribution of a particle, where each circle represents a hit associated with a charge value and the star represents the vertex of the hit cluster. The illustration is in 2D for simplicity, however the variables are computed in 3D.

The first variable is the halo-total ratio, illustrated in Fig. 6.4a. The Moliere radius in liquid argon is 10 cm, defined such that average 90% of a cylindrical energy deposition is contained within this radius [57]. The region outside the Moliere radius is considered the halo region. The hits in the halo are shown as green circles whereas any other hits are shown as grey circles. The halo-total ratio is then defined as:

$$\text{Halo - Total Ratio} = \frac{\text{Charges in the Halo}}{\text{Total Charges}}. \quad (6.1)$$

The second variable is called concentration, accounting for how concentrated the charge distribution is to the centre of the cluster. This is depicted in Fig. 6.4b, where each hit is assigned a colour showing how weighted it is with respect to its orthogonal distance to the cluster direction. The closer the hit to the centre, the more weighted it is. The concentration variable is defined as the total weighted charges divided by the total

6.2 Time Projection Chamber Reconstruction

charge as following:

$$\text{Concentration} = \frac{\sum \text{Charge} \times \text{Weight}}{\text{Total Charges}}. \quad (6.2)$$

Finally, the conicalness variable examines the hit distribution at the end and the start of the cluster as depicted in Fig. 6.4c. It is defined as the ratio between the concentration at the end of the cluster compared to that at the start of the cluster:

$$\text{Conicalness} = \frac{\text{Concentration at the End}}{\text{Concentration at the Start}}. \quad (6.3)$$

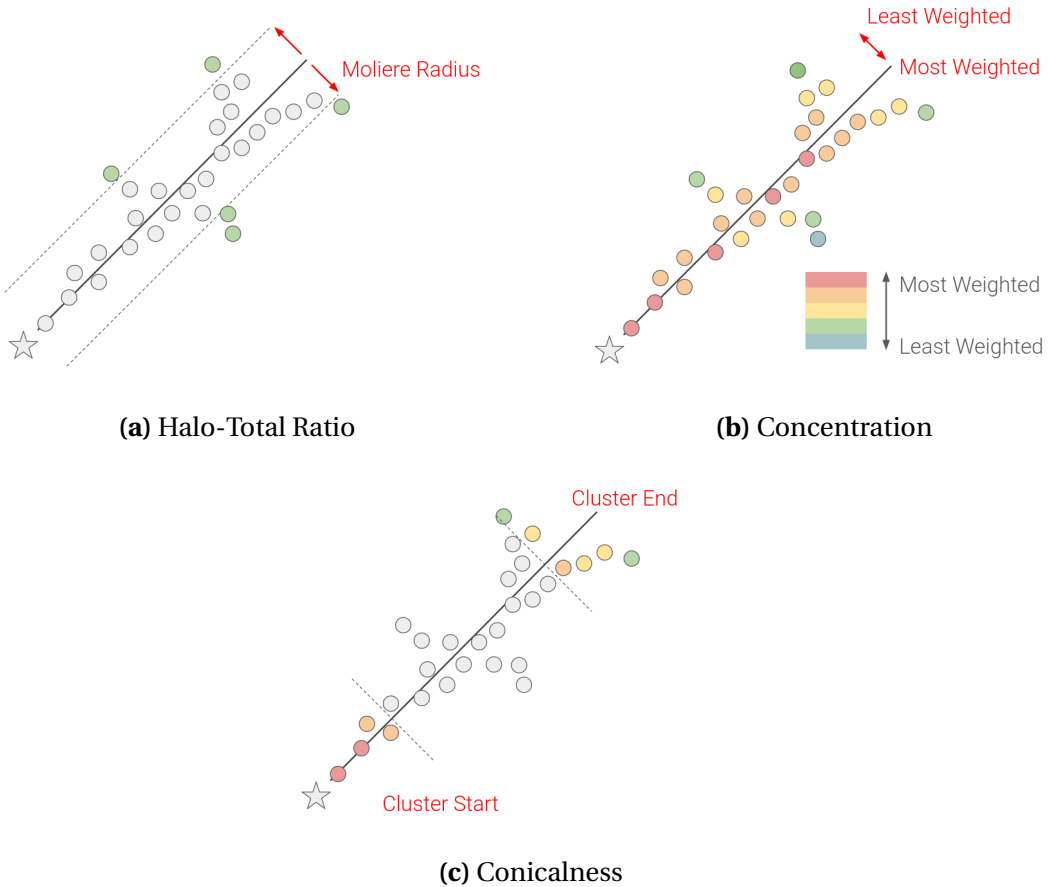


Fig. 6.4 Variables describing how cone-like the charge distribution is.

On top of the cone variables, another variable was added to the track-shower separation BDT to describe the hierarchy of the particle within a slice. For a given particle, the daughters originating from that particle are identified and their number of hits are counted. Distributions of the four new variables are shown in Fig. 6.5, with track-like particles shown in blue and shower-like particles shown in red. The concentration and

conicalness variables display the strongest separation power between tracks and showers compared to the halo-total ratio and the number of daughter hits variables.

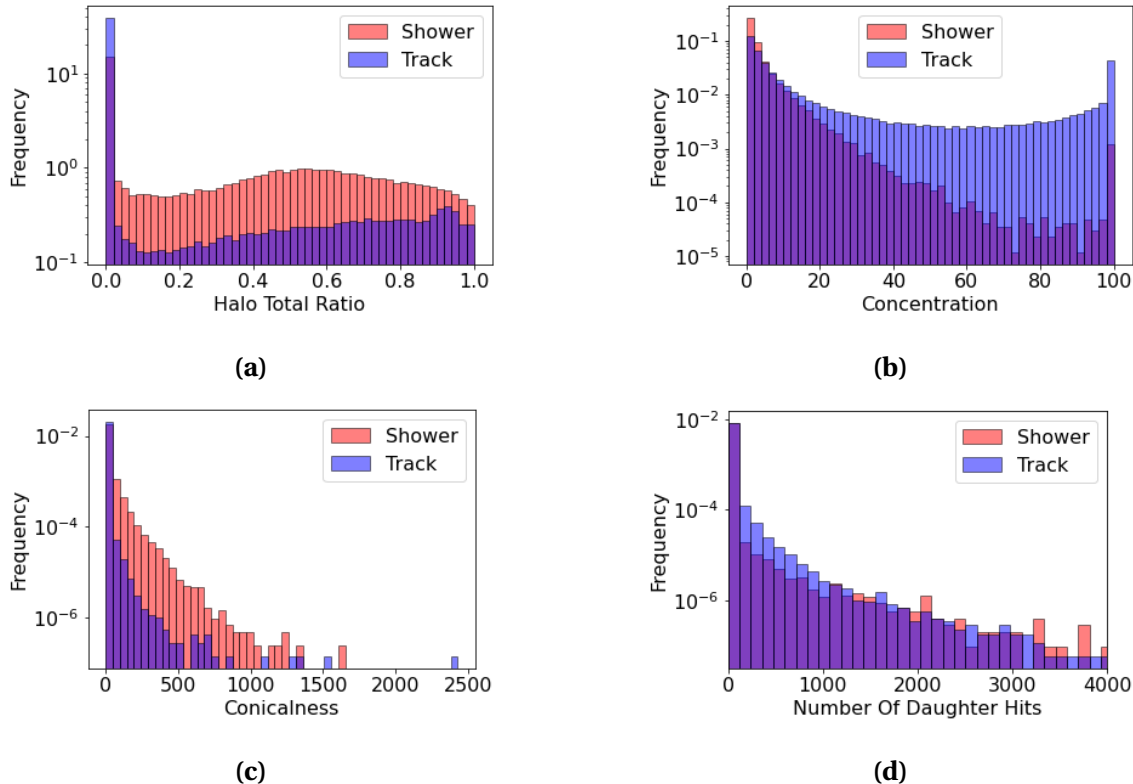


Fig. 6.5 Distributions of four new variables: (a) halo-total ratio, (b) concentration, (c) conicalness and (d) number of daughter hits.

Fig. 6.6 shows the score distribution of the BDT retrained with the four new variables. The left figure shows two distinct distributions in red and blue for showers and tracks respectively. This demonstrates a good separation power of the BDT, where particles with a score < 0.5 closely resemble showers whilst particles with a score > 0.5 are more track-like. The score distribution is broken down into different particle types as shown in the right figure. The distribution is expected given that electrons and photons leave electromagnetic shower activities inside the detector whilst charged particles like muons, charged pions and protons leave track-like signatures (See Section 3.2.1). The updated BDT resulted in a $0.1 \sim 2.0\%$ improvement in correctly classifying a particle type as shower-like or track-like. The track-shower separation score distribution is used in downstream high level analysis tools as detailed in Section 6.4.1 next. It is also employed as a cut variable in the selection of Heavy Neutral Leptons (HNLs), to be discussed in Chapter 9.

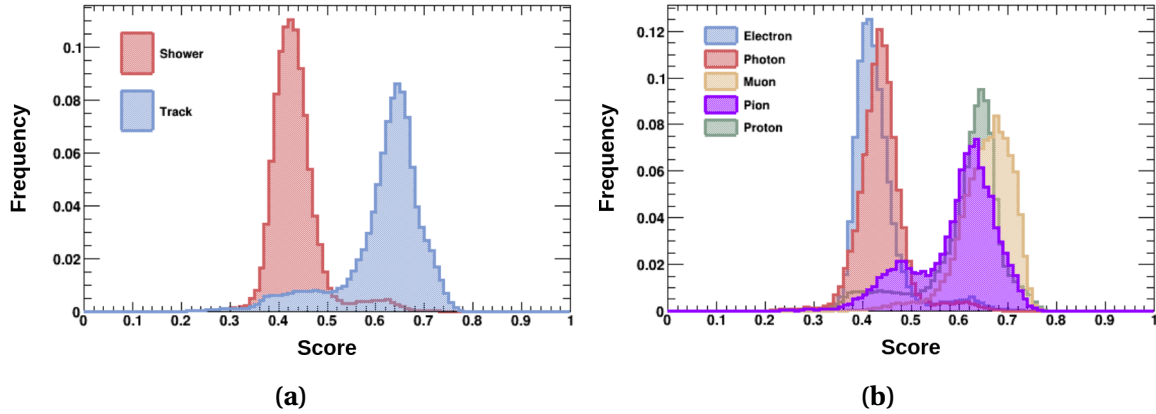


Fig. 6.6 Score distribution of the updated track-shower BDT, plotted for (a) track-like and shower-like particles and (b) different particle types.

6.3 Photon Detection System and Cosmic Ray Tagger Reconstruction

The reconstruction workflows of the two detection subsystems, PDS and CRT, are given in Sections 6.3.1 and 6.3.2.

6.3.1 Photon Detection System Reconstruction

Details on the PDS reconstruction at SBND can be found in Ref. [73]. Here the focus is on the reconstruction of PMT waveforms, which have an averaged Single Electron Response (SER) pulse peaking at ~ 25 ADC and a full width at half maximum of ~ 10 ns. The fast response of PMT signals plays a key role in the nanosecond timing resolution requirement for the HNL search.

Fig. 6.7a depicts an example of a simulated PMT waveform before and after the deconvolution. The top panel shows the number of *true* PhotoElectrons (PEs) seen by a PMT as a function of time in green. The middle panel shows the raw waveform in blue, convolved with the PMT response and noise. A 1D deconvolution and a high frequency filter are applied subsequently for noise removal. The deconvolved waveform is shown in orange in the bottom panel, demonstrating that over/undershoot features are removed while peaks' magnitudes and positions are maintained.

Baseline of deconvolved PMT waveforms is estimated using the 400 ns portion at the start and end of the waveform. Optical hits are identified after baseline subtraction, by

finding pulses above the threshold of 1/4 the amplitude of the deconvolved SER and 3 times the baseline root mean square. Fig. 6.7b depicts a simulated deconvolved and baseline-subtracted PMT waveform with five identified optical hits. Peak times, corresponding to the maximum of an optical hit, are denoted with red triangles. The first optical hit contains multiple peaks merged into a single optical hit due to multiple photons arriving very closely in time to the PMT. The rise time of an optical hit is when its first peak goes above 15% of its amplitude, denoted with blue stars. It is an estimation of the arrival time of the first photon contributing to the optical hit. The integral of the optical hit is used to compute the number of PEs.

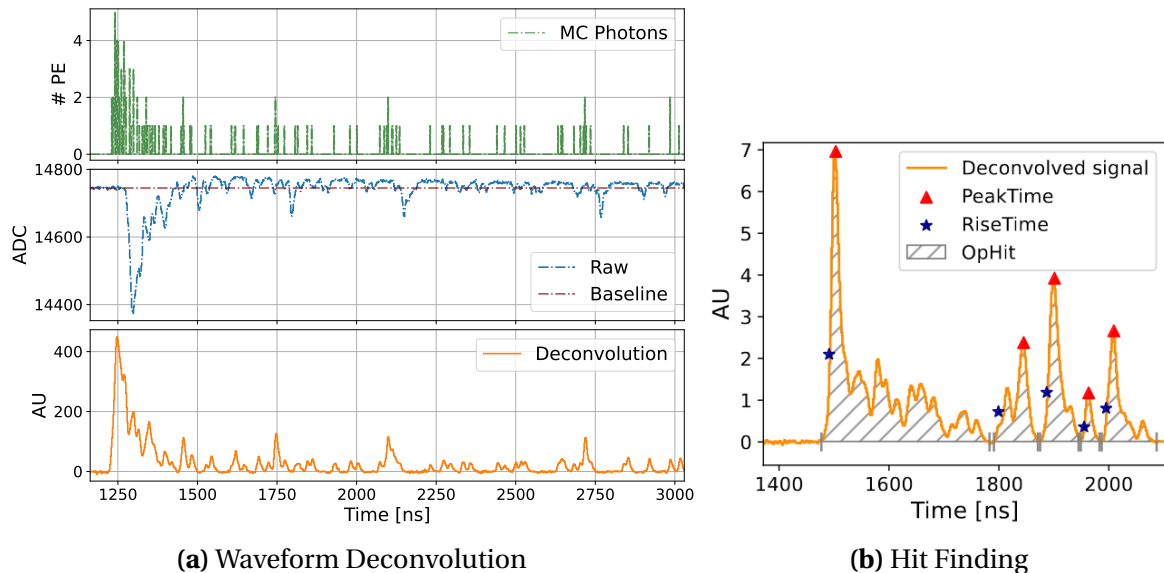


Fig. 6.7 Example demonstrating (a) waveform deconvolution and (b) hit finding applied to a PMT waveform [73].

Optical hits from at least 3 PMTs are clustered into an *optical flash*. The length of an optical flash is set as $8 \mu\text{s}$ to account for the total light produced in a neutrino interaction in the TPC, from both prompt and slow components of scintillation photons. The clustering algorithm is based on the number of PEs of optical hits, the timing distribution between hits and the geometrical location of the PMTs. The number of PEs in a flash is the total PEs of hits clustered in that flash.

The start time of the optical flash represents the start time of an interaction, t_0 , which is the key variable of the HNL search, and therefore requires great care in reconstruction. The flash start time is the average of the rise time of optical hits in a flash, only considering PMTs that contribute 50% of the prompt light in the 30 ns window of the largest number of PEs. This ensures that the scintillation photons originates close to the interaction vertex.

6.3 Photon Detection System and Cosmic Ray Tagger Reconstruction

A correction is applied to the flash start time to account for the propagation time of the photons from the scintillation location to PMTs for detection, which heavily depends on the drift distance in relation to the anode or the cathode. Closer to the anode at $d_{drift} = 0$ cm, the first photons arriving at PMTs are direct VUV components. In the region of $0 \text{ cm} < d_{drift} < 145$ cm, the propagation time increases from ~ 4 ns to ~ 15 ns. At $d_{drift} = 145$ cm, this is the tipping point where the propagation time of the direct and reflected components is identical and reaches its maximum. Closer to the cathode at $d_{drift} = 200$ cm, and hence the reflective foils, the first photons arriving at PMTs are instead the reflected visible component. VUV photons arriving at cathode are wavelength shifted with an averaged time constant of 10 ns, and then reflected backwards to PMTs with a faster group velocity (See Section 3.3.2, Fig. 3.9). In the region $145 \text{ cm} < d_{drift} < 200$ cm, the propagation time decreases from ~ 15 ns to ~ 8 ns with drift distance.

The propagation correction is computed by exploiting the high density of PMTs as well as having (un)coated PMTs sensitive to direct VUV light and reflected visible light (See Section 4.2.2). Fig. 6.8a shows the reconstructed light yield seen by (un)coated PMTs based on simulation, as a function of the photon mean drift distance, d_{drift} . The error bars show the uncertainty due to the border effects, where the amount of collected light varies greatly depending on the position of energy deposition relative to the detector edge.

Closer to the anode at $d_{drift} = 0$ cm, the light yield primarily comes from direct VUV photons, detected by coated PMTs as shown in purple. Closer to the cathode at $d_{drift} = 200$ cm, the light yield from reflected visible photons increases, detected by uncoated PMTs as shown in red. For a given scintillation location, the amount of direct VUV and visible photons leads to a specific ratio of the two components, which is used to compute the correction for propagation time. Fig. 6.8b shows the resulting timing resolutions and biases of the flash start time as a function of the mean drift distance after applying the correction, based on simulation. The timing resolution stays relatively constant at $\mathcal{O}(2)$ ns across the entire drift distance, demonstrating the excellent capability of the PDS reconstruction at SBND [73].

6.3.2 Cosmic Ray Tagger Reconstruction

The CRT reconstruction is the simplest of the three detection subsystems. Outputs of the CRT readout electronics are in a group of 32 ADC values, for a single ADC per SiPM (See Section 4.2.4). The reconstruction begins with a hit finding algorithm to identify which pair of SiPMs in the group goes above a threshold. The SiPM pair determines the

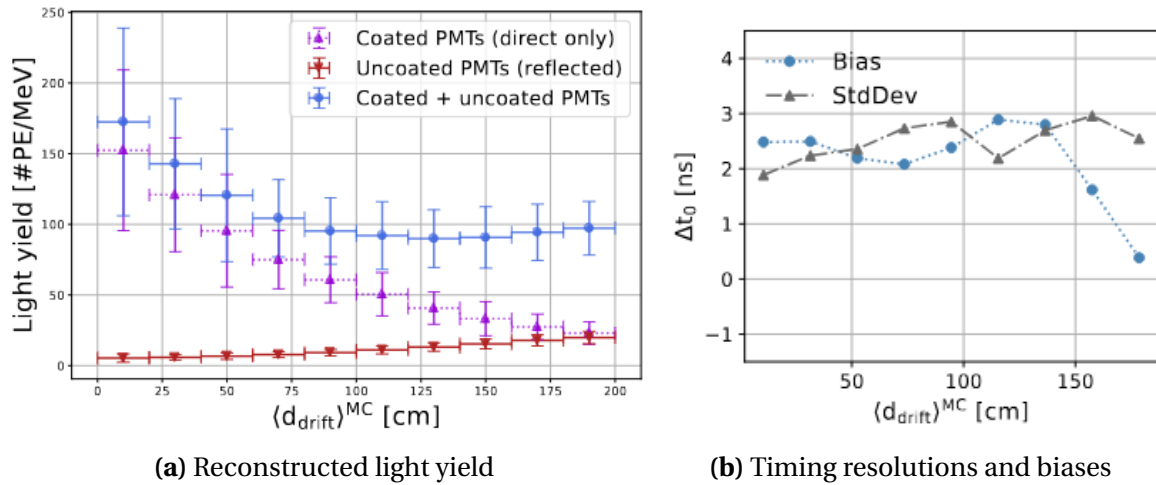


Fig. 6.8 (a) Reconstructed light yield and (b) timing biases and resolutions of reconstructed t_0 after propagation correction as a function of the mean drift distance based on simulation [73].

lateral position of a cosmic muon hit within a CRT strip. A clustering algorithm groups hits from orthogonal CRT strips of the same wall within a 50 ns window to yield 3D space points. For each CRT space point, the timing and calorimetry information is calculated and corrected for the propagation effect from the hit position to the SiPM. CRT space points from multiple CRT walls are matched together to form a CRT track based on the timing agreement and prioritising three-point tracks over two-point tracks. The outputs are both CRT space points and tracks.

6.4 High Level Analysis Tools

Reconstructed variables from each detection subsystem: slices from the TPC, flashes from the PDS, space points and tracks from the CRTs, are used collectively by downstream algorithms to compute useful characteristics regarding the interaction. This section covers the main high level analysis tools used in the selection of HNLs, to be detailed in Chapter 9. Section 6.4.1 provides a description of how variables from different detection subsystems can be matched to the same interaction. Presented in Section 6.4.2 is the cosmic rejection tool. Particle identification tool is given Section 6.4.3 .

6.4.1 Subsystem Matching

Reconstructed tracks from the TPC reconstruction can be matched to a CRT space point or tracks to provide additional information for cosmic rejection. An example is that a through-going cosmic muon produces a long track in the TPC as well as deposits energy in the nearest CRT walls where the track starts and ends. Two types of TPC-CRT matching are performed: (1) matching a TPC track to CRT space points and (2) matching a TPC track to CRT tracks. The former method extrapolates the TPC track and matches with the nearest CRT space points by computing a Distance of Closest Approach (DCA), confining the matching to a single CRT wall. The latter method uses a compound score from the DCA of a TPC track to many CRT tracks and the angle between them, enabling matching a TPC track to many CRT walls. Both methods use the CRT timing information for further constraints and no matching duplications are allowed.

An interaction reconstructed using the TPC, a slice, can be matched to an interaction reconstructed using PMTs, an optical flash, referred to as *slice-to-flash* matching. The flash time matched to a slice represents the start time of the interaction reconstructed in that slice. It is the key variable to compute the arrival time of a particle, enabling the reconstruction of the bucket structure of the Booster Neutrino Beam.

The slice-to-flash matching is based on the prediction of number of PEs estimated from the measured charge in a slice, and whether it is in good agreement with the number of PEs measured by PMTs [124]. The measured charge of a slice is first converted to deposited energy, which is then used to compute the total light produced from an interaction. The semi-analytical light library is re-run to estimate the number of PEs that would be measured by PMTs. This results in the number of PEs predicted from the measured charge, referred to as L_Q . The prediction is compared to the number of PEs measured by PMTs L of any given flash by a χ^2 computation. The flash best matched to a slice has the lowest χ^2 . Only one-to-one match is allowed so that only a single flash is matched to a slice.

A useful fraction variable is computed from L_Q and L as follows:

$$\frac{L_Q - L}{L}. \quad (6.4)$$

This fraction indicates the level of agreement between L_Q and L , and thus, the level of agreement of the energy deposition reconstructed from the measured charge and the measured light. If the fraction is positive, the predicted light from the measured charge is overestimated compared to the measured light, otherwise, it is underestimated. This

variable is particularly useful in the selection of HNL signals as it enables the identification of boosted topologies.

6.4.2 Cosmic Rejection

Cosmic Rejection Using a Multi-system Boosted decision tree Score (CRUMBS) is a binary classification BDT that outputs a score whether a reconstructed slice is cosmic-like or neutrino-like [125]. Reconstruction variables from all three detection subsystems that are complementary to each other are input into CRUMBS, thereby reducing inefficiencies compared to using a single subsystem. The TPC information includes variables describing a particle as both neutrino-like and cosmic-like, accounting for its charge distribution, location within the TPC and deposited energy. The PDS information is from the flash best matched to the slice of interest, particularly the number of PEs in the flash and the χ^2 from the slice-to-flash matching. The CRT information consists of both TPC-CRT matching algorithms, including the timing information of the CRT space points/tracks and the matching score. The score distribution of CRUMBS shows a significant separation between neutrino-like signals and cosmic-like backgrounds, enabling an effective cosmic rejection (See Fig. 9.5a, Section 9.2.3).

6.4.3 Particle Identification

The main particle identification tool at SBND is called Razzled [126], which is a multi-classification BDT designed to identify five particle types: e , γ , μ , π and p . The reconstruction variables input into Razzled are only TPC reconstruction variables from the Pandora package. There are three categories of variables for training Razzled: (1) generic reconstruction variables, (2) track-like variables and (3) shower-like variables. The generic variables describe the particle multiplicity, topology, directionality and charge distribution. Track variables include track lengths, energy deposition, kinematics in the stopping region to identify Bragg peak, and multiple Coulomb scattering for μ - π separation. Shower variables include shower conversion gaps, opening angles and energy deposition aiming towards γ - e separation. This collection of variables allows Razzled to exploit the correlation between variables, thereby significantly improving the identification performance over traditional hand cuts. A full description of the input variables and its performance can be found in Ref. [122]. For each reconstructed particle, Razzled outputs a score for each particle type and assigns the highest particle type score to that particle.

6.5 Concluding Remarks

The reconstruction workflow of SBND is described, outlining the reconstruction process for each detection subsystem: the TPC, PDS and CRTs. The three subsystems provide complementary information regarding the underlying reconstructed interaction and are used collectively by different analysis tools for various purposes. Focusing on the selection of HNLs, the background rejection and signal selection employ the tools described here to achieve a high signal-to-background ratio as discussed later in Chapter 9.

Particularly, the most important variable is the reconstructed interaction time, t_0 , which is used to compute the arrival time at the front face of SBND. The timing reconstruction having a resolution $\mathcal{O}(2 \text{ ns})$ is able to resolve the Gaussian-shaped bucket of SM neutrinos. To achieve such high timing resolution at the high level reconstruction, the low level readout electronics must have sufficient timing resolution to maintain a high quality data stream at a high sampling rate. The timing performance of the readout electronics is discussed in Chapter 7 next.

Chapter 7

Timing Performance of the Data Acquisition System

A pivotal goal for the Data Acquisition (DAQ) at the Short-Baseline Near Detector (SBND) is to achieve and maintain the electronics timing resolution $\mathcal{O}(1 \text{ ns})$ or less. Cosmic Ray Taggers (CRTs) and PhotoMultiplier Tubes (PMTs) are the two detection subsystems with sub-nanosecond electronics timing resolution that can resolve the nanosecond bucket structure of the Booster Neutrino Beam (BNB). More importantly, PMT signals are used to reconstruct the interaction start time with a reconstruction timing resolution $\mathcal{O}(2 \text{ ns})$ as demonstrated in Section 6.3.1, based on the simulation having an assumption that the PMT readout electronics have a resolution $\mathcal{O}(0.6 \text{ ns})$ at a sampling rate of 500 Hz. Therefore, it is crucial to validate and characterise the timing performance of the readout electronics so that areas for improvement can be identified in preparation for the nanosecond goal.

The work undertaken to assess the timing performance of the DAQ electronics is outlined in this chapter. An overview of the timing system at SBND is first given in Section 7.1. The timing characterisation of the CRT and PMT readout electronics are detailed in Section 7.2 and 7.3 respectively. Finally, Section 7.4 provides some concluding remarks.

7.1 Timing Reference System of the Data Acquisition

The event building process of the DAQ relies entirely on fragment timestamps to construct a physics event, as detailed in Section 4.2.7. The timestamp of each subsystem readout electronics must be generated with a high level of precision and synchronisation. At

SBND, the strategy is to utilise the White Rabbit (WR) timing system. It is a collaborative project developed at the European Organisation for Nuclear Research (CERN) and is now a widely-used synchronisation solution in the scientific community [127]. The WR has the capability to offer fully deterministic time transfer with sub-nanosecond accuracy over distances exceeding 80 km. The application of the WR timing system at SBND for time transferring and timestamping is detailed in Section 7.1.1 and Section 7.1.2 as follows.

7.1.1 Time and Frequency Transfer to Subsystems

Fig. 7.1 provides an overview of the WR timing system at SBND. Starting from the first column of the figure is the Grandmaster switch. It distributes time and frequency to all other slave WR switches within the WR network via optical links. The WR switch has dynamic calibration and thus, is a very reliable and robust delivery system. The system ensures that the Pulse Per Second (PPS), which is of 1 Hz, from all slave switches are aligned to the Grandmaster's PPS with sub-nanosecond accuracy. The Grandmaster switch is also connected to an atomic clock locked to a global navigation satellite system. As a result, the time and frequency distributed by the WR system are derived from the International Atomic Time (TAI) and the Coordinated Universal Time (UTC) format.

At SBND, there are two slave WR switches, as shown in the second column labelled *Servers Hosting Slave Switches*. Each slave switch server hosts a different module of Field programmable gate arrays Mezzanine Card (FMC). The first server contains two SVEC-FD modules, which are Fine Delay (FD) cards carried by Simple VME FMC Carrier (SVEC). The second server hosts a single SPEC-TDC module, a Time to Digital Converter (TDC) card carried by a Simple PCIe FMC Carrier (SPEC). The usage of SVEC-FD modules is discussed here, whilst the usage of the SPEC-TDC is discussed in Section 7.1.2 next.

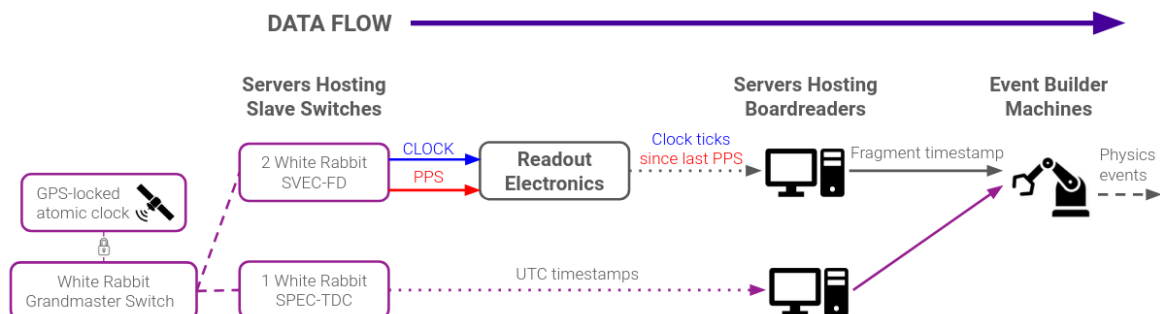


Fig. 7.1 Distribution of the White Rabbit timing system.

7.1 Timing Reference System of the Data Acquisition

SVEC-FD modules are high precision pulse generators, with 10 ps resolution when used within a WR network [127]. They are used to generate frequencies sent to readout electronics to ensure timing synchronisation across all subsystems of the DAQ. There are two types of frequencies: (1) clock as shown by the blue arrow and (2) PPS as shown by the red arrow in Fig. 7.1.

The clock signal provides a *metronome frequency* customised for each readout hardware's internal clocks. This signal behaves as the master clock that the internal clocks of readout electronics can latch onto, thereby maintaining their accuracy and stability over time. The PPS signal provides the *same reference frame* for all readout electronics in the DAQ. All internal clock counters of readout electronics reset upon the arrival of a PPS and thus share the same reference frame as the PPS. Details of the PPS and clock distribution are provided in Appendix C.

Raw data sent from the readout electronics to computer servers, as shown by the dotted grey arrow, contains timing information regarding the arrival time of the trigger at the readout. The timing information at this stage is only the number of clock ticks since last the PPS arrived, and therefore, does not contain sufficient information for event building across multiple subsystems.

To facilitate event building, raw data is packaged into *fragments*, previously detailed in Section 4.2.7. The fragment timestamp is in the UTC format, which is defined as the number of seconds since the Unix Epoch on the 1st of January 1970. This is the *universal* reference frame and allows for direct comparison of fragment timestamps from different subsystems required by event building. The number of seconds is generated by the computer servers under the network time protocol with a precision level $\mathcal{O}(100 \text{ ms})$.

The nanosecond-level of precision of fragment timestamps are derived from the number of clock ticks since the last PPS, generated by internal clocks of each readout electronics. They are converted to the number of nanoseconds since the last whole second using the tick-to-time conversion. This level of precision of fragment timestamp necessitates the event building process, as well as, is stored for downstream reconstruction and analysis.

7.1.2 Precise Timestamping

Also shown in Fig. 7.1, another component of the WR timing system is the SPEC-TDC module. This module timestamps signals in tick of 2 ps with a precision of 700 ps. The output timestamps are in the UTC format. The timestamps can be acquired by the DAQ and be built within a physics event, as shown by the dotted and solid purple arrows.

At SBND, SPEC-TDC is employed to timestamp the arrival time of important signals, recording additional timing information on top of the Time Projection Chamber (TPC), Photon Detection System (PDS) and Cosmic Ray Tagger (CRT) data. This timing information can be leveraged for different physics applications. For instance, it can be used to characterise the timing resolution of the readout electronics. The recorded timestamps can be also used to derive the correction for hardware synchronisation or enable an alternative method to reconstruct the timing of a physics event.

Fig. 7.2 shows the five signals input to the SPEC-TDC. Two beam signals, shown in blue, provide the status of the BNB. The first one is the Booster Extraction Signal (BES), which is an early warning indicating when protons are extracted in the Booster. The second one is the Resistor Wall Monitor (RWM), which measures the time and intensity of protons striking the target. The RWM signal arrives at the SBND detector building almost instantaneously with the beam itself due to the close proximity of SBND to the target. Additionally, two trigger signals, shown in green, are recorded to monitor the DAQ synchronisation with respect to the triggers. These include flash and event triggers (See Section 4.2.5). Finally, clock reset signals for the CRT readout electronics are recorded in the last channel as shown in pink.

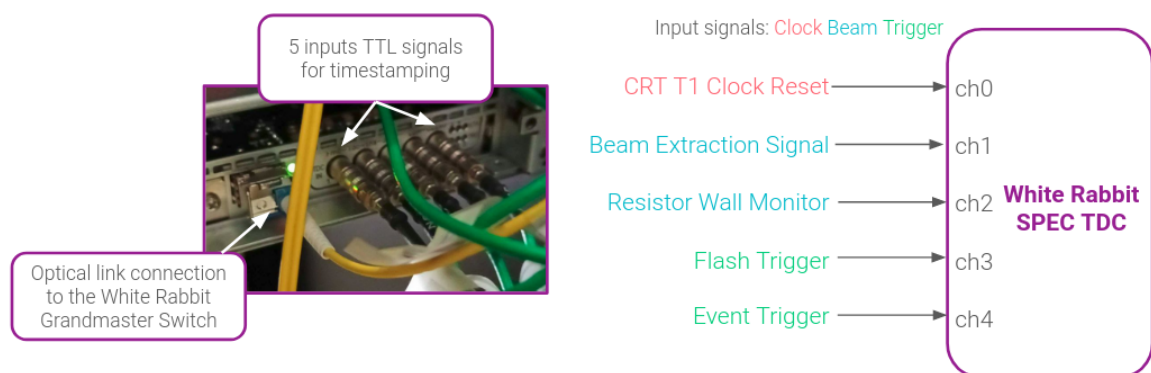


Fig. 7.2 The SPEC-TDC module installed at SBND (left) and signals input to the module for timestamping (right).

Two applications of the SPEC-TDC to characterise the timing precision of the readout electronics were explored for CRT and PMT readout electronics in Sections 7.2 and 7.3 respectively. For the CRT, an alternative timing reconstruction was also derived using the timing information recorded by the SPEC-TDC. For the PMT, SPEC-TDC timestamps helped validate the timing synchronisation across multiple digitisers.

7.2 Timing Performance of Front End Board Modules

This section provides a description of the characterisation of the timing performance of the CRT readout electronics, Front End Board (FEB) modules, in Section 7.2.1 and an alternative timing reconstruction in Section 7.2.2.

7.2.1 Evaluation of Internal Clock Resolution

The readout electronics of CRTs are FEB modules as detailed in Section 4.2.4. Here, the focus is on the precision of the internal clocks of FEB modules. Internal clocks of FEB modules are TDC units with a coarse counter of 4 ns per tick (250 MHz frequency) [99]. A high resolution time interpolation method is implemented within the TDC clock cycle to improve the counter to 1 ns per tick [128].

There are two internal clocks per FEB module. The first one is referred to as *T0 clock*, which is reset by the PPS signal, therefore its *T0 timestamps* share the same PPS reference frame as all other readout electronics. The second internal clock is referred to as *T1 clock*, which is reset by the BES signal of the frequency ~ 5 Hz. It produces *T1 timestamps*, referencing to the BES signal coincident with the beam arrival time. In addition, FEB modules timestamp the arrival time of reset signals, whether a PPS or a BES, and store the timestamps as *T0 or T1 clock reset events*. Reset events are timestamped by both the T0 and T1 clocks, and therefore have both T0 and T1 timestamps.

The work to characterise the internet clock was undertaken at Fermilab in 2022 during the commissioning of SBND. It was conducted using a temporary setup called *CRT Sharps*. The setup was made up of two sets of CRT panels, where each set was placed upstream and downstream of the cryostat centred on the BNB. The downstream setup is photographed in Fig. 7.3, showing 4 CRT panels arranged perpendicular to each other. Each panel was read out by a FEB module, totalling 8 FEB modules with 4 upstream and 4 downstream. The CRT Sharps was commissioned during the period at which the BNB beam was on so that it functioned as a beam telescope. The triggering condition was to have signal coincidences between the upstream and downstream panels during the beam spill to record events produced by muons from neutrino interactions.

The T0 clock is characterised using T0 timestamps of T0 clock reset events. To measure the clock variation, one can simply compare these timestamps with respect to a whole second. An example is shown in Fig. 7.4 for a single FEB module numbered 79. The left plot shows the timestamp variation with respect to the event number to check for clock



Fig. 7.3 Downstream panels of the CRT Sharps installed on the downstream wall of the SBND cryostat.

stability over a period of time. The right plot is a 1D histogram to check for the spread of the distribution. The standard deviation of this distribution is a direct measurement of the T0 clock variation. It is 2.37 ns with a mean of -1.89 ns, indicating that the FEB module 79 consistently received the PPS signal every second to reset its T0 clock. This measurement was repeated for all 8 FEB modules of the CRT Sharps. The T0 clock resolution was found to be $\mathcal{O}(2 \text{ ns})$, consistent across all FEB modules.

The characterisation of the T1 clock is less trivial since its T1 timestamps do not share the same reference frame with any other readout electronics. The only direct comparison is via T0 timestamps, which contain the T0 clock resolution. T0 timestamps of T1 clock reset events were compared against the SPEC-TDC timestamps of the BES signal since they both measured the same signal and reference to the PPS. The comparison was motivated since the SPEC-TDC has a higher precision than FEB clocks.

The left plot of Fig. 7.5 shows the variation of T1 clock with respect to the event number, indicating that the FEB module 79 regularly received BES signals to reset its T1 clock. The right plot shows the 1D histogram of the variation. The standard deviation here is not a direct measurement of the T1 clock resolution. It is expected to be lower than the T0 clock resolution since the T1 clock is reset more frequently at $\sim 5 \text{ Hz}$. The standard deviation is smaller at 1.95 ns and the mean is closer to 0 at -0.443 ns. This measurement was carried out for all FEB modules and the same results were observed.

7.2 Timing Performance of Front End Board Modules

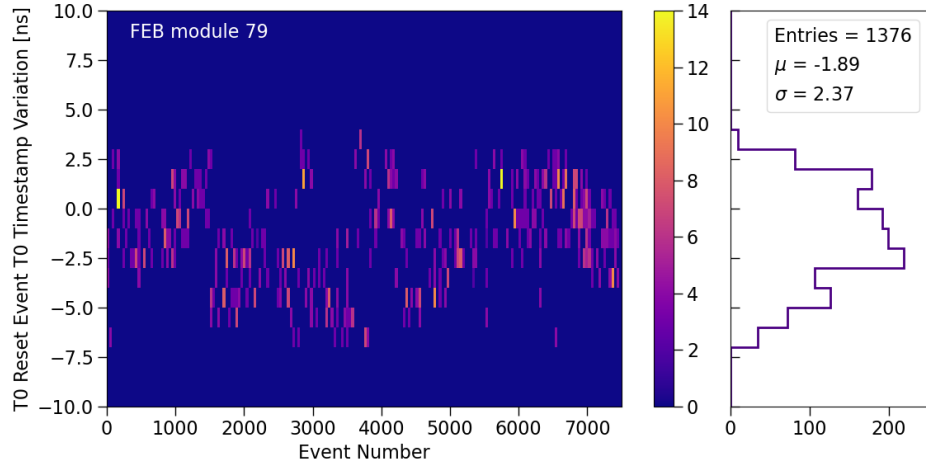


Fig. 7.4 Variation of T0 timestamps of T0 clock reset events with respect to a whole second as a function of event numbers.

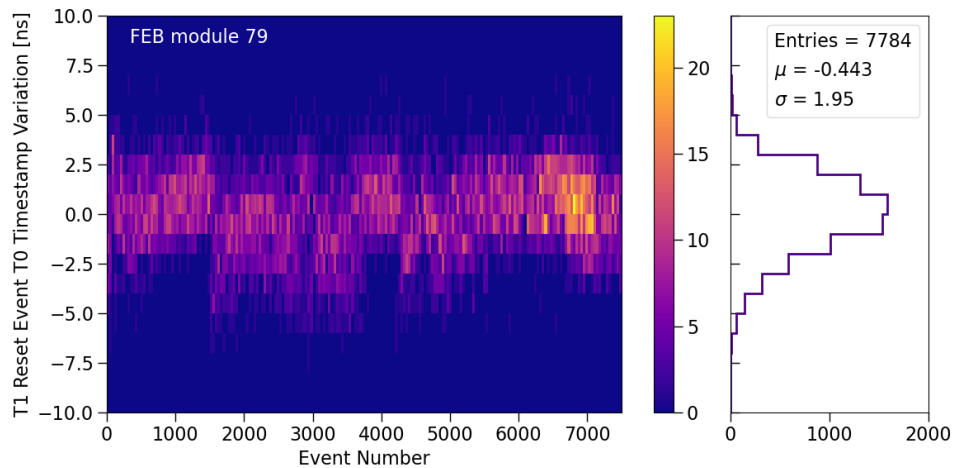


Fig. 7.5 Variation of T0 timestamps of T1 clock reset events with respect to the SPEC-TDC's recorded timestamp of the BES signal as a function of event numbers.

T1 clock reset events also provide a method to monitor the drift of the T0 clock. By plotting the variation of T0 timestamps of T1 clock reset events as a function of the T0 timestamps, it enables the monitoring of the T0 timestamp precision with respect to when it is generated in the clock cycle. An example is shown in Fig. 7.6 for the FEB module 79. Early in the clock cycle, when T0 timestamps are close to 0 ns, small variations within 2 ns can be seen. However, later in the clock cycle, when T0 timestamps are close to a whole second, larger variations up to 7 ns occur. This demonstrates that the precision of T0 timestamps depends on at which point in the clock cycle they are generated. It is also

possible that the T0 clock counter can overflow, resulting in meaningless T0 timestamps. This clock drift behaviour is expected to be more prevalent with the T0 clocks than the T1 clocks due to the lower reset frequency.

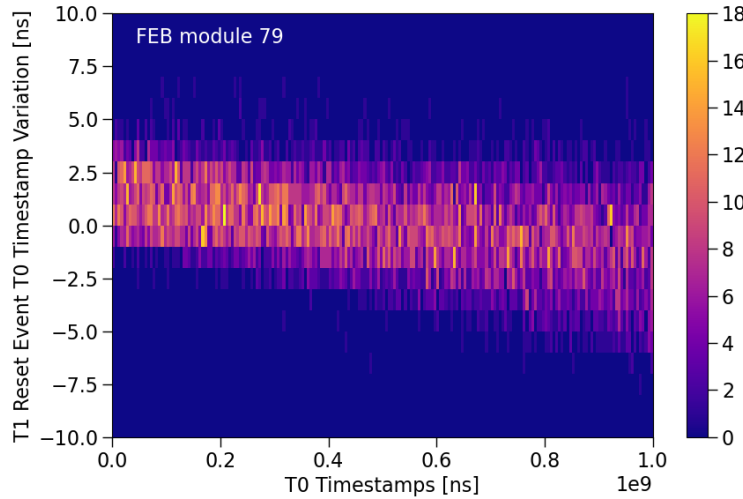


Fig. 7.6 Variation of T0 timestamps of T1 clock reset events as a function of T0 timestamps.

These plots are useful diagnostic tools to characterise the timing of the FEB modules, including monitoring the magnitude and stability of the T0 and T1 clocks as well as the drift of the T0 clock. It is important to note that the T0 and T1 clocks of the FEB can potentially vary with time, and they are very sensitive to external noises. The plots were reproduced during the CRT installation as apart of the quality control procedure to track the clock stability and resolution of the FEB modules.

7.2.2 Alternative Timing Reconstruction

The SPEC-TDC can also provides an alternative timing reconstruction method for events recorded by CRTs. The study here was performed using a data set recorded by the CRT Sharps consisting of ~ 9000 beam events. CRT 2D hit time was reconstructed from coincidental hits of 2 cross scintillator strips, and corrected for cable and propagation delay. CRT hit time T0 was reconstructed using the T0 timestamp whilst the CRT hit time T1 was reconstructed using the T1 timestamp. Commonly, the timing reconstruction of CRT data only uses the CRT hit time T1 in reference to the beam, as previously shown in Fig. 4.9, Section 4.3. Here, the timing reconstruction using CRT hit time T0 instead is presented.

7.2 Timing Performance of Front End Board Modules

Firstly, the beam spill was reconstructed as shown in Fig. 7.7a and 7.7b using CRT hit time T1 and T0 respectively. The beam spill in Fig. 7.7a was plotted directly using CRT hit time T1 since it is a reference to the BES signal. The plot shows a beam excess to the cosmic background, corresponding to the BNB beam arriving $333 \mu\text{s}$ after the BES signal and lasting for $1.6 \mu\text{s}$. On the other hand, CRT hit time T0 is in the reference frame of the PPS and needs to be corrected to the beam arrival time to reconstruct the beam spill. The correction was done using BES signals recorded by the SPEC-TDC, of which the timestamps are also with respect to the PPS. The beam spill structure acquired from this method shows a good agreement as shown in Fig. 7.7b, where the same beam excess can be seen. It is important to note that the reconstruction of the beam spill only requires a resolution $\mathcal{O}(1 \mu\text{s})$, which is satisfied by both the T0 and T1 clock resolution $\mathcal{O}(2 \text{ ns})$.

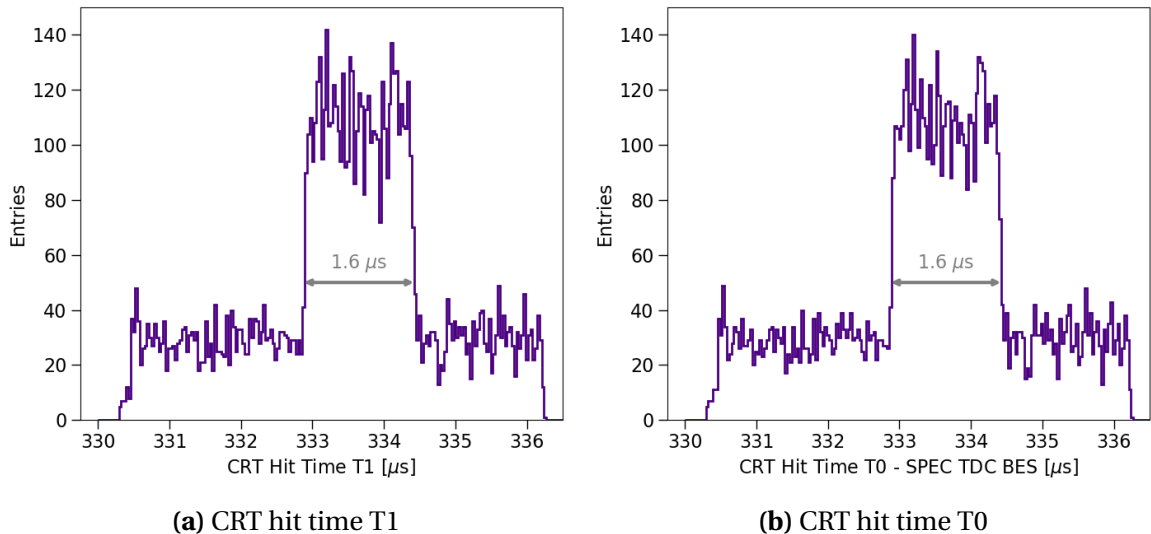


Fig. 7.7 Beam spill reconstructed using (a) CRT hit time T1 and (b) CRT hit time T0 combined with the SPEC-TDC timing information.

The next step was to reconstruct the bucket structure of the BNB, made up of 81 buckets of Gaussian width 1.308 ns and separated by 19 ns . Given the limited statistics of the sample to fully plot 81 buckets of a whole beam spill, the buckets were overlaid on top of each other by applying a modulus of 19 ns . The resulting beam buckets using CRT hit time T1 and CRT hit time T0 combined with the SPEC-TDC timestamps are shown in Fig. 7.8a and 7.8b respectively. Using the CRT hit time T1, the beam bucket was resolved even with the limited statistics, recovering a Gaussian width of 3.2 ns . However, from the CRT hit time T0 distribution, the Gaussian bucket is more smeared out with a larger width of 3.5 ns . This is due to the resolution of the T0 clock being shown to be $\mathcal{O}(2 \text{ ns})$, which is larger than the width of the beam bucket.

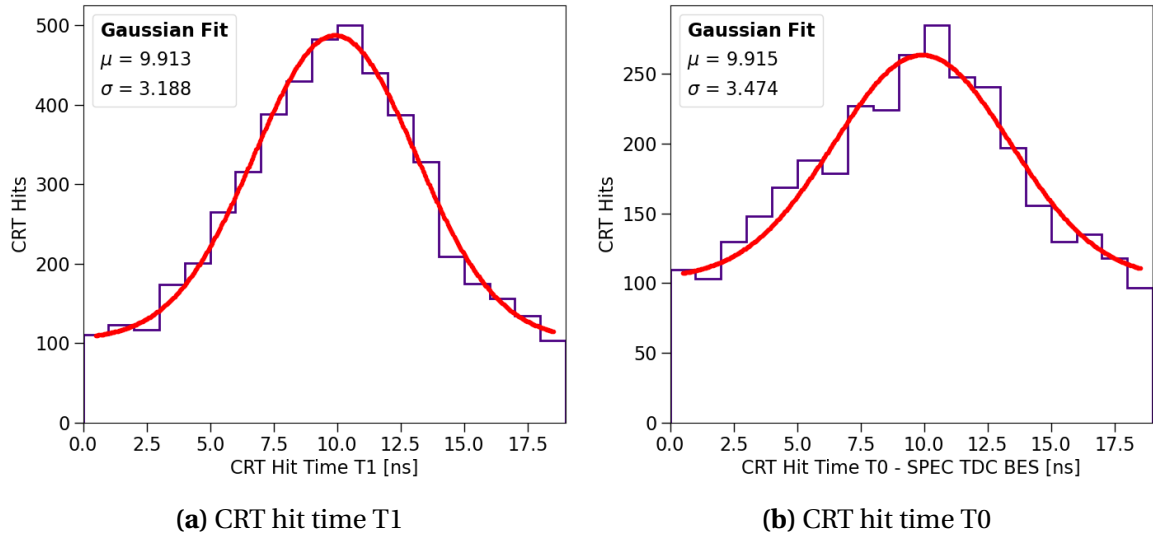


Fig. 7.8 Beam bucket reconstructed using (a) CRT hit time T1 and (b) CRT hit time T0 combined with the SPEC-TDC timing information.

Both the reconstruction of the beam spill and beam bucket demonstrate that the CRT hit time T0 can be utilised together with the timing information recorded by the SPEC-TDC. This alternative timing reconstruction shows promising early results and certainly has the potential for more improvements. Additionally, this showcases the versatile usages of the SPEC-TDC, where its recorded timestamps can be used in conjunction with other detection subsystems.

7.3 Timing Performance of CAENV1730 Digitisers

The next focus is on the timing characterisation of PMT readout electronics, CAENV1730SB digitisers. Section 7.3.1 provides a description of the CAENV1730's internal clocks. An evaluation of the timing synchronisation across multiple digitisers is presented in Section 7.3.2 and a clock jittering correction method is given in Section 7.3.3.

7.3.1 Internal Clock and Timestamp Structure

A description of the PMT readout electronics, CAENV1730SB digitisers, is summarised in Section 4.2.4. The internal clock of interest is called REF-CLOCK in the clock domains of a CAEN digitiser [97]. The REF-CLK is a clock chain responsible for a synchronous sampling and triggering rate, and thus, the timing precision of the CAEN digitiser. Its frequency

7.3 Timing Performance of CAENV1730 Digitisers

serves as an input to a clock distribution device AD9510, generating three clock types: (1) an ADC sampling clock, (2) a trigger clock and (3) an output clock for external use. The AD9510 device must be programmed for the input REF-CLK frequency so that all three clocks are in phase with the input and with each other.

The ADC sampling clock has a frequency of 500 MHz to enable waveform sampling with the tick value of 2 ns/tick. The trigger clock operates at 125 MHz with a tick value of 8 ns/tick, and is responsible for handling the triggering and synchronisation logic. However, since it is read every two clock cycles, it potentially has a fluctuation of up to 16 ns/tick. The last clock is a programmable frequency output via the CLK-OUT connector and can be propagated to another CAEN digitiser for synchronisation purposes.

At SBND, CAEN digitisers are configured to use an external clock input to the REF-CLK with signals from the WR timing system described in Section 7.1.1. The external clock is input via the CLK-IN connector of the digitiser, with frequency depending on the clock synchronisation scheme. This signal behaves as a *metronome frequency* for all three clocks described above. Additionally, the PPS signal is input to the S-IN connector of the digitiser and is used by the trigger clock. It resets the counter of the trigger clock every second so that the timestamps output by CAEN digitisers share the *same reference frame* with respect to the whole second as other readout electronics.

Unlike the timestamp generated by FEB modules or the SPEC-TDC, where it is the number of clock ticks upon receiving a signal, the timestamp produced by CAEN digitisers is structured differently. Fig. 7.9 illustrates the time structure of a waveform recorded by CAEN digitisers. Upon receiving a trigger at the TRG-IN connector, as shown in grey, there is a latency before the digitiser acting on the trigger, as shown in red. The waveform length can be any portion pre- or post-trigger as shown by the red and blue boxes. For



Fig. 7.9 Timing structure of a waveform digitised by CAEN digitisers.

every trigger, the CAEN trigger clock produces a timing object called a trigger time tag. However, the trigger time tag is not instantaneous upon the trigger arrival, it is instead the timestamp value of the last tick on the waveform, as shown in green. Therefore, a careful timing reconstruction is needed when decoding the waveforms.

7.3.2 Evaluation of Clock Synchronisation

Multiple CAEN digitisers can be synchronised to behave as if a single digitiser. It is crucially important to record PMT waveforms in synchronisation since they are the key ingredients for timing reconstruction with a resolution $\mathcal{O}(2 \text{ ns})$ as previously detailed in Sec 6.3.1. The synchronisation can be achieved through two different clock synchronisation schemes: (1) fan out and (b) daisy chain, as shown in Fig. 7.10a and 7.10b respectively.

In fan out mode, each digitiser is input with the clock signal set at 10 MHz clock. The 10 MHz was chosen at the time since it is the highest frequency produced by the SVEC-FD module. The clock signal is distributed to a fan out module, and then into the CLK-IN connector of each digitiser. The cable length of each clock signal is identical so that all clock signals arrive at CAEN digitisers at the same time.

In daisy chain mode, the first CAEN digitiser in the daisy chain receives the 10 MHz clock, referred to as the master clock. Its clock is then propagated to the next digitiser in the chain, referred to as the slave clock. The master clock can be precisely programmed with a delay in step of 300 ps to account for cable lengths, ensuring that the master and slave clocks are in phase with each other. The clock propagation continues from one digitiser to the next digitiser in the chain, until the last digitiser in the chain is in the same clock phase as the first one.



Fig. 7.10 Diagram illustrating two clock synchronisation schemes for CAENV1730SB digitisers, (a) fan out and (b) daisy chain.

7.3 Timing Performance of CAENV1730 Digitisers

The timing characterisation study was carried out to determine which clock synchronisation scheme provides the best precision and stability. The setup consisted of 8 CAEN digitisers located in the same crate. Each digitiser received an identical trigger with the same cable length so every digitiser was triggered simultaneously. The trigger rate was set as 1 Hz for simplicity.

To evaluate the synchronisation of CAEN digitisers, their timestamps of triggered events were directly compared against the same timestamps recorded by the SPEC-TDC since both are referenced to the PPS signal. Similar to the approach with the CRT readout electronics, the SPEC-TDC offers a higher level of precision compared to the CAEN digitiser. For an ideal synchronisation, the timestamps of every triggered event from every digitiser should be identical with respect to each other, and also with respect to the SPEC-TDC after cable correction.

Some results of synchronisation using the daisy chain are shown in Fig. 7.11, depicting the differences of timestamps CAEN digitisers from the SPEC-TDC as a function of the event number. Only 4 out of 8 CAEN digitisers are shown for run 7980 and run 8060, however, similar results were observed for the rest of the digitisers. Run 7980 in Fig. 7.11a demonstrates a perfect synchronisation across all 8 CAEN digitisers. Their differences with respect to the SPEC-TDC are constant at 0 across all the events and all the digitisers. This shows a very good and stable synchronisation.

In contrast, run 8060 exhibited some interesting effects as shown in Fig. 7.11b. Firstly, board 5 shows a straddling effect, where the observed differences jitters between 0 and 8 ns. This behaviour could be due to the CAEN trigger clock of the CAEN digitiser being read out every 2 clock cycles, introducing some fluctuations. Moreover, board 7, which received a clock signal from board 5 in the daisy chain, drifted by 8 ns. Following that, board 9, receiving clock from board 7, also drifted by 8 ns. This demonstrates that if one clock in the daisy chain drifts, subsequently clocks in the chain also drift.

The same test was repeated for the fan out scheme. Some example results are shown in Fig. 7.12 for run 8178 and run 8196. Firstly, in both of these runs, board 5 shows the same straddling effect, causing its timestamps to jitter by 8 ns. The second observation is that the timestamp differences vary randomly between digitisers and across different runs. For instance, the timestamp difference of board 9 is stable at -8 ns in run 8178 but stays at +8 ns in run 8196.

This behaviour is due to the input frequency to the CLK-IN connector set at 10 MHz. As previously explained, the trigger clock is generated by the AD9510 device, which must be in phase with the input frequency. However, the trigger clock operates at a frequency

Timing Performance of the Data Acquisition System

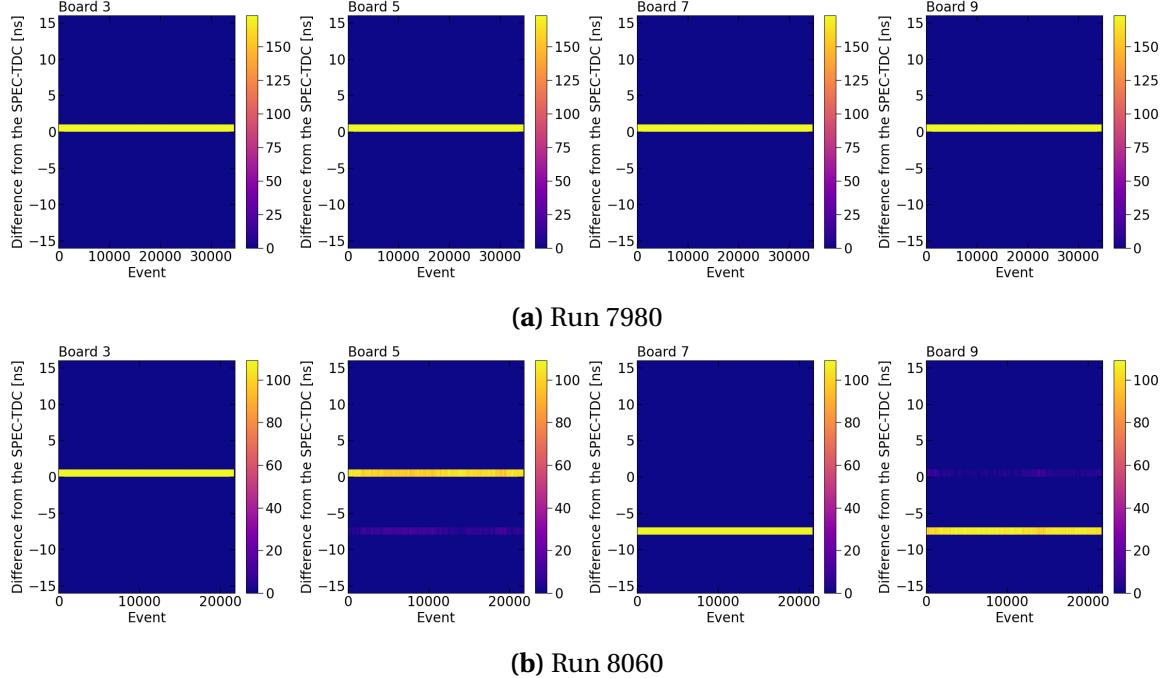


Fig. 7.11 Differences in trigger timestamps between CAEN digitisers and the SPEC-TDC with the CAEN digitisers using the daisy chain clock scheme.

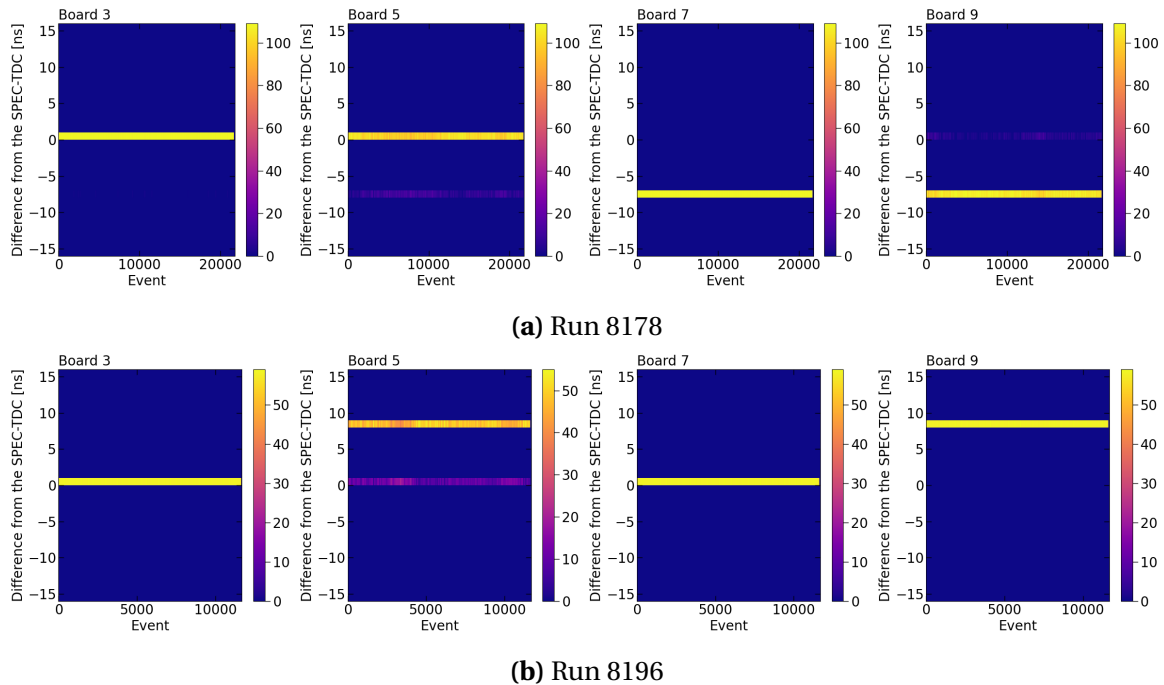


Fig. 7.12 Differences in trigger timestamps between CAEN digitisers and the SPEC-TDC with the CAEN digitisers using the fan out clock scheme.

7.3 Timing Performance of CAENV1730 Digitisers

of 125 MHz, while the input frequency is at 10 MHz. Since these frequencies are not multiples of each other, they cannot be in phase. To generate an out-of-phase frequency, the AD9510 device latches onto the first rising edge of the input frequency upon the digitiser initialisation. This results in a random phase offset at the beginning of every run, causing the timestamps to vary from run to run and from board to board.

Comparing the two clock schemes, the daisy chain mode offers a better synchronisation across the 8 CAEN digitisers compared to the fan out mode. In the daisy chain scheme, only the first digitiser in the daisy chain receives the external 10 MHz clock. The master clock will have a random phase offset that is propagated down the daisy chain, resulting in synchronisation across all digitisers. However, the clock drift effect was observed during the testing of the daisy chain scheme and therefore, a correction is necessary.

7.3.3 Clock Jittering Correction

To further characterise the timing of the CAEN digitiser, another study was carried out to verify if all 8 CAEN digitisers can digitise waveform in synchronisation with each other within 1 ns. The same setup was used as described in the previous section, with a new addition of digitising the waveform of the trigger signal in channel 15 of every digitiser. All cable lengths were identical so that all trigger signals took the same amount to propagate to the digitisers. The daisy chain clock scheme was also calibrated so that the clock propagation from the master clock to the slave clock was delayed by a precise amount so that their clocks were exactly in phase. This was to ensure that trigger signals were simultaneously timestamped and digitised.

Examples of digitised waveforms of trigger signals are plotted in Fig. 7.13a for four digitisers, where trigger signals can be seen as a single square wave per digitiser. To examine if trigger signals were digitised simultaneously, zooming into the rising edges of trigger signals is plotted in Fig. 7.13b. Board 3, 5 and 9 are in synchronisation except for board 7. The rising edge of board 7 is at a different location compared to other boards, showing that its clock jittered. This behaviour although did not occur frequently, it was unpredictable and could appear across different events, different runs and different boards. Therefore, a jittering correction was derived to account for clock jittering scenarios.

The timestamp of the rising edge of trigger signals digitised by CAEN digitisers was compared against the timestamp recorded by the SPEC-TDC of the same trigger signal. This comparison helps the understanding of the clock jittering behaviour of the CAEN digitiser. Three identified cases of jittering are illustrated in Fig. 7.14a. The trigger

Timing Performance of the Data Acquisition System

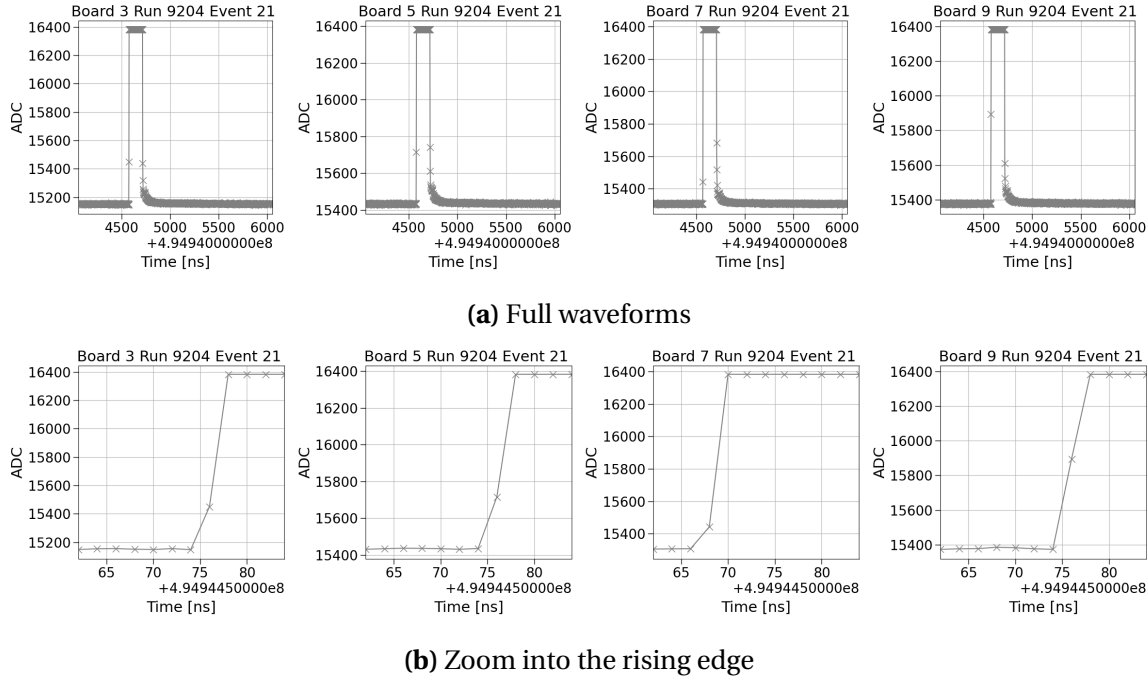


Fig. 7.13 Digitised waveforms trigger signals, including (a) full waveforms and (b) zoom into the rising edge.

waveform is plotted in grey, the rising edge is marked with a red cross and the timestamp of the trigger signal recorded by the SPEC-TDC is plotted as the vertical green line.

In the far left plot, the timestamp of the rising edge and the SPEC-TDC agree with each other and hence, the red cross and the green line align. The middle left plot shows the first case of clock jittering of one whole sampling tick, equivalent to 2 ns. This is due to the ADC sampling clock jitters while the triggering clock remains stable, resulting in a different tick value of the rising edge. In the second case, the opposite situation arises such that the tick value of the rising edge timestamp is stable however the trigger clock jitters in the step of 8 ns. This is illustrated in the middle right plot, where the rising edge and the SPEC-TDC differ by exactly 8 ns. The last case is the combination of jittering from both sampling and trigger clocks. This is shown in the far right plot, where the difference between the rising edge and the SPEC-TDC is equal to the sum of the trigger and ADC sampling clock tick, totalling at 10 ns.

This comparison exercise also demonstrated a possible clock jittering correction. By digitising the trigger signal simultaneously on every digitiser, the recorded waveform of the trigger in combination with the SPEC-TDC provide all the necessary information to apply a correction. One can simply derive the correction amount by performing the comparison

7.3 Timing Performance of CAENV1730 Digitisers

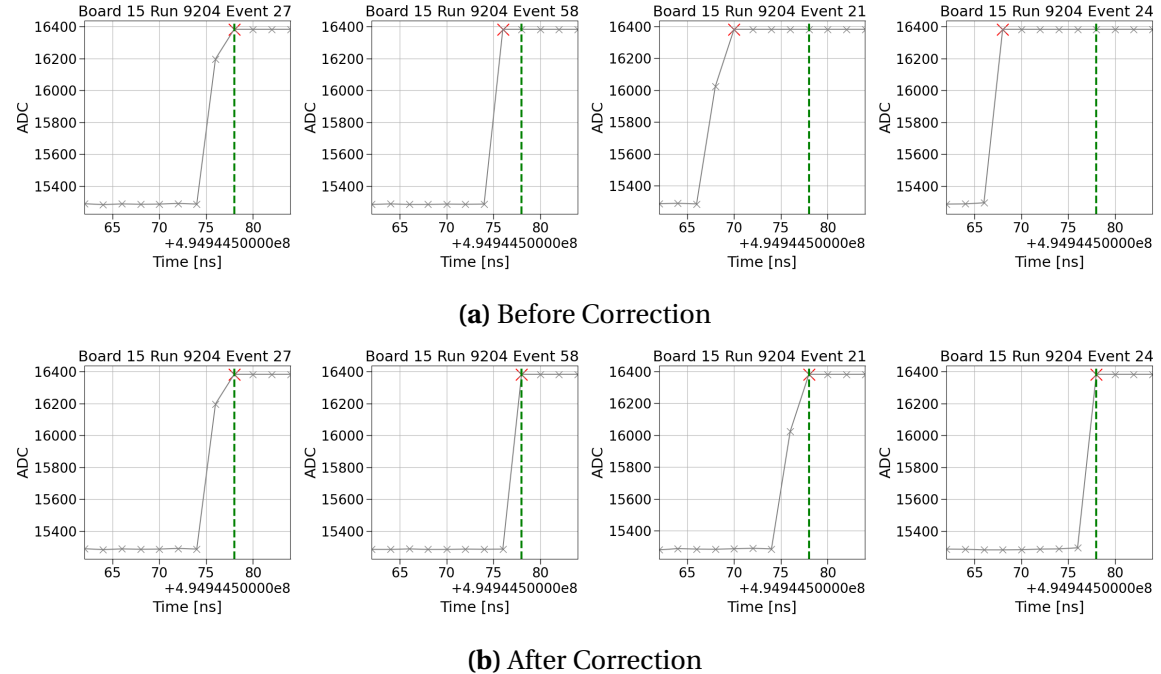


Fig. 7.14 Digitised waveforms of trigger signals zoom into the rising edge (a) before correction and (b) after correction.

as above. The digitised trigger waveforms after applying correction are illustrated in Fig. 7.14b, showing all the waveforms perfectly aligned to each other.

This correction method was validated using multiple runs over one month. Each run duration varied from less than 1 hour up to more than 10 hours. Fig. 7.15a demonstrated the results conducted on a dataset of 30 runs, showing the 1D histogram of the difference between the timestamp of the rising edge as compared to the SPEC-TDC. The plots are area normalised to directly compare across different run durations. Before correction, some amount of jittering can be seen across different digitisers, events and runs, with peaks at 4 and 8 ns. The correction was first applied event by event, as shown in Fig. 7.15b. Then, the correction was applied run by run, as shown in Fig. 7.15c. The result is a perfect alignment between the CAEN digitisers and the SPEC-TDC, with their differences forming a single peak at 0 ns.

This clock jittering study presented here resulted in a new hardware implementation at SBND. This includes to digitise the trigger signal in channel 15 of every CAEN digitiser as this will provide the necessary timing information for downstream jittering correction. An additional CAEN digitiser was also installed specifically for digitising beam signals. It

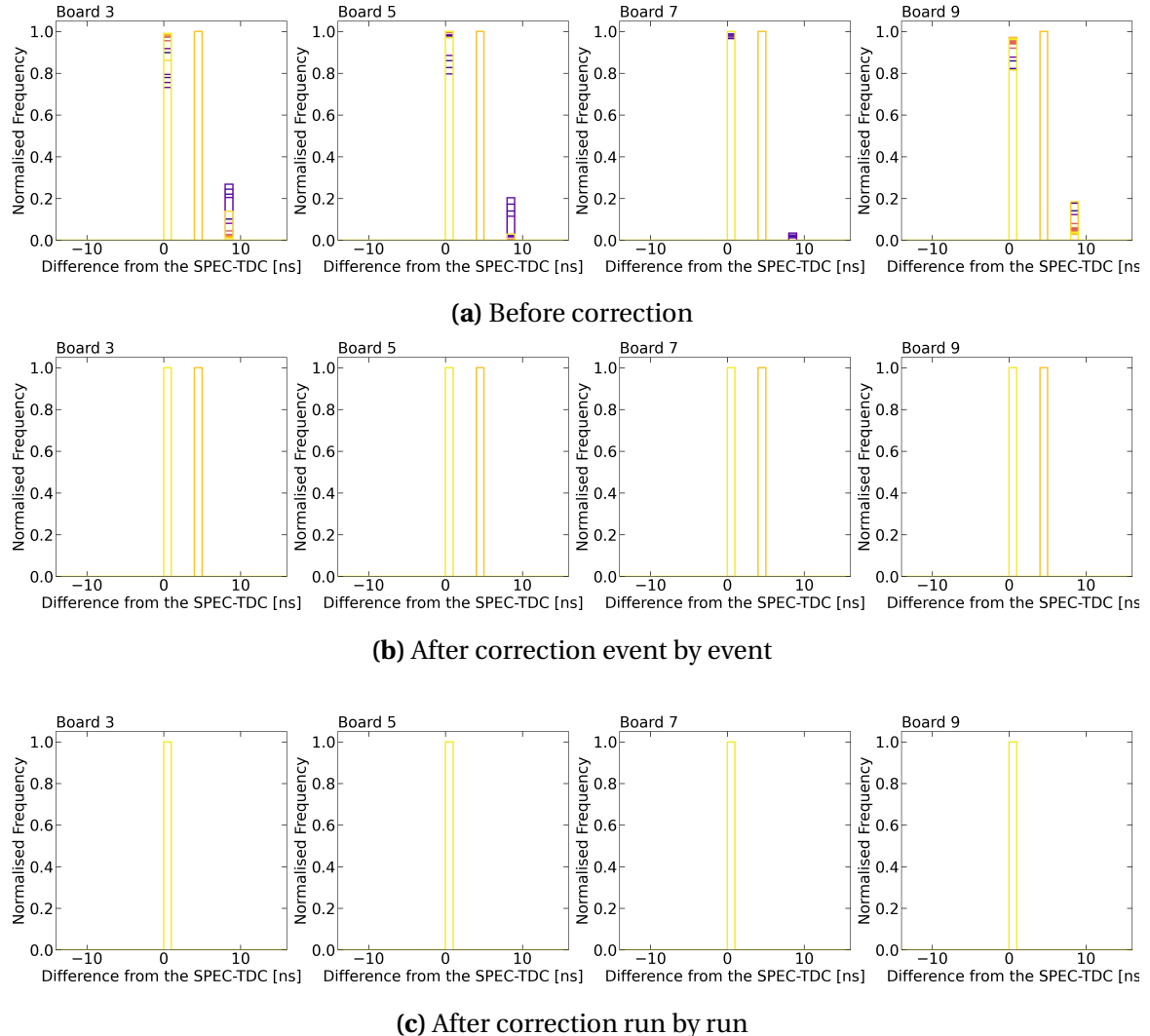


Fig. 7.15 Differences in trigger timestamps between CAEN digitisers and the SPEC-TDC at each correction step.

will digitise waveforms of important timing signals needed by downstream analysis to reconstruct the BNB as demonstrated by the MicroBooNE collaboration [129].

At the time of writing, the clock setup of CAEN digitisers have changed. Further consultation with the CAEN manufacturer led to a new clock synchronisation scheme. A 6.25 MHz clock is now distributed in a fan out mode to every digitiser. Even though it is a lower frequency than 10 MHz, it is a multiple of both the trigger clock (125 MHz) and the sampling clock (500 MHz) so that they can be in phase with each other. The same clock synchronisation study was performed and the digitised trigger waveforms showed a good agreement to the SPEC-TDC within 1 ns. This configuration shows an improvement

7.4 Concluding Remarks

in clock synchronisation and stability than the two methods explored in Section 7.3.2. Additionally, digitised waveforms trigger signals, as shown in Fig. 7.13 and 7.14, were found to be saturated. Hardware attenuators were installed, followed by an adjustment of the waveform baseline. This ensures to capture of the full shape of the trigger waveforms without damaging the digitisers.

7.4 Concluding Remarks

The timing system at SBND is outlined, detailing the timing signal distribution to ensure synchronisation across different DAQ subsystems. As part of the timing system, the SPEC-TDC module records extra timing information applicable for versatile usages with a high timing precision of 700 ps. The module was used to characterise the timing performance of the CRT and PMT readout electronics.

FEB modules, readout electronics of CRTs, contain two internal clocks T0 and T1, where the T0 (T1) clock is reset with a PPS (BES) signal of the frequency 1 Hz (~ 5 Hz). The resolution of T0 clocks was directly measured to be $\mathcal{O}(2)$ ns. The clock drift effect was also observed with the T0 clock, such that the precision of T0 timestamps decreased since the last clock reset. On the other hand, the resolution of T1 clocks could not be directly measured and was determined via T0 timestamps. The determined T1 resolution containing some smearing from the T0 clock was found to be slightly less than $\mathcal{O}(2)$ ns due to a higher reset frequency. Both T0 and T1 clock resolutions enable the reconstruction of the beam bucket structure, of which an alternative reconstruction using the T0 timestamps with the SPEC-TDC timing information was demonstrated.

The clock synchronisation of CAENV1730 digitisers, readout electronics of PMTs, was examined. Of the digitiser clock distribution, the two most important clocks are the ADC sampling clock (500 MHz) and the trigger clock (125 MHz). This work led to a fan out clock scheme, where each receives an external clock of 6.25 MHz. This frequency was chosen so that the sampling and trigger clocks can be locked in phase with the external clock. Additionally, a correction method to account for clock jittering was to digitise the trigger waveform in channel 15 of every digitiser. Digitised waveforms can be aligned with respect to the trigger timestamp measured by the SPEC-TDC. This is a crucial correction to ensure that PMT waveforms are synchronised at the nanosecond level to necessitate the reconstruction of the beam bucket with a high timing resolution. In the following, Chapter 8 focuses on the calibration of the TPC of SBND, which is another essential step to pin down detector effects affecting high precision physics measurements.

Chapter 8

Calibration of Time Projection Chambers

Calibrating the Time Projection Chamber (TPC) is a crucial step to study and correct for physics processes and detector effects impacting the deposited charges on wire planes. Key processes affecting the production, propagation and detection of ionisation electrons are detailed in Chapter 3, including recombination, diffusion, electron attenuation and Space Charge Effect (SCE). These effects have been well-studied by other LArTPC experiments like MicroBooNE [55, 130], ArgoNeuT [65], and ICARUS [69, 131]. Their results have demonstrated an improvement in the spatial, temporal, and energy resolution of charge signals after correcting for these effects, demonstrating the importance of calibration to achieve high precision measurements.

Two Monte Carlo (MC) studies within the scope of charge calibration at the Short-Baseline Near Detector (SBND) are presented in this chapter, focusing on electron attenuation and recombination. The first study of electron lifetime measurement is presented in Section 8.1. The second study is an assessment of the impacts of delta ray fluctuations on recombination, given in Section 8.2. Section 8.3 concludes the chapter with some remarks.

8.1 Electron Lifetime Measurement

Ionisation electrons can be captured by electronegative impurities present in liquid argon, as previously described in Section 3.3.1. The reduction of the number of charges collected on a wire can be modelled as an exponential decay function following Eq. 3.6, where

the electron lifetime τ indicates the argon purity level of the detector. A higher electron lifetime corresponds to a higher purity and vice versa. The electron lifetime can be precisely measured and used to recover the original charge deposition on the wires.

At SBND, there are several methods to measure the electron lifetime. Firstly, three purity monitors were installed, two inside the cryostat and one outside, which provide quick and real-time monitoring of the argon purity. Another method requires a dedicated extraction of electron lifetime using deposited charges as measured by the wires. This calibration procedure is often performed on a sample of cosmic muons that fully cross the drift distance of the TPC, known as *anode-to-cathode* cosmic tracks. Since they traverse the whole drift distance, they make a good sample to study the charge deposited per unit length dQ/dx dependence on the drift distance. The MicroBooNE experiment also employed the same anode-to-cathode-crossing cosmic tracks to study and correct for position- and time-dependent response of their TPCs[130].

The study aims to develop a procedure to measure electron lifetime and investigate detector effects that can introduce biases in the measurement, such as diffusion and SCE. Anode-to-cathode cosmic tracks were simulated to perform the lifetime measurement. The procedure for electron lifetime measurement is outlined in Section 8.1.1, followed by Section 8.1.2 describing biases in lifetime measurement due to detector effects.

8.1.1 Electron Lifetime Extraction Procedure

The electron lifetime measurement requires information on the deposited charge per unit length dQ/dx and the respective drift time t_{drift} of that charge cluster arrive at the wire. The charge reconstruction follows the workflow described in Section 6.2, whilst additional calculation is required to deduce the drift time. The drift time is defined as:

$$t_{drift} = \frac{x}{v_d}, \quad (8.1)$$

where x is the location the charge deposition in the drift direction (x -axis) and v_d is the drift velocity. At SBND, the drift velocity is expected to be at 0.1563 cm/ μ s at an electric field of 0.5 kV/cm and temperature of 88.4 K (See Section 3.3.1). The drift time can be calculated using the time recorded by the TPC readout when a charge cluster arrives at a wire t_m which is defined as [132]:

$$t_m = t_0 - t_{trigger} + t_{drift}, \quad (8.2)$$

8.1 Electron Lifetime Measurement

where t_0 is the time when the particle enters the detector and $t_{trigger}$ is the time when the TPC readout is triggered. For a beam neutrino that triggers the TPC readout, the readout window is configured to align with when the beam arrives at the detector such that $t_{trigger} = t_0$, as illustrated in Fig. 4.8 in Section 4.2.7. On the other hand, a cosmic muon can occur anytime within the readout window and the time when it enters the detector t_0 is unknown.

A *cathode stitching* process was developed by the ProtoDUNE and Pandora collaboration to determine the t_0 of cosmic muons that cross the cathode [132]. This can be applied to any LArTPC experiments that have two TPCs sharing the same cathode. Fig. 8.1 depicts the *stitching* process. The reconstruction algorithm begins with an initial and incorrect assumption of $t_0 = 0$, so that two cosmic track segments, shown by the red and blue lines, appear at the wrong positions in both drift volumes. The algorithm then shifts the drift coordinate in each TPC by an equal and opposite amount until the two segments are *stitched* at the cathode, shown by the black line, to recover the correct t_0 .

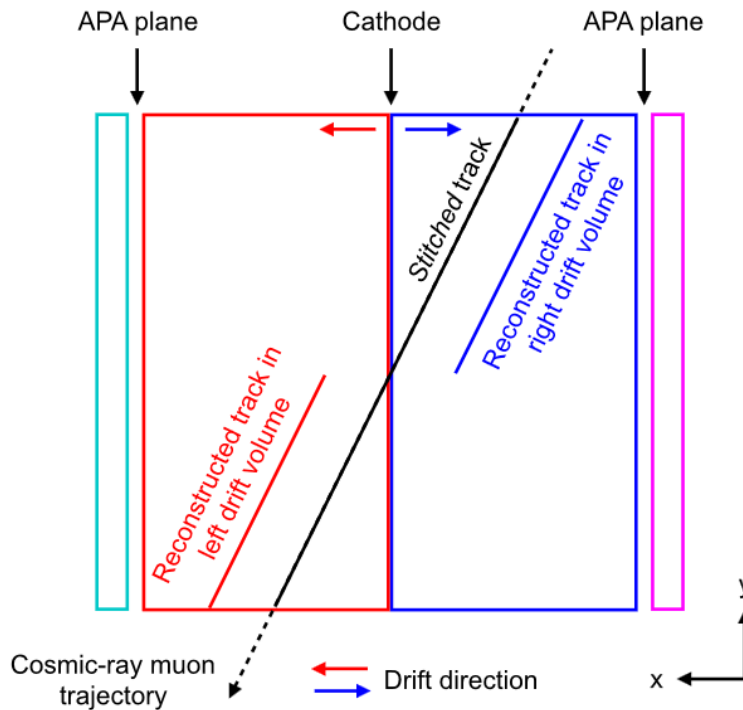


Fig. 8.1 Cathode stitching process to determine the t_0 of cathode-crossing track [132].

The performance of the stitching method was validated by ProtoDUNE, considering biases introduced by SCE [132]. It is important to note that ProtoDUNE shares many similarities with SBND, including a TPC drift distance of 3.1 m, a nominal drift velocity of

$0.159 \text{ cm}/\mu\text{s}$ and being an above ground detector highly susceptible to SCE. As demonstrated by ProtoDUNE, the stitching method achieves almost zero biases without SCE. When SCE is present, the reconstructed t_0 contains a bias $\mathcal{O}(10 \mu\text{s})$. This method has been implemented in the reconstruction workflow of SBND, and it was applied to reconstruct the sample of anode-to-cathode-crossing tracks in this study.

The next step in the lifetime extraction procedure was to plot the deposited charge per unit length dQ/dx in bins of the drift time t_{drift} . Fig. 8.2 shows an example dQ/dx profile in the drift time bin from 0.925 to 0.95 ms. A Landau-Gaussian convolution was fitted to the profile to extract the Most Probable Value (MPV) of dQ/dx [57]. This process was repeated for every drift time bin across the full drift distance of the TPC.

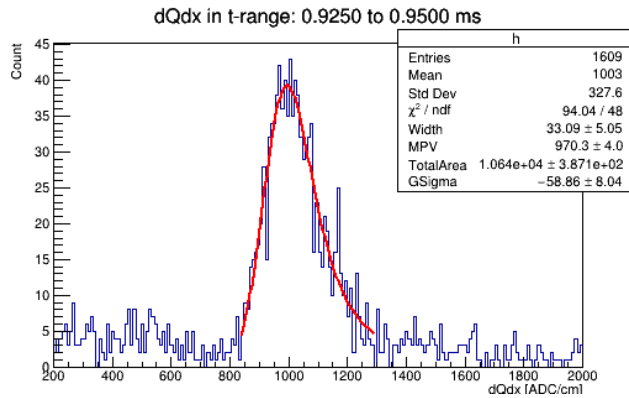


Fig. 8.2 Example of a dQ/dx profile in a drift time bin of 0.925–0.95 ms, fitted with a Landau-Gaussian convolution.

Fig. 8.3 shows the MPV dQ/dx as a function of drift time, for TPC 0 (east) and 1 (west) of SBND. Bins of drift time less than 0.25 ms and larger than 1.15 ms were excluded due to the close proximity to the anode and cathode respectively. Close to the anode, the local field around the wire planes can introduce some boundary effects on charge depositions. Close to cathode, charge depositions electrons have to traverse the whole drift distance and therefore, are more susceptible to smearing due to diffusion and SCE. The MPV dQ/dx distribution is fitted with Eq. 3.6 to determine the electron lifetime constant. The MC sample input to Fig. 8.3 was simulated with a lifetime of 10 ms and no detector effects enabled to validate the procedure. The lifetimes were determined to be 10.12 ± 0.24 and 10.40 ± 0.29 ms, for TPC 0 and 1 respectively, showing a good agreement between the result and the simulation.

8.1 Electron Lifetime Measurement

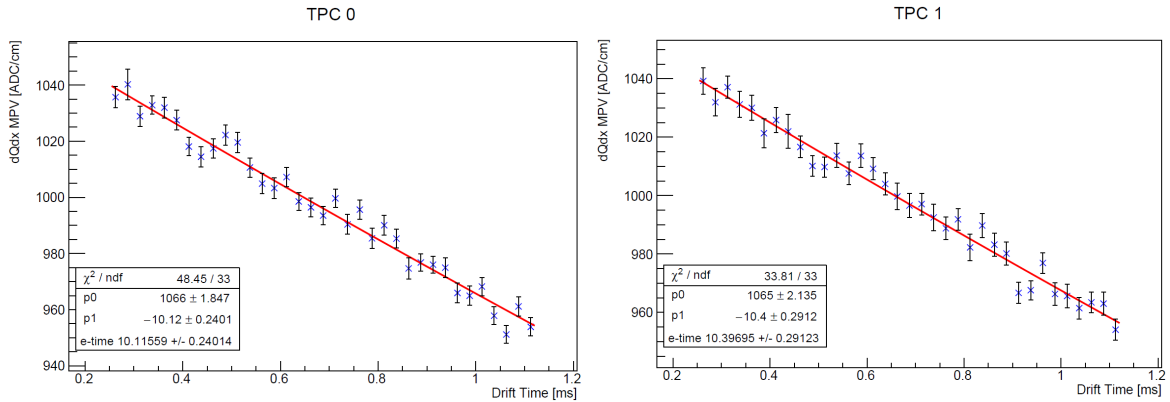


Fig. 8.3 MPV dQ/dx as a function of drift time, fitted with an exponential function.

8.1.2 Bias Study of Diffusion and Space Charge Effects

Some detector effects can introduce biases to the electron lifetime measurement, specifically those that can influence the propagation path of drifting electrons such as diffusion and SCE. Diffusion smears both spatial and temporal resolutions of the drifting electrons, and consequently the number of wires seen by the charge and the arrival time of charge measured by the wires. SCE impacts both the amplitude of the deposited charge as well as the temporal and spatial resolution due to electric field distortion. A study was undertaken to understand how each effect introduces biases to the measurement of electron lifetime.

Three dedicated MC samples were simulated: (1) No SCE nor diffusion enabled, (2) only diffusion enabled and (3) only SCE enabled. In the diffusion-only MC sample, the longitudinal diffusion coefficient was set at $D_L = 4.0 \text{ cm}^2/\text{s}$, as measured by MicroBooNE [68], and the transverse diffusion coefficient was set at $D_T = 8.8 \text{ cm}^2/\text{s}$, as measured by ProtoDUNE [70] (See Section 3.3.1). In the SCE-only MC sample, the simulation of electric field distortion followed the description in Ref. [72].

Biases in the lifetime compared to the simulated lifetime are shown in Fig. 8.4, for two simulated electron lifetimes at 3 ms (top) and 10 ms (bottom). When no detector effects are enabled in the simulation, the determined lifetimes are very similar to the simulated lifetimes, with biases well below the 2% level. When either diffusion or SCE was enabled in the simulation, biases in the lifetimes can be seen. Biases due to diffusion are at $\sim 2\%$ and $\sim 4\%$ for the simulated lifetimes of 3 ms and 10 ms respectively. On the other hand, biases due to SCE are higher at $\sim 5\%$ and $\sim 22\%$ at the simulated 3 ms and 10 ms lifetime. The observed biases are also consistent across the two TPC volumes of SBND.

The first observation is that the magnitude of the biases due to SCE is much greater than due to diffusion at both simulated lifetimes. This is consistent with the observations from an electron lifetime measurement carried out by MicroBooNE [55]. The paper demonstrated that both SCE and the transverse component of diffusion cause biases in the lifetime, however, biases due to transverse diffusion are smaller in magnitude than SCE. The paper also pointed out that the longitudinal component of diffusion causes insignificant biases in the lifetime.

The second observation is that the longer the lifetime, the larger the biases as compared between the lifetimes at 3 ms and 10 ms. This is most likely due to the precision of this method worsening with increasing lifetimes. Larger lifetime leads to a more uniform dQ/dx distribution across the drift distance, and thus, fitting an exponential function can become less reliable.

Since the results of this study, an investigation at the ICARUS experiment demonstrated that transverse diffusion breaks down the Landau-Gaussian MPV approximation of the measured charge [69], which was employed in this study. This is due to transverse diffusion

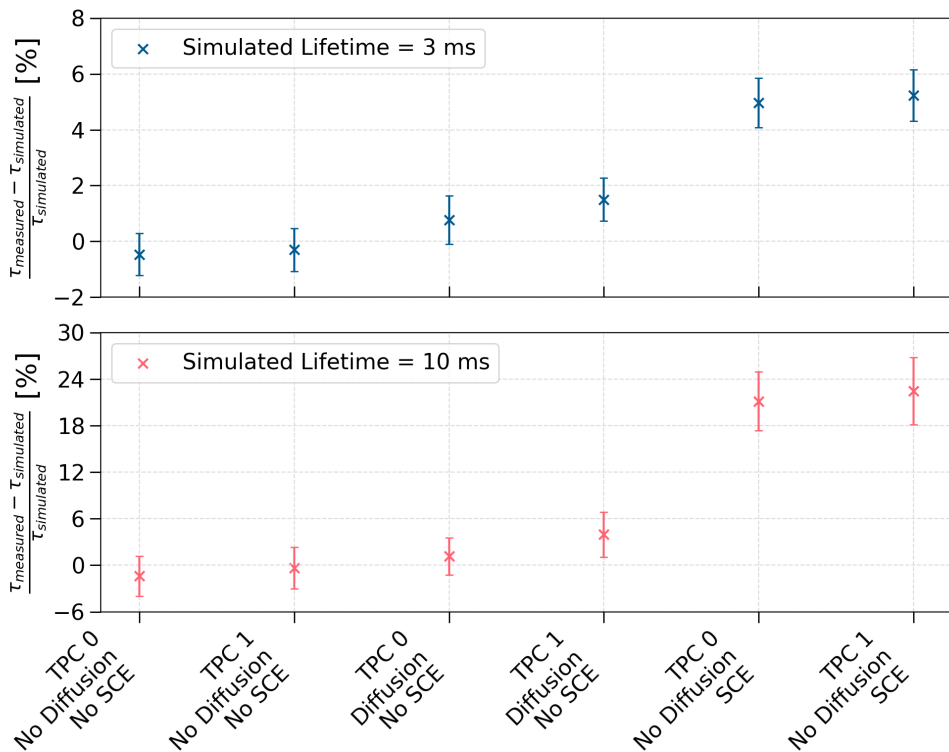


Fig. 8.4 Biases in electron lifetimes compared to the simulated values at 3 ms (top) and 10 ms (bottom).

8.2 Delta Ray Fluctuations on Recombination

smearing the charge cluster across multiple wires, resulting in a shift in the MPV value. The paper recommends using an averaged dQ/dx from a group of wires instead of dQ/dx from a single wire to mitigate the effect. The suggestion has been implemented at SBND.

The study presented here demonstrates a method to measure electron lifetime using a sample of anode-to-cathode crossing cosmic tracks. These tracks have the advantage of spanning over a full drift distance and a reconstructable t_0 time tagging when the particle enters the detector. The electron lifetime measured by this method is the most affected by SCE, followed by diffusion, which is consistent with the results from MicroBooNE. At the time of writing, this procedure has now been replicated in preparation for the calibration run of SBND. A trigger requiring coincidence in the east and west CRT wall was deployed to produce dedicated samples containing anode-to-cathode crossing cosmic muon tracks. Additionally, a new method of reconstructing t_0 time using CRT information only has been developed, applicable for cosmic tracks crossing opposite CRT walls surrounding the TPC. This new method will also be studied as part of electron lifetime measurement.

8.2 Delta Ray Fluctuations on Recombination

Recombination is a physics process that drives the charge and light yield as previously described in Section 3.2.3. SBND currently employs the Modified Box (ModBox) model for simulating recombination, with experimentally-derived parameters from ArgoNeuT [65]. The model approximates the recombination probability based on a cylindrical column surrounding a track-like charge deposition, effectively accounting for microphysics processes along the track. This approximation has proven to work well for the MeV to GeV-scale interactions, however, it breaks down at the keV-scale.

Delta rays are microphysics processes that can affect recombination, highlighted by both NEST [133] and ArgoNeuT [65] collaborations. They are knock-out electrons with low energy but high energy loss per unit length dE/dx . As shown in Fig. 8.5, delta rays are short blips produced along a longer primary track, in this case, a cosmic muon. Due to their high dE/dx , they are associated with a smaller recombination factor R (See Fig. 3.6 Section 3.2.3). A smaller R corresponds to a smaller probability of ionisation electrons surviving recombination. As a result, delta rays can lead to non-linear fluctuations in recombination that is not well-described by the ModBox model.

This study is motivated to assess the impacts of delta ray fluctuations on recombination, and consequently, the charge to energy loss conversion of different particle types using MC. An overview of the simulation of delta rays and recombination is given in

Section 8.2.1. Following this, Sections 8.2.2 and 8.2.3 provide a description of the delta ray impacts on the recombination magnitude and smearing respectively. A summary of recombination studies carried out by the ICARUS collaboration is given in Section 8.2.4.

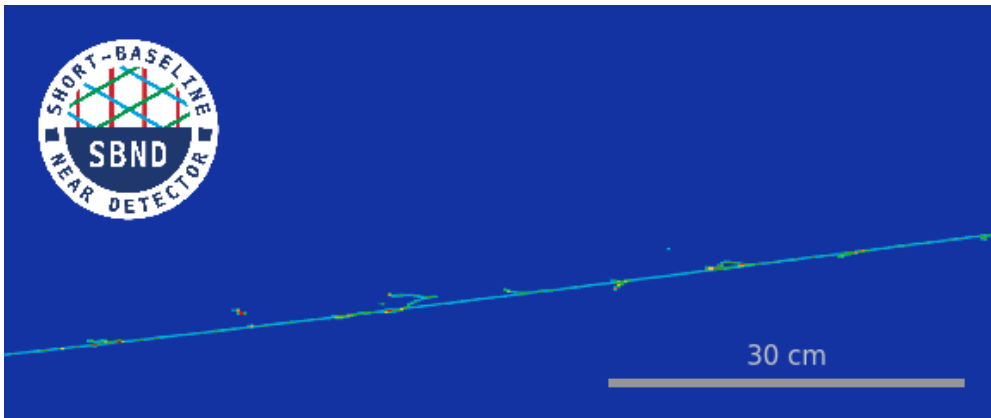


Fig. 8.5 Event display of a simulated cosmic muon track segment, with many delta rays produced along the track.

8.2.1 Simulation of Delta Rays and Recombination

Delta rays and recombination are simulated as part of the particle propagation simulation performed by the Geant4 toolkit [105], with details provided in Section 5.4.1. The simulation propagates the primary particle step by step and applies physics processes at each step of length dx . Particularly, this study focuses on the energy loss due to ionisation. It is simulated as two dependent processes: (1) a continuous energy loss dE of the primary particle along the step dx and (2) a discrete energy loss dE at the end of the step producing delta rays [105].

The continuous energy loss of the primary particle is simulated by Geant4 using complementary models depending on the particle Kinetic Energy (KE) [117]. For particles with KE > 2 MeV, the Bethe-Bloch formalism [57], detailed in Section 3.2.1, is used to compute the mean dE/dx . In the intermediate KE range range < 2 MeV, simulation models parameterised on data from Ref. [134] and Ref. [135] are implemented. In the low KE < 1 keV, Geant4 uses the free electron gas model since no data is available.

The discrete energy loss to produce delta rays is determined by a user-defined energy threshold. The energy threshold defines the lower limit of the KE of delta rays so that only delta rays with sufficient energy can be produced. This is to suppress the simulation of all low energy delta rays that would exhaust computation resources. This also means that the

8.2 Delta Ray Fluctuations on Recombination

energy of the non-produced delta rays is transferred to the continuous energy loss of the primary particle. This is equivalent to setting the energy threshold as the upper limit for the primary particle so that its mean continuous energy loss is less than the threshold.

In Geant4 terminology, the energy threshold is also known as the secondary production threshold, where the minimum KE requirement for delta ray production is defined as the minimum distance the generated delta ray must be able to traverse in a given material. These thresholds will be referred to as *delta ray thresholds* in short from this point onwards in this study. Moreover, the maximum length dx that the particle can propagate per step is configured as 0.3 mm, one order of magnitude smaller than the wire pitch of 3 mm. This setup allows for a feasible computation of generating delta rays.

For each step dx , the number of electron-ion pairs N_i resulting from a continuous loss energy deposition dE is calculated by dividing dE by the ionisation work function of argon $W_{ion} = 23.6$ eV [136]. The recombination factor R is applied N_i according to the charge-light anti-correlation described by Eq. 3.2 and 3.3 to determine the number of surviving electrons resulting from the step dx . Using the ModBox formalism, R is computed as [65]:

$$R = \frac{\log(\alpha + (\beta \cdot dE/dx) / \varepsilon)}{(\beta \cdot dE/dx) / \varepsilon}, \quad (8.3)$$

where ε (kV/cm) is the electric field at the position of the step, dE/dx (MeV/cm) is the energy loss per unit length, and parameters $\alpha = 0.93 \pm 0.02$ and $\beta = 0.212 \pm 0.002$ (kV/cm)(g/cm²)/MeV were experimentally derived by ArgoNeuT [65]. Eq. 8.3 is plotted in Fig. 3.6 in Section 3.2.3. It is important to note that R is dependent on the electric field and therefore can be influenced by local distortions of the field.

The simulation of delta rays and recombination described here gives rise to some concerns. The first concern is the assumption of a *universal* recombination factor R . The parameters α and β were measured by ArgoNeuT using a stopping proton sample, and wire planes with a pitch of 3 mm [65]. Nonetheless, they are applied to any type of ionising particles, which can influence the local ionisation density differently. Secondly, the delta ray thresholds remove low energy electrons in simulation. However, they are produced in reality and can affect recombination at a local scale.

The study was set up to address the individual concerns outlined above to better understand their impacts on recombination. Identical MC samples of muons and protons were simulated to investigate if recombination is particle-dependent. The particles were generated with a fixed energy of 1 GeV, uniform in positional and angular distributions. The Geant4 simulation was configured such that the particle can only deposit energy

via ionisation. The *true* energy loss per unit length dE/dx was computed from the *true* number of electrons per unit length dQ/dx , where *true* indicates no detector simulations were applied. The computation follows the ModBox formalism for charge to energy loss conversion as [65]:

$$\frac{dE}{dx} = \frac{1}{\beta} \left[\exp \left(\beta W_{ion} \frac{dQ}{dx} \right) - \alpha \right], \quad (8.4)$$

where parameters are the same as Eq. 8.3. For each particle type, a range of delta ray thresholds were simulated. The largest value, and also the current value being used by SBND, was set at $700 \mu\text{m}$, equivalent to delta rays with a minimum KE of 273 keV. The smallest threshold was $1 \mu\text{m}$, enabling the simulation of delta rays with KE as low as 1 keV. This variation was chosen to study the impacts due to delta ray fluctuations.

8.2.2 Impacts of Delta Rays on Recombination Magnitude

Fig. 8.6 shows the simulated charge to energy loss conversion, dQ/dx to dE/dx , for protons at the delta ray threshold of $700 \mu\text{m}$ and $1 \mu\text{m}$. The distribution was plotted for the proton residual range from 1 cm to 90 cm to cover the full track length. The proton dE/dx ranges from 2 MeV/cm to 18 MeV/cm, allowing for the examination of delta ray fluctuation impacts at both low and high parts of the dE/dx spectrum. For the delta ray threshold of $700 \mu\text{m}$ shown in Fig. 8.6a, the distribution precisely follows the ModBox model with the ArgoNeuT parameters defined in Eq. 8.4. A good agreement is expected since the simulation of SBND is similar to that of ArgoNeuT [65].

However, for the delta ray threshold of $1 \mu\text{m}$ shown in Fig. 8.6b, deviations away from the ModBox model occur, such that the distribution shifts at both low and high parts of the dE/dx spectrum. Lowering the delta ray threshold leads to more energy loss carried by the delta rays instead of the primary proton, and thus, delta rays have a greater influence on recombination. At the low dE/dx spectrum of the proton, delta rays have higher dE/dx and a smaller recombination factor R than that of the proton. This results in the *effective recombination factor* being reduced, decreasing dQ/dx at the same value of dE/dx . The opposite effect is seen at the high dE/dx spectrum of the proton, where dQ/dx is higher than the ModBox model. This indicates that the effective recombination factor increases, accounting for both the primary proton and delta rays.

The proton charge to energy loss conversion at the thresholds of 700, 10, 5, and $1 \mu\text{m}$, equivalent to delta rays with a minimum KE of 272.58, 14.60, 2.58, 1.06, and 0.99 keV are shown in Fig. 8.7. To compare dQ/dx quantitatively at the same dE/dx bin, the mean dQ/dx was calculated per dE/dx bin as shown in Fig. 8.7a. The percentage difference

8.2 Delta Ray Fluctuations on Recombination

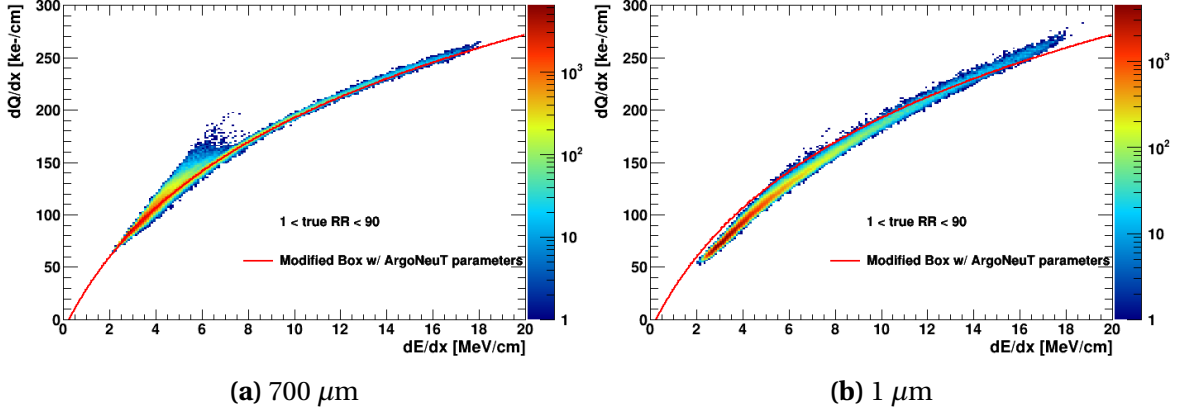


Fig. 8.6 dQ/dx as a function of dE/dx for a 1 GeV proton at the delta ray threshold of (a) $700 \mu\text{m}$ and (b) $1 \mu\text{m}$.

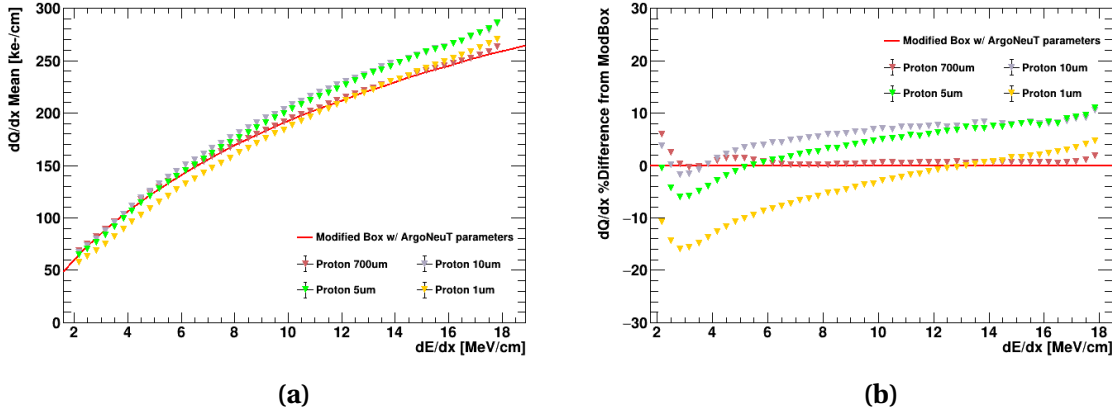


Fig. 8.7 (a) Mean dQ/dx and (b) its percentage difference relative to the ModBox model as a function of dE/dx for a 1 GeV proton.

of the mean dQ/dx relative to the ModBox model is depicted in Fig. 8.7b to quantify the magnitude of the differences.

Lowering the KE of delta rays results in two key trends. Firstly, the dE/dx position at which the proton charge to energy loss conversion shifts in upward/downward directions, increases with lower delta ray KE. This shift position can be seen in Fig. 8.7b. Secondly, the magnitude of the deviations depends on the delta ray threshold. At low $dE/dx < \sim 8$ MeV/cm, the effective recombination is reduced the most at the 1 μm threshold, as shown in yellow. At high $dE/dx > \sim 8$ MeV/cm, the effective recombination is the highest at the 5 μm threshold, as shown in green. This is evidence that delta ray fluctuations can greatly influence the proton charge to energy loss conversion. The more energy loss is carried away by very low KE delta rays, the more distorted the charge to energy scale becomes.

The charge to energy loss conversion for muons is plotted in Fig. 8.8, for the delta ray threshold at $700 \mu\text{m}$ and $1 \mu\text{m}$. Fig. 8.8a and 8.8b contain the full muon residual range, covering the track length 1–400 cm. Two distinct distributions can be seen here, one linear from the Minimum Ionising Particle (MIP) region, and another one that follows the ModBox model indicating the stopping region. The linear charge to energy loss conversion of MIP muons has been well-observed by LArTPC experiments, including MicroBooNE [130] and ICARUS [131].

To examine only the stopping region, a residual range requirement of less than 10 cm was applied, as shown in Fig. 8.8c and 8.8d. The effects of lowering the delta ray can be seen by comparing the two figures. The same behaviour as protons at the same low $dE/dx < \sim 8 \text{ MeV/cm}$ is observed, where low energetic delta rays result in a smaller effective recombination factor, reducing dQ/dx at the same value of dE/dx .

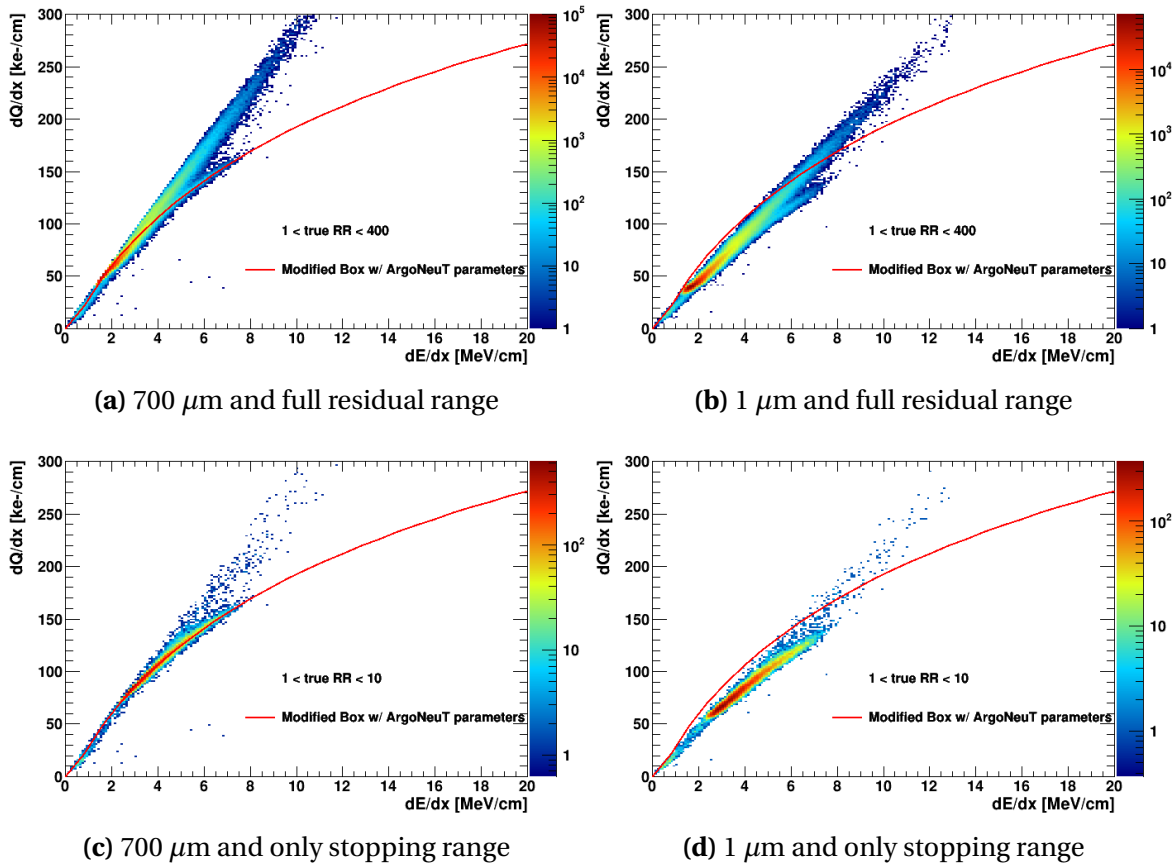


Fig. 8.8 dQ/dx as a function of dE/dx for a 1 GeV muon at the delta ray threshold of $700 \mu\text{m}$ (left) and $1 \mu\text{m}$ (right) and for the full residual range (top) and only the stopping range (bottom).

8.2 Delta Ray Fluctuations on Recombination

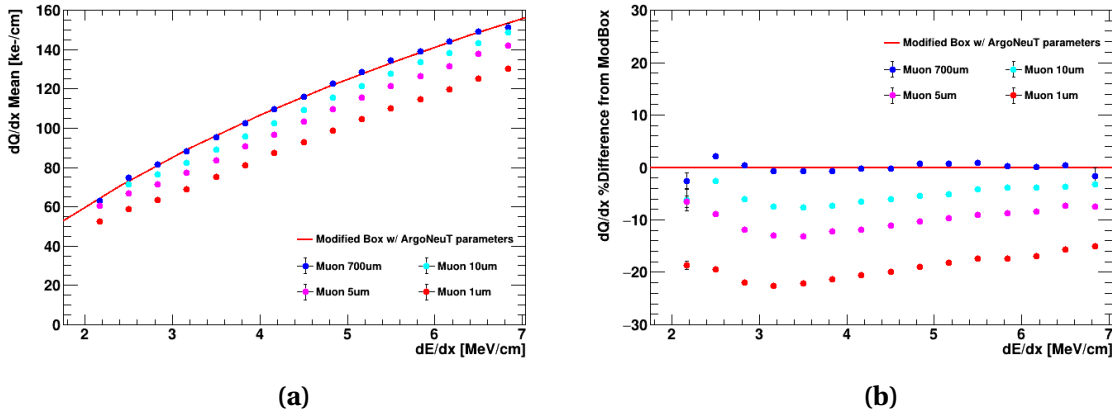


Fig. 8.9 (a) Mean dQ/dx and (b) its percentage difference relative to the ModBox model as a function of dE/dx for a 1 GeV muon.

The mean dQ/dx of muons and its percentage difference relative to the ModBox model are also shown in Fig. 8.9, at various values of delta thresholds. Similar to protons, the effective recombination reduces with lower delta ray KE. The recombination factor is also the most affected at the threshold of 1 μm , as shown in red. It is also important to note that the magnitude of the reduction is larger for muons compared to protons, which is likely due to the amount of delta rays produced by each particle type. For instance, at the same dE/dx of 3 MeV/cm and the delta ray threshold of 1 μm , the percentage difference is at $\sim 24\%$ for muons and $\sim 16\%$ for protons.

The study demonstrates that fluctuations of delta rays can affect recombination. Delta rays have a different dE/dx compared to the primary particle and therefore, can influence the effective recombination factor. At low $dE/dx < \sim 8$ MeV/cm, this results in a reduction of the effective recombination accounting for both the primary particle and delta rays. Meanwhile, at high $dE/dx > \sim 8$ MeV/cm, delta rays can increase the effective recombination factor. This leads to a distortion of the observed charge to energy loss conversion of a particle. The magnitude of the distortion is more significant for muons than protons.

8.2.3 Impacts of Delta Rays on Recombination Smearing

Delta rays affect not only the magnitude of the recombination factor but also its smearing, and consequently, the smearing of the charge to energy loss conversion. To disentangle how Geant4 handles the smearing due to delta rays, an additional study was carried out in which the energy deposition of the primary particle was isolated from delta rays.

Fig. 8.10 shows the simulated dE/dx of the primary proton as a function of its residual range, compared against the Landau-Vavilov distribution [57]. Energy loss due to delta rays is included in the top two plots, Fig. 8.10a and Fig. 8.10b, for the delta thresholds of 700 μm and 1 μm . Meanwhile, the bottom two plots, Fig. 8.10c and Fig. 8.10d, only include the energy loss of the primary proton and do not account for the energy loss of delta rays. The same set of plots for the case of muons are also shown in Fig. 8.11.

When delta rays are included in the energy loss, the dE/dx distribution agrees with the Landau-Vavilov distribution with some smearing in dE/dx across all residual range bins. The energy distributions are indistinguishable between the delta ray threshold of 700 μm and 1 μm . This can be seen for both protons, comparing Fig. 8.10a and Fig. 8.10b, and muons, comparing Fig. 8.11a and 8.11b. This is expected since the total energy loss of the primary particle and the delta rays must stay the same regardless of the delta ray threshold. Moreover, comparing the protons and muons, including delta rays in the total energy loss introduces greater smearing in the dE/dx distribution for muons than protons.

When delta rays are excluded in the energy loss, some noticeable effects can be seen. At the threshold at 700 μm , the dE/dx distribution of only the primary particle but no delta rays still follows closely the Landau-Vavilov distribution, similarly to that containing both the primary particle and delta ray energy loss. This can be seen comparing Fig. 8.10a and Fig. 8.10c for protons, and comparing Fig. 8.11a and 8.11c for muons. However, less smearing in dE/dx is observed when delta rays are excluded in the energy loss, especially visible in Fig. 8.11c for muons. At this configuration, the majority of the energy loss is carried away by the primary particle, and Geant4 already accounts for delta ray fluctuations when sampling its mean energy loss [105]. Introducing energy loss by delta rays only adds some additional smearing to the total dE/dx distribution.

On the other hand, when the delta ray threshold is set to 1 μm and no delta rays are considered, the dE/dx distribution of only the primary particle becomes narrow without any smearing and fails to follow the Landau-Vavilov distribution. This can be seen in Fig. 8.10d for protons and Fig. 8.11d for muons. Isolating only the energy deposition of the primary particle is equivalent to observing a *bare* proton or muon track without any delta rays produced along its path, which has not been experimentally measured before. In this case, the stopping power distribution of the primary particle is computed by Geant4 using interpolation instead of using data-based parametrisation [105]. This potentially leads to inaccuracy in simulating the energy loss due to ionisation.

This study demonstrates another effect of delta ray fluctuations on recombination. Having a different dE/dx to the primary particle also means that delta rays can smear

8.2 Delta Ray Fluctuations on Recombination

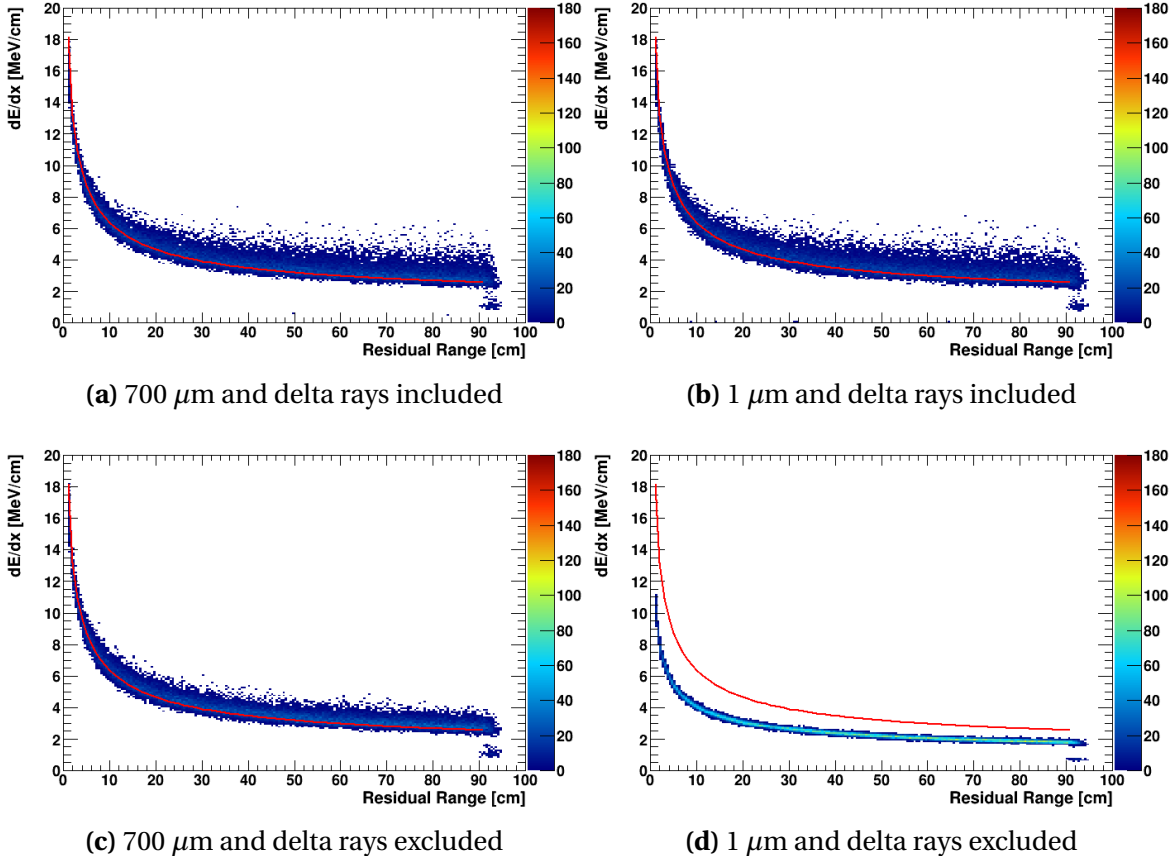


Fig. 8.10 dE/dx as a function of residual range for a 1 GeV proton at the delta ray threshold of 700 μm (left) and 1 μm (right), including (top) and excluding (bottom) the energy loss of delta rays.

the observed charge to energy loss conversion. The amount of smearing vary differently between protons and muons, where including delta rays in the energy loss lead to more smearing in the dE/dx distribution for muons than protons. Combining with the results from Section 8.2.2, this suggests a need for a particle-dependent recombination factor.

8.2.4 Recombination Studies from the ICARUS Experiment

A very similar study was carried out by the ICARUS collaboration in 2004 in Italy, to investigate delta ray fluctuations impacting recombination and also to compare against their experimental data [131]. The result is shown in Fig. 8.12, showing the recombination factor as a function of the delta ray threshold in MC. The dotted line is the expected recombination factor for a MIP muon with a KE of 250 MeV. The recombination factor

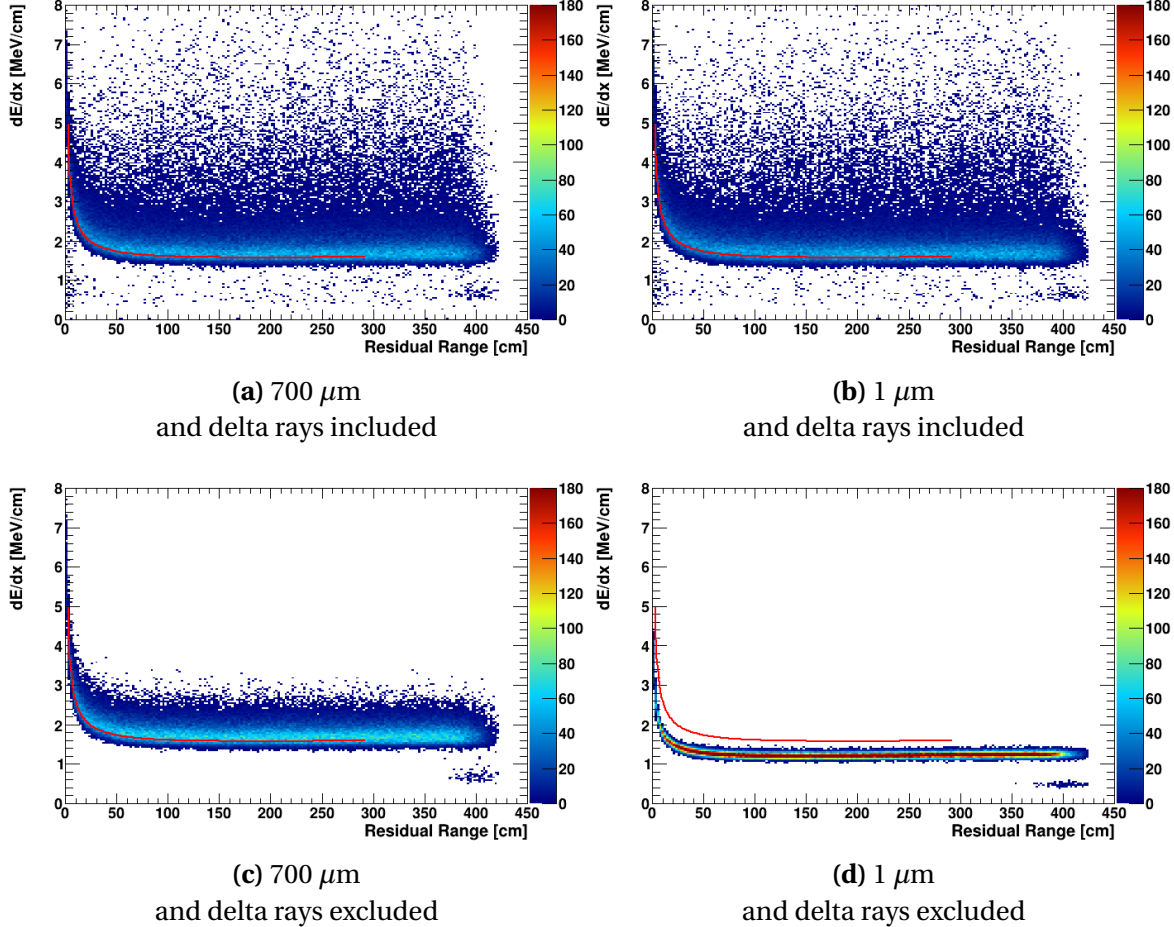


Fig. 8.11 dE/dx as a function of residual range for a 1 GeV muon at the delta ray threshold of 700 μm (left) and 1 μm (right), including (top) and excluding (bottom) the energy loss of delta rays.

increases with the threshold and peaks at ~ 0.7 , then decreases with higher thresholds. This result is similar to the observation of the study described above, where the effective recombination factor reduces at small values of delta ray thresholds.

The ICARUS collaboration proposed a few different approaches toward the simulation of recombination so that delta ray fluctuations can be more accurately simulated [131]. The first approach was to simulate *as microscopic as possible*, by simulating delta rays with KE $\mathcal{O}(1 \text{ eV})$ and range $\mathcal{O}(10 \text{ nm})$. However, they concluded that this approach was not feasible. Firstly, the effective recombination factor of a particle always contains effects due to delta rays, and secondly, computing resources are limited. Another proposal was an empirical approach, to choose the best delta ray threshold in simulation to reproduce

8.3 Concluding Remarks

the data with a reasonable computing consumption. This number was found to be $3 \mu\text{m}$, equivalent to simulating delta rays having a KE as low as 10 keV.

Also recently from the ICARUS collaboration, now with the detector relocated to Fermilab, a study in 2024 of recombination showed a clear dependence of recombination on the angle of the particle track to the drift electric field [137]. An ellipsoidal modification to the ModBox recombination model was proposed and able to describe the data across all measured angles. This result has significantly improved the observed charge to energy loss conversion of a particle, which is critical for particle identification of an LArTPC.

These results from the ICARUS collaboration have collectively enhanced the understanding of recombination, as well as guided how to model recombination at SBND. In the scope of calibrating the SBND detector, it is highly recommended to follow a data-driven approach such that the simulation of delta rays and recombination should be tuned to best match the observed data, as done by earlier experiments like ICARUS and ArgoNeuT.

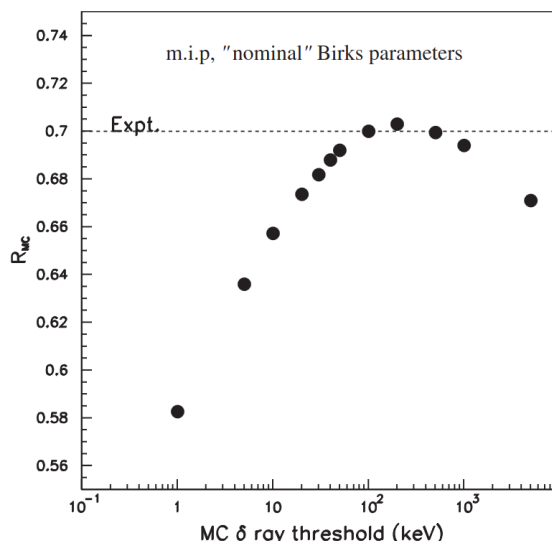


Fig. 8.12 Recombination factor as a function of the delta ray threshold [131].

8.3 Concluding Remarks

Two studies within the scope of calibrating ionisation electron signals were presented. The first study describes a procedure to measure the electron lifetime using anode-to-cathode crossing cosmic muons and quantify biases in the acquired lifetime due to SCE and diffusion. At the simulated lifetimes of 3 ms (10 ms), SCE was found to introduce a

large bias than diffusion in the electron life time measurement, $\sim 5\%$ compared to $\sim 2\%$ ($\sim 22\%$ compared to $\sim 4\%$). This strongly suggests for a need to apply a correction for SCE before performing the electron lifetime measurement.

The second study based on simulation examines the simulation of delta rays and recombination. Since delta rays have a different dE/dx to the primary particle, fluctuations in delta rays can influence the effective recombination factor, consequently, distorting and smearing the energy loss profile of the primary particle. The magnitude of the effects was determined to be particle-dependent when comparing between protons and muons. Following earlier experiments like ICARUS and ArgoNeuT, it is highly recommended for SBND to tune the simulation of delta rays to best match data.

These studies help understanding how different detector effects and physics processes can impact the charge depositions on wires, which can be pinned down and corrected for. This calibration process necessitates high precision measurements, which are essential for any physics analysis at SBND, including the search for HNLs. The following Chapter 9 focuses on the selection of HNLs, of which many reconstruction variables describing the energy deposition and topology of a particle relies on having an accurate charge information.

Chapter 9

Selection of Heavy Neutral Leptons

The selection of Heavy Neutral Lepton (HNL) signals from Standard Model (SM) neutrino and cosmic backgrounds using Monte Carlo (MC) is presented. MC samples were simulated using the framework detailed in Chapter 5 and reconstructed using the framework detailed in Chapter 6. This is the very first exploration of the Short-Baseline Near Detector (SBND) physics capabilities to search for HNLs, and this selection provides the first benchmark for understanding the current reconstruction performance of HNL signals based on MC. The selection exploits the boosted topology and late arrival features of HNL signals using the reconstructed charge and light signals from the Time Projection Chamber (TPC) and Photon Detection System (PDS) combined. This set up the ground work that can be carried out on data once the detector is operational.

The following chapter covers details on the selection workflow to identify HNL signals from backgrounds. The foundation of the selection is given in Section 9.1, including a description of signals and backgrounds, MC samples and relevant parameters to evaluate to selection. The first stage of the selection is to reject cosmic backgrounds as discussed in Section 9.2 and the second stage is to reject SM neutrino backgrounds as discussed in Section 9.3. Following this, Section 9.4 contains details of the last stage of the selection to identify HNL showers from shower-like backgrounds. The result of the selection procedure is summarised in Section 9.5. A discussion of possible improvements in sensitivity with a better timing resolution is given in Section 9.6. Finally, some concluding remarks are provided Section 9.7.

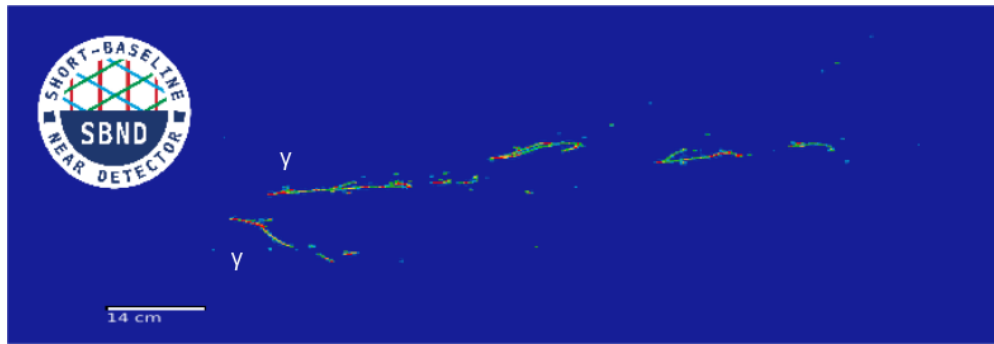
9.1 Selection Introduction

This section provides details of all the ground work before performing the selection. Definitions of signals and backgrounds are presented in Section 9.1.1. Descriptions of MC samples used in the selection are provided in Section 9.1.2. Parameters to evaluate the selection, including definitions of efficiency and the arrival time distribution, are detailed in Sections 9.1.3 and 9.1.4 respectively.

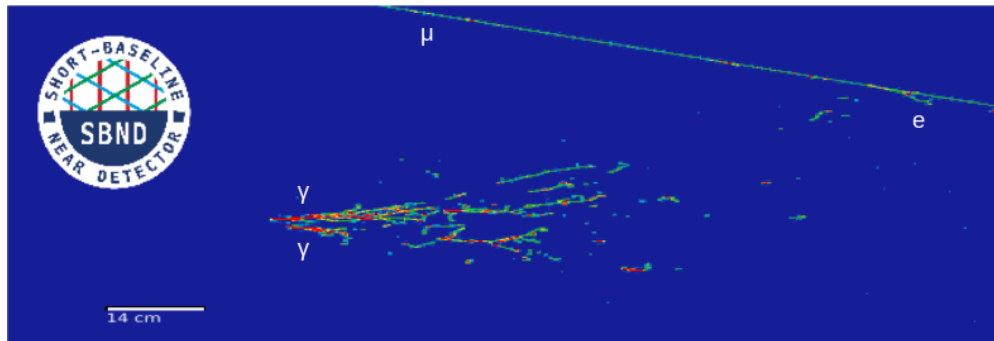
9.1.1 Signal and Background Definitions

The selection begins with defining the signal topology, namely $\pi^0 \rightarrow \gamma\gamma$ showers resulting from HNLs decaying inside the Fiducial Volume (FV) of the SBND detector. FV is a smaller volume approximately 70% of the active volume, to be defined in the forthcoming Section 9.3.1. The di-photon showers of HNLs result in one or more showers without any hadronic activities at the vertex. Fig. 9.1a shows an event display of two separable photon showers, where each shower can be seen distinctively. In the case where only a single shower is reconstructed, two scenarios can happen. The first scenario is that only a single photon deposits energy inside the detector while the other one escapes. The second scenario is that the di-photon showers are very boosted and forward-going. Fig. 5.4 in Section 5.2 shows that the angle of π^0 is very beam-collimated for HNLs in the mass range of 140-260 MeV. Thus, the resulting di-photon showers can overlap each other, in which case the opening angle between the two showers is too small to be reconstructed as two distinct showers. Fig. 9.1b shows an event display of very boosted di-photons showers, which are likely to be reconstructed as a single energetic shower.

Given this signal topology, the first-order background topology from SM neutrinos is Neutral Current interactions that produce π^0 (NC π^0). This interaction type also produces di-photon showers with little or no hadronic activities at the vertex. The second-order background topology is from Charged Current electron (anti-)neutrinos (CC ν_e) interactions. This interaction type typically produces one or multiple hadrons in addition to a single electron shower. However, in some scenarios, the hadrons are too low in energy to be reconstructed, resulting in a single shower topology after reconstruction. Fig. 9.2 shows an event display of the observable di-photon showers from NC π^0 interaction, which is indistinguishable from the di-photon showers from HNLs. The key distinction separating HNL showers from these SM neutrino showers is the boosted topology of HNLs, where HNL di-photon showers have smaller opening angles and tend to travel preferably in the beam direction.



(a) Separable di-photon showers



(b) Overlapped di-photon showers

Fig. 9.1 Event displays showing two common topologies of simulated di-photon showers from HNLs.

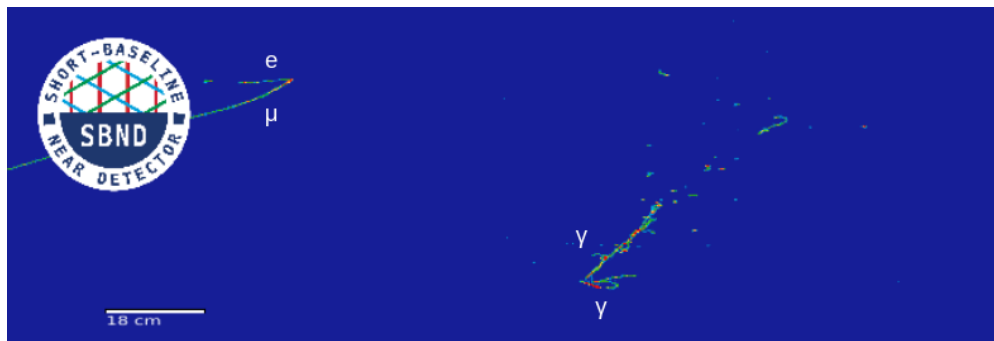


Fig. 9.2 Event display showing di-photon showers from a simulated NC π^0 interaction and a cosmic stopping muon.

SM neutrino interactions can occur outside the FV, but their products can have sufficient energy to propagate inside the FV. Interactions occurring outside the FV but inside the detector volume are referred to as Non-FV interactions. Interactions occurring completely outside the detector volume are referred to as dirt neutrino interactions. As previously discussed in Section 5.3.1, despite interacting outside of the FV, these interac-

tions can introduce non-negligible backgrounds, especially if their products also produce showers in the final states.

Finally, any background interactions that produce tracks are considered low-priority backgrounds since a track topology is easily distinguishable from a shower topology. From SM neutrinos, these interactions are from Charged Current muon (anti-)neutrinos (CC ν_μ) or any Neutral Current interactions that do not produce a neutral pion (Other NC). Fig. 9.3 shows an event display of a common observable from CC ν_μ interactions containing 1 muon and 1 proton in the final state. Similarly, cosmic muons typically leave very long tracks crossing the entire detector with features of delta rays or Michel electrons (See Sections 8.2 and 3.2.1). Fig. 9.1b (top right) and Fig. 9.3 (bottom left) both show a long cosmic track with some delta rays along the track. Fig. 9.2 (top left) shows a cosmic muon coming to a stop and decaying into a Michel electron.

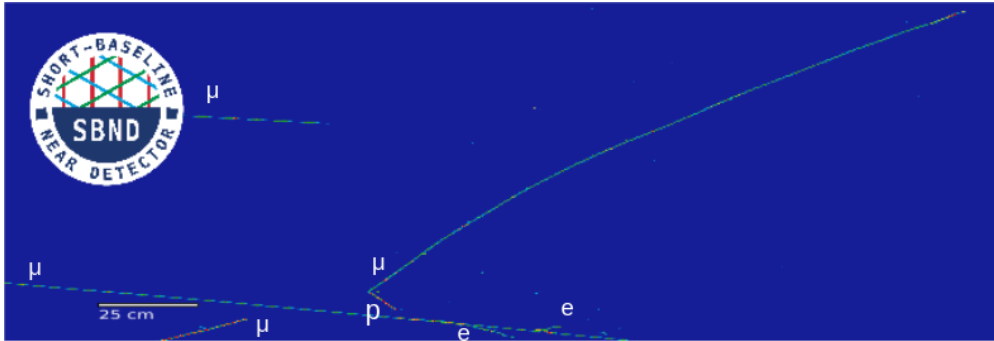


Fig. 9.3 Event display showing a muon and a proton track from a simulated CC ν_μ interaction together with a few cosmic muons.

9.1.2 Description of Monte Carlo Samples

HNL signals were overlaid with cosmic muons occurring within the TPC readout window. Samples at the HNL mass of 140, 160, 180, 200, 220, 240 and 260 MeV were generated, totalling 7 samples with 60,000 events per sample. The number of events per sample can be re-weighted from the simulated coupling $|U_{\mu 4}|^2$ to another coupling $|U'_{\mu 4}|^2$ by applying a weight as follows:

$$w = \left(\frac{|U_{\mu 4}|^2}{|U'_{\mu 4}|^2} \right)^2. \quad (9.1)$$

Eq. 9.1 allows for the signal scaling required to perform the limits setting in Chapter 10.

Three samples of SM neutrinos were also generated. The first one is a core sample with all SM neutrino interactions occurring inside as well as outside the detector (See Section

9.1 Selection Introduction

5.3.1). Two additional dedicated samples of enriched NC π^0 and CC ν_e backgrounds were also generated, to improve the limited statistics of these interactions in the core sample. The three samples were normalised to an exposure of 1×10^{21} Protons On Target (POT) to account for 3 years of data taking. This yields $\sim 331,000$ NC π^0 interactions and $\sim 33,000$ CC ν_e interactions which are the primary background. Other background from CC ν_μ and Other NC interactions make a total of ~ 5 million interactions. An additional ~ 2 million and ~ 3 million interactions from Non-FV and dirt interactions are also considered as backgrounds, although only a fraction of them deposits energy in the detector.

Finally, a cosmic-only sample was generated to account for in-time cosmics (See Section 5.3.2). This sample consists of events triggered by cosmic-only interactions. However, it is important to note that a dedicated trigger efficiency study will be carried out to better understand the rate of in-time cosmic events once SBND is operational. The cosmic-only sample was also normalised to the same POT exposure, and combined with SM neutrino samples to form a single background sample.

The unit of the selection relies on *events*, where a single event corresponds to a single trigger (See Fig. 4.8 Section 4.2.7). After reconstruction, each event contains multiple *slices*, which are interactions reconstructed by Pandora (See Section 6.2.2). A slice consists of a hierarchy of particles starting from the interaction vertex, where each particle can resemble a track or a shower. The equivalent unit to a slice from the PDS reconstruction is a *flash*, where a flash contains all the light produced from an interaction (See Section 6.3.1). The selection is performed on slices, where slices are accepted or rejected based on cuts using the reconstructed information of the slice or by matching a slice to a flash.

9.1.3 Selection Efficiency Definition

For monitoring and quantifying the impacts of selection cuts, selection efficiencies are defined for signals and backgrounds respectively. Selection efficiencies are defined as:

- **Signal Efficiency:** The fraction of reconstructed signal slices that are selected with completeness $> 50\%$.
- **Background Efficiency:** The fraction of reconstructed background slices that are selected.

The requirement of reconstructed slices indicates that they are reconstructed as neutrino-like by the Pandora workflow. As stated in Section 6.2.2, Pandora performs

a cosmic rejection to identify cosmic-like and neutrino-like slices, and only neutrino-like slices are fully reconstructed. The Pandora cosmic rejection is also employed as the first cosmic cut detailed in Section 9.2.1. Additionally for the signal efficiency, the requirement of $> 50\%$ completeness implies that at least 50% of the slice energy must be deposited by a HNL. This prevents double counting so that only well-reconstructed signal slices are considered.

The selection aims for a high background *rejection* without compromising the signal *efficiency*. This is equivalent to achieving a low background efficiency and a high signal efficiency defined here. Both efficiencies are discussed for each cut and included in the legends of the upcoming plots.

9.1.4 The Arrival Time Distribution

The late arrival of HNLs relative to SM neutrinos is previously depicted in Fig. 5.7 in Section 5.2, showing the arrival time distribution of HNLs and SM neutrinos. The distribution of SM neutrinos resembles a Gaussian-shaped bucket as they travel nearly at the speed of light. HNLs travel at a slower velocity and smear the Gaussian, resulting in excesses on either sides of the bucket. This is the key distribution for estimating the sensitivity to HNLs since it demonstrates the distinct shape difference between the signal and the background, to be further discussed in Chapter 10.

To reconstruct the arrival time distribution, the required information is the flash time matched to a slice that corresponds to the start time t_0 of the interaction. The flash time reconstruction using PMT signals is detailed in Sections 6.3.1 with a resolution $\mathcal{O}(2 \text{ ns})$. The slice-to-flash matching relies on the level of agreement between reconstructed energy from measured charge and light as summarised in Section 6.4.1.

From the interaction time t_0 , the arrival time at the upstream wall of the detector was computed by shifting from the interaction vertex z -position to $z = 0$. The arrival time corresponds to 81 buckets in a single beam spill. To overlay 81 buckets as a single one, a modulus equal to the spacing between buckets is applied. The spacing was measured to be 18.936 by the MicroBooNE experiment [129]. Discussion on different smearing contributors to the arrival time reconstruction is given in Section 9.6.

The arrival time distributions are shown throughout this chapter to demonstrate the impacts of the selection. In the following plots, both signals and backgrounds are normalised to the same exposure of 1×10^{21} POT. HNL signals are plotted as a solid red line, with the mass value of 200 MeV and normalised to the coupling $|U_{\mu 4}|^2 = 3.16 \times 10^{-7}$.

9.2 Cosmic Background Removal

Components of backgrounds are plotted as a stacked histogram, including NC π^0 shown in dark blue, Other NC shown in light blue, CC ν_μ shown in green, CC ν_e shown in light purple, dirt neutrinos shown in brown and cosmic muons shown in light grey. The number of slices for each component is also shown in the legend. The signal and background efficiencies detailed in Section 9.1.3 are added at the bottom of the legend.

9.2 Cosmic Background Removal

Cosmic rejection is the first step of selection, targeting two cosmic components: (1) in-time cosmics occurring inside the beam spill and (2) out-of-time cosmics occurring outside the beam spill but inside the readout window (See Section 5.3.2). The cosmic removal by Pandora is the first cut, presented in Section 9.2.1. The beam spill cut is given in Section 9.2.2 and the last cut employing a Boosted Decision Tree (BDT) is provided in Section 9.2.3.

9.2.1 Pandora Cosmic Removal

Being a surface detector, SBND is exposed to a high rate of cosmic rays, expecting ~ 185 million reconstructed slices from cosmics for the POT exposure of 1×10^{21} . As a comparison, the expected rate of reconstructed slices from SM neutrino interactions is ~ 11 million slices. The first cosmic rejection step targets primarily at removing out-of-time cosmic muons. As described in Sections 6.2.2 and 9.1.3, Pandora performs a cosmic removal early in the reconstruction and only neutrino-like slices are fully reconstructed. The selection thus begins with selecting only slices reconstructed as a neutrino. This rejects 90% of the ~ 185 million slices from cosmic, leaving behind only 19.5 million slices. Meanwhile, only 0.6% of the reconstructed slices from HNL signals are removed, with similar reductions across different SM neutrino interactions.

9.2.2 Beam Spill Cut

The second cut to remove cosmics is to consider the flash time of a slice, corresponding to the start time t_0 of an interaction. Only slices matched to a valid flash are selected and the matched flash time is required to be within the beam spill window. In the simulation of MC samples, the beam spill window is configured to be between $[0.367, 1.967] \mu\text{s}$, with $t = 0 \mu\text{s}$ corresponding to the first POT of a beam spill. Moreover, an interaction can occur

anywhere along the 500 cm z -length of the detector, equivalent to a smearing of 17 ns in timing. Thus, the beam spill acceptance window is widened to $[0.350, 1.984]$ μ s. The beam spill cut is illustrated in Fig. 9.4a, with the acceptance window shown as dashed red lines.

The cut rejects 4 million cosmic slices while minimally reducing signal efficiency by 3%. Fig. 9.4b shows the arrival time distribution after applying the cut, where two components of cosmic rays can be observed. There is a flat distribution coming from out-of-time cosmics and a very small Gaussian-shaped distribution coming from in-time cosmics.

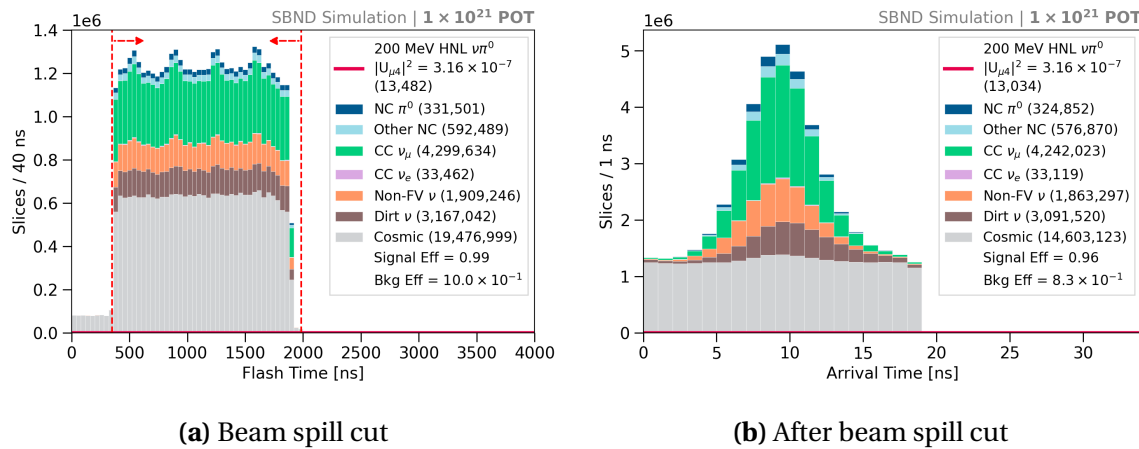


Fig. 9.4 Flash time distribution with the cut (left) and the arrival time distribution after the cut (right).

9.2.3 CRUMBS Cut

The third cut targets the out-of-time cosmic components by employing the CRUMBS score of a slice, which is scored by a BDT to distinguish between a neutrino-like slice and a cosmic-like slice (See Section 6.4.2). The score distribution of CRUMBS is plotted in Fig. 9.5a, showing a good separation between neutrino-like and cosmic-like. A cut is placed to reject any slices with CRUMBS scores less than 0, effectively removing 14 million of the remaining cosmic slices.

Comparison the arrival time distribution before and after the CRUMBS cut, Fig. 9.4b and 9.5b, demonstrates that the majority of the removed cosmics are the out-of-time component. The remaining cosmic slices are the in-time component, concentrating at the centre of the arrival time distribution. This cut results in an effective background rejection as the background efficiency reduces more than half from 8.3×10^{-1} to 3.0×10^{-1} , whilst the signal efficiency only drops by 5%. By the end of the cosmic rejection, only

9.3 Neutrino Background Removal

~ 432,000 of the starting 185 million cosmic slices remain, equivalent to a 99.9% removal of the cosmic background alone.

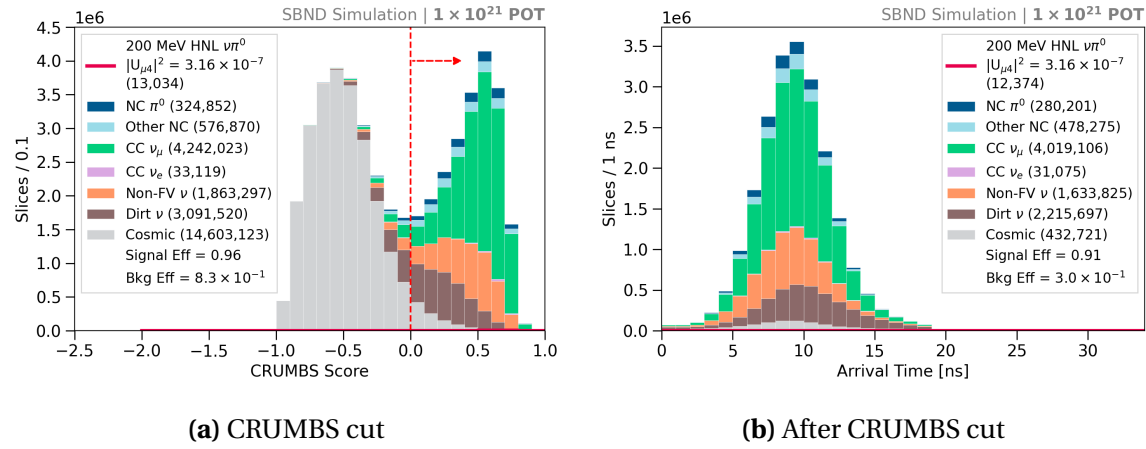


Fig. 9.5 CRUMBS score distribution with the cut (left) and the arrival time distribution after the cut (right).

9.3 Neutrino Background Removal

The next set made up of three cuts focusing on rejecting backgrounds of SM neutrinos. The cut on detector volume is presented Section 9.3.1. The cut on the reconstruction quality is detailed in Section 9.3.2. Finally, the cut targeting at removing track-like particles from SM neutrino interactions is provided in Section 9.3.3.

9.3.1 Fiducial Volume Cut

The cut on detector volume aims to remove backgrounds from Non-FV neutrinos and dirt neutrinos that interact outside of the FV but their products can deposit energy inside the FV. The cut requires the reconstructed vertex of a slice to be inside the FV, which is approximately 70% of the entire active volume of the detector. The FV is defined as follows:

- x -position: $-180 < x < -5, 5 < x < 180$ cm,
- y -position: $-180 < y < 180$ cm,
- z -position: $10 < z < 450$ cm.

The boundary is set on the x -axis to reject vertices reconstructed close to the anode and cathode. Vertices close to the cathode means the charge clusters must traverse the full drift distance before reaching the anode for detection, therefore, are more susceptible to detector effects (See Section 3.3.1). Meanwhile, vertices close to the anode might also indicate particles entering from the side of the detector which are likely to be cosmic muons and Non-FV/dirt neutrino backgrounds. The boundary on the y -axis rejects interactions that might enter the detector from the top like cosmic muons, or bottom like Non-FV/dirt neutrinos. Finally, the boundary on the z -axis for $z > 10$ cm rejects entering particles and $z < 450$ cm requires enough downstream volume for a shower to grow. Overall, these cuts ensure the quality of reconstruction.

The distribution of vertices reconstructed inside and outside of the FV is shown in Fig. 9.6a and the result of the cut is demonstrated in Fig. 9.6b. Dirt neutrino slices reduce from ~ 2 million slices to only $\sim 306,000$ slices while Non-FV neutrino slices drop from ~ 1.6 million slices to only $\sim 99,000$ slices. The cut reduces both the background efficiency and signal efficiency by a third as it is consistent with rejecting 30% of the detector volume.

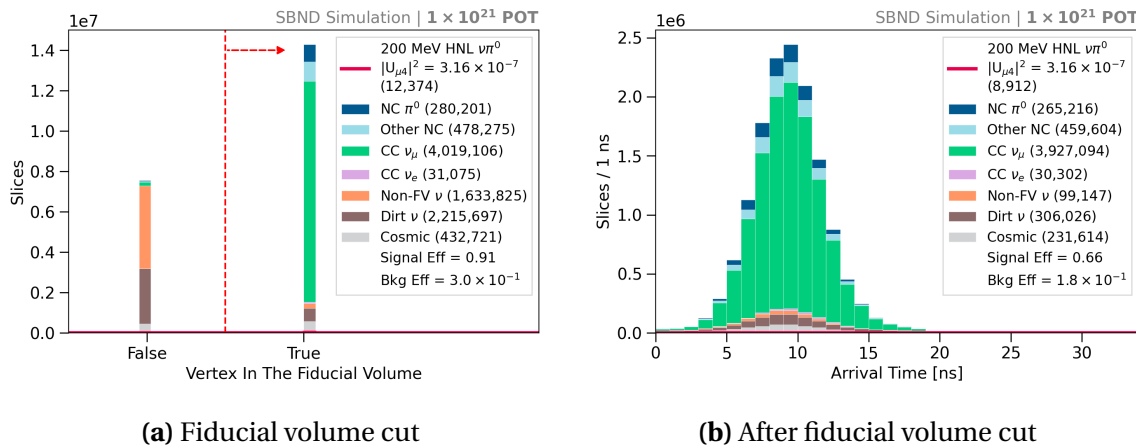


Fig. 9.6 Distribution of vertices reconstructed inside and outside of the FV with the cut (left) and the arrival time distribution after the cut (right).

9.3.2 Number of Hits Cut

This cut aims to select well-reconstructed slices by examining the number of hits of the primary particle in a slice that deposits the most energy. The number of hits is particularly important given that Pandora relies on hit information to reconstruct 3D information of particles in a slice (See Sections 6.2.1 and 6.2.2). The more hits associated with a particle,

9.3 Neutrino Background Removal

the more information is available for Pandora to reconstruct its topology and calorimetry. The number of hits requirement for the primary particle is ≥ 50 hits to provide sufficient information for a reliable Pandora reconstruction. Fig. 9.7a demonstrates the distribution of the number of hits of the primary particle in a slice. Only the first bin is rejected by this cut, demonstrating that only a small amount of slices containing primary particles with < 50 hits, which are likely to be poorly reconstructed. The arrival time distribution after the cut is shown in Fig. 9.7b, where it can be seen that the cut reduces the signal and background efficiency by $< 1\%$.

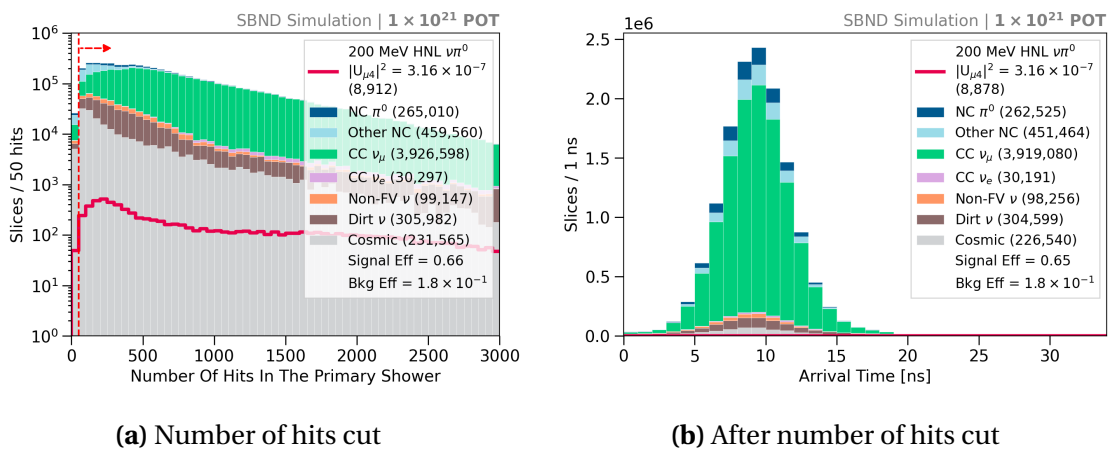


Fig. 9.7 Number of hits in the primary particle distribution with the cut (left) and the arrival time distribution after the cut (right).

9.3.3 Neutrino Track Removal

The next sets of cuts focus on rejecting SM neutrino backgrounds that produce tracks originating from muons, protons and charged pions. The cut uses the score distribution from the Razzled BDT (See Section 6.4.3). There are two types of Razzled variables examined for this cut: (1) the number of p , μ , π in a slice as identified by Razzled and (2) the Razzled p , μ , π scores of all particles in a slice. The former cut relies on Razzled assigning a type to a particle based on its highest particle type score from the BDT. The latter cut is to further reject slices if they contain particles with a Razzled score higher than a chosen threshold.

Fig. 9.8a and 9.8b demonstrate the two cuts respectively for rejecting muons. Fig. 9.8a shows the requirement on the number of Razzled-identified muons is 0 while Fig. 9.8b shows that only slices containing particles with Razzled muon score < 0.04 are selected. The cuts are very aggressive without compromising signal efficiency due to the distinction

between HNL signals and muon tracks. Comparison between the arrival time distribution before and after the muon cut, Fig. 9.7b and Fig. 9.8c, the muon cut effectively rejects 96% of the 4 million CC ν_μ slices, leaving only $\sim 161,000$ slices remaining. HNL slices are also affected by the cut such that the signal efficiency reduces from 65% to 51%.

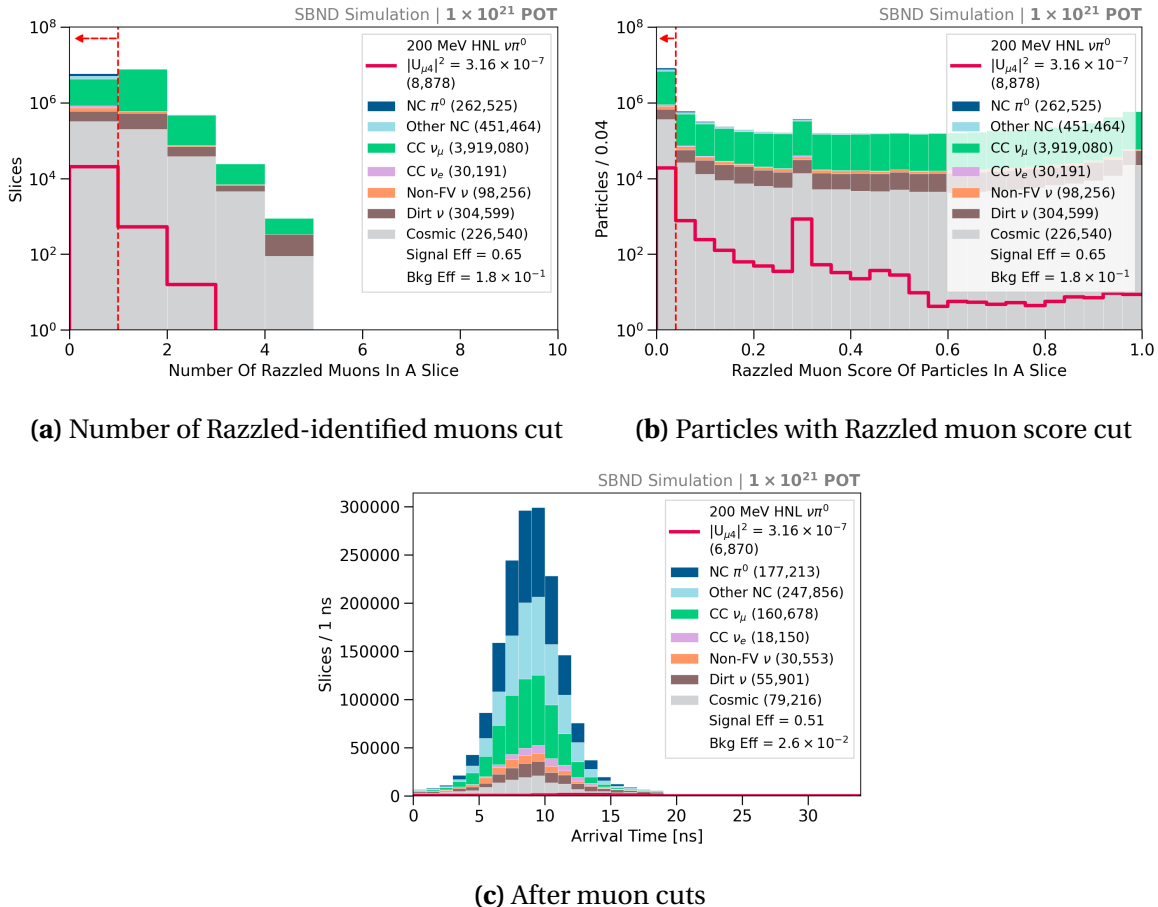


Fig. 9.8 Number of Razzled muons in a slice and Razzled muon score distributions with the cuts (top) and the arrival time distribution after the cuts (bottom).

Similar cuts are applied consecutively to reject protons and charged pions. As with the muon cuts, the cuts on the number of p , μ , π as identified by Razzled in a slice are also aggressive to require that the selected slices not contain any track-like particles. On the other hand, the cuts on the Razzled p , μ , π scores were optimised for each particle type to maximise the background rejection without costing the signal efficiency. Additional conditions are required on the reconstructed Kinetic Energy (KE) to be > 32.7 MeV for protons and < 32.1 MeV for charged pions to ensure particles are well-reconstructed. The energy requirements were found to identify protons and charged pions more effectively.

9.4 Heavy Neutral Lepton Shower Selection

The cuts to reject protons are illustrated in Fig. 9.9a and 9.9b. The impacts of the proton cut can be seen in the arrival time distribution in Fig. 9.9e, as any interactions producing protons are removed, significantly reducing SM neutrino backgrounds. The most impacted interaction modes are Other NC interactions reducing from $\sim 249,000$ to $\sim 17,000$ slices, CC ν_μ interactions reducing from $\sim 161,000$ to $\sim 46,000$ slices and NC π^0 interactions reducing from $\sim 177,000$ to $\sim 88,000$ slices.

The pion cuts are depicted in Fig. 9.9c and 9.9b. The result of the pion cut can be observed in the arrival time distribution shown in Fig. 9.9f, where the cut further cleans up any SM neutrino slices that are not already rejected by the muon and proton cuts. CC ν_μ interactions are the most affected, decreasing from $\sim 46,000$ to $\sim 30,000$ slices. This is followed by a reduction of Other NC interactions reducing from $\sim 17,000$ to $\sim 9,000$ slices.

To summarise, the cuts to reject muons, protons and charged pions are as follows:

1. Muon cuts:

- Number of Razzled-identified muons in a slice = 0,
- Slices containing only particles with Razzled muon score < 0.04.

2. Proton cuts:

- Number of Razzled-identified protons with KE > 32.7 MeV in a slice = 0,
- Slices containing only particles with Razzled proton score < 0.96.

3. Pion cuts:

- Number of Razzled-identified pions KE > 32.1 MeV in a slice = 0,
- Slices containing only particles with Razzled pion score < 0.82.

The background efficiency at the end of the track removal significantly decreases by two orders of magnitudes from $\mathcal{O}(10^{-1})$ to $\mathcal{O}(10^{-3})$, demonstrating the effectiveness of these cuts. Meanwhile, the HNL signal efficiency only decreases by 65% to 46%.

9.4 Heavy Neutral Lepton Shower Selection

After the track removal, the next five cuts target at identifying HNL showers from shower-like backgrounds. The electron shower cut is provided in Section 9.4.1. The track score cut, to keep only very shower-like signals, is detailed in Section 9.4.2. The calorimetry and

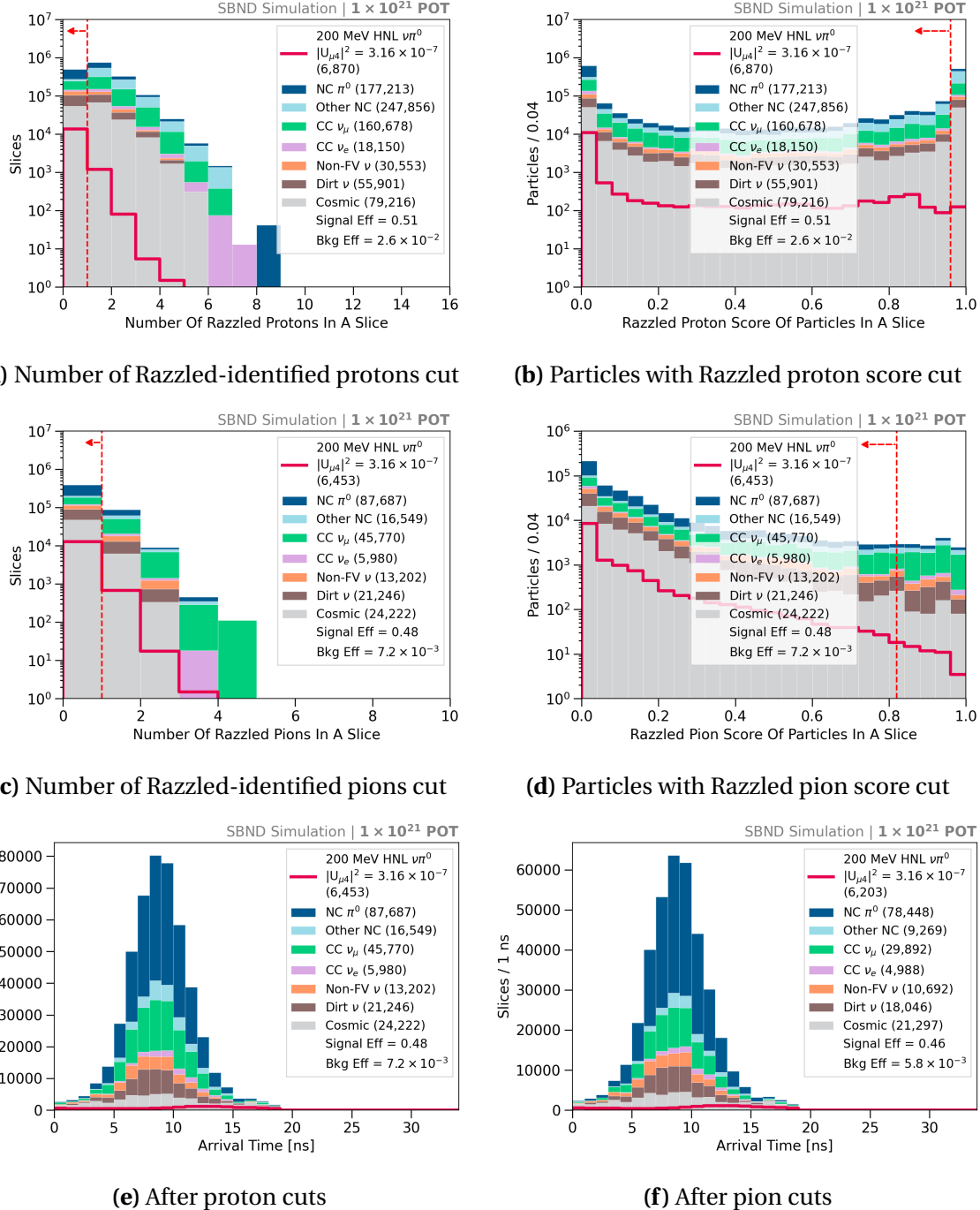


Fig. 9.9 Number of Razzled protons (pions) in a slice and Razzled proton (pion) score distributions with the cuts shown at the top (middle) and the arrival time distribution after the proton (pion) shown at the bottom left (bottom right).

9.4 Heavy Neutral Lepton Shower Selection

theta cuts in Sections 9.4.3 and 9.4.4 exploit the boosted topology of HNL showers. Finally, the cut on the π^0 invariant mass is given in Section 9.4.5.

9.4.1 Electron Shower Removal

The first cut of the HNL shower selection aims at rejecting showers originating from electrons. Key differences between electron showers and photon showers are the conversion gap and dE/dx (See Section 3.2.1). The conversion gap describes the gap between the interaction vertex and the start of the shower, where electron showers start immediately at the vertex but photon showers might propagate away from the vertex before showering. The dE/dx describes the energy loss distribution per unit length, such that the dE/dx of a photon shower is twice that of an electron shower since a photon shower is from pair production. Both these shower characteristics are provided during the training of the Razzled BDT for classifying photons and electrons.

The Razzled electron score is examined for the primary shower that deposits the most energy in a slice. The cut is demonstrated in Fig. 9.10, where only slices containing primary showers with a Razzled electron score < 0.96 . The rejected slices are clearly-identified CC ν_e showers with high Razzled electron scores. This is a very soft cut compared to the previous track removal cuts since showers from CC ν_e interactions and showers from HNLs are very similar to each other. The cut rejects 31% of the remaining $\sim 5,000$ CC ν_e slices while minimally reduces HNL slices by only 3%.

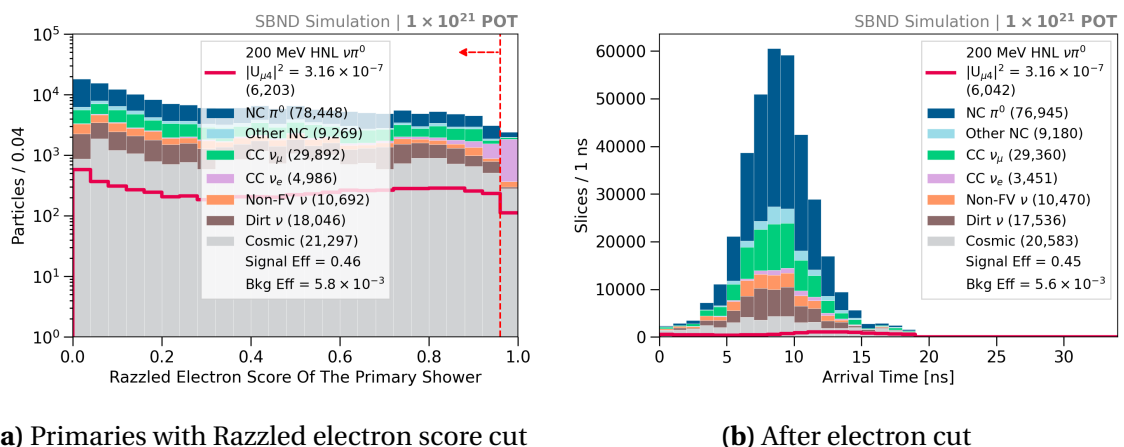


Fig. 9.10 Razzled electron score of the primary shower distribution with the cut (left) and the arrival time distribution after the cut (right).

9.4.2 Track Score Cut

To further reject backgrounds containing showers, careful considerations were taken into developing cuts by separating the shower topology into subsets. As previously stated, di-photon showers from HNLs can result in either a single shower topology or multiple shower topology. Thus, two cases can be considered when applying cuts: (1) slices containing only one shower and (2) slices containing two or more showers. The distribution of signal and background slices in the phase space of the cut variable vary differently between the two cases. This results in a different signal-to-background ratio across the distribution for each case. From this cut onwards, individual cut is examined per case to optimise the efficiency of background rejection and signal selection.

The second cut of the HNL shower selection employs the track-shower separation BDT, that outputs a track score to a particle indicating if it is track-like or shower-like (See

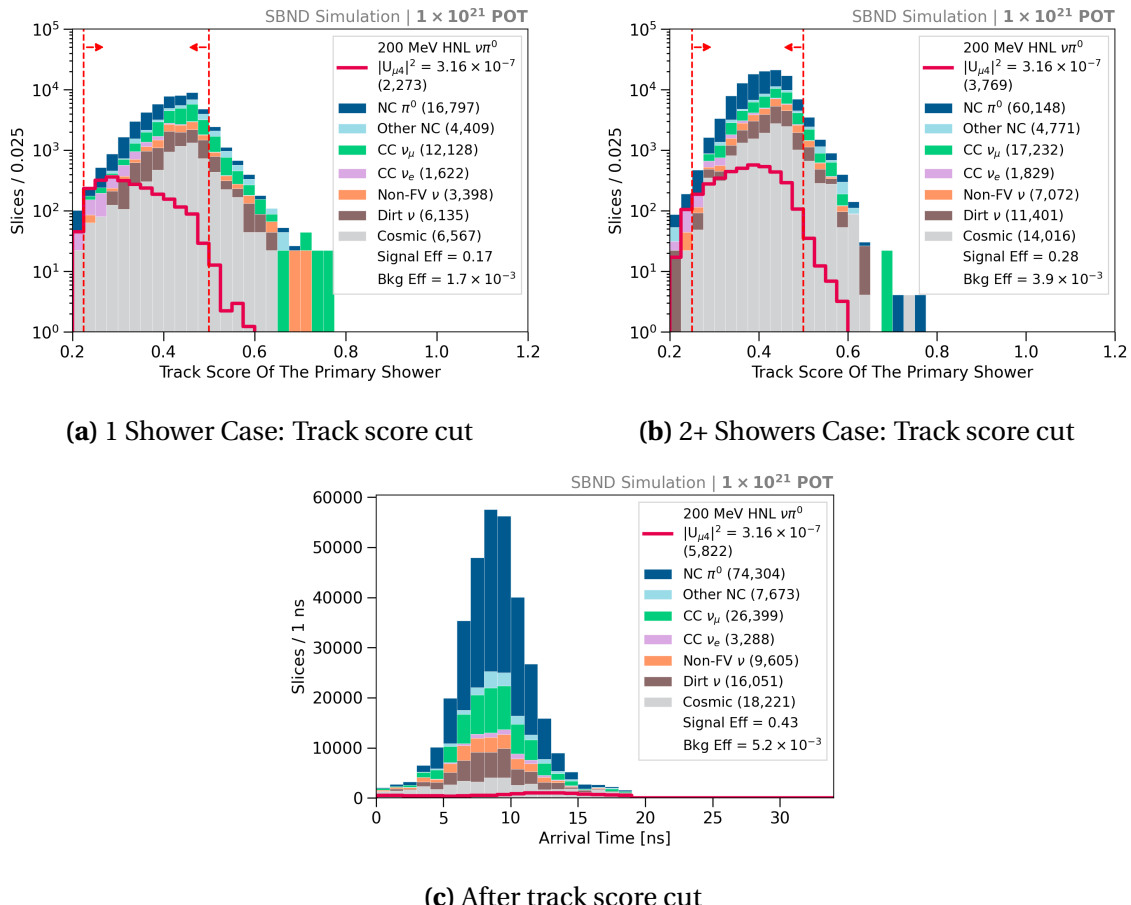


Fig. 9.11 Track score distributions with the cuts (top) and the arrival time distribution after the cut (bottom).

Section 6.2.3). The track score is examined for the primary shower that deposits the most energy in a slice. Fig. 9.11 displays the track score distribution of primary particles for the two cases of slices containing 1 shower and 2+ showers. For both cases, the remaining primary particles are already shower-like since the track score concentrates at < 0.5 .

The cut sets the upper boundary of the track score at 0.5 for both cases, to reject any primary particles leaning towards track-like. On the other hand, the cut on the lower boundary of track score aims at trimming some shower-like backgrounds. The cut is optimised for each case depending on its signal-to-background distribution. A more lenient cut is applied for the single shower case selecting primary showers with a track score of ≥ 0.225 . The cut is tightened up for the multiple showers case for better background rejection, requiring primary showers to have a track score of ≥ 0.25 . The resulting arrival time distribution is depicted in Fig. 9.11c, showing a reduction of 3-16% across different SM neutrino interaction types. The signal selection efficiency only reduces from 45% to 43%.

9.4.3 Calorimetry Cut

The third cut of the HNL shower selection targets the highly energetic aspect of HNL showers compared to SM neutrino showers. Outputs from the slice-to-flash matching process are examined, particularly the fraction variable defined in Eq. 6.4 in Section 6.4.1. The fraction describes the level of agreement between L_Q and L , where L_Q is the number of PhotoElectrons (PEs) predicted from the reconstructed charge and L is the number of PEs measured by PMTs. A large disagreement indicates poor reconstruction, whether under or overestimation in between reconstructed energy from charge and light.

The fraction is useful to identify showers originated from HNLs due to their boosted topologies. Very forward-going HNL showers are likely to overlap and reconstructed as a single shower merged from multiple showers. The reconstructed charge of the merged HNL shower tends to be much higher than that for SM neutrinos. The number of PEs predicted from the reconstructed charge L_Q is therefore likely to be overestimated compared to the number of PEs measured by PMTs L .

The overestimation is demonstrated in Fig. 9.12, where it can be seen that HNL slices mainly concentrate in the region $\frac{(L_Q - L)}{L} \geq 0$. The calorimetry cut exploits this feature and is optimised for the single shower as well as the multiple shower case. For slices containing a single shower, the requirement on the fraction is between -0.1 and 0.4 to select well-predicted showers with the fraction centred around 0, as well as overestimated showers

with the fraction > 0 . For slices containing multiple showers, the requirement on the fraction is restricted to between 0.04 and 0.3 to select only overestimated showers, rejecting backgrounds more aggressively. The arrival time distribution after the cut is shown in Fig. 9.12c, demonstrating the effectiveness of the cut as the background efficiency decreases by a whole order of magnitude from $\mathcal{O}(10^{-3})$ to $\mathcal{O}(10^{-4})$. Meanwhile, the signal selection efficiency only decreases from 43% to 35%.

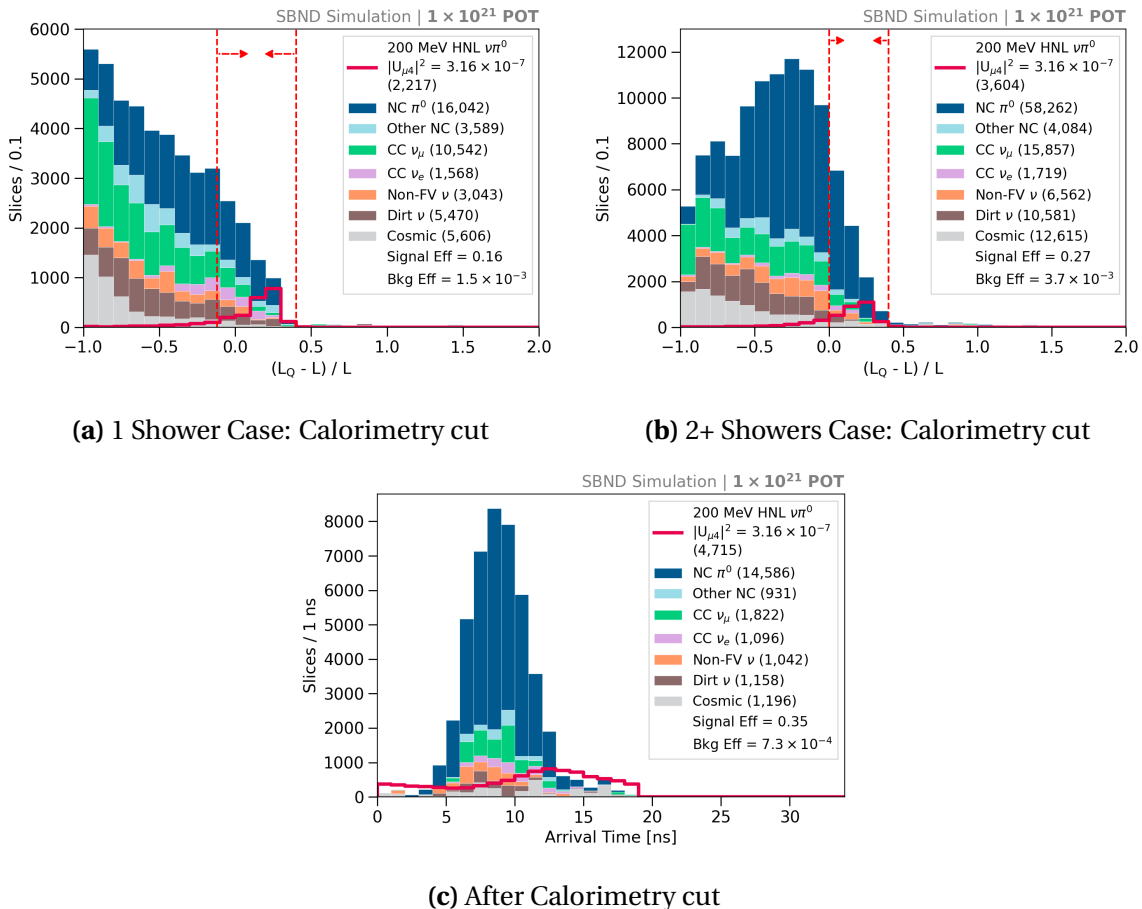


Fig. 9.12 Distributions of the $(L_Q - L)/L$ with the cuts (top) and the arrival time distribution after the cut (bottom).

9.4.4 Theta Angle Cut

The fourth cut exploits the topology of the forward-going HNL showers such that their angles with respect to the beam direction, referred to as *theta angles*, are small. Fig. 9.13a shows the angular distribution for slices containing a single shower. In this case, the signals are mainly highly energetic and boosted di-photon showers reconstructed as a

9.4 Heavy Neutral Lepton Shower Selection

single merged and beam-collimated shower. As a result, their theta angles concentrate in the region $< 25^\circ$. An aggressive selection of $< 25^\circ$ can be placed without compromising signal efficiency.

Fig. 9.13b shows the theta angle distribution for slices containing multiple showers. In this case, HNL showers are less boosted and more likely to result in separated showers. Their theta angles with respect to the beam are larger compared to the single shower case. To preserve signal selection efficiency, a widened selection of $< 30^\circ$ is applied.

Fig. 9.13c shows the arrival time distribution after applying the cut. The theta angle cut effectively rejects any shower-like backgrounds that are not beam-collimated, resulting in a reduction across all SM neutrino interaction types. This is a very impactful cut given that the background efficiency decreases by half from 7.3×10^{-4} to 3.6×10^{-4} . The signal efficiency of HNL slices only drops from 35% to 32%.

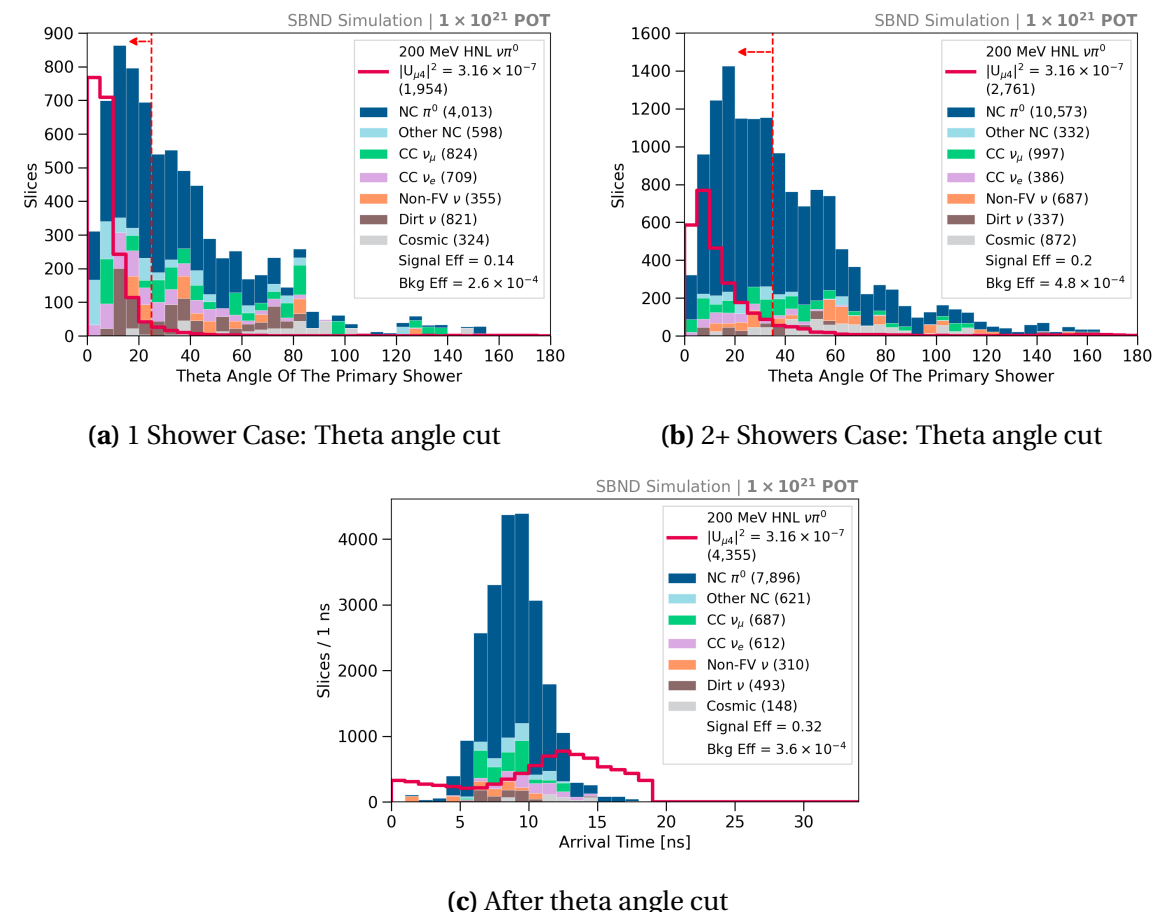


Fig. 9.13 Theta angle distributions with the cuts (top) and the arrival time distribution after the cut (bottom).

9.4.5 Neutral Pion Invariant Mass Cut

The final cut of the HNL shower selection exploits the fact that di-photon showers originate from a π^0 decay, allowing for the reconstruction of π^0 invariant mass, m_{π^0} . For slices containing multiple showers, the invariant mass is reconstructed using the reconstructed momenta of any two shower combination in the slice. For two massless photon showers with an opening angle α and a total energy E_1 and E_2 respectively, m_{π^0} is computed as:

$$m_{\pi^0} = \sqrt{2E_1 E_2 \times (1 - \cos\alpha)}. \quad (9.2)$$

For a given slice, the π^0 invariant mass was reconstructed for all combinations of two showers, and the best mass was considered for the cut. The cut is illustrated in Fig. 9.14, where the solid red line indicates the π^0 mass of 135 MeV. A cut is applied to select slices corresponding to a reconstructed invariant mass of 300 MeV or less. This rejects any slices with a poorly reconstructed π^0 mass, which could be due to backgrounds from SM neutrino interactions such as CC ν_μ , Other NC, Non-FV and dirt as well as energetic cosmic rays. However, poor shower reconstruction can also result in di-photon showers from π^0 getting mistakenly rejected by this cut, as it is evident that some NC π^0 interactions and HNL signals are affected. This cut reduces both signal and background slices by < 3%.

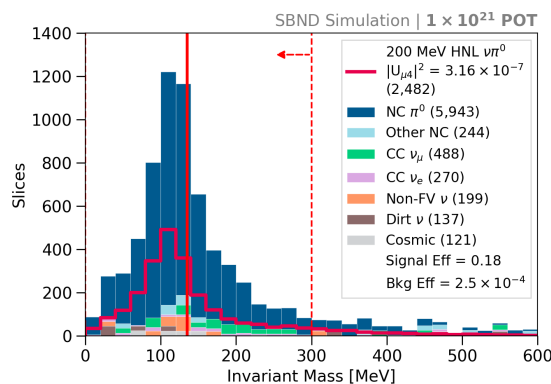


Fig. 9.14 π^0 invariant mass distribution with the cut applied to the multiple showers case.

9.5 Selection Results

Fig. 9.15a shows the arrival time distribution after the selection. The background efficiency is 3.3×10^{-4} , demonstrating the extreme background rejection achieved amounting to

9.5 Selection Results

four orders of magnitude. Meanwhile, the signal efficiency is well-preserved at 30%. The remaining background is dominated by NC π^0 interactions, which are tricky to remove due to their similarities with HNLs. A combination of CC ν_μ and Other NC interactions remain, likely undergo deep inelastic scattering, producing shower-like products like π^0 or e^\pm . CC ν_e interactions persist as they can produce a single shower topology. Some Non-FV and dirt neutrino interactions can still be seen, since their products can propagate to the FV and deposit energy. Finally, cosmic muons are almost fully rejected.

The multi-binned analysis for determining sensitivity depends on signal-rich bins. Fig. 9.15c zooms into the first and last 4 bins of the arrival time distribution, which are the highest the signal-to-background ratio bins. These contribute towards sensitivity significantly more than bins located at the centre region of the distribution. A *timing cut* can be applied to select only these bins, which would result in a background efficiency decreasing from $\mathcal{O}(10^{-4})$ to $\mathcal{O}(10^{-6})$ while still maintain a signal efficiency of 10%. However, the cut is not formally applied as part of the selection, but to highlight the importance of these edge bins due to their excellent signal-to-background ratio. The timing cut is discussed further in Chapter 10.

To better understand the sensitivity dependence on the signal-to-background ratio, two selections were developed. The selection presented up until this point is referred to as *the lenient cut*. An additional more aggressive cut, referred to as *the stringent cut*, was developed by tightening the two most impactful cuts on calorimetry and theta angle. The resulting arrival time distribution for the stringent cut is shown in Fig. 9.15b and 9.15d for the entire distribution and only the edge bins. The key difference between these two cuts is that the lenient cut retains more signals however at a lower purity, whilst the stringent cut results in higher purity at the cost of signal efficiency. The two selections are summarised in Table 9.1.

Fig. 9.16 shows the signal and background rejection efficiency cut by cut. The signal efficiency is plotted using the left axis in pink and the background efficiency is plotted using the right axis in blue. It is important to note that the right axis is in the logarithm scale as the background rejection is very aggressive. The band of signal efficiency corresponds to the efficiency across the entire mass range of HNLs from 140 to 260 MeV, with efficiency increasing with masses. The selection differs from the calorimetry cut onwards, where the lenient cut is shown in solid line and the stringent cut is shown in dotted line. Overall, the most significant cuts are the muon/proton/pion cut for track removal, followed by the calorimetry and theta angle cut by exploiting the boosted topology of HNLs that significantly reject backgrounds without compromising signal efficiency.

Table 9.1 Summary of the lenient and stringent selection.

	Common Cut	
Cosmic Removal:		
Slice reconstructed by Pandora as a neutrino Flash time inside the beam spill CRUMBS score	True [0.350, 1.984] μ s ≥ 0	
SM Neutrino Removal:		
Reconstructed vertex inside the FV # of hits in the primary shower	True ≥ 50	
# of Razzled muons	0	
Razzled muon score of particles in a slice	< 0.04	
# of Razzled protons with KE > 32.7 MeV	0	
Razzled proton score of particles in a slice	< 0.96	
# of Razzled pions with KE > 31.2 MeV	0	
Razzled pion score of particles in a slice	< 0.82	
HNL Shower Selection:		
Razzled electron score of the primary shower	< 0.96	
Track score of the primary shower		
1 shower case	0.225 < score < 0.5	
2+ shower case	0.250 < score < 0.5	
(L _Q - L) / L fraction of a slice		
1 shower case	-0.12 < frac < 0.40	-0.10 < frac < 0.40
2+ showers case	0.00 < frac < 0.40	0.04 < frac < 0.30
Theta angle of the primary shower		
1 shower case	$\leq 25^\circ$	$\leq 20^\circ$
2+ showers case	$\leq 35^\circ$	$\leq 30^\circ$
Invariant mass of any 2 showers in a slice	≤ 300 MeV	
Timing Cut *(applied when setting limits):		
Arrival time within the arrival time	[0, 4] ns and [15, 19] ns	

9.5 Selection Results

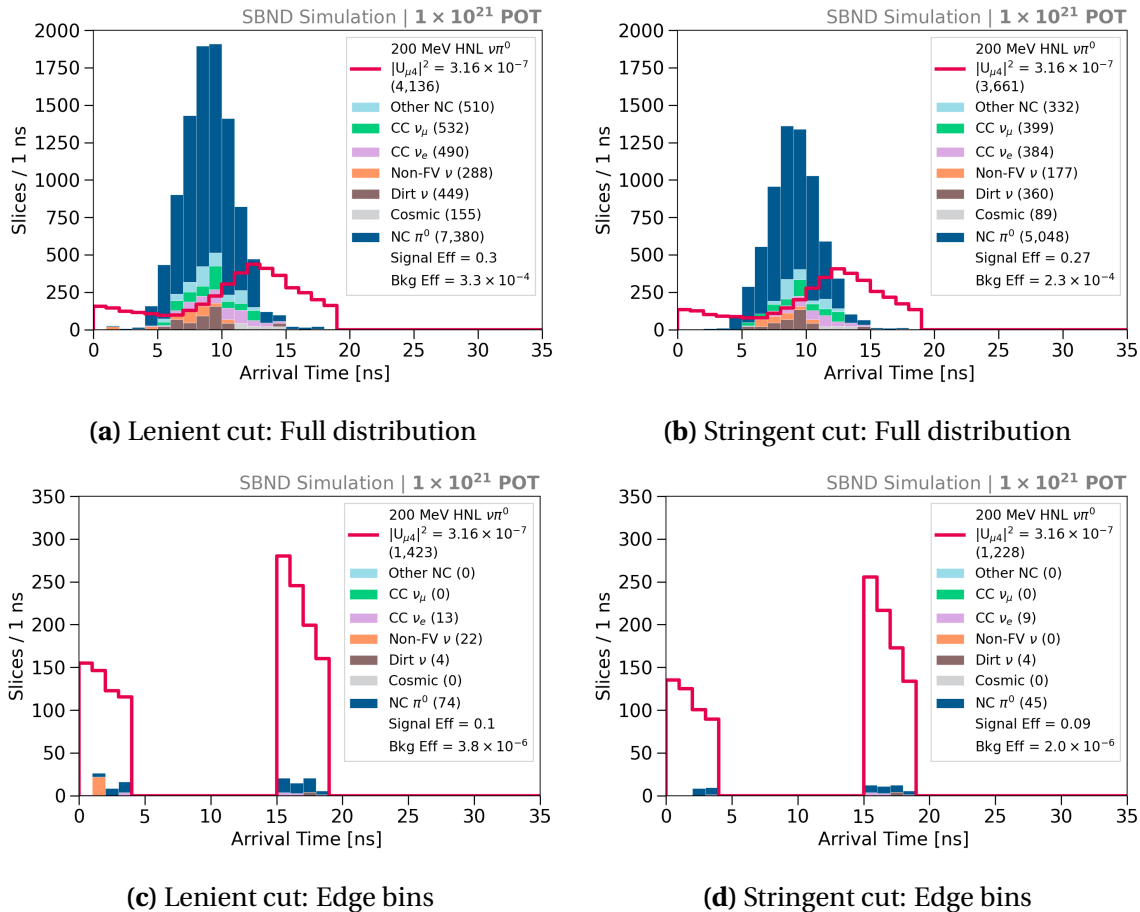


Fig. 9.15 Arrival time distributions after the lenient (left) and stringent cut (right).

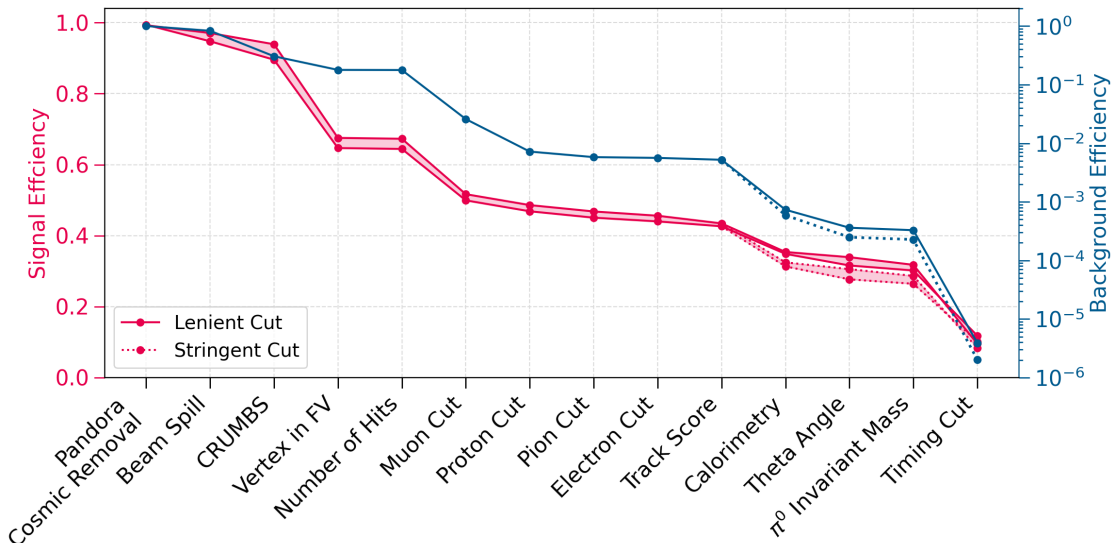


Fig. 9.16 Summary of signal (left axis) and background efficiencies (right axis).

9.6 Study of Timing Resolution Improvement

The timing cut described above demonstrates the importance of a high precision timing reconstruction in this analysis and thus, a study was carried out to understand the smearing contributors to the arrival time distribution. Fig. 9.17 illustrates several factors that can smear the arrival time of a SM neutrino at SBND, and consequently smearing the Gaussian shape of the bucket. The intrinsic Gaussian width of the proton bucket from the Booster synchrotron is 1.308 ns, as shown by the brown arrow (See Section 4.3). This structure is then smeared out due to the time of secondary mesons t_{meson} , accounting for their interaction time and time of flight, as shown by the blue arrow. The time of flight of the tertiary SM neutrinos from the production location to the detector t_{ν} to detector further smears the Gaussian, as shown by the pink arrow.

Once the neutrino arrives at the detector, two additional smearing factors need to be considered. The first one is its time of flight inside the detector until the interaction vertex t_{ν} inside detector, as shown by the purple arrow. The second one is the time of flight of the photon from the production to the detection location t_{γ} , assuming the photon production location is close to the interaction vertex, as shown by the green arrow.

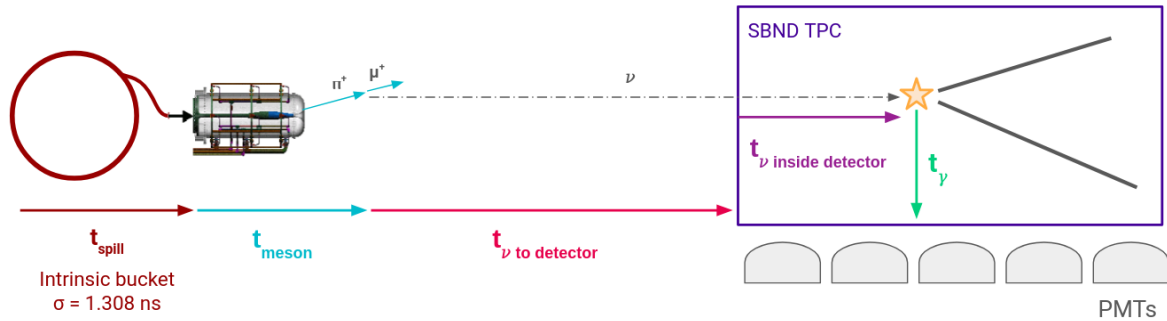


Fig. 9.17 Diagram showing smearing contributors to the arrival time.

The true arrival time distribution of SM neutrinos is shown in the left of Fig. 9.18, where true indicates that no detector simulation and reconstruction are applied. This distribution was computed using the true interaction time at the vertex, marked by the yellow star in Fig. 9.17, and corrected for t_{ν} inside detector. It can be seen that the combination of t_{meson} and t_{ν} to detector smears the Gaussian width by a negligible amount from 1.308 ns to 1.37 ns.

The reconstructed arrival time distribution of SM neutrinos is depicted in the right of Fig. 9.18. The arrival time was computed from the flash time matched to a slice (See Sections 6.3.1 and 6.4.1). The flash time was reconstructed using the prompt light in

9.6 Study of Timing Resolution Improvement

the first 30 ns window so that the scintillation location is close to the interaction vertex, and was also corrected for t_γ . The correction for t_ν inside detector was applied by a shift from the reconstructed vertex z -position to $z = 0$ at the detector's front face. As a result, the reconstruction depends on three variables: (1) the matching of slice-to-flash, (2) the flash time and (3) the slice vertex. Each of these variables has its own reconstruction uncertainty, adding more smearing to the reconstructed arrival time.

Comparing the two distributions in Fig. 9.18, the Gaussian mean is shifted by 1.82 ns from 7.44 to 9.26 ns. This includes a shift of 1.45 ns introduced by the light reconstruction [73]. The rest might be due to the slice vertex reconstruction and/or the slice-to-flash matching. Additionally, the Gaussian width is smeared from 1.37 ns to 2.26 ns. The width smearing is detrimental to the HNL search since it results in more SM neutrinos in the edge bins of the distribution, reducing the signal-to-background ratio in this region.

This motivates the assessment of sensitivity assuming a better timing reconstruction. The two assumptions of the arrival time distribution reconstructed with an improved timing resolution are as follows:

1. A shifted Gaussian mean of 1.45 ns,
2. A smeared Gaussian width of 1.73 ns.

The first assumption is motivated by the impact of the light reconstruction in SBND reported in Ref. [73]. The second assumption is motivated by the MicroBooNE experiment reporting on their intrinsic timing resolution in Ref. [129]. Although ambitious, it is an achievable goal for SBND to have a reconstructed timing resolution < 2 ns, given that

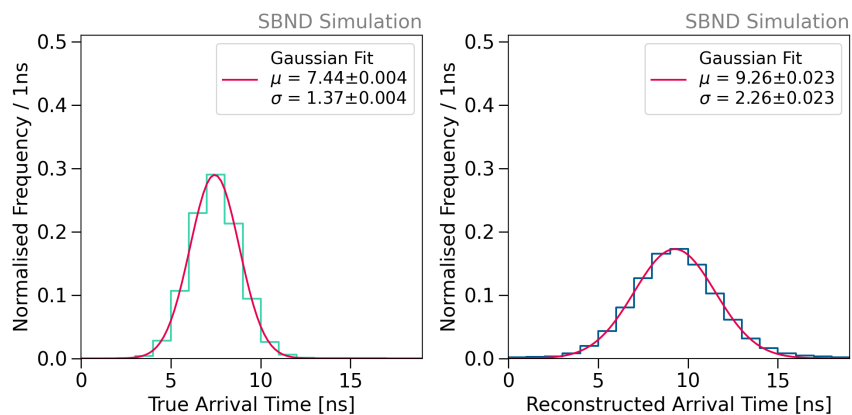


Fig. 9.18 Arrival time distributions of SM neutrinos from true (left) and reconstructed variables (right).

SBND employs a similar detector technology to MicroBooNE. Moreover, Chapter 7 details the excellent timing performance of the SBND data acquisition and the preparation that already took place to achieve a better timing resolution. Particularly, the SPEC-TDC device, as discussed in Section 7.1.2, records important timing information of triggers and beam arrivals that can only improve downstream reconstruction once incorporated.

For modelling the background using true variables under these assumptions, only SM neutrinos are considered and not cosmics for simplicity. The true arrival time distribution of SM neutrinos was smeared with the two assumptions. Fig. 9.19 shows the true, smeared true and the reconstructed distribution after selection, normalised to the same area for direct comparison. The left figure shows the true distribution without any smearing applied with a width of 1.37 ns. The middle figure shows the smeared true distribution with the assumed width of 1.73 ns. The right figure shows the reconstructed distribution after applying the lenient selection with a width of 1.99 ns.

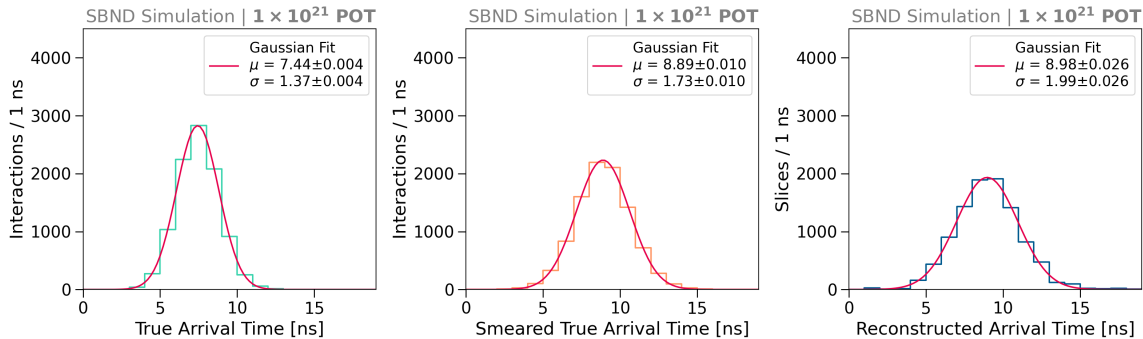


Fig. 9.19 Arrival time distributions of SM neutrinos from true (left), smeared true (middle) and reconstructed variables after the lenient selection (right).

It is important to note the difference between the reconstructed arrival time before and after selection such that the distribution after selection has a less shifted Gaussian mean and a smaller Gaussian width. It was observed in this work that different topologies have different timing reconstruction resolutions that result in slightly different Gaussian shapes. This might lead to cuts having non-uniform effects on the arrival time distribution.

For modelling the signal, the same smearing assumptions are applied to the true arrival time distribution of HNLs. Unlike the background modelling approach of normalising the same area, an efficiency of 30% was applied to the true distribution to account for the combined effects of reconstruction and selection. Fig. 9.20 shows the arrival time distribution of SM neutrinos and HNLs from true, smeared true and reconstructed variables after selection for comparison. The smeared true distribution shows a higher signal-to-background

9.7 Concluding Remarks

ratio particularly for edge bins compared to the reconstructed distribution. Thus, it is also used for determining the sensitivity alongside the reconstructed distributions in order to assess the impacts of timing resolution improvement.

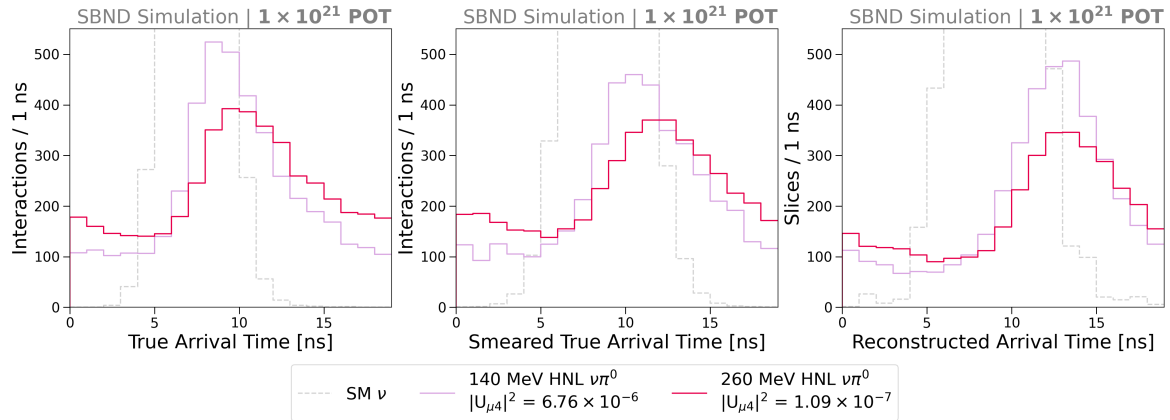


Fig. 9.20 Arrival time distributions of SM neutrinos and HNLs from true (left), smeared true (middle) and reconstructed variables after the lenient selection (right).

9.7 Concluding Remarks

The selection of HNLs using MC samples is provided in this chapter, as a procedure to identify HNL signals from SM neutrino and cosmic backgrounds. The selection exploits the highly energetic and forward-going features of HNL showers to achieve an excellent background rejection without compromising signal efficiency. One of the strongest separation variables is reconstructed energies using charge and light information. As HNL showers are forward-going, they tend to be reconstructed as a single shower merged from multiple showers, resulting in higher reconstructed energies. Another useful variable is the shower angle to the beam direction as HNL showers are very beam-collimated. These two key variables provide some guidelines for future work on improving shower reconstruction, specifically on shower energies and topologies.

Two selection procedures on reconstructed variables are presented, the lenient and stringent cut, with the stringent rejecting backgrounds more aggressively than the lenient. For both approaches, the resulting background efficiency is $\mathcal{O}(10^{-4})$ while the signal selection efficiency still maintains at $\sim 30\%$. When considering only bins at the edge of the arrival time distribution, or the so-called *timing cut*, the background efficiency decreases significantly by two orders of magnitude to $\mathcal{O}(10^{-6})$. Meanwhile, the signal efficiency

only decreases from $\sim 30\%$ to $\sim 10\%$. This demonstrates that these edge bins contain an exceptional signal-to-background ratio, which is the main factor driving the sensitivity.

Furthermore, a study was motivated to explore the impact on sensitivity if a better timing reconstruction is achieved. The study resulted in a arrival time distribution acquired by smearing true variables, assuming it is reconstructed with an improved timing resolution of 1.73 ns compared to the current $\mathcal{O}(2 \text{ ns})$. All three arrival time distributions, from both the lenient and stringent cut on reconstructed variables and from the smeared true variables, are used for studying the sensitivity to HNLs in Chapter 10 next.

Chapter 10

Limits Predictions for Heavy Neutral Leptons at SBND

After the selection performed on Monte Carlo (MC) samples, the analysis continues with assessing and propagating uncertainties. This is a critical step which includes an evaluation of statistical fluctuations due to the size of the MC samples as well as uncertainties due to the simulated physics models of the Booster Neutrino Beam (BNB) flux, Standard Model (SM) neutrinos and the Short-Baseline Near Detector (SBND). Following this, the sensitivity of SBND to Heavy Neutral Leptons (HNLs) is determined by setting an upper limits on the coupling $|U_{\mu 4}|^2$ of HNLs, under the assumption of no detected signals to allow for direct comparison with existing limits. The limits setting is performed using the likelihood-based hypothesis testing for exclusion limits [8]. The arrival time distribution with fully propagated uncertainties is the input of the limits setting, which exploits the exceptionally high signal-to-background ratio of bins at the edge of the distribution to achieve competitive limits.

The following chapter provides details of the analysis steps employing the three arrival time distributions after the selection. This includes two acquired from the lenient and stringent selection performed on reconstructed variables and a third acquired by smearing true variables under the assumption of an improved timing resolution as previously discussed in Chapter 9. Section 10.1 outlines the assessment of statistical as well as systematics uncertainties. Following that, Section 10.2 delves into the limits setting procedure. Results of the upper limits on the coupling $|U_{\mu 4}|^2$ of HNLs are presented in Section 10.3. Finally, Section 10.4 concludes the chapter with some remarks.

10.1 Uncertainty Assessment

Since many physics measurements to be made by SBND will heavily rely on comparing data and MC samples, it is vitally important to understand the input physics models used to simulate MC samples. As previously discussed in Chapter 4 describing the detector and Chapter 5 detailing the simulation framework, many different theoretical as well as data-driven models are used to predict the incoming fluxes from the BNB, the SM neutrino interaction cross sections and the detector responses. Each model has its own uncertainty, of which the uncertainty needs to be propagated to the final physics result.

The assessment of statistical and systematics uncertainties is presented in this section. Section 10.1.1 details the reweighting method to assess uncertainties of the BNB flux and SM neutrino predictions. Following this, the error propagation is given in Section 10.1.2. Sections 10.1.3 and 10.1.4 provide a description of uncertainties of the HNL signal and SM neutrino and cosmic backgrounds respectively.

10.1.1 The Reweighting Method

The impact of systematics uncertainties on a physics measurement can be assessed by simulating and reconstructing a number of different samples, referred to as *universes*, each with a physics parameter being varied within its uncertainty range. The physics measurement is then performed in each universe in the same manner as done on the Central Value (CV) sample that does not have any parameters varied. The variation of the results across universes compared to the CV sample describes the uncertainty that the varied parameter has on the measurement.

However, since fully simulating and reconstructing a large MC sample for multiple systematics parameters can be computationally intensive, the *reweighting* technique is used instead by producing a weight associated with the varied parameter per universe. The weight can be applied to smear the physics result by an amount as expected by the varied parameter. Or vice versa, the smeared physics result can be unweighted to recover the original result without any uncertainties from the varied parameter [138].

The reweighting technique begins with transforming a physics parameter x to x' as:

$$x' = x \cdot f(x), \quad (10.1)$$

10.1 Uncertainty Assessment

where $f(x)$ describes a transformation function of x . If $f(x) = 1$, then x' is equal to the unweighted x . A common form of the transformation function is a Gaussian function, where the physics parameter x is thrown to x' by randomly sampling from a unit Gaussian with its mean and width set as 1. Another common formalism is the Delta function, where x' can take only the value of 0 or 1. Each value of x determines the probability $P(x)$ describing an outcome of physics measurements.

The weight w describing whether the probability $P(x')$ is more or less likely to occur given the transformed parameter x' compared to the CV parameter x is computed as:

$$w = \frac{P(x')}{P(x)}. \quad (10.2)$$

The distribution of w therefore describes the Probability Density Function (PDF) of the parameter x . A universe associated with a weight w represents an outcome sampled from the PDF. Moreover, the weight example shown in Eq. 10.2 is associated with a single physics parameter x that is uncorrelated to any other parameters. A weight associated with multiple correlated parameters can also be computed in the same manner.

The reweighting framework provides a quick way to compute PDFs, allowing for the assessment of the impact of systematics uncertainties without the computational expense of simulating and reconstructing the sample multiple times. A series of universes is first simulated and weights for every interaction, whether SM neutrino or HNL, and are then calculated from the PDFs for each universe. The variation of the physics results across universes is used to quantify the uncertainties of the weighted parameters on the physics measurement, of which the error propagation is given in Section 10.1.2 next.

In some cases, reweighting is not applicable such as evaluating uncertainties due to detector effects. For example, recombination, as detailed in Section 8.2, influences not only the charge and light yield but also the non-uniformity of charge deposition on wires [137]. Consequently, it is non-trivial to quantify analytically the downstream impacts due to the variation in recombination on the charge reconstruction by Pandora or any high level analysis tools using the reconstructed charge information. A full simulation and reconstruction of a single universe using the varied recombination parameter is needed to fully assess the impact on the physics measurement. This method is commonly used for assessing detector systematics uncertainties.

10.1.2 Uncertainty Propagation

The impact of uncertainties can be evaluated for a distribution of a physics measurement, of which the distribution of interest is the arrival time at the front face of SBND (See Section 9.1.4). The reweighting method results in a series of observations n of the arrival time distribution, consisting of the CV observation n^{CV} and observations n^k from a total of U universes. A covariance matrix V is constructed from these observations, describing the deviation of the value in bins i and j of the observation n^k in the universe k from the CV observation n^{CV} , averaged over U universes. The matrix is computed as:

$$V_{ij} = \frac{1}{U} \sum_k^U (n_i^k - n_i^{CV})(n_j^k - n_j^{CV}). \quad (10.3)$$

The diagonal term of the covariance matrix represents the variance in a given bin and the uncertainty σ can be derived as:

$$V_{ii} = \sigma_i^2. \quad (10.4)$$

Since there are multiple sources of uncertainties, the total covariance matrix is computed by summing the covariance matrix of each uncertainty together, effectively adding the uncertainties in quadrature as follows:

$$V_{ij}^{Total} = \sum_{Sources} V_{ij}^{Source} = V_{ij}^{Stat} + V_{ij}^{Flux} + V_{ij}^{Cross Section} + \dots \quad (10.5)$$

The total uncertainty is computed from the total covariance matrix V_{ij} using Eq. 10.4.

Additionally, the fractional covariance matrix describing the relative uncertainty in each bin is computed as:

$$V_{ij}^{Frac} = \frac{V_{ij}}{n_i^{CV} n_j^{CV}}, \quad (10.6)$$

which allows for a direct comparison of uncertainty across signals and backgrounds.

10.1.3 Uncertainties of Heavy Neutral Leptons

For the HNL signal, there are four primary sources of uncertainties that will affect physics measurements made by SBND: (1) statistical, (2) cosmic mistagging, (3) flux and (4) detector. The statistical uncertainty is evaluated using the number of signals selected. Meanwhile, the cosmic mistagging uncertainty is evaluated using the number of cosmic muons occurring in the same readout window of HNLs that remain after selection. The

10.1 Uncertainty Assessment

impact of the uncertainties due to flux modelling is assessed using the reweighting method. Detector systematics are not reweightable and require fully simulated and reconstructed MC sample for uncertainty assessment. At the time of writing, the SBND detector is not yet operational, and it is undetermined which detector parameters are impactful on physics measurements. Thus, detector systematics are not included in this work but should be included in future iterations.

Uncertainties discussed here were assessed using the arrival time distribution (See Section 9.1.4). The following plots show the arrival time distribution after the lenient selection, with the HNL mass of 200 MeV and normalised to the coupling $|U_{\mu 4}|^2 = 1 \times 10^{-7}$.

Statistical uncertainty indicates the statistical fluctuation of the MC sample. The uncertainty of each bin in the distribution is defined as follows:

$$\sigma_{\text{statistics}} = \sqrt{\text{Number of entries in the bin}}. \quad (10.7)$$

It was computed using the number of HNL signals remaining after the selection, binned to the arrival time distribution. The uncertainty computation was done before the normalisation to the exposure of 3 years equivalent to 1×10^{21} Protons On Target (POT). After the normalisation, the resulting statistical uncertainty is plotted in Fig. 10.1a, showing the uncertainty is minimal across the entire distribution. The fractional statistical uncertainty, as depicted by the blue line in the bottom panel of Fig. 10.2, shows that it is well-constrained under < 6%.

The cosmic mistagging uncertainty accounts for the selected cosmic muons occurring in the same readout window as HNLs. In some cases, highly energetic cosmic muons can overlap with showers from HNLs, resulting in a pile-up of charge clusters at the same location in the detector. These charges arriving at the same wires and at the same time can mislead the clustering process of Pandora during reconstruction, such that a reconstructed shower object might contain more charges from cosmic muons than HNLs. This reconstruction failure results in several cosmic muons remaining after the selection, and therefore, is considered as the cosmic mistagging uncertainty. The cosmic mistagging uncertainty is plotted in Fig. 10.1b, however, the uncertainty is so small that it is not visible in the plot. The uncertainty can be seen in the fractional format in the bottom panel of Fig. 10.1 in the gray line, demonstrating it is almost negligible at < 1%.

The flux systematics was assessed using the reweighting method. The flux prediction and the reweighting framework for assessing the uncertainties were developed by the MiniBooNE experiment and furthered by the MicroBooNE experiment [3, 139]. The frame-

Limits Predictions for Heavy Neutral Leptons at SBND

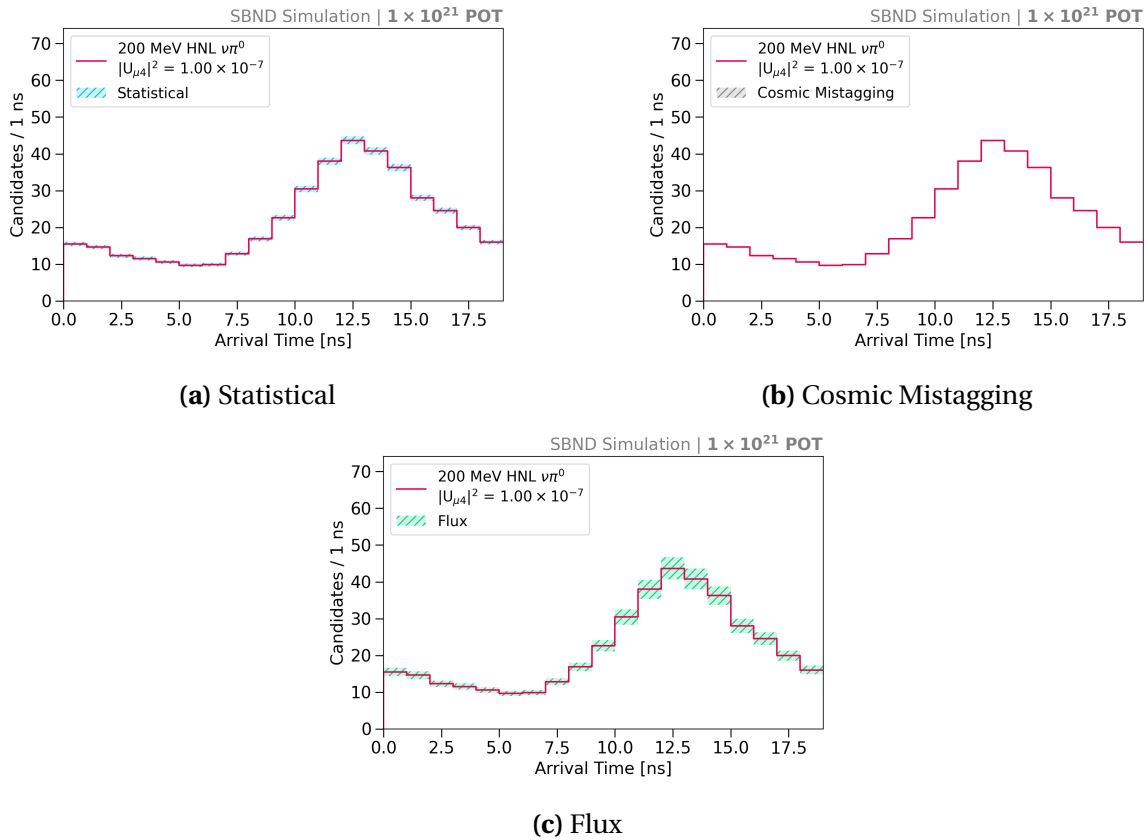


Fig. 10.1 Arrival time distributions of 200 MeV HNLs with (a) statistical, (b) cosmic mistagging and (c) flux uncertainties, normalised to the exposure of 1×10^{21} POT and $|U_{\mu 4}|^2 = 1 \times 10^{-7}$.

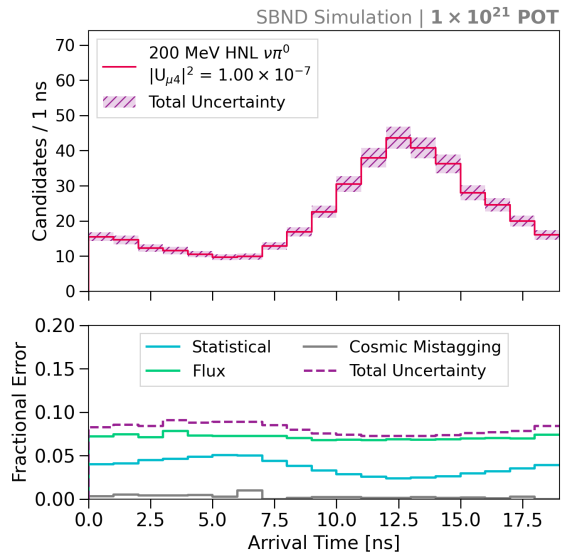


Fig. 10.2 Arrival time distribution of 200 MeV HNLs with the total uncertainty (top) and fractional uncertainties (bottom), normalised to the exposure of 1×10^{21} POT and $|U_{\mu 4}|^2 = 1 \times 10^{-7}$.

10.1 Uncertainty Assessment

work has been implemented for SBND and intended for a consistent reweighting method across the experiments in the Short-Baseline Neutrino program. The flux systematics uncertainties as defined in Ref. [3] are as follows:

- **Proton Delivery:** The proton intensity on the target of the BNB is measured using two toroids, which have an uncertainty of 2% attributed to calibration.
- **Particle Production:** The flux prediction for the number of secondary mesons produced in the BNB has an uncertainty associated with each particle type (See Section 4.3). The K^+ meson parent of HNLs has the production extrapolated from the global data of K^+ using the Feynman Scaling to the relevant BNB energy range, and is constrained by the SciBooNE's direct measurement of K^+ from the BNB.
- **Hadronic Interactions:** Hadrons produced in the Be target may interact with Be elastically or inelastically, affecting the kinematics of secondary mesons and consequently, tertiary daughter particles like HNLs and SM neutrinos. Cross section uncertainties of $p/n + \text{Be}$ and $\pi^\pm + \text{Be}$ are propagated through the flux prediction.
- **Horn Magnetic Field:** The magnetic field of the horn impacts the focusing of charged particles produced in the target. Uncertainties associated with the horn magnetic field including the current pulsed through the horn and the skin current induced on the surface of the target are computed.

Fig. 10.1c shows the combined uncertainty of all the flux systematics listed here for HNLs, where the uncertainty is consistent across every bin. The flux fractional uncertainty is plotted in green in the bottom panel of Fig. 10.2, showing that it is constrained $< 8\%$.

Finally, the top figure of Fig. 10.2 shows the total uncertainty combining the statistical, cosmic mistagging and flux uncertainties. It can be seen that the total uncertainty is evenly distributed across the arrival time distribution with little biases in any bins. The total fractional uncertainty is shown in the purple line in the bottom panel of Fig. 10.2, demonstrating that it is well-constrained $< 10\%$ across the entire distribution.

10.1.4 Uncertainties of Neutrino and Cosmic Backgrounds

For the background of SM neutrinos and cosmic muons, there are four primary sources of uncertainties: (1) statistical, (2) flux, (3) SM neutrino cross section and (4) detector. The uncertainties due to statistics and flux were computed in the same manner as the uncertainty treatment of the HNL signal. The detector systematics uncertainty is not

included but should be considered in future work. A new addition is the SM neutrino cross section uncertainty, of which the impact due to the cross section modelling is evaluated using the reweighting method. Similarly to HNLs, background uncertainties were assessed using the arrival time distribution.

The statistical uncertainty of the background was computed using Eq. 10.7, taking the number of SM neutrinos and cosmic muons remained after the selection and binned to the arrival time distribution. Fig. 10.3a shows the statistical uncertainty of the background. It can be seen that the background statistics are abundant for bins at the centre of the distribution however, limited for bins at the edge. Therefore, the statistical uncertainty is better constrained for bins at the centre, while bins at the edge have a higher statistical fluctuation. This is also visually evident in the statistical fractional uncertainty plotted in the blue line in the bottom panel of Fig. 10.4. For bins at the centre of the distribution, the statistical fractional uncertainty is constrained at < 20%. For bins at the edge of the arrival time distribution, particularly the first and last 4 bins, the statistical fractional uncertainty reaches the level about 100%.

The flux systematics of the background was measured using the reweighting method similar to HNLs. One key difference in the flux systematics is that unlike HNLs coming from only K^+ , SM neutrinos can result from π^\pm , K^\pm and K_L^0 . Particularly, the Sanford-Wang parametrisation for modelling the π^+ production introduces large biases for Neutral Current (NC) π^0 interactions [122], which is the main background contributor. The resulting flux uncertainty of the background is plotted in Fig. 10.3b and the flux fractional uncertainty is plotted in the green line in the bottom panel of Fig. 10.4. The flux fractional uncertainty is constrained < 20% and consistent across the entire arrival time distribution.

The SM neutrino cross section uncertainty was assessed using the reweighting method, with systematics of models employed by the GENIE generator provided in Ref. [113]. Fig. 10.3c shows the resulting combined uncertainty of all the SM neutrino interaction cross section systematics. Compared to statistical and flux uncertainties, the magnitude of the cross section uncertainty is significantly larger. This is due to the primary background after selection being NC π^0 , of which the cross section is not well-measured. Uncertainties associated with NC coherent and NC resonant scattering are the main contributors to this channel. Moreover, a small fraction of Charged Current (CC) ν_e interactions remains after selection and the cross section is also not well-measured. For this channel, uncertainties associated with CC quasi-elastic scattering systematics contribute the most. Finally, uncertainties for modelling hadron transport interactions are significant contributors to the cross section uncertainty.

10.1 Uncertainty Assessment

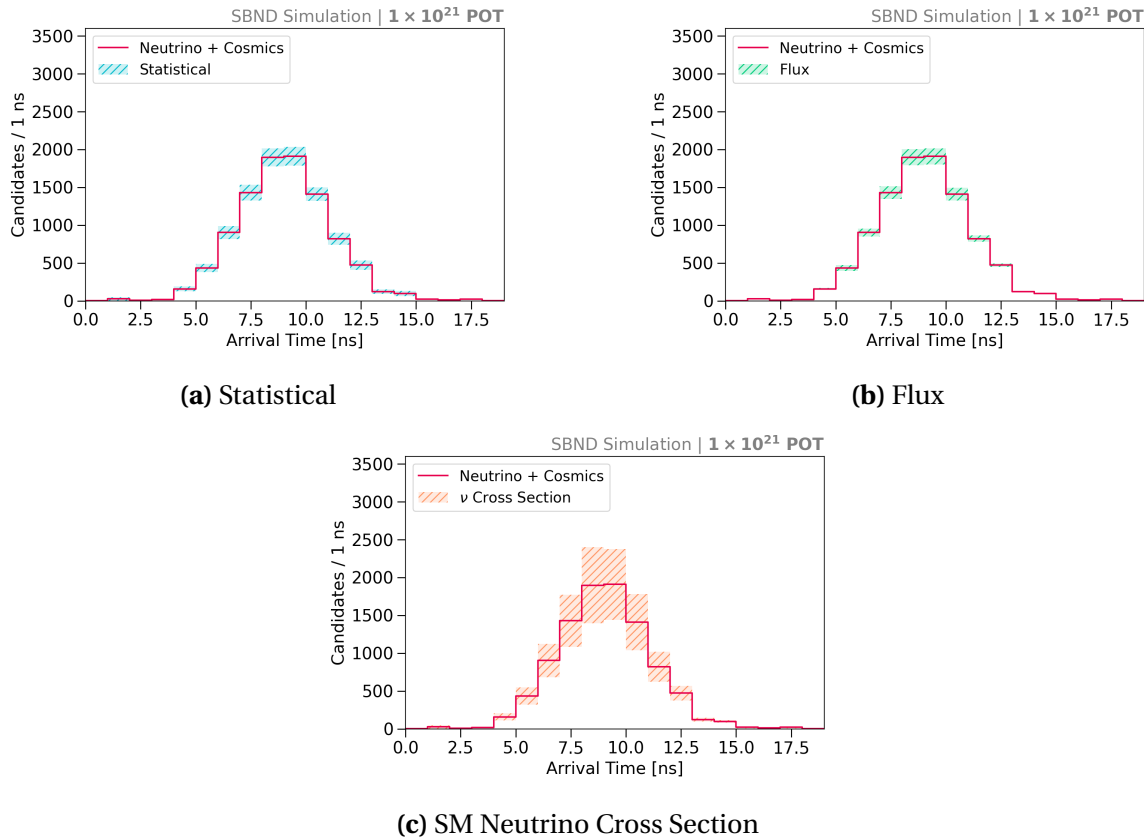


Fig. 10.3 Arrival time distributions of SM neutrino and cosmic backgrounds with (a) statistical, (b) flux and (c) SM neutrino cross section uncertainties, normalised to the exposure of 1×10^{21} POT.

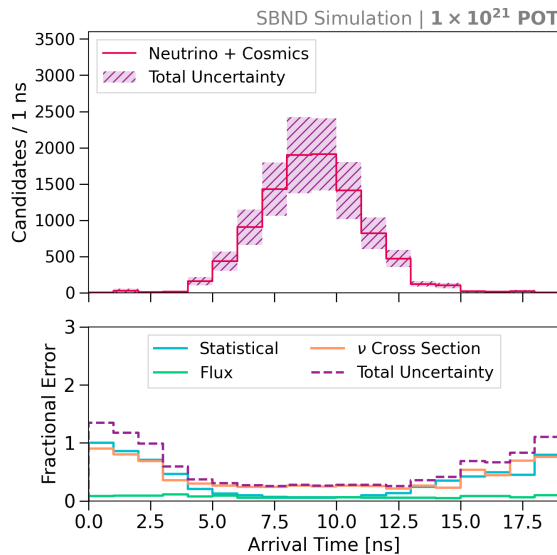


Fig. 10.4 Arrival time distributions of SM neutrino and cosmic backgrounds with the total uncertainty (top) and fractional uncertainties (bottom), normalised to the exposure of 1×10^{21} POT.

The cross section fractional uncertainty is plotted in the orange line in the bottom figure of Fig. 10.4. Bins at the centre of the arrival time distribution have the lowest cross section uncertainty in the entire distribution at < 50%. The uncertainty increases towards the bins at the edge of the distribution, reaching almost 100% for very low statistics bins.

The total fractional uncertainty combining the statistical, flux and cross section uncertainty, is plotted in purple in the bottom panel of Fig. 10.4. For bins at the edge of the distribution, which are the bins driving the limits, the total uncertainty is particularly high at > 100% due to the combined contribution from all three uncertainty sources.

10.2 Limits Setting Procedure

The sensitivity of SBND to Majorana HNLs is determined as the upper limits on the coupling $|U_{\mu 4}|^2$ of HNLs (See Chapter 2). The upper limits are set under the assumption of no detected signals so that the results can be directly compared against existing limits in the mass range 140–260 MeV, as previously summarised in Fig. 2.5 in Section 2.4. The limits setting procedure employs the likelihood-based hypothesis test [8], of which likelihood functions are constructed using the arrival time distribution of signals and backgrounds. The end-to-end procedure was performed using the `pyhf` package [7].

The section begins with the hypothesis definitions for upper limits in Section 10.2.1 and the construction of the test statistic for each hypothesis in Section 10.2.2. The CL_s method to determine p -values of test statistics is described in Section 10.2.3. Presented in Section 10.2.4 is the computation of test statistics using asymptotic approximation. Finally, an overview of the limits setting using `pyhf` is given in Section 10.2.5

10.2.1 Hypothesis Definition

The setting limit procedure employs the frequentist approach by performing hypothesis testing to quantify the level of agreement between the observed data and a given hypothesis H . To exclude a signal region, the test hypothesis H_b is defined as describing only known processes, or a background-only model. Meanwhile, the null hypothesis H_{s+b} is defined as the model including both background and signal processes.

A given hypothesis H is constructed to represent the expectation value for an observable distribution, which is chosen to be the arrival time distribution. For a series of

10.2 Limits Setting Procedure

observations n , the expectation value of the bin i can be constructed as:

$$E[n_i] = \mu s_i + b_i. \quad (10.8)$$

s_i is the number of entries from the HNL signal distribution depicted in Fig. 10.2 and b_i are the number of entries from the background distribution depicted in Fig. 10.4. The *parameter of interest* μ determines the strength of the signal process, where $\mu = 0$ corresponds to the background-only H_b hypothesis and $\mu = 1$ corresponds to the nominal signal H_{s+b} hypothesis. It is written separately from other parameters in the hypothesis.

In the HNL search, varying the parameter μ is equivalent to varying the coupling $|U_{\mu 4}|^2$. The signal rate observed at the detector is proportional to the coupling at the HNL production as well as the coupling at the HNL decay. The proportionality of the signal strength parameter to the coupling is therefore $\sqrt{\mu} \propto |U_{\mu 4}|^2$. For the HNL distribution shown in Fig. 10.2, the nominal signals strength $\mu = 1$ corresponds to $|U_{\mu 4}|^2 = 1 \times 10^{-7}$.

Other parameters in the hypothesis represent *nuisance parameters*, denoted as θ . The null and test hypotheses are formally written as:

$$\text{Null hypothesis: } H_{s+b} = H(\mu = 1, \theta), \quad (10.9)$$

$$\text{Test hypothesis: } H_b = H(\mu = 0, \theta). \quad (10.10)$$

10.2.2 Likelihood-based Test Statistic

To exclude the null hypothesis H_{s+b} at some Confidence Levels (C.L.), a test statistic is performed for a hypothesised μ against H_{s+b} and H_b . Likelihood-based functions are chosen to construct the test statistic for a multi-binned histogram. The likelihood function is the product of Poisson probabilities of all bins in the histogram [8]:

$$L(\mu, \theta) = \prod_{i=1}^N \frac{(\mu s_i + b_i)^{n_i}}{n_i!} e^{-(\mu s_i + b_i)} \prod_{\theta \in \Theta} c_\theta(a_\theta | \theta). \quad (10.11)$$

The first product describes the likelihood of the distribution n with bin i , which is constructed using the arrival time distribution of HNLs as signals and SM neutrinos with cosmics as backgrounds as described in Eq. 10.8. The second product is a function of constrained parameters Θ , containing constraint term $c_\theta(a_\theta | \theta)$ with measurement a_θ constraining the nuisance parameter θ . Each uncertainty of signals and backgrounds, as discussed in Section 10.1, corresponds to a constraint term.

For a hypothesised value of μ , the profile likelihood ratio can be constructed from the likelihood function as [8]:

$$\lambda(\mu) = \frac{L(\mu, \hat{\theta}(\mu))}{L(\hat{\mu}, \hat{\theta})}. \quad (10.12)$$

The numerator is the *conditional* likelihood, where L is maximised for a value μ being tested and $\hat{\theta}(\mu)$ is a function of μ . The denominator is the *unconditional* maximised likelihood, where $\hat{\mu}$ and $\hat{\theta} = \hat{\theta}(\hat{\mu})$ are the best fit parameters to the observed data.

A modification in the likelihood ratio is required for cases where the signal process only increases the mean event rate, such that $\mu \geq 0$. If the observed data results in the best fit $\hat{\mu} < 0$, then the best level of agreement between the data and the prediction is forced to occur at $\hat{\mu} = 0$. This is equivalent to the late arrival of HNLs relative to the SM neutrino bucket, which can only increase the event rate for bins on either side of the bucket. The profile likelihood ratio is modified as [8]:

$$\tilde{\lambda}(\mu) = \begin{cases} \frac{L(\mu, \hat{\theta}(\mu))}{L(0, \hat{\theta}(0))} & \hat{\mu} < 0, \\ \frac{L(\mu, \hat{\theta}(\mu))}{L(\hat{\mu}, \hat{\theta})} & \hat{\mu} \geq 0, \end{cases} \quad (10.13)$$

where $\hat{\theta}(0)$ is a function of $\mu = 0$.

From the modified profile likelihood ratio, the test statistic for upper limits is [8]:

$$\tilde{q}_\mu = \begin{cases} -2 \ln \tilde{\lambda}(\mu) & \hat{\mu} \leq \mu \\ 0 & \hat{\mu} > \mu \end{cases} = \begin{cases} -2 \ln \frac{L(\mu, \hat{\theta}(\mu))}{L(0, \hat{\theta}(0))} & \hat{\mu} < 0, \\ -2 \ln \frac{L(\mu, \hat{\theta}(\mu))}{L(\hat{\mu}, \hat{\theta})} & 0 \leq \hat{\mu} \leq \mu, \\ 0 & \hat{\mu} > \mu. \end{cases} \quad (10.14)$$

In the region $\hat{\mu} > \mu$, equivalent to an upward fluctuation in the data compared to the input models, the test statistic \tilde{q}_μ is set to 0. For setting an upper limit, this fluctuation does not represent less incompatibility and therefore is not taken into the rejection region of the test. The resulting value of \tilde{q}_μ indicates the level of agreement between the observed data and the prediction, where a larger value corresponds to an increasing disagreement.

The distribution $f(\tilde{q}_\mu | \mu')$ of a test statistic \tilde{q}_μ can be interpreted as a PDF. The subscript of \tilde{q} refers to the value of μ being tested in the numerator of the likelihood ratio in Eq. 10.12. The second argument μ' refers to the value of μ being assumed in the denominator of Eq. 10.12. For setting an upper limit with hypotheses testing, the PDF of interest is \tilde{q}_μ under the assumption of a different strength parameter $\mu' \neq \mu$. Therefore, the corresponding

PDFs for a test signal strength μ , under the assumption of the null hypothesis H_{s+b} and the test hypothesis H_b , are respectively as:

$$f(\tilde{q}_\mu|s+b) = f(\tilde{q}_\mu|\mu' = 1), \quad (10.15)$$

$$f(\tilde{q}_\mu|b) = f(\tilde{q}_\mu|\mu' = 0). \quad (10.16)$$

10.2.3 The CL_s Method

To quantify the level of significance of a test statistic, a p -value is computed as an integration of the PDF $f(\tilde{q}_\mu|\mu')$ on either side of $\hat{q} = \tilde{q}_\mu(\mu = \hat{\mu})$, where \hat{q} is the test statistic value from the observed data. Typically, the p -value resulting from a right-sided integration is used to exclude the null hypothesis. This represents the probability of finding data more background-like assuming that the signal is true.

However, this approach does not factor in the probability of finding data under the assumption of the background-only hypothesis. In scenarios where the test statistic is not sensitive to the prediction models, the PDFs of the H_{s+b} and H_b hypotheses would greatly overlap each other. One might make the mistake of interpreting having observed data highly contaminated with backgrounds as a statement on the signal hypothesis [10]. The CL_s method addresses this issue by introducing a modified p -value, to include a penalty accounting for the sensitivity of the test statistic is to the models.

The CL_s method defines the p -values of the hypotheses H_{s+b} and H_b as follows [8–10]:

$$p_{s+b} = \int_{\hat{q}}^{\infty} f(\tilde{q}_\mu|s+b) d\tilde{q}_\mu, \quad (10.17)$$

$$p_b = \int_{-\infty}^{\hat{q}} f(\tilde{q}_\mu|b) d\tilde{q}_\mu. \quad (10.18)$$

p_{s+b} represents the probability of finding data more background-like under the assumption of the signal+background hypothesis H_{s+b} and p_b represents the probability of finding data more signal-like under the assumption of the background-only hypothesis H_b . The modified p -value is computed from the p -value for each hypothesis as [8–10]:

$$CL_s = \frac{p_{s+b}}{1 - p_b}. \quad (10.19)$$

The threshold was chosen to be 0.1, such that $CL_s < (1 - 0.9)$, equivalent to setting an upper limit with at a C.L. of 90%. This level was motivated in order to compare against existing experiment results.

10.2.4 Computing Test Statistic Distributions

One method to calculate the test statistic \tilde{q}_μ and its PDF is by asymptotic approximation. This approach assumes that $\hat{\mu}$ follows a Gaussian distribution around a mean of μ' with a standard deviation of σ . Via the pyhf package, PDFs are computed according to the formulae provided by Ref. [8]. To determine $CL_s < 0.1$, pyhf scans over a range of μ and the best value is calculated using interpolation.

For a study using MC samples without having the observed data to determine \hat{q} , one can consider the distribution under the assumption of the background-only hypothesis H_b . In this case, $\hat{q} = \hat{q}_{expected}$ represents the *expectation* given the model prediction and is taken as the median of the H_b test statistic distribution, equivalent to assuming the observed data is the same as the background-only model.

Fig. 10.5 shows an example PDF of \tilde{q}_μ computed using the asymptotic approximation. The expected $\hat{q}_{expected}$ is plotted as the dashed red line. The median p -values under the H_{s+b} and H_b hypotheses are plotted as shaded green and yellow areas respectively. The test signal strength μ shown here gives $CL_s < 0.1$. Standard deviations of the CL_s can also be computed by substituting μ' with $\mu' \pm N\sigma$, where $N\sigma$ is the number of standard deviations away from the mean μ' .

10.2.5 Setting the Upper Limits

The setting limit procedure was performed fully using the pyhf package, with the test statistic described in the previous section. The arrival time distributions were input into

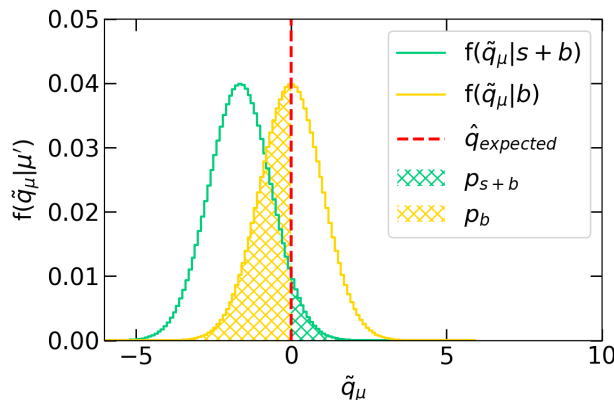


Fig. 10.5 Example of \tilde{q}_μ distributions using the asymptotic approximation.

10.2 Limits Setting Procedure

the pyhf package to infer the upper limit at a C.L. of 90%. The distributions input to the background-only H_b and the signal+background H_{s+b} hypotheses are as following:

- H_b : The SM neutrinos and cosmic arrival time distribution.
- H_{s+b} : The HNL arrival time distribution on top of the background distribution.

These distributions are the ingredients for the first product in Eq. 10.11. Since the likelihood functions are products of individual bins of the distributions, one can reduce the computing time by considering only high signal-to-noise bins that contribute the most to the limits. As previously stated as the timing cut (See Section 9.5), the relevant high signal-to-noise bins are the first and last 4 bins of the arrival time distribution, which lead to the same result to be demonstrated later.

Three arrival time distributions were used in the limits setting. Appendix D and E contain the arrival time distributions for signals and backgrounds after the lenient and stringent cut respectively (See Section 9.5), with all uncertainties propagated (See Section 10.1). Additionally, Appendix F contains the smeared true distributions under the assumption of a timing reconstruction improvement (See Section 9.6).

The uncertainties of the arrival time distribution discussed in Section 10.1 are the constraints on the nuisance parameters $c_\theta(a_\theta|\theta)$ in the second product Eq. 10.11. Different types of constraints can take different statistical shapes, which are called *modifiers* in the pyhf package [7]. Table 10.1 summarises the uncertainties and their corresponding modifiers of the signal and background distribution.

For the HNL signal distribution, the assumption is that the signal rate is relatively low and expected to follow a Poisson distribution. Similarly, the cosmic mistagging rate falls under the same assumption since it is proportional to the signal rate. Thus, the modifier for both statistical and cosmic mistagging uncertainties of the signal distribution follows a Poisson shape, treating each bin uncorrelated. The flux uncertainty of the signal distribution uses a Gaussian-shaped modifier instead, to enable correlation bin-wise.

For the background distribution, the treatment of statistical uncertainty employs a modified version of the Beeston-Barlow method [140] to account for statistical fluctuations due to finite statistics. The modifier in this case follows a Gaussian shape for bins with high statistics and falls back to a Poisson shape for bins with low statistics while treating each bin uncorrelated. Moreover, the flux and SM neutrino cross section uncertainty also use a Gaussian-shaped modifier, however, with correlation bin-by-bin.

Table 10.1 Summary of modifiers used to constrain uncertainties.

	Uncertainty	Modifier	Sample Correlation	Bin Correlation
Signal	Statistical	Poisson	False	False
	Cosmic mis-tagging	Poisson	False	False
	Flux	Gaussian	False	True
Background	Statistical	Gaussian	False	False
	Flux	Gaussian	False	True
	SM Neutrino Cross Section	Gaussian	False	True

For a single mass point, pyhf performs a scanning of signal strength μ until the desired μ value giving the 90% C.L. is determined. To infer from the signal strength μ to the coupling $|U_{\mu 4}|^2$, the proportionality $\sqrt{\mu} \propto |U_{\mu 4}|^2$ is employed. This process was repeated for all HNL masses to acquire the limit contour between 140 and 260 MeV.

10.3 Results

Upper limits from three different arrival time distributions are presented in this section. The first two distributions were acquired by using fully reconstructed MC samples mimicking data, of which one was applied with a lenient selection as shown in Fig. 10.6a and the other one was applied with a stringent selection as shown in Fig. 10.6b. The third distribution is the smeared true as shown in Fig. 10.6c, which was acquired by smearing *true* variables without any detection simulation and reconstruction applied. The smeared true distribution is motivated by a better timing reconstruction to resolve the beam bucket with a resolution of 1.73 ns. Unlike the reconstructed distributions with uncertainties propagated, the smeared true distribution does not contain any uncertainties for simplicity. The first and last 4 bins of every distribution are also shown to demonstrate the exceptionally high signal-to-background ratio of these bins.

10.3 Results

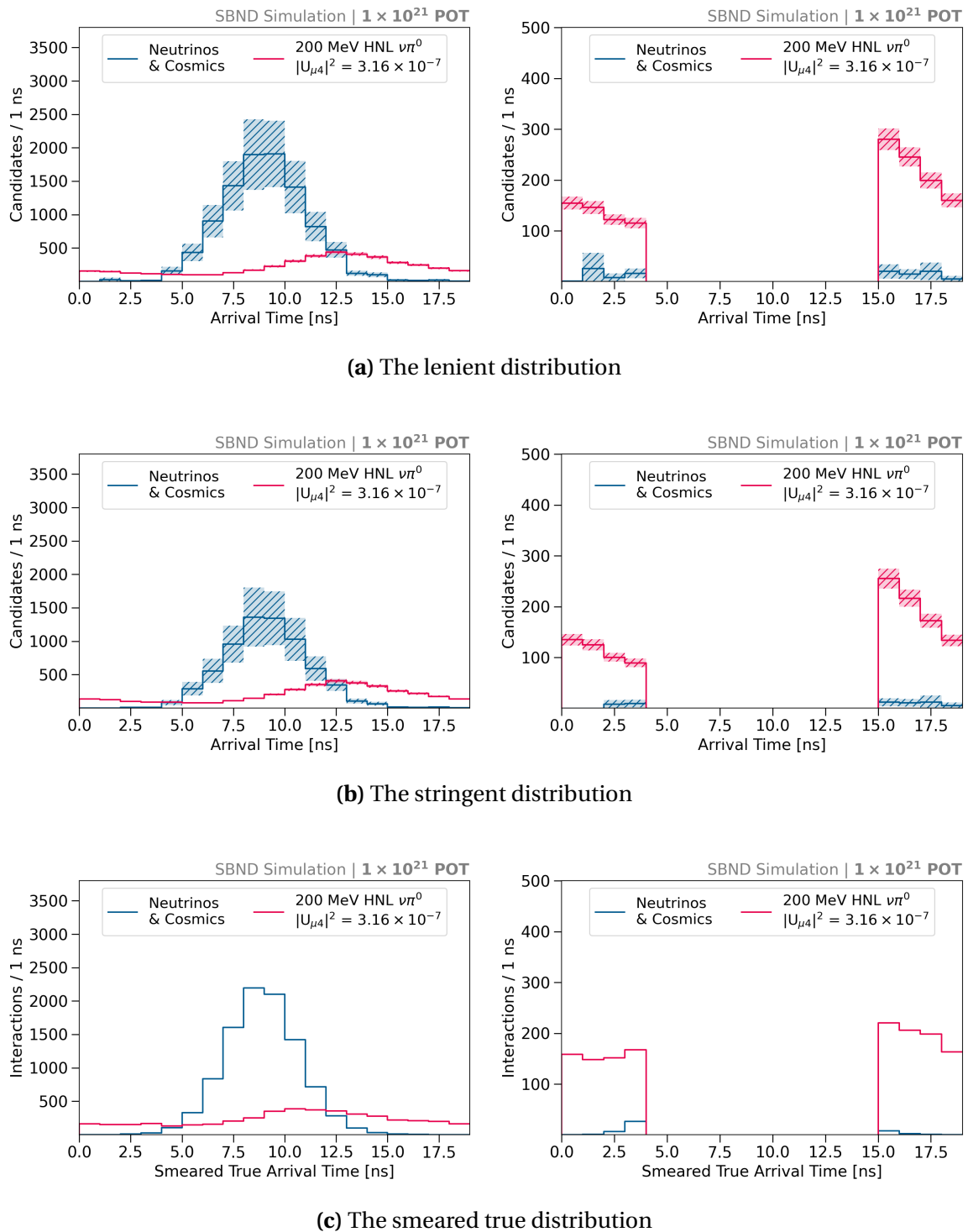


Fig. 10.6 Arrival time distributions used in the limits setting, including (a) the lenient, (b) the stringent and (c) the smeared true distribution, normalised to the exposure of 1×10^{21} POT. HNLs of mass 200 MeV is normalised to the coupling $|U_{\mu 4}|^2 = 3.16 \times 10^{-7}$.

10.3.1 Comparison Across Different Arrival Time Distributions

Expected upper limits on the coupling $|U_{\mu 4}|^2$ of Majorana HNLs at the 90% C.L. are presented in Fig. 10.7, comparing results from the arrival time distribution after the lenient and stringent selection. The expected limit is plotted as the solid black line. The deviation band at 1σ and 2σ away from the expectation, also known as the *Brazil* band, is plotted in shaded green and yellow respectively. The lenient arrival time distribution results in limits excluding the coupling $|U_{\mu 4}|^2$ at the level from 9.18×10^{-7} to 1.35×10^{-8} across the mass range from 140 to 260 MeV.

On the other hand, the stringent distribution results in more competitive limits, pushing the exclusion region of the coupling further at the level from 5.37×10^{-7} to 7.65×10^{-9} at the same mass range. This is due to the stringent distribution having a better signal-to-background ratio for bins at the edge of the distribution. This is evident when comparing between Fig. 10.6a and 10.6b, where the signal rate is very similar across the two distributions but the background rate is much lower in the stringent than the lenient distribution. Particularly, the first two bins of the stringent distribution are background-free, thus, driving the limits significantly.

However, the width of the Brazil band of the stringent result is larger than the lenient result, indicating that the stringent result has larger uncertainties. This is likely due to the limited statistics of the background MC samples after the stringent selection. As can be observed from bins at the edge of the arrival time distribution shown in Fig. 10.6b, the limited background statistics might be insufficient to describe the underlying distribution,

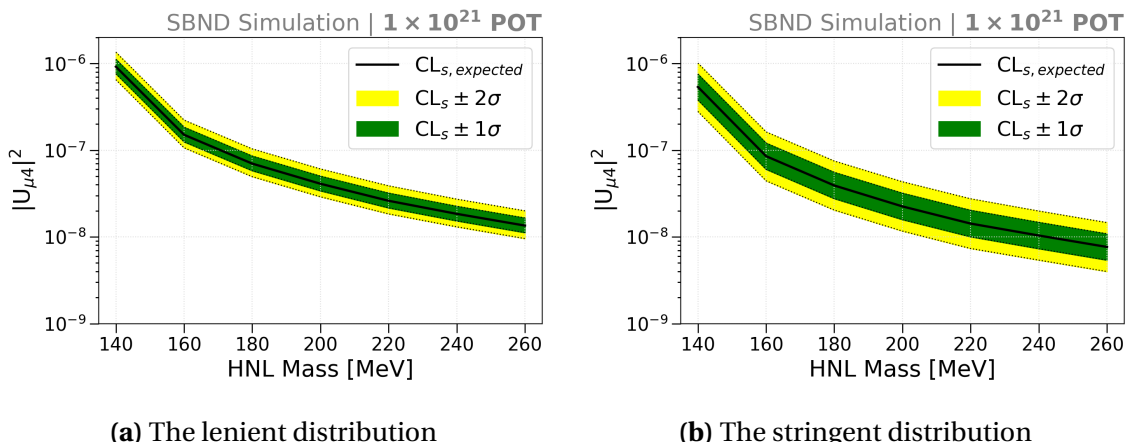


Fig. 10.7 Expected limits and the Brazil bands on the coupling $|U_{\mu 4}|^2$ for Majorana HNLs from (a) the lenient and (b) stringent arrival time distribution.

10.3 Results

which can lead to large statistical fluctuations. Although the stringent distribution leads to a more competitive result, a future iteration of this selection is recommended to perform on larger statistics MC samples so that the statistical uncertainty can be better constrained.

Fig. 10.8 shows the comparison between limits setting using the entire distribution and only the first and last 4 bins, which are referred to as the timing cut (See Section 9.5). The expected limits are the same for both cases. The result demonstrates that the first and last 4 bins are the highest signal-to-background ratio bins of the entire distribution, and therefore are the main contributor to the limits. This provides a useful insight for future iterations of this analysis indicating the region on the arrival time distribution should be focused on when performing the selection. A recommendation is to focus on optimising the signal-to-background only in the edge region. Another recommendation is to develop different selections for different regions of the arrival time distribution, capitalising on their different signal-to-background ratios.

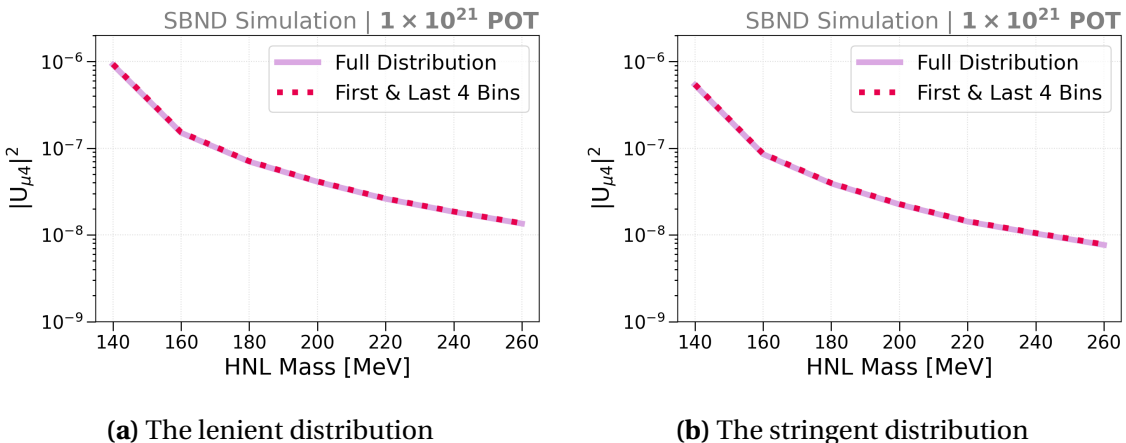


Fig. 10.8 Comparison between limits setting using the entire distribution and only the edge bins of (a) the lenient and (b) stringent arrival time distribution.

Fig. 10.9 shows the upper limits from all three arrival time distributions. The result from the smeared true distribution, as shown by the green line, is significantly more competitive than the results using reconstructed distributions, as shown by the red and blue lines. Limits from the smeared true distribution range from the level of 1.81×10^{-7} to 2.46×10^{-9} across the mass range of 140 - 260 MeV. As detailed in Section 9.6, the smeared true distribution was produced under the assumption of an improved timing resolution to explore its impact on sensitivity. The smeared true arrival time distribution of backgrounds has a Gaussian width of 1.73 ns as compared to 1.99 ns of the lenient/stringent distribution. The impact of the timing resolution improvement is evident in Fig. 10.6c, where the background rate is lower and the signal rate is significantly higher for edge bins of the

smeared true distribution. The exceptionally high signal-to-background ratios of the edge bins therefore drives the limits more aggressively.

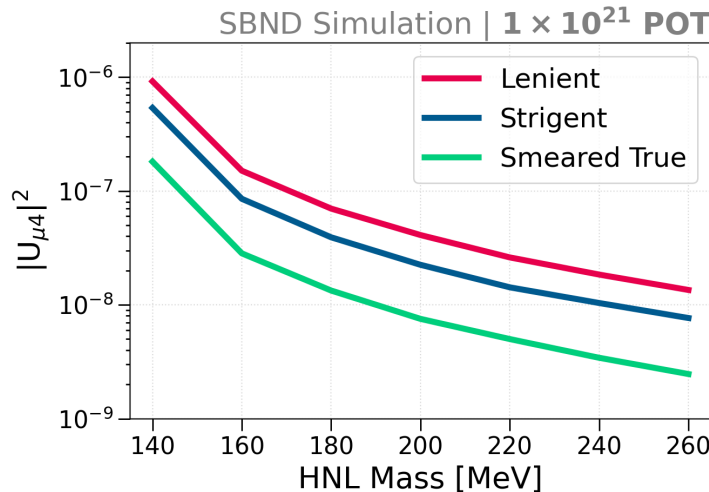


Fig. 10.9 Comparison between limits resulting from the lenient and stringent reconstructed distributions and the smeared true arrival time distribution.

This presents a positive outlook as an area for improvement for SBND to achieve more competitive results in the search for HNLs. Particularly, this can be done with a more sophisticated timing reconstruction that can resolve the beam bucket with higher resolution < 2 ns. The expected upper limits at the 90% C.L. and the Brazil bands acquired from the three arrival time distributions are summarised below in Table 10.2.

10.3.2 Comparison With Other Experiments

Fig. 10.10 shows the expected upper limits of SBND on the coupling $|U_{\mu 4}|^2$ of Majorana HNLs, comparing against existing experimental results as previously discussed in Section 2.4. All limits presented here are at the 90% C.L.

For the limits acquired from the lenient and stringent distributions, as shown by the solid red and blue line respectively, they are comparable to existing limits. The lenient limit is almost the same as the limit achieved by the MicroBooNE experiment [43–45], as shown by the solid light blue line. On the other hand, the stringent limit is slightly more competitive than MicroBooNe, excluding a new region of the coupling in the mass range < 200 MeV. However, in the mass range > 200 MeV, the phase space is already excluded by the E949 [35] and NA62 experiments [36, 37], as shown by the dashed pink and orange lines.

10.3 Results

Table 10.2 Summary of expected limits on the coupling $|U_{\mu 4}|^2$ of Majorana HNLs at the C.L. of 90% predicted for SBND.

	Mass [MeV]	Expected Limit	+1 σ	-1 σ	+2 σ	-2 σ
Lenient	140	9.18×10^{-7}	1.12×10^{-6}	7.62×10^{-7}	1.35×10^{-6}	6.51×10^{-7}
	160	1.51×10^{-7}	1.84×10^{-7}	1.25×10^{-7}	2.22×10^{-7}	1.07×10^{-7}
	180	7.00×10^{-8}	8.57×10^{-8}	5.80×10^{-8}	1.04×10^{-7}	4.95×10^{-8}
	200	4.10×10^{-8}	5.02×10^{-8}	3.40×10^{-8}	6.08×10^{-8}	2.90×10^{-8}
	220	2.61×10^{-8}	3.20×10^{-8}	2.16×10^{-8}	3.88×10^{-8}	1.84×10^{-8}
	240	1.84×10^{-8}	2.26×10^{-8}	1.53×10^{-8}	2.73×10^{-8}	1.30×10^{-8}
	260	1.35×10^{-8}	1.65×10^{-8}	1.12×10^{-8}	2.00×10^{-8}	9.55×10^{-9}
Stringent	140	5.37×10^{-7}	7.56×10^{-7}	3.80×10^{-7}	1.01×10^{-6}	2.80×10^{-7}
	160	8.53×10^{-8}	1.21×10^{-7}	6.02×10^{-8}	1.63×10^{-7}	4.43×10^{-8}
	180	3.92×10^{-8}	5.56×10^{-8}	2.76×10^{-8}	7.50×10^{-8}	2.04×10^{-8}
	200	2.25×10^{-8}	3.20×10^{-8}	1.58×10^{-8}	4.32×10^{-8}	1.17×10^{-8}
	220	1.42×10^{-8}	2.03×10^{-8}	1.00×10^{-8}	2.75×10^{-8}	7.34×10^{-9}
	240	1.04×10^{-8}	1.47×10^{-8}	7.31×10^{-9}	1.99×10^{-8}	5.39×10^{-9}
	260	7.65×10^{-9}	1.09×10^{-8}	5.39×10^{-9}	1.46×10^{-8}	3.98×10^{-9}
Smeared True	140	1.81×10^{-7}	2.45×10^{-7}	1.35×10^{-7}	3.21×10^{-7}	1.05×10^{-7}
	160	2.83×10^{-8}	3.84×10^{-8}	2.11×10^{-8}	5.05×10^{-8}	1.63×10^{-8}
	180	1.33×10^{-8}	1.81×10^{-8}	9.94×10^{-9}	2.38×10^{-8}	7.70×10^{-9}
	200	7.52×10^{-9}	1.02×10^{-8}	5.62×10^{-9}	1.34×10^{-8}	4.38×10^{-9}
	220	5.00×10^{-9}	6.78×10^{-9}	3.73×10^{-9}	8.90×10^{-9}	2.90×10^{-9}
	240	3.42×10^{-9}	4.65×10^{-9}	2.55×10^{-9}	6.10×10^{-9}	1.99×10^{-9}
	260	2.46×10^{-9}	3.34×10^{-9}	1.84×10^{-9}	4.39×10^{-9}	1.44×10^{-9}

These two limits feature the first benchmark of SBND in the HNL regime as compared to other experiments, given the current detector and reconstruction capabilities.

The limits acquired from the smeared true distribution, as shown by the green line, is the most competitive out of the three limits presented here. The limits are projected to exclude a new region beyond the existing limits from the MicroBooNE, E949 and NA62 experiments. This demonstrates the potential of the physics capability of SBND, under the assumption of an exposure of 1×10^{21} POT and an exceptional timing reconstruction with a resolution of 1.73 ns. The POT exposure presented here is equivalent to 3 years of physics data taking, which allows for a lot of time and opportunities to work on improving the timing reconstruction of SBND to achieve the target resolution from the time of writing. In comparison to the future DUNE experiment [26], DUNE is projected to have statistics to set upper limits surpassing SBND and nearly all existing limits in this mass range.

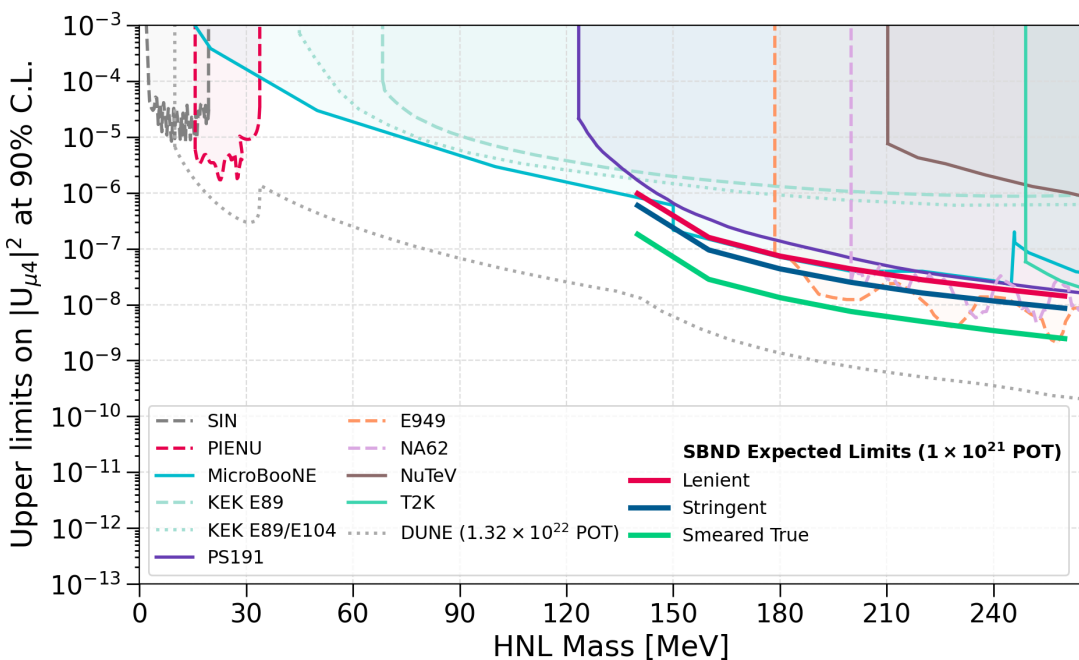


Fig. 10.10 Upper limits on the coupling $|U_{\mu 4}|^2$ at the 90% confidence level for Majorana HNLs in the mass range of $0 < m_N < 265$ MeV. SBND expected limits are compared with existing experimental results, including SIN [30], PIENU [31], MicroBooNE [43–45], KEK E89 [33], KEK E89/E104 [34], PS191 [40], E949 [35], NA62 [37], NuTeV [41], T2K [42] and expected results from DUNE [26].

10.4 Concluding Remarks

Three expected upper limits on the coupling $|U_{\mu 4}|^2$ of Majorana HNLs are presented in this chapter to demonstrate the range of the physics capability of SBND. The limits from the lenient and stringent arrival time distribution demonstrate the current performance of SBND, which is currently comparable to existing experimental limits. The limits from the smeared true distribution are the most competitive that can probe region not yet explored by other experiments. These limits also demonstrate the potential that SBND can achieve if the timing reconstruction is improved with a better resolution.

The first iteration of this analysis provides some guidelines applicable to future work in the next couple of years to further the search for HNLs at SBND. Detector systematics should be included in uncertainty propagation, with parameters that are impactful to physics measurements identified when SBND is operational. Secondly, due to the aggressive background rejection, the analysis should be performed on larger background MC samples, $\mathcal{O}(10^6)$ events compared to the present $\mathcal{O}(10^5)$ events, to avoid statistical fluctuations. Moreover, improving the shower reconstructions will enable better identification of the boosted features of HNL showers, including high energy profiles and forward-going angles. Finally, developing a more sophisticated method incorporating the extra timing information of beam arrival and trigger signals can further improve the resolution of the timing reconstruction. These improvements will benefit not only the HNL analysis but any other analysis that exploits the Gaussian tails of the beam bucket to either look for a new signal or reject cosmic backgrounds.

Chapter 11

Conclusions

This thesis presents the first assessment of the physics capabilities of the Short-Baseline Near Detector (SBND) to search for Heavy Neutral Leptons (HNLs) in the mass range of 140–260 MeV. This right-handed heavy neutrino state is motivated to provide a mechanism to generate mass for the left-handed SM neutrinos. HNLs can be produced from the Booster Neutrino Beam (BNB) from meson decays and subsequently decay into SM observables inside SBND. Due to having relatively large masses, the two exploitable features of HNLs are their boosted topologies and late arrival compared to SM neutrinos. Particularly, the late arrival of HNLs can be observed as an excess in the tails of the Gaussian-shaped neutrino beam bucket. The bucket structure can be reconstructed using the arrival time with a resolution $\mathcal{O}(2 \text{ ns})$ from PMT signals, as part of the Photon Detection System (PDS).

Towards this goal of achieving nanosecond resolution, the timing performance of readout electronics in the Data Acquisition (DAQ) was evaluated. An overview of the White Rabbit timing system was given, including the description of the SPEC-TDC as a precise timestamping device with a resolution of 700 ps to record important signals, including beam arrivals and triggers. This additional timing information enables many high precision physics analyses. For instance, the SPEC-TDC was used to perform the timing characterisation of the readout electronics of the Cosmic Ray Taggers (CRTs), of which their clock resolutions were determined to be $\mathcal{O}(2 \text{ ns})$. Moreover, the SPEC-TDC was used to assess the timing synchronisation of the readout electronics of the PDS. This resulted in a clock scheme and a correction method to synchronise multiple digitisers, which are vitally important since PMT signals are the ingredients for the timing reconstruction.

Two selection workflows were additionally developed to identify di-photon showers resulting from HNLs while rejecting backgrounds from SM neutrinos and cosmic muons. One selection is more lenient while the other is more stringent in rejecting backgrounds more aggressively. Both selections result in a background efficiency of the same magnitude $\mathcal{O}(10^{-4})$ while still maintaining the signal efficiency at $\sim 30\%$. If only bins at the edge of the arrival time distribution are considered, equivalent to the so-called *timing cut*, the background efficiency decreases by two orders of magnitude to $\mathcal{O}(10^{-6})$ while the signal efficiency only reduces to 10%. The timing cut demonstrates the importance of the edge bins having an exceptionally high signal-to-background ratio, which is the driving factor for a competitive sensitivity. This motivates an assessment of the detector performance under the assumption of an improved in timing reconstruction, resulting in an additional arrival time distribution by smearing true variables.

Building upon the selection previously discussed, setting upper limits on the coupling $|U_{\mu 4}|^2$ of HNLs at the confidence level of 90% was performed on three sets of arrival time distributions after selection on MC samples: (1) lenient, (2) stringent and (3) smeared truth. It was found that the stringent distribution results in a more competitive limit than the lenient distribution due to having background-free bins, however, the stringent limit suffers large statistical fluctuations. These two limits were found to probe the phase space already explored by the MicroBooNE [43–45], NA62 [36, 37] and E949 [35] experiments. However, they are the first benchmark of the current physics capability of SBND in the search for HNLs. Moreover, it was demonstrated that the edge bins of the distribution are the key bins that drive the upper limits. The smeared true distribution led to the most competitive limits out of the three, surpassing existing results from other experiments.

The first iteration of searching for HNLs at SBND identifies areas for improvements to be taken as the next steps. The most important focus should be on improving reconstructing timing and showers. The results of the smeared true distribution motivate the need for a resolution improvement when reconstructing the arrival time distribution. This can be achieved by developing a more sophisticated timing reconstruction method as well as incorporating timing information of beam and trigger arrivals recorded by the SPEC-TDC as presented in Chapter 7. Moreover, as discussed in Chapter 9, improving the reconstruction of shower topology and energy will help identify the boosted features of showers resulting from HNLs. These improvements will not only be beneficial towards the HNL search but many other analyses at SBND. For example, the timing improvement is applicable for analyses examining the Gaussian tails of the beam bucket, either to look for a new signal or to reject cosmic backgrounds. On the other hand, the shower improvement

is useful to any analyses containing showers in the final states. These goals are certainly within reach in the next three years of operation for SBND.

The search for HNLs at SBND will help improve the sensitivity of HNLs in the mass region of tens to hundreds MeV, with an expected time scale of 2024-2027. In the near future, the landscape of the coupling $|U_{\mu 4}|^2$ illustrated in Fig. 10.10 will expect minimal changes until the DUNE experiment comes online in the 2030s-2040s [19, 26]. For the projected 12 years of operation, the 1.32×10^{22} POT collected by DUNE will provide immense statistics to set competitive upper limits extending beyond existing results in this mass range. In the case where a discovery of HNLs is made, this will lead to the next steps to understand the properties of HNLs. Particularly, for neutrino beam experiments like SBND and DUNE, being able to detect and identify the final states of HNLs can help determine the possibility of lepton number violation and thus, the Dirac and Majorana nature of HNLs. Their existence can provide solutions to outstanding questions in particle physics, including the mass mechanism of neutrinos, the nature of dark matter and the observed matter-antimatter asymmetry.

References

- [1] P. A. Machado et al., “The Short-Baseline Neutrino Program at Fermilab”, *Annu. Rev. Nucl. Part. Sci.* **69**, 363–387 (2019).
- [2] R. Acciarri et al. (SBND), “Construction of precision wire readout planes for the Short-Baseline Near Detector (SBND)”, *JINST* **15**, P06033 (2020).
- [3] A. A. Aguilar-Arevalo et al. (MiniBooNE), “Neutrino flux prediction at MiniBooNE”, *Phys. Rev. D* **79**, 072002 (2009).
- [4] G. Cheng et al. (SciBooNE), “Measurement of K^+ production cross section by 8 GeV protons using high-energy neutrino interactions in the SciBooNE detector”, *Phys. Rev. D* **84**, 012009 (2011).
- [5] C. Adams et al., “Ionization electron signal processing in single phase LArTPCs. Part I. Algorithm Description and quantitative evaluation with MicroBooNE simulation”, *JINST* **13**, P07006 (2018).
- [6] J. S. Marshall et al., “The Pandora Software Development Kit for Pattern Recognition”, *Eur. Phys. J. C* **75**, 439 (2015).
- [7] L. Heinrich et al., “pyhf: pure-Python implementation of HistFactory statistical models”, *JOSS* **6**, 2823 (2021).
- [8] G. Cowan et al., “Asymptotic formulae for likelihood-based tests of new physics”, *Eur. Phys. J. C* **71**, 1554 (2011).
- [9] T. Junk, “Confidence level computation for combining searches with small statistics”, *Nucl. Instrum. Meth. A* **434**, 435–443 (1999).
- [10] A. L. Read, “Presentation of search results: The CL_s technique”, *J. Phys. G* **28**, 2693–2704 (2002).
- [11] M. Thomson, *Modern particle physics* (Cambridge University Press, 2013).
- [12] E. Majorana, “Teoria simmetrica dell’elettrone e del positrone”, *Nuovo Cim.* **14**, 171–184 (1937).
- [13] C. Giunti et al., *Fundamentals of Neutrino Physics and Astrophysics* (Oxford University Press, 2007).
- [14] S. F. King, “Neutrino mass models”, *Rept. Prog. Phys.* **67**, 107–158 (2004).
- [15] P. Ballett et al., “MeV-scale sterile neutrino decays at the Fermilab Short-Baseline Neutrino program”, *JHEP* **04**, 102 (2017).
- [16] A. Aguilar et al. (LSND), “Evidence for neutrino oscillations from the observation of $\bar{\nu}_e$ appearance in a $\bar{\nu}_\mu$ beam”, *Phys. Rev. D* **64**, 112007 (2001).

- [17] A. A. Aguilar-Arevalo et al. (MiniBooNE), “Significant Excess of Electronlike Events in the MiniBooNE Short-Baseline Neutrino Experiment”, Phys. Rev. Lett. **121**, 221801 (2018).
- [18] M. A. Acero et al., “White Paper on Light Sterile Neutrino Searches and Related Phenomenology”, arXiv:2203.07323 (2022).
- [19] A. M. Abdullahi et al., “The present and future status of heavy neutral leptons”, JPhysG **50**, 020501 (2023).
- [20] T. Asaka et al., “The ν MSM, dark matter and neutrino masses”, Phys. Lett. B **631**, 151–156 (2005).
- [21] T. Asaka et al., “The ν MSM, dark matter and baryon asymmetry of the universe”, Phys. Lett. B **620**, 17–26 (2005).
- [22] J. M. Berryman et al., “Searches for Decays of New Particles in the DUNE Multi-Purpose Near Detector”, JHEP **02**, 174 (2020).
- [23] A. Atre et al., “The Search for Heavy Majorana Neutrinos”, JHEP **05**, 030 (2009).
- [24] P. Coloma et al., “GeV-scale neutrinos: interactions with mesons and DUNE sensitivity”, Eur. Phys. J. C **81**, 78 (2021).
- [25] P. A. Zyla et al. (Particle Data Group), “Review of Particle Physics”, PTEP **2020**, 083C01 (2020).
- [26] P. Ballett et al., “Heavy Neutral Leptons from low-scale seesaws at the DUNE Near Detector”, JHEP **03**, 111 (2020).
- [27] O. Goodwin, “Search for Higgs Portal Scalars and Heavy Neutral Leptons Decaying in the MicroBooNE Detector”, PhD thesis (The University of Manchester, 2022).
- [28] R. Abela et al., “Search for an Admixture of Heavy Neutrino in Pion Decay”, Phys. Lett. B **105**, 263–266 (1981).
- [29] R. C. Minehart et al., “Search for Admixtures of Massive Neutrinos in the Decay $\pi^+ \rightarrow \mu^+ + \bar{\nu}$ ”, Phys. Rev. Lett. **52**, 804–807 (1984).
- [30] M. Daum et al., “Search for admixtures of massive neutrinos in the decay $\pi^+ \rightarrow \mu^+ + \nu$ ”, Phys. Rev. D **36**, 2624–2632 (1987).
- [31] A. Aguilar-Arevalo et al. (PIENU), “Search for heavy neutrinos in $\pi \rightarrow \mu\nu$ decay”, Phys. Lett. B **798**, 134980 (2019).
- [32] Y. Asano et al., “Search for a Heavy Neutrino Emitted in $K^+ \rightarrow \mu^+$ Neutrino Decay”, Phys. Lett. B **104**, 84–88 (1981).
- [33] R. S. Hayano et al., “Heavy-Neutrino Search Using $K_{\mu 2}$ Decay”, Phys. Rev. Lett. **49**, 1305–1309 (1982).
- [34] T. Yamazaki et al., “Search for Heavy Neutrinos in Kaon Decay”, Conf. Proc. C **840719**, 262 (1984).
- [35] A. V. Artamonov et al. (E949), “Search for heavy neutrinos in $K^+ \rightarrow \mu^+ \nu_H$ decays”, Phys. Rev. D **91**, 052001 (2015).
- [36] E. Cortina Gil et al. (NA62), “Search for heavy neutral lepton production in K^+ decays”, Phys. Lett. B **778**, 137–145 (2018).

References

- [37] E. Cortina Gil et al. (NA62), “Search for K^+ decays to a muon and invisible particles”, Phys. Lett. B **816**, 136259 (2021).
- [38] G. Bernardi et al., “Search for neutrino decay”, Phys. Lett. B **166**, 479–483 (1986).
- [39] G. Bernardi et al., “Further limits on heavy neutrino couplings”, Phys. Lett. B **203**, 332–334 (1988).
- [40] C. A. Argüelles et al., “Heavy neutral leptons below the kaon mass at hodoscopic neutrino detectors”, Phys. Rev. D **105**, 095006 (2022).
- [41] A. Vaitaitis et al. (NuTeV, E815), “Search for neutral heavy leptons in a high-energy neutrino beam”, Phys. Rev. Lett. **83**, 4943–4946 (1999).
- [42] K. Abe et al. (T2K), “Search for heavy neutrinos with the T2K near detector ND280”, Phys. Rev. D **100**, 052006 (2019).
- [43] P. Abratenko et al. (MicroBooNE), “Search for Heavy Neutral Leptons Decaying into Muon-Pion Pairs in the MicroBooNE Detector”, Phys. Rev. D **101**, 052001 (2020).
- [44] P. Abratenko et al. (MicroBooNE), “Search for long-lived heavy neutral leptons and Higgs portal scalars decaying in the MicroBooNE detector”, Phys. Rev. D **106**, 092006 (2022).
- [45] P. Abratenko et al. (MicroBooNE), “Search for Heavy Neutral Leptons in Electron-Positron and Neutral-Pion Final States with the MicroBooNE Detector”, Phys. Rev. Lett. **132**, 041801 (2024).
- [46] V. Hewes et al. (DUNE), “Deep Underground Neutrino Experiment (DUNE) Near Detector Conceptual Design Report”, Instruments **5**, 31 (2021).
- [47] C. Rubbia, *The liquid-argon time projection chamber: a new concept for neutrino detectors*, tech. rep., CERN-EP-INT-77-8 (1977).
- [48] J. N. Marx et al., “The Time Projection Chamber”, Phys. Today **31N10**, 46–53 (1978).
- [49] D. R. Nygren, “Origin and development of the TPC idea”, Nucl. Instrum. Meth. A **907**, 22–30 (2018).
- [50] W. J. Willis et al., “Liquid Argon Ionization Chambers as Total Absorption Detectors”, Nucl. Instrum. Meth. **120**, 221–236 (1974).
- [51] R. Acciarri et al., “Design and construction of the MicroBooNE detector”, JINST **12**, P02017 (2017).
- [52] S. Amerio et al. (ICARUS), “Design, construction and tests of the ICARUS T600 detector”, Nucl. Instrum. Meth. A **527**, 329–410 (2004).
- [53] B. Abi et al. (DUNE), “Deep Underground Neutrino Experiment (DUNE), Far Detector Technical Design Report, Volume IV: Far Detector Single-phase Technology”, JINST **15**, T08010 (2020).
- [54] R. S. Jones, “Muon-neutrino disappearance with multiple liquid argon time projection chambers in the Fermilab Booster neutrino beam”, PhD thesis (The University of Liverpool, 2021).
- [55] R. Acciarri et al. (MicroBooNE,), *A Measurement of the Attenuation of Drifting Electrons in the MicroBooNE LArTPC*, tech. rep., FERMILAB-MICROBOONE-NOTE-1026-PUB (2017).

- [56] S. Andringa et al., “Low-energy physics in neutrino LArTPCs”, JPhysG **50**, 033001 (2023).
- [57] D. E. Groom et al., “Passage of particles through matter”, Eur. Phys. J. C **15**, 163–173 (2000).
- [58] C. Anderson et al., “The ArgoNeuT detector in the NuMI low-energy beam line at Fermilab”, JINST **7**, P10019 (2012).
- [59] C. Adams et al. (MicroBooNE), “Reconstruction and measurement of $\mathcal{O}(100)$ MeV energy electromagnetic activity from $\pi_0 \rightarrow \gamma\gamma$ decays in the MicroBooNE LArTPC”, JINST **15**, P02007 (2020).
- [60] R. Acciarri et al. (MicroBooNE), “Michel Electron Reconstruction Using Cosmic-Ray Data from the MicroBooNE LArTPC”, JINST **12**, P09014 (2017).
- [61] W. Foreman et al. (LArIAT), “Calorimetry for low-energy electrons using charge and light in liquid argon”, Phys. Rev. D **101**, 012010 (2020).
- [62] A. Hitachi et al., “Effect of ionization density on the time dependence of luminescence from liquid argon and xenon”, Phys. Rev. B **27**, 5279–5285 (1983).
- [63] T. Doke et al., “Estimation of absolute photon yields in liquid argon and xenon for relativistic (1 MeV) electrons”, Nucl. Instrum. Meth. A **291**, 617–620 (1990).
- [64] T. Doke et al., “Absolute Scintillation Yields in Liquid Argon and Xenon for Various Particles”, Jap. J. Appl. Phys. **41**, 1538–1545 (2002).
- [65] R. Acciarri et al., “A study of electron recombination using highly ionizing particles in the ArgoNeuT Liquid Argon TPC”, JINST **8**, P08005 (2013).
- [66] S. Kubota et al., “Dynamical behavior of free electrons in the recombination process in liquid argon, krypton, and xenon”, Phys. Rev. B **20**, 3486–3496 (1979).
- [67] Y. Li et al., “Measurement of longitudinal electron diffusion in liquid argon”, Nucl. Instrum. Meth. A **816**, 160–170 (2016).
- [68] P. Abratenko et al. (MicroBooNE), “Measurement of the longitudinal diffusion of ionization electrons in the MicroBooNE detector”, JINST **16**, P09025 (2021).
- [69] G. Putnam et al., “Effect of diffusion on the peak value of energy loss observed in a LArTPC”, JINST **17**, P10044 (2022).
- [70] B. Abi et al., “First results on ProtoDUNE-SP liquid argon time projection chamber performance from a beam test at the CERN Neutrino Platform”, JINST **15**, P12004 (2020).
- [71] M. Antonello et al., “Study of space charge in the ICARUS T600 detector”, JINST **15**, P07001 (2020).
- [72] P. Abratenko et al. (MicroBooNE), “Measurement of space charge effects in the MicroBooNE LArTPC using cosmic muons”, JINST **15**, P12037 (2020).
- [73] P. Abratenko et al. (SBND), “Scintillation Light in SBND: Simulation, Reconstruction, and Expected Performance of the Photon Detection System”, [Eur. Phys. J. C (to be published)] (2024).
- [74] E. Grace et al., “Index of refraction, Rayleigh scattering length, and Sellmeier coefficients in solid and liquid argon and xenon”, Nucl. Instrum. Meth. A **867**, 204–208 (2017).

References

- [75] M. Babicz et al., “A measurement of the group velocity of scintillation light in liquid argon”, JINST **15**, P09009 (2020).
- [76] B. J. P. Jones et al., “A Measurement of the Absorption of Liquid Argon Scintillation Light by Dissolved Nitrogen at the Part-Per-Million Level”, JINST **8**, P07011 (2013).
- [77] B. J. P. Jones et al., “The Effects of Dissolved Methane upon Liquid Argon Scintillation Light”, JINST **8**, P12015 (2013).
- [78] J. Calvo et al. (ArDM), “Measurement of the attenuation length of argon scintillation light in the ArDM LAr TPC”, Astropart. Phys. **97**, 186–196 (2018).
- [79] P. J. Green, “Light and Dark in Liquid argon time Projection Chamber Neutrino Detectors”, PhD thesis (The University of Manchester, 2022).
- [80] E. Segreto, “Evidence of delayed light emission of tetraphenyl-butadiene excited by liquid-argon scintillation light”, Phys. Rev. C **91**, 035503 (2015).
- [81] R. Acciarri et al., “Demonstration and Comparison of Operation of Photomultiplier Tubes at Liquid Argon Temperature”, JINST **7**, P01016 (2012).
- [82] A. Gola et al., “Nuv-sensitive silicon photomultiplier technologies developed at fondazione bruno kessler”, Sensors **19**, 10.3390/s19020308 (2019).
- [83] E. Segreto et al., “First liquid argon test of the X-ARAPUCA”, JINST **15**, C05045 (2020).
- [84] E. Segreto, “Evidence of delayed light emission of TetraPhenyl Butadiene excited by liquid Argon scintillation light”, Phys. Rev. C **91**, 035503 (2015).
- [85] G. Mention et al., “Reactor antineutrino anomaly”, Phys. Rev. D **83**, 073006 (2011).
- [86] P. Huber, “Determination of antineutrino spectra from nuclear reactors”, Phys. Rev. C **84**, 024617 (2011).
- [87] W. Hampel et al., “GALLEX solar neutrino observations: results for GALLEX IV”, Phys. Lett. B **447**, 127–133 (1999).
- [88] J. N. Abdurashitov et al., “The SAGE and LNGS experiment: Measurement of solar neutrinos at LNGS using gallium from SAGE”, Astropart. Phys. **25**, 349–354 (2006).
- [89] L. Alvarez-Ruso et al. (NuSTEC), “NuSTEC White Paper: Status and challenges of neutrino–nucleus scattering”, Prog. Part. Nucl. Phys. **100**, 1–68 (2018).
- [90] V. De Romeri et al., “DUNE-PRISM sensitivity to light dark matter”, Phys. Rev. D **100**, 095010 (2019).
- [91] E. Bertuzzo et al., “Neutrino masses and mixings dynamically generated by a light dark sector”, Phys. Lett. B **791**, 210–214 (2019).
- [92] E. Bertuzzo et al., “Dark Neutrino Portal to Explain MiniBooNE Excess”, Phys. Rev. Lett. **121**, 241801 (2018).
- [93] R. Acciarri et al. (MicroBooNE, SBND, ICARUS), “A Proposal for a Three Detector Short-Baseline Neutrino Oscillation Program in the Fermilab Booster Neutrino Beam”, arXiv:1503.01520 (2015).
- [94] R. Acciarri et al., “Construction of precision wire readout planes for the Short-Baseline Near Detector (SBND)”, JINST **15**, P06033 (2020).

- [95] *HAMAMATSU Datasheet - R5912*, Accessed: 25-02-2023, https://www.hamamatsu.com/resources/pdf/etd/LARGE_AREA_PMT TPMH1376E.pdf.
- [96] S. Gao (SBND), “Low Noise Cold Electronics System for SBND LAr TPC”, in APS DPF Meeting (Oct. 2019).
- [97] *730 Digitizer Family 16/8 Ch. 14-bit 500 MS/s Digitizer*, Accessed: 25-02-2023, <https://www.caen.it/products/v1730/>.
- [98] *740 Digitizer Family 64/32 Ch. 12-bit 62.5 MS/s Digitizer*, Accessed: 25-02-2023, <https://www.caen.it/products/vx1740/>.
- [99] I. Kreslor (SBND), *SBND CRT Technical Note*, tech. rep. (2016).
- [100] M. Stancari, “Capabilities of the SBND Trigger System”, in CPAD Workshop (2022).
- [101] K. Biery et al., “Flexible and Scalable Data-Acquisition Using the artdaq Toolkit”, in IEEE Real Time Conference (2018).
- [102] A. A. Aguilar-Arevalo et al. (MiniBooNE), “Neutrino flux prediction at MiniBooNE”, Phys. Rev. D **79**, 072002 (2009).
- [103] M. Backfish, *Measuring the Bunch Length of the Booster Neutrino Beamline Beam*, tech. rep. (2015).
- [104] M. Backfish, *MiniBooNE Resistive Wall Current Monitor*, tech. rep., FERMILAB-TM-2556-AD (2015).
- [105] S. Agostinelli et al., “Geant4—a simulation toolkit”, Nucl. Instrum. Meth. A **506**, 250–303 (2003).
- [106] D. W. Schmitz, “A Measurement of Hadron Production Cross Sections for the Simulation of Accelerator Neutrino Beams and a Search for ν_μ to ν_e Sscillations in the δm^2 about equals $1 - eV^2$ Region”, PhD thesis (Columbia University, 2008).
- [107] E. L. Snider et al., “LArSoft: Toolkit for Simulation, Reconstruction and Analysis of Liquid Argon TPC Neutrino Detectors”, J. Phys. Conf. Ser. **898**, 042057 (2017).
- [108] B. Patt et al., “Higgs-field portal into hidden sectors”, arXiv:0605188 (2006).
- [109] S. Weinberg, “A New Light Boson?”, Phys. Rev. Lett. **40**, 223–226 (1978).
- [110] S. D. Porzio, “Searches for Heavy Neutral Lepton Decays in the MicroBooNE Detector”, PhD thesis (The University of Manchester, 2019).
- [111] L. Alvarez-Ruso et al. (GENIE), “Recent highlights from GENIE v3”, Eur. Phys. J. ST **230**, 4449–4467 (2021).
- [112] D. Heck et al., *CORSIKA: A Monte Carlo code to simulate extensive air showers*, tech. rep., FZKA-6019 (1998).
- [113] J. Tena-Vidal et al. (GENIE), “Neutrino-nucleus CC0 π cross-section tuning in GENIE v3”, Phys. Rev. D **106**, 112001 (2022).
- [114] *Liquid Argon Experiment tune*, Visited 06/05/2024, https://github.com/GENIE-MC/Generator/tree/master/config/AR23_20i.
- [115] C. Berger et al., “Erratum: lepton mass effects in single pion production by neutrinos [phys. rev. d 76, 113004 (2007)]”, Phys. Rev. D **77**, 059901 (2008).
- [116] MicroBooNE et al., “Measurement of the atmospheric muon rate with the microboone liquid argon tpc”, JINST **16**, P04004 (2021).

References

- [117] V. N. Ivanchenko et al., *GEANT4 simulation of energy losses of ions*, tech. rep., CERN-OPEN-99-300 (1999).
- [118] D. Garcia-Gamez et al., “Predicting Transport Effects of Scintillation Light Signals in Large-Scale Liquid Argon Detectors”, *Eur. Phys. J. C* **81**, 349 (2021).
- [119] H. Yu et al., “Augmented signal processing in Liquid Argon Time Projection Chambers with a deep neural network”, *JINST* **16**, P01036 (2021).
- [120] L. Tung, “Signal Processing in SBND with WireCell”, in APS April Meeting (2024).
- [121] *GausHitFinder*, (Visited 03/04/2024), https://github.com/LArSoft/larreco/larreco/HitFinder/GausHitFinder_module.cc.
- [122] E. Tyley, “Reconstructing and Selecting Electron Neutrino and Anti-Neutrino Interactions on Argon in the Short-Baseline Near Detector”, PhD thesis (The University of Sheffield, 2023).
- [123] *MVAAlg*, (Visited 21/05/2024), <https://github.com/LArSoft/larana/blob/develop/larana/ParticleIdentification/MVAAlg.cxx>.
- [124] *OpT0Finder*, (Visited 22/05/2024), https://github.com/SBNSoftware/sbndcode/blob/develop/sbndcode/OpT0Finder/SBNDOpT0Finder_module.cc.
- [125] *CRUMBS*, (Visited 22/05/2024), https://github.com/SBNSoftware/sbncode/blob/develop/sbncode/CosmicID/CRUMBS_module.cc.
- [126] *Razzled*, (Visited 22/05/2024), https://github.com/SBNSoftware/sbncode/blob/develop/sbncode/PID/Razzled_module.cc.
- [127] J. Serrano et al., “The White Rabbit Project”, in *ICALEPCS*, Vol. 1 (2009), p. 93.
- [128] A. Aloisio et al., “FPGA implementation of a high-resolution time-to-digital converter”, in *IEEE Nuclear Science Conference*, Vol. 1 (2007), p. 504.
- [129] P. Abratenko et al. (MicroBooNE), “First demonstration of $\mathcal{O}(1 \text{ ns})$ timing resolution in the MicroBooNE liquid argon time projection chamber”, *Phys. Rev. D* **108**, 052010 (2023).
- [130] C. Adams et al. (MicroBooNE), “Calibration of the charge and energy loss per unit length of the MicroBooNE liquid argon time projection chamber using muons and protons”, *JINST* **15**, P03022 (2020).
- [131] S. Amoruso et al., “Study of electron recombination in liquid argon with the ICARUS TPC”, *Nucl. Instrum. Meth. A* **523**, 275–286 (2004).
- [132] A. A. Abud et al. (DUNE), “Reconstruction of interactions in the ProtoDUNE-SP detector with Pandora”, *Eur. Phys. J. C* **83**, 618 (2023).
- [133] M. Szydagis et al., “A Review of Basic Energy Reconstruction Techniques in Liquid Xenon and Argon Detectors for Dark Matter and Neutrino Physics Using NEST”, *Instrum.* **5**, 13 (2021).
- [134] H. H. Andersen et al., *Hydrogen Stopping powers and ranges in all elements* (Pergamon Press, 1977).
- [135] “ICRU Report 49, Stopping Power and Ranges for Protons and Alpha Particles”, *Journal of the ICRU* **os-25** (1993).
- [136] M. Miyajima et al., “Average energy expended per ion pair in liquid argon”, *Phys. Rev. A* **9**, 1438–1443 (1974).

- [137] P. Abratenko et al. (ICARUS), “Angular dependent measurement of electron-ion recombination in liquid argon for ionization calorimetry in the ICARUS liquid argon time projection chamber”, arXiv:2407.12969 (2024).
- [138] G. Cowan, *Statistical data analysis* (Clarendon Press, 1998).
- [139] *SBN Event Weighting*, (Visited 26/06/2024), <https://github.com/SBNSoftware/sbncode/tree/develop/sbncode/SBNEventWeight>.
- [140] R. J. Barlow et al., “Fitting using finite Monte Carlo samples”, Comput. Phys. Commun. **77**, 219–228 (1993).
- [141] G. V. Stenico, “SBND Trigger System: Status and MTC/A Configuration”, Phys. Sci. Forum **8** (2023).

Appendix A

Hardware Triggering at SBND

The hardware triggering at SBND is discussed in Section 4.2.5, Chapter 4. Here a detailed description of the trigger signal distribution is provided. Fig. A.1 depicts the flow chart of signal inputs and outputs to and from the Penn Trigger Board (PTB), shown as the pink box, across different subsystems. The PTB receives the beam signal from the beam subsystem, shown as the green box. The beam signal denoted as *early warning* informs the PTB about the status of the Booster Neutrino Beam (BNB), indicating whether the beam has arrived at the detector hall. Also shown by the green box is the White Rabbit timing subsystem that distributes the Pulse Per Second (PPS) and clock signals to the PTB and other subsystems to maintain synchronisation. Description of the White Rabbit timing subsystem is given in Chapter 7.

From the detection subsystems, the input signals to the PTB are from PhotoMultiplier Tubes (PMTs) and Cosmic Ray Taggers (CRTs). The PMTs provide information regarding the energy deposited inside the detector and whether its magnitude and location are consistent with a neutrino interaction. The readout electronics of the PMTs are CAENV1730SB digitisers, shown as the light blue boxes. Each digitiser sends a *majority trigger* directly to the PTB if its channels cross a threshold. In addition, the number of channels above a threshold from the digitisers, denoted as *board sums*, are directed to the Master Trigger Card Analog (MTC/A), shown as the red box. The MTC/A performs a simple logic gate calculation to determine the number of PMT pairs above a threshold, denoted as *threshold crossing*, informing the PMT signal intensity and location. This signal from the MTC/A is input directly to the PTB. On the other hand, signals from the CRTs for triggering are much simpler. Coincident hits from any CRT walls, shown by the purple box, form *CRT triggers*, which are input straight to the PTB.

Once a trigger is formed, the PTB sends the trigger signals to subsequent readout subsystems to acquire the event, shown as the pink arrows leaving the PTB in Fig. A.1. An event contains two types of trigger signals: a single Event Trigger (ETRIG) and multiple Flash Triggers (FTRIGs). The ETRIG is issued to the TPC readout, shown as the orange box labelled Nevis Trigger Board (Nevis TB) to acquire waveforms from the wire planes. The FTRIGs are issued to the readouts of the PDS, shown as the light and dark blue boxes, to capture waveforms from the optical detectors.

An additional usage of the PTB is that it can output clock signals to some of the readout electronics. For the Nevis TB of the Time Projection Chamber (TPC) readout electronics, it sends a PPS signal that is locked to the PPS signal that it receives from the White Rabbit timing system. This is depicted as the light pink arrow leaving the PTB to the Nevis TB. Moreover, the PTB sends a T1 Reset to CRT readout electronics shown as the pink arrows leaving the PTB to CRT, of which the CRT T1 clock is detailed in Section 7.2. The T1 Reset signal here is locked to a very early warning signal from the beam system called \$1D, with some added delay so that it occurs some time *before* when the beam spill begins. Originally, the T1 Reset signal to the CRT readouts was the BES signal from the beam system, which occurred *right* when a beam spill begins. Resetting the T1 clock enforces some dead time on CRT readouts. Therefore, the T1 Reset signal was switched from the beam system to the PTB to have dead time outside of the beam spill window.

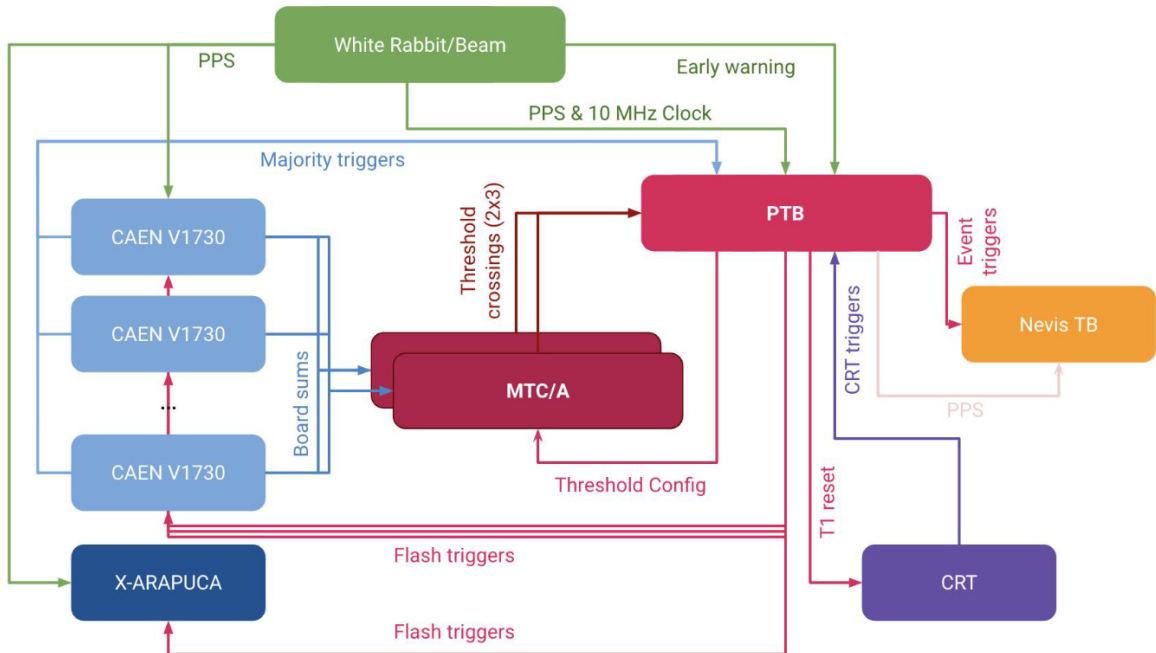


Fig. A.1 Distribution of the signals in the hardware triggering [141].

Appendix B

Data Streaming at SBND

The data streaming as the final step of the Data Acquisition (DAQ) at SBND is previously summarised in Section 4.2.6, Chapter 4. Details of the data streaming process is given here. After the event builder machines complete building a physics event, the resulting event can be filtered and sent to various storage locations for different analysis purposes, commonly referred to as data streaming. The artdaq Toolkit provides options to incorporate customisable filtering steps in real time [101]. This allows the event builders to apply complex software metrics based on the fragment contents of an event. Once an event successfully passes through the filter, the event builders send it to a location defined by the filter for storage. However, if an event fails to pass the filters, it will be discarded during data taking.

The artdaq Toolkit also includes a built-in process for streaming data between event builder machines and online monitoring platforms. While operating in real time, fragments from boardreaders and physics events can be transmitted to these platforms for various monitoring purposes. SBND currently employs two online platforms: (1) Grafana and (2) Minargon.

Grafana provides real time monitoring of the status of DAQ processes. A section of the Grafana website is displayed in Fig. B.1 for the boardreaders of PMTs. In the top left panel, the run number 9307 and a dial indicating the trigger rate issued by the PTB at 5.60 Hz are shown. The right panels display 9 dials, corresponding to 9 CAEN digitisers, showing the PMT fragment rates sent by the digitisers to the event builders, which is in good agreement with the trigger rate. The bottom left graph illustrates the PMT fragment rates as a function of time. The bottom middle and right graphs depict the rates of empty

and missing PMT fragments as a function of time, which remain flat at zero, indicating a healthy DAQ state.

On the other hand, Minargon provides monitoring of the quality of data acquired by the DAQ. This online monitoring process applies simple reconstruction and event display to quantitatively verify the physics characteristics of an event. An example metric is displayed in Fig. B.2, which shows the root mean square of a PMT waveform baseline as a histogram in the left plot and as a function of time in the right plot. This metric helps monitor the baseline equalisation and stability over time.



Fig. B.1 Web page showing a section of Grafana for monitoring the status of PMT DAQ.

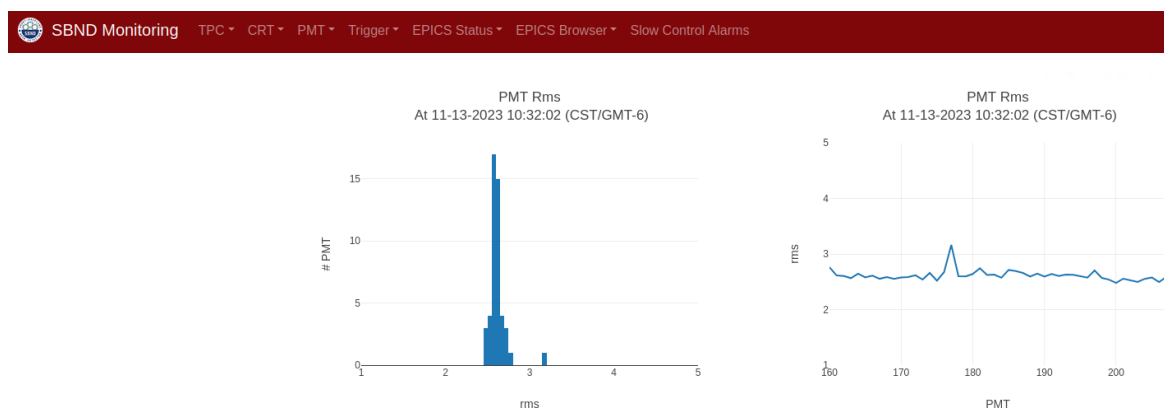


Fig. B.2 Web page showing a section of Minargon for monitoring the root mean square of a PMT waveform baseline.

Appendix C

Timing Distribution at SBND

The White Rabbit (WR) timing system at SBND is summarised in Section 7.1.1, Chapter 7. The signal distribution from the WR system is detailed here. Fig. C.1 illustrates the clock distribution across the Data Acquisition (DAQ) components. Starting from the SVEC-FD module, two clock frequencies are generated: (1) 10 MHz and (2) 6.25 MHz, shown by the green and blue arrows respectively. The 10 MHz clock signal is directed through an LVDS fan out, and input to the Penn Trigger Board (PTB), as shown by the green box. The 6.25 MHz clock signal is directed through an LVDS fan out, and distributed in a fan out mode to all CAEN digitisers, as shown by the blue box. Moreover, the PTB also propagates a very early warning signal \$1D from the Multi-Function Timing Unit (MFTU), as shown by the solid orange arrow and box. The \$1D signal is delayed by the PTB, and directed to a CRT T1 fan out module to make multiple copies, which are all input to the FEB modules, as

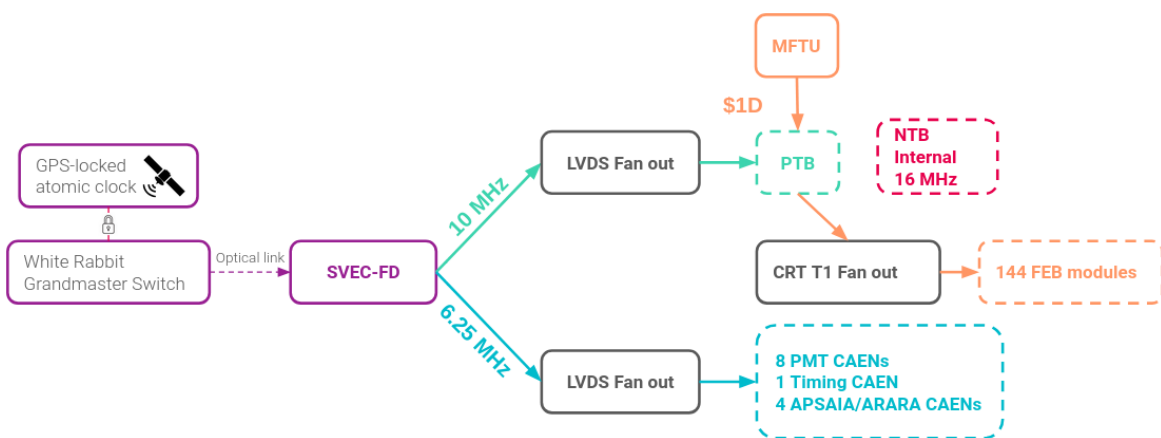


Fig. C.1 Clock signal distribution from the White Rabbit timing system to the DAQ subsystems.

shown by the dashed orange box. The Nevis Trigger Board (NTB), as shown by the red box, is the only readout component that does not receive an external clock. It instead uses an internal clock of 16 MHz.

Fig. C.2 shows the distribution of the Pulse Per Second (PPS) signal. The PPS is first generated by the SVEC-FD and input to fan out modules to make multiple copies. The copies are distributed to the PTB, CAEN digitisers and FEB modules (See Section 4.2.4). The NTB is a special case, where it receives the PPS from the PTB, where the TTL PPS signal is shifted to a NIM signal.

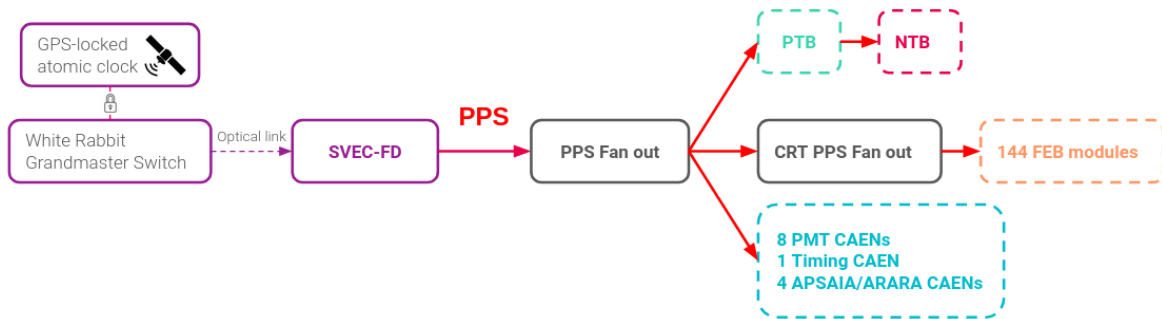


Fig. C.2 PPS signal distribution from the White Rabbit timing system to the DAQ subsystems.

Appendix D

Lenient Arrival Time Distributions

Arrival time distributions of HNLs, SM neutrinos and cosmic muons after the lenient selection are presented. Descriptions of the arrival time distribution are given in Section 9.1.4 and details of the lenient selection are provided in Section 9.5.

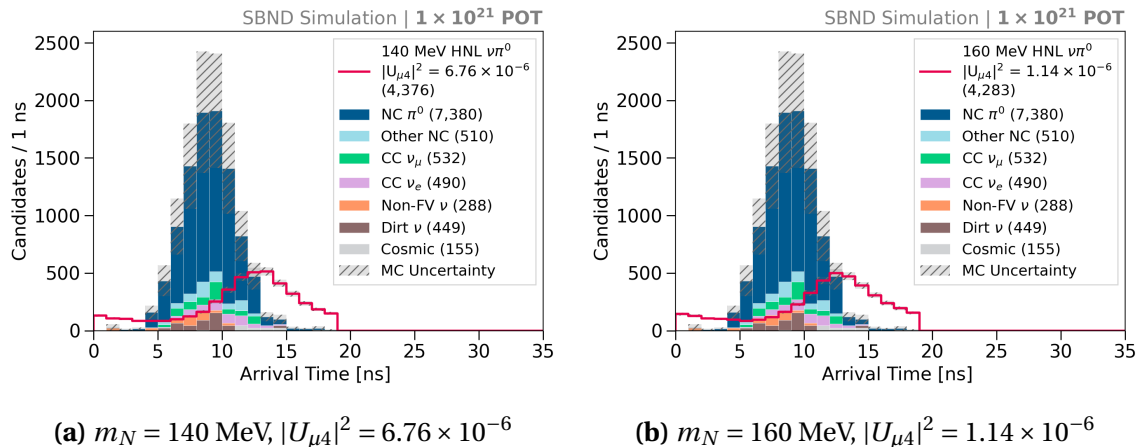


Fig. D.1 Arrival time distributions of HNLs, SM neutrinos and cosmic muons after the lenient selection, normalised to the exposure of 1×10^{21} POT. HNLs of mass m_N is normalised to the listed coupling $|U_{\mu 4}|^2$.

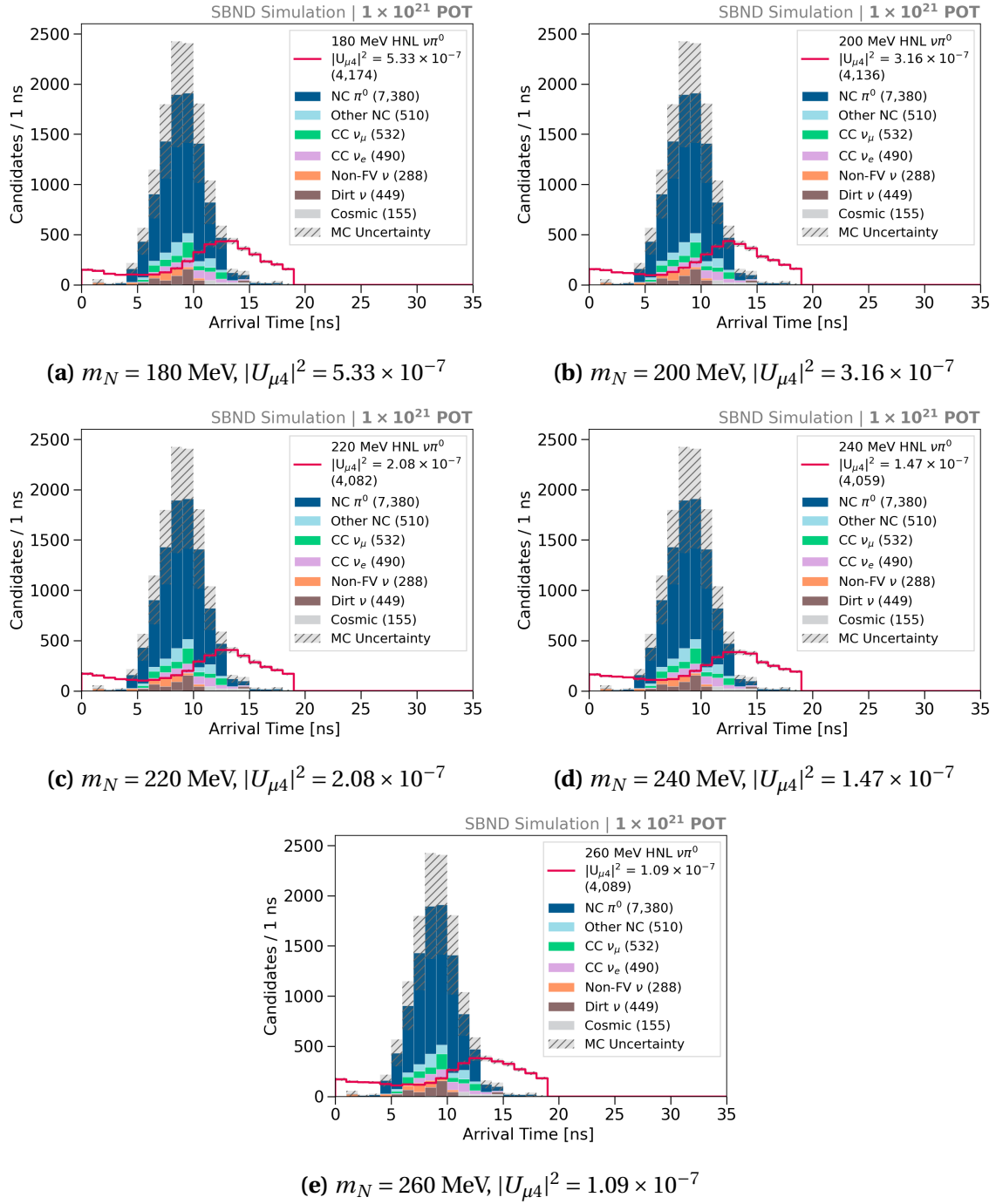


Fig. D.2 Arrival time distributions of HNLs, SM neutrinos and cosmic muons after the lenient selection, normalised to the exposure of 1×10^{21} POT. HNLs of mass m_N is normalised to the listed coupling $|U_{\mu 4}|^2$.

Appendix E

Stringent Arrival Time Distributions

Arrival time distributions of HNLs, SM neutrinos and cosmic muons after the stringent selection are presented. Descriptions of the arrival time distribution are given in Section 9.1.4 and details of the stringent selection are provided in Section 9.5.

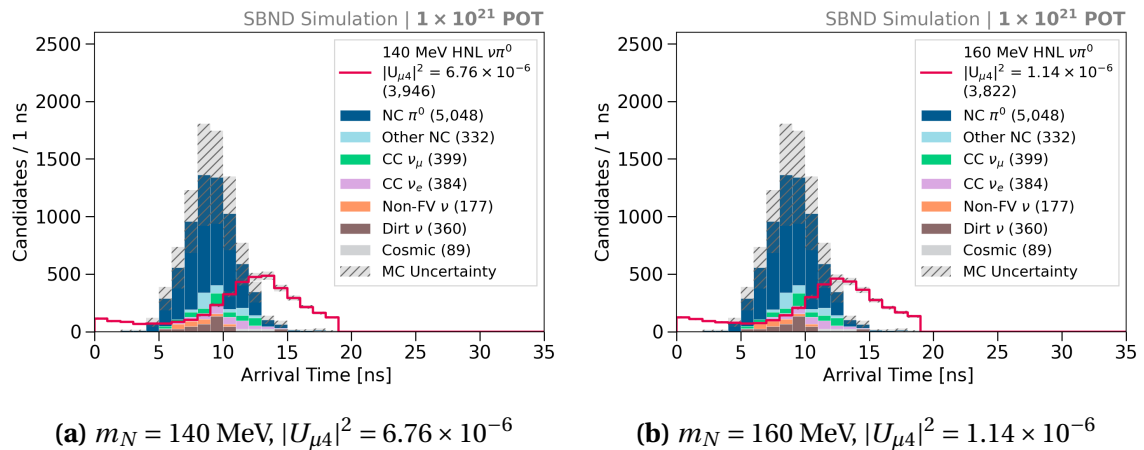


Fig. E.1 Arrival time distributions of HNLs, SM neutrinos and cosmic muons after the stringent selection, normalised to the exposure of 1×10^{21} POT. HNLs of mass m_N is normalised to the listed coupling $|U_{\mu 4}|^2$.

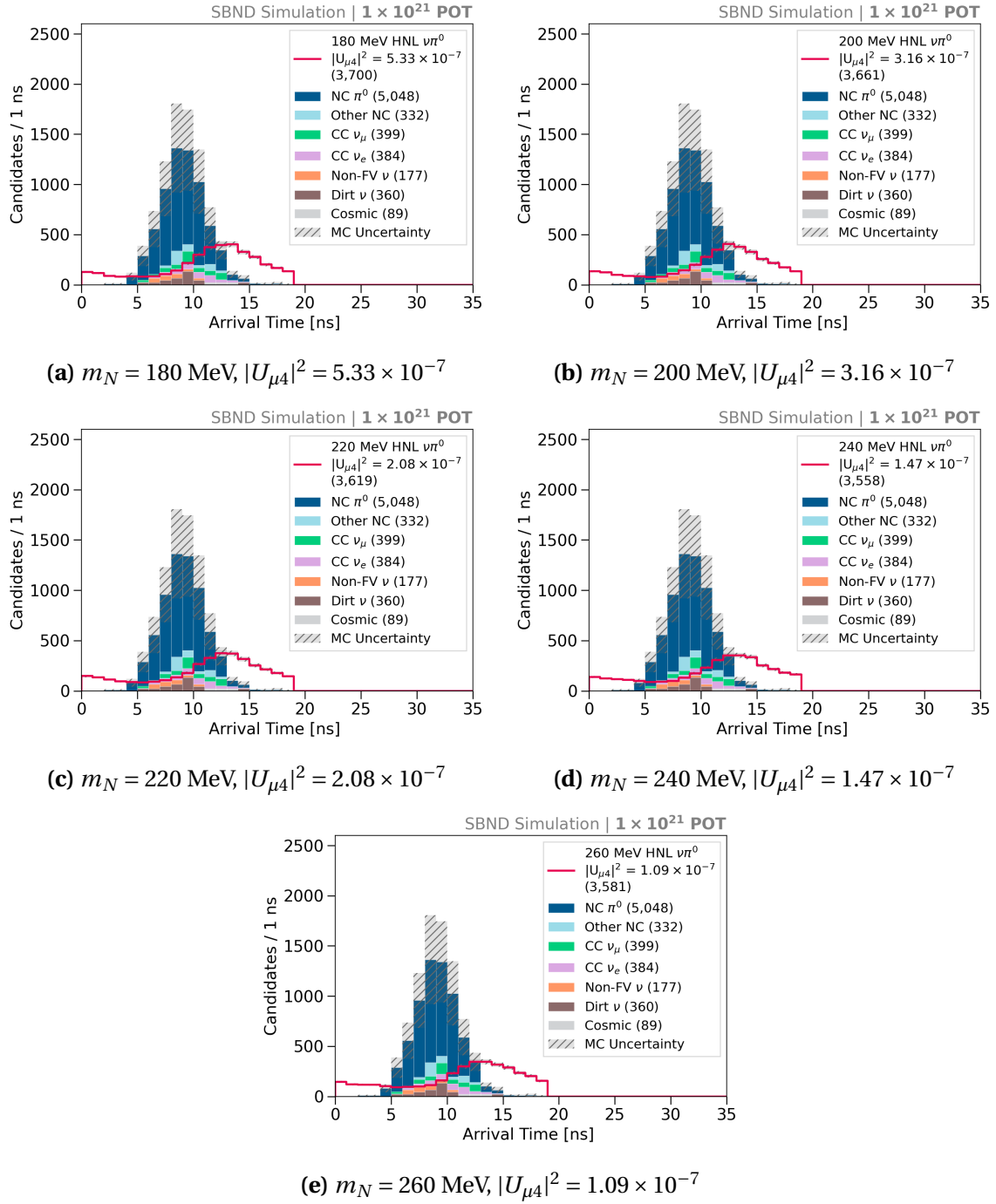


Fig. E.2 Arrival time distributions of HNLs, SM neutrinos and cosmic muons after the stringent selection, normalised to the exposure of 1×10^{21} POT. HNLs of mass m_N is normalised to the listed coupling $|U_{\mu 4}|^2$.

Appendix F

Smeared True Arrival Time Distributions

Arrival time distributions of HNLs, SM neutrinos and cosmic muons acquired by smearing true variables under the assumption of a timing resolution improvement are presented. Descriptions of the arrival time distribution are given in Section 9.1.4 and details of the smearing process are provided in Section 9.6.

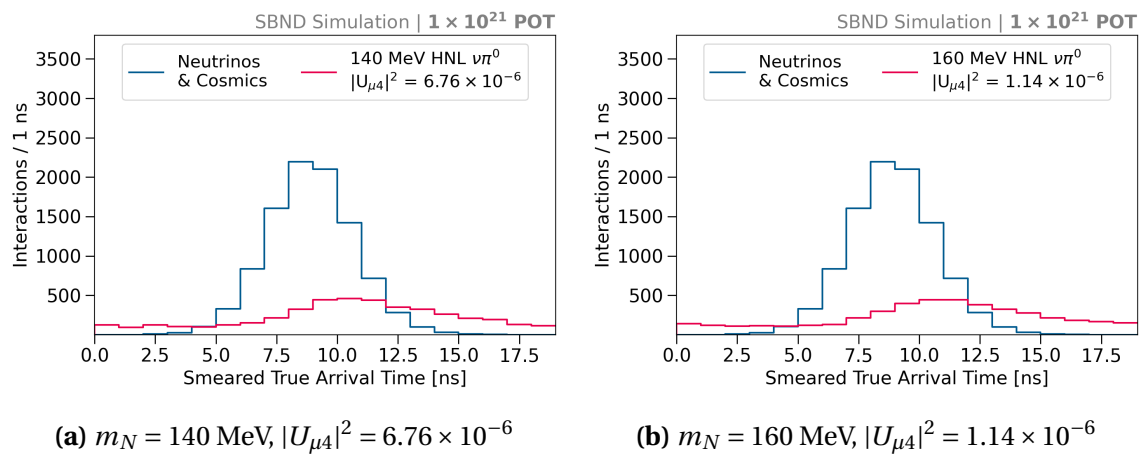


Fig. E.1 Arrival time distributions of HNLs, SM neutrinos and cosmic muons under the assumption of a timing resolution improvement, normalised to the exposure of 1×10^{21} POT. HNLs of mass m_N is normalised to the listed coupling $|U_{\mu 4}|^2$.

Smeared True Arrival Time Distributions

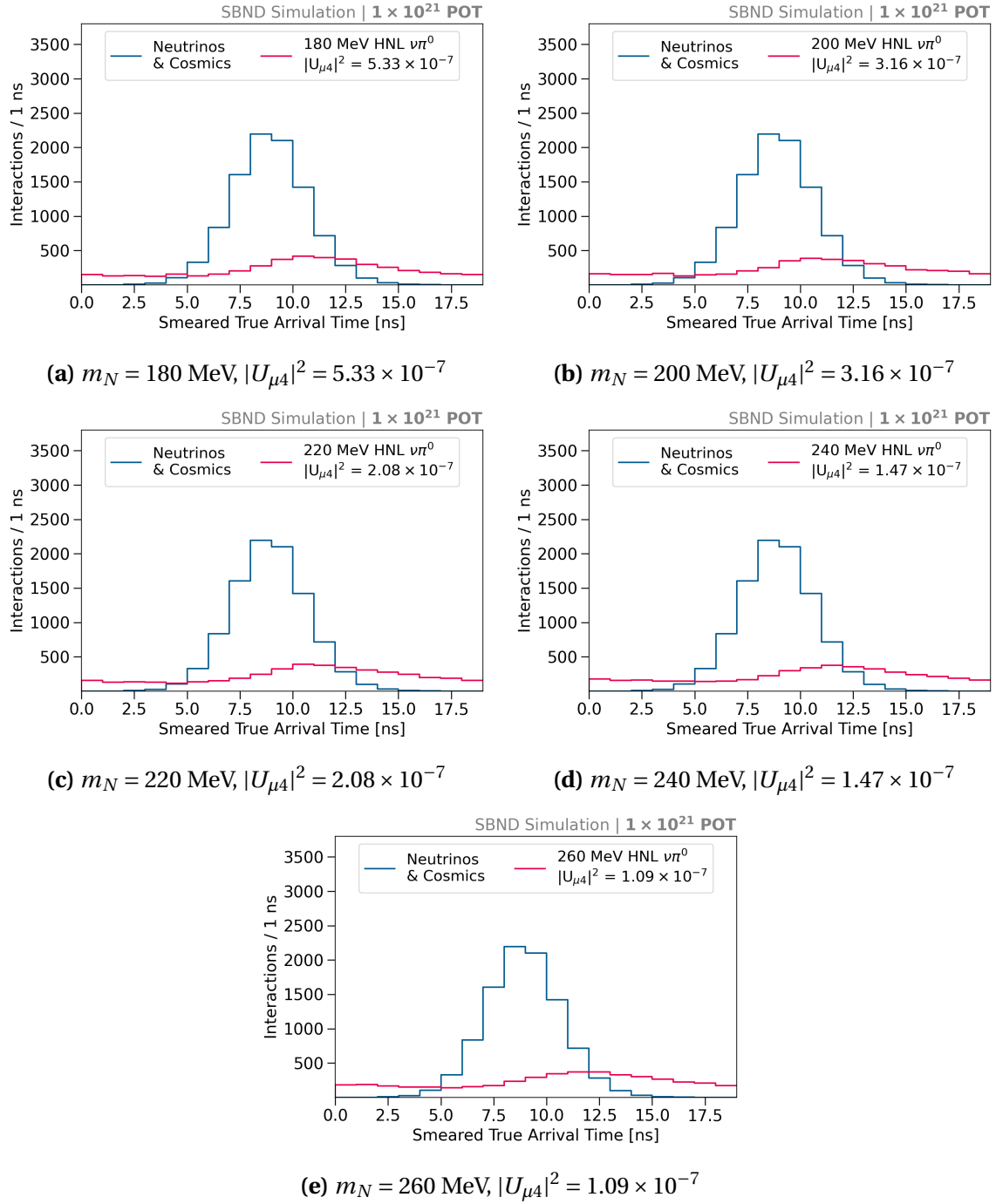


Fig. F.2 Arrival time distributions of HNLs, SM neutrinos and cosmic muons under the assumption of a timing resolution improvement, normalised to the exposure of 1×10^{21} POT. HNLs of mass m_N is normalised to the listed coupling $|U_{\mu 4}|^2$.